Institut für Angewandte Photophysik
Fachrichtung Physik
Fakultät Mathematik und Naturwissenschaften
der Technischen Universität Dresden

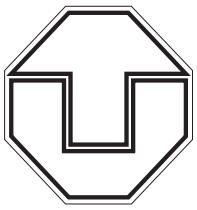

Controlling Excitons: Concepts for Phosphorescent Organic LEDs at High Brightness

DISSERTATION

zur Erlangung des akademischen Grades

DOCTOR RERUM NATURALIUM

vorgelegt von

Sebastian Reineke

geboren in Eisenach am 9. Dezember 1979

November 2009

1. Gutachter: Prof. Dr. Karl Leo
2. Gutachter: Prof. Dr. Josef Salbeck

Diese Arbeit wurde am 27. November 2009 eingereicht und am 1. Juli 2010 verteidigt.

"Junge, hast Du einen guten Vortrag gehabt?"

– In Erinnerung an meine Mutter Berit Reineke.

Abstract

This work focusses on the high brightness performance of phosphorescent organic light-emitting diodes (OLEDs). The use of phosphorescent emitter molecules in OLEDs is essential to realize internal electron-photon conversion efficiencies of 100 %. However, due to their molecular nature, the excited triplet states have orders of magnitude longer time constants compared to their fluorescent counterparts which, in turn, strongly increases the probability of bimolecular annihilation. As a consequence, the efficiencies of phosphorescent OLEDs decline at high brightness – an effect known as efficiency roll-off, for which it has been shown to be dominated by triplet-triplet annihilation (TTA).

In this work, TTA of the archetype phosphorescent emitter $Ir(ppy)_3$ is investigated in time-resolved photoluminescence experiments. For the widely used mixed system CBP:$Ir(ppy)_3$, host-guest TTA – an additional unwanted TTA channel – is experimentally observed at high excitation levels. By using matrix materials with higher triplet energies, this effect is efficiently suppressed, however further studies show that the efficiency roll-off of $Ir(ppy)_3$ is much more pronounced than predicted by a model based on Förster-type energy transfer, which marks the intrinsic limit for TTA. These results suggest that the emitter molecules show a strong tendency to form aggregates in the mixed film as the origin for enhanced TTA. Transmission electron microscopy images of $Ir(ppy)_3$ doped mixed films give direct proof of emitter aggregates. Based on these results, two concepts are developed that improve the high brightness performance of OLEDs. In a first approach, thin intrinsic matrix interlayers are incorporated in the emission layer leading to a one-dimensional exciton confinement that suppresses exciton migration and, consequently, TTA. The second concept reduces the efficiency roll-off by using an emitter molecule with slightly different chemical structure, i.e. $Ir(ppy)_2(acac)$. Compared to $Ir(ppy)_3$, this emitter has a much smaller ground state dipole moment, suggesting that the improved performance is a result of weaker aggregation in the mixed film.

The knowledge gained in the investigation of triplet-triplet annihilation is further used to develop a novel emission layer design for white organic LEDs. It comprises three phosphorescent emitters for blue, green, and red emission embedded in a multilayer architecture. The key feature of this concept is the matrix material used for the blue emitter FIrpic: Its triplet energy is in resonance with the FIrpic excited state energy which enables low operating voltages and high power efficiencies by reducing thermal relaxation. In order to further increase the device efficiency, the OLED architecture is optically optimized using high refractive index substrates and thick electron transport layers. These devices reach efficiencies which are on par with fluorescent tubes – the current efficiency benchmark for light sources.

Kurzfassung

Diese Arbeit richtet ihren Fokus auf die Untersuchung der Leistungsfähigkeit von phosphoreszenten, Licht-emittierenden organischen Dioden (OLEDs) im Bereich hoher Betriebshelligkeiten. Phosphoreszente Emittermoleküle werden in OLEDs eingesetzt, um interne Elektron-Photon Konversionseffizienzen von 100 % zu erreichen. Begründet in ihrer chemischen Struktur, weisen die angeregten Triplett-Zustände dieser Emitter um Größenordnungen längere Zeitkonstanten als die Emission fluoreszenter Materialien auf, sodass die Wahrscheinlichkeit bimolekularer Auslöschung stark ansteigt. Dies resultiert in einem deutlichen Effizienzrückgang phosphoreszenter OLEDs bei großen Leuchtdichten. Dieser als Roll-off bekannter Effekt wird bei hohen Anregungsdichten hauptsächlich durch Triplett-Triplett Annihilation (TTA) bestimmt.

In der Arbeit wird TTA an einem Modellmolekül, dem phosphoreszenten Emitter $Ir(ppy)_3$, in zeitaufgelösten Photolumineszenz Experimenten untersucht. Für das bekannte Emittersystem CBP:$Ir(ppy)_3$ wird bei hohen Anregungsdichten Host-Guest TTA beobachtet, was einen zusätzlichen, ungewünschten TTA Kanal darstellt. Dieser Effekt wird durch das Verwenden von Matrix Materialien mit höherer Triplett Energie vermieden, jedoch zeigt sich in weiteren Untersuchungen, dass der Roll-off deutlich stärker ist als von einem auf Förster Energieübertrag basierendem Modell vorhergesagt, welches selbst ein intrinsisches Limit für TTA in phosphoreszenten Systemen beschreibt. Die Diskrepanz zwischen experimenteller Beobachtung und Modellvorhersage wird durch eine strarke Tendenz des Emitters, Aggregate zu bilden, erklärt, was TTA deutlich verstärkt. Diese Aggregate werden mit Hilfe von Transmissionselektronenmikroskopie an $Ir(ppy)_3$-dotierten Mischsystemen direkt nachgewiesen. Basierend auf diesen Resultaten werden zwei Konzepte entwickelt, um die Effizienz phosphoreszenter Systeme bei hohen Helligkeiten zu verbessern. Im ersten Ansatz werden dünne intrinsische Schichten des Matrixmaterials in die Emissionsschicht eingebaut, was die Exzitonenbewegung in einer Raumrichtung und damit auch TTA stark unterdrückt. Das zweite Konzept reduziert den Effizienz Roll-off durch die Verwendung eines phosphoreszenten Emitters $Ir(ppy)_2(acac)$ mit einer leicht abgeänderten Molekularstruktur. Im Vergleich mit $Ir(ppy)_3$ weist dieser ein deutlich kleineres Dipolmoment im molekularen Grundzustand auf, wodurch die Aggregation vermindert wird.

Aufbauend auf den Ergebnissen der TTA wird ein neuartiges Emissionsschicht-Design für weißes Licht entwickelt. In diesem Konzept werden drei phosphoreszente Materialien für blaue, grüne und rote Farbe in eine Vielschicht-Architektur eingebracht. Das Hauptmerkmal der Emissionsschicht ist die Wahl des Matrix-Materials für dem blauen Emitter FIrpic: Seine Triplett Energie liegt resonant zu dem FIrpic Triplett Zustand, wodurch niedrige Betriebsspannungen und hohe Leistungseffizienzen ermöglicht werden, da die thermische Relaxierung reduziert wird. Um die Effizienz dieser weißen OLEDs weiter zu erhöhen, wird die entwickelte OLED Architektur zusätzlich durch die Verwendung von hochbrechenden Substraten und dicken Elektronen-Transportschichten optisch optimiert. Bei beleuchtungsrelevanten Helligkeiten erreichen diese OLEDs das Effizienzniveau von Leuchtstoffröhren – letztere stellen heute den Effizienz-Maßstab dar.

Contents

List of Publications

Articles

[1] Q. Huang, S. Reineke, K. Walzer, M. Pfeiffer, and K. Leo, "Quantum efficiency enhancement in top-emitting organic light-emitting diodes as a result of enhanced intrinsic quantum yield," *Applied Physics Letters* **89**, 263512 (2006).

[2] S. Reineke, K. Walzer, and K. Leo, "Triplet-exciton quenching in organic phosphorescent light-emitting diodes with Ir-based emitters," *Physical Review B* **75**, 125328 (2007).

[3] Q. Huang, R. Meerheim, K. Fehse, G. Schwartz, S. Reineke, K. Walzer, and K. Leo, "2nd generation organics: High power efficiency, ultra long life, and low-cost OLED devices," *SID 07 Digest International Symposium, Digest Of Technical Papers, Vol XXXVIII* **38**, 1282 (2007).

[4] S. Reineke, G. Schwartz, K. Walzer, and K. Leo, "Reduced efficiency roll-off in phosphorescent organic light emitting diodes by suppression of triplet-triplet annihilation," *Applied Physics Letters* **91**, 123508 (2007).

[5] G. Schwartz, M. Pfeiffer, S. Reineke, K. Walzer, and K. Leo, "Harvesting triplet excitons from fluorescent blue emitters in white organic light-emitting diodes," *Advanced Materials* **19**, 3672 (2007).

[6] S. Reineke, F. Lindner, Q. Huang, G. Schwartz, K. Walzer, and K. Leo, "Measuring carrier mobility in conventional multilayer organic light emitting devices by delayed exciton generation," *Physica Status Solidi B-Basic Solid State Physics* **245**, 804 (2008).

[7] G. Schwartz, S. Reineke, K. Walzer, and K. Leo, "Reduced efficiency roll-off in high-efficiency hybrid white organic light-emitting diodes," *Applied Physics Letters* **92**, 053311 (2008).

[8] R. Meerheim, S. Scholz, S. Olthof, G. Schwartz, S. Reineke, K. Walzer, and K. Leo, "Influence of charge balance and exciton distribution on efficiency and lifetime of phosphorescent organic light-emitting devices," *Journal Of Applied Physics* **104**, 014510 (2008).

[9] R. Meerheim, S. Scholz, G. Schwartz, S. Reineke, S. Olthof, K. Walzer, and K. Leo, "Efficiency and lifetime enhancement of phosphorescent organic devices - art. no. 699917," *Organic Optoelectronics And Photonics III* **6999**, 99917 (2008).

[10] S. Winter, S. Reineke, K. Walzer, and K. Leo, "Photoluminescence degradation of blue OLED emitters - art. no. 69992N," *Organic Optoelectronics And Photonics III* **6999**, N9992 (2008).

[11] S. Reineke, G. Schwartz, K. Walzer, and K. Leo, "Direct observation of host-guest triplet-triplet annihilation in phosphorescent solid mixed films," *Physica Status Solidi RRL* **3**, 67 (2009).

[12] S. Mladenovski, S. Reineke, and K. Neyts, "Measurement and simulation of exciton decay times in organic light-emitting devices with different layer structures," *Optics Letters* **34**, 1375 (2009).

[13] S. Mladenovski, S. Reineke, and K. Neyts, "Modeling exciton decay time and radiative efficiency in organic light-emitting diodes," *Proceedings of the 29th International Display Research Conference EuroDISPLAY* , 43 (2009).

[14] G. Schwartz, S. Reineke, T. C. Rosenow, K. Walzer, and K. Leo, "Triplet Harvesting in Hybrid White Organic Light-Emitting Diodes," *Advanced Functional Materials* **19**, 1319 (2009).

[15] S. Reineke, G. Schwartz, K. Walzer, M. Falke, and K. Leo, "Highly phosphorescent organic mixed films: The effect of aggregation on triplet-triplet annihilation," *Applied Physics Letters* **94**, 163305 (2009).

[16] S. Reineke, F. Lindner, G. Schwartz, N. Seidler, K. Walzer, B. Lüssem, and K. Leo, "White organic light-emitting diodes with fluorescent tube efficiency," *Nature* **459**, 234 (2009).

[17] S. Reineke, T. C. Rosenow, B. Lüssem, and K. Leo, "Improved High-Brightness Efficiency of Phosphorescent Organic LEDs Comprising Emitter Molecules with Small Permanent Dipole Moments," *Advanced Materials* , DOI: 10.1002/adma.201000529 (2010).

Conference Contributions

[1] S. Reineke, M. Pfeiffer, K. Walzer, and K. Leo, "Triplet exciton quenching in organic phosphorescent LEDs," *Frühjahrstagung der Deutschen Physikalischen Gesellschaft, Dresden*, poster CPP 23.34 (2006).

[2] S. Reineke, K. Walzer, M. Pfeiffer, and K. Leo, "Triplet Exciton Quenching in Organic Light-Emitting Diodes with Ir-based Emitters," *MRS Fall, Boston*, talk S13(5) (2006).

[3] S. Reineke, F. Lindner, Q. Huang, K. Walzer, and K. Leo, "Delayed recombination in organic phosphorescent light-emitting diodes due to charge storage," *DPG Physics School: Charge Transport in Organic Materials: From Single Molecules to Devices, Bad Honnef*, poster (2007).

[4] S. Reineke, G. Schwartz, K. Walzer, and K. Leo, "Improved efficiency of phosphorescent organic light-emitting devices at high brightness," *Frühjahrstagung der Deutschen Physikalischen Gesellschaft, Berlin*, poster SYSA 5.62 (2008).

[5] S. Reineke, G. Schwartz, and K. Walzer, K. Leo, "All-phosphor white light-emitting diodes based on endothermic population of the blue phosphor leading to high power efficiency," *SPIE Optics and Photonics, San Diego*, talk 7051(30) (2008).

[6] S. Reineke, G. Schwartz, and K. Leo, "Exciton dynamics of phosphor-doped mixed solid films at high brightness: The effect of aggregation," *International Conference of Electroluminescence 7, Dresden*, talk OR 8a.2 (2008).

[7] S. Reineke, "White Organic LEDs with Fluorescent Tube Efficacy," *OLEDs World Summit, San Francisco*, invited talk (2009).

[8] S. Reineke, "Realizing white organic LEDs with fluorescent tube efficiency," *International Workshop on Flexible and Printable Electronics, Muju Resort*, invited talk (2009).

Patent Applications

[1] S. Reineke, K. Walzer, and K. Leo, "Bauelement zur phosphoreszenten Lichtemission aus Triplett-Zuständen und Verfahren zur Herstellung solcher Bauelemente," Patent Application DE 10 2007 033 209 A1 (2007).

[2] S. Reineke, K. Walzer, and K. Leo, "Phosphoreszierendes Bauelement mit organischen Schichten," Patent Application DE 10 2007 061 755.2 (2007).

[3] T. C. Rosenow, S. Reineke, B. Lüssem, and K. Leo, "Organisches, elektrolumineszentes Bauelement zur Erzeugung weißen Lichts," Patent Application DE 10 2009 048 604.6 (2009).

Chapter 1

Introduction

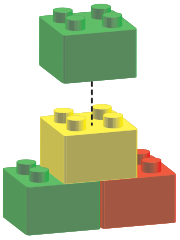

In some respects, working with organic semiconductors is best compared to playing with LEGO™. For both, it is not the set of building blocks but rather the imagination that defines how far one gets. Mainly due to the apparently infinite number of organic molecules, which are known already or available from synthesis, almost any application can be realized. Representing the first devices made of organic materials, organic light-emitting diodes (OLEDs) have attracted much interest. Based on early investigations of electrically generated emission from single crystals [1], Tang and VanSlyke developed the first thin film device in 1987, consisting of two organic layers with a total thickness of 135 nm sandwiched in between two electrodes. This simple OLED reached attractive values for both the electron-photon conversion efficiency and operating voltage, the latter for the first time being below 10 V [2]. By diluting highly efficient fluorescent laser dyes in the organic layers, the electroluminescent efficiency could be more than doubled [3]. Shortly after achieving these results, further investigations showed that the internal electroluminescence efficiency is rather limited due to the fact that in organic amorphous systems approximately three triplet excited states (excitons) are generated for each singlet exciton [4, 5]. Therefore, only 25 % of the excitation could be utilized for radiative recombination in these early devices. In the mid-1990s, Thompson and colleagues introduced a new kind of emitting material: An organometallic complex with the ability to efficiently emit from a triplet excited state (phosphorescence) [6]. It opened the door to internal electron-photon conversion efficiencies of one, a fourfold increase compared to OLEDs based on fluorescence, as now both singlet and triplet excited states could be harvested for light emission [7]. Today, in conjunction with electrically doped transport layers, phosphorescent devices with very high external quantum efficiencies [8] and outstanding long-term stability [9] have been reported. Furthermore, much effort is spent on the development of white organic LEDs, as they are the only flat, large-area light source with very high efficiency [10, 11].

Among other applications like organic solar-cells [12] and organic thin-film transistors [13–15], which are intensively investigated as well, the OLED technology has already reached industrial levels – first products like cellular phones, digital cameras,

and picture frames with OLED-based displays are being sold worldwide. Recently, Sony introduced the world's first 11" active matrix OLED TV, the XEL-1, which entered mass production. In contrast to many point-source technologies, the OLED with its layered architecture offers an unique design freedom, spanning from small display pixels with an excellent wide viewing angle and brilliant colour to large-area, flat lighting tiles for indoor illumination [16]. Whenever large areas are desired to be uniformly lit up, organic LEDs will be the first choice as they do not need extra diffusers to homogenously distribute the light. Additionally, the OLED technology offers much freedom in the choice of substrate and contact materials. The softness of the organic materials allows to fabricate OLEDs on flexible plastic substrates, which will capture completely new markets. Furthermore, transparent devices can be fabricated by using appropriate contact materials, so that they can be integrated into common window glass, to use the window as light source during the night time.

For many future applications, especially for general lighting and outdoor signage, the OLEDs are required to operate at high brightness, typically a few thousand candela per meter square, in order to compete with existing technologies. However, OLEDs suffer from a strong reduction of efficiency at higher intensities – an effect referred to as *efficiency roll-off*. It is particularly pronounced for phosphorescent emitters which is due to the long radiative lifetime τ of the emitting species. Here, optimized organometallic complexes have radiative lifetimes down to microseconds [6], while typical fluorescent molecules are accompanied with time constants of few nanoseconds, which is about three orders of magnitude shorter [17, 18].

One of the open issues is to minimize this efficiency decrease of phosphorescent systems, in order to benefit from the very high phosphorescence quantum yield in organic LEDs also at high device brightness. In literature, there is broad agreement that triplet-triplet annihilation, among other processes like triplet-polaron quenching and field assisted exciton dissociation, is the dominant bimolecular quenching process at high brightness, as it scales quadratically with the generated exciton density n within the device [19, 20]. Additionally, for white OLEDs it becomes an inevitable task to realize a balanced emission from differently emitting compounds within an emission layer (typical thickness 20 - 30 nm), because the exciton generation very often takes place in the very proximity (a few nanometers) of adjacent layers. Therefore, concepts must be found to manage the exciton distribution – at best without losses.

This introduction is followed by a brief motivation in Chapter 2 for the work presented in subsequent chapters. It highlights that phosphorescent emitters, which are inevitable for efficient devices, suffer from a strong reduction of their efficiency at high brightness, due to their molecular electronic properties. Furthermore, it points out that most of the potential OLED applications will demand high luminance levels, thus, it is not always possible to fully benefit from the potential of electrophosphorescence. Chapter 3 discusses the basic theory of organic semiconductors with the focus on high brightness non-linearities caused by bimolecular annihilation. This chapter

closes with an introduction to state-of-the-art organic LEDs and the materials used in this work. Chapter 4 covers all experimental aspects including sample preparation, device evaluation and experimental set-ups used.

Chapters 5 and 6 investigate triplet-triplet annihilation (TTA) in state-of-the-art phosphorescent emitting systems. It is the scope of this study to gain a deeper understanding of its underlying *mechanisms*. While it is a widely accepted opinion among experts that the *process* TTA , i.e. the quenching of a triplet excited state upon interaction of two triplets, dominantly causes the efficiency roll-off [19–22], the manifold microscopic *mechanisms*, which keep this process running, are not fully explored. For instance, it is still an open issue to what extent the microscopic film composition affects exciton motion within the mixed film and, consequently, the strength of TTA. Chapter 5 investigates triplet-triplet annihilation in two systems, where the host material, in which the phosphor is diluted, is varied. These host materials mainly differ in the energy of their triplet excited state (T_1). When the energy difference between host and phosphor T_1-state is reduced, unwanted host-guest TTA occurs in addition to the commonly observed guest-guest TTA [23]. This is followed by Chapter 6, in which the process TTA is linked to the microscopic composition of the phosphorescent mixed films. It turns out that diffusion based TTA in densely packed aggregates of emitter molecules within the mixed film is responsible for enhanced annihilation that is not predicted from both model and experiment [24]. Based on these results, a novel emission layer design with 1D exciton confinement abilities is introduced that suppresses exciton migration and, consequently, the diffusion based TTA contribution [25]. This chapter is closed by a comparison of two very similar, green emitting phosphorescent molecules that show differences in their roll-off characteristics. They are appointed to the different strength of aggregate formation as a result of different dipole moments of the emitters [26].

Chapter 7 introduces a novel multicolour emission layer for highly efficient white organic LEDs. Here, the EML concept with 1D exciton confinement from Chapter 6, comprising interlayers to suppress exciton motion, sets the basis for this approach. Both, thin intrinsic interlayers between differently emitting sublayers and a host material for the blue phosphor with resonant triplet energy, establish a basis for white OLEDs with the highest power efficiencies reported so far. Additionally adopting high refractive index glass substrates to the white OLED architecture, an optimized device yields a power efficiency of 90 lumen per watt at an illumination relevant brightness of 1,000 candela per meter square [27]. This value exceeds the power efficiencies of fluorescent tubes in a fixture with typical values of 60-70 lumen per watt, clearly proving OLEDs to have the potential to become the next generation light source.

The last Chapter 8 summarizes this work and provides an outlook for future research in the field of high brightness electrophosphorescence. For white OLEDs, it gives an efficiency forecast by considering the current performance status.

Chapter 2

Organic LEDs at High Brightness

A brief motivation for this work is given in this chapter. Illustrative examples are used to highlight the fundamental problems that are faced at high brightness OLED operation. After providing a definition of the quantity brightness, the range of high brightness, especially for organic LEDs, will be subsequently explained. Various potential OLED applications that demand high excitation levels are introduced and, if reasonable, compared to existing technologies. Finally, this chapter discusses the need for phosphorescence in efficient electroluminescence and outlines, why high brightness is still challenging, especially for phosphorescent systems.

2.1 OLEDs in Brief

Light-emitting diodes (LEDs) are known for decades. The first observation of light being emitted from a diode as current was passed through it, dates back to the year 1927 [28]. Today, they are used for manifold applications like car headlights, LCD backlights, flashlights, etc. They even find their way into the general lighting sector.

In contrast to conventional LEDs, the functional materials of organic light-emitting diodes (OLEDs) are organic semiconducting compounds. LEDs are perfect point sources to the human perception because they are very small, owing to the crystallinity of the semiconductors used. OLEDs, however, are ultra-thin, area-emitting light sources, which presumably can be scaled to any size. Figure 2.1 shows a schematic cross-section of a standard OLED on the left and a photograph of a white OLED with a 2 x 2 cm^2 active area on the right hand side. Typical state-of-the-art devices comprise a multilayer stack of different organic materials, which is sandwiched between the anode and cathode, with a total thickness of only a few hundred nanometers. As an external voltage is applied to the contacts, positive (holes) and negative (electrons) charge carriers are injected from anode and cathode into the organic semiconductors, respectively, and forced to move towards each other. These charges meet in the organic material to form excited molecular states, which will eventually emit light as they recombine.

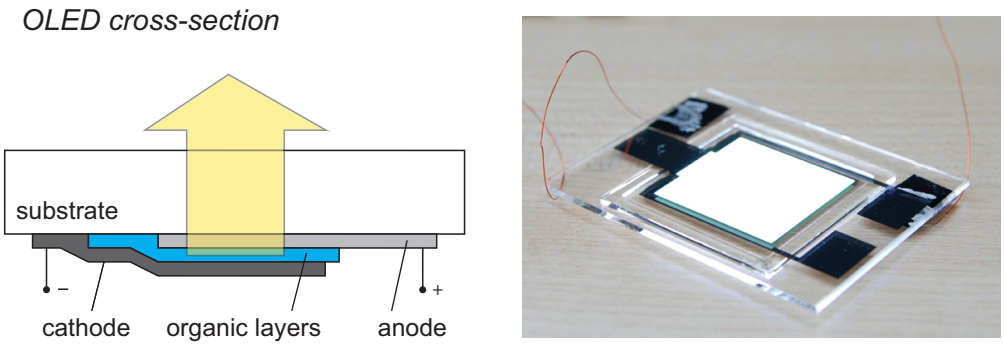

Figure 2.1: Left: Schematic cross-section of a bottom-emitting OLED. Typically, the substrate is 1 mm and the OLED stack (including electrodes) a few hundred nanometers thick. The anode is transparent, the cathode highly reflective. Right: Photograph of a white OLED in operation.

There are two fundamentally different types of OLEDs: small molecule based OLEDs and polymer based OLEDs (also called PLEDs). Owing to the nature of the materials used for these two types of OLEDs, they require different preparation methods. While OLEDs comprising small molecules are typically prepared by thermal evaporation or organic vapor phase deposition (OVPD), PLEDs can be fabricated by spin-coating or printing technologies.

The direction of light emission can be easily modified by a variation of the electrode materials. As depicted in Figure 2.1, OLEDs with a transparent electrode in contact to a glass substrate and a highly reflective electrode capping the device will emit light through the substrate. This conventional layout is referred to as *bottom-emitting* OLED. By switching transparent and reflective electrode, a change in the direction of emission, away from the substrate, is achieved – these devices are consequently called *top-emitting* OLEDs [29]. This provides an additional design freedom to use opaque substrates. Finally, by using transparent electrodes on both sides, *transparent* organic LEDs can be realized [30], which is very interesting for 'see-through' applications. Using interconnecting layers, *stacked* devices can be fabricated by consecutively preparing more than one OLED on top of each other [31–33].

A rapidly growing research field are organic LEDs emitting white light (*white* OLEDs) for general illumination applications. This is realized by additive colour mixing of the emission of differently emitting molecules, spanning the visible spectrum. Two very common approaches are distinguished: the stacked white OLEDs, where differently emitting monochrome OLEDs are vertically stacked (see above) [32, 33], and the single unit white OLEDs. In the latter, the white light originates from a single, but often complex emission layer [10, 11, 34–39].

The OLEDs that will be discussed in this work are small molecule based OLEDs in the bottom-emitting device layout. A more detailed description of the working principle of organic LEDs will be given in Sections 3.6 and 3.7.

2.2 High Brightness Applications

Before investigating the *brightness* of certain applications, this physical quantity needs to be defined briefly. Organic LEDs, among many other light-emitting applications, are usually characterised by *photometric* quantities, which include brightness, and its synonym *luminance*. Photometry, in contrast to radiometry, weights light of different wavelength differently, according to the sensitivity of the human eye. This assures that light sources of different colour, which appear equally bright to the eye of observer, have the same brightness.

In Figure 2.2, the weighting functions $s(\lambda)$ and $V(\lambda)$ are shown. In radiometry ($s(\lambda) = 1$), the radiation of a light source is treated in an absolute fashion while the photometry weights the radiation with the sensitivity of the human eye, $V(\lambda)$. In general, for continuous emission, the *radiant flux* Φ_r (unit: Watt = W) – the radiometric quantity describing the power emitted from a light source – is linked to its photometric analogue, the *luminous flux* Φ_ph (unit: Lumen = lm), using the following equation:

$$\frac{\mathrm{d}\Phi_\mathrm{r}}{\mathrm{d}\lambda} = K_\mathrm{m} \cdot V(\lambda) \cdot \frac{\mathrm{d}\Phi_\mathrm{ph}}{\mathrm{d}\lambda}. \tag{2.1}$$

The conversion factor $K_\mathrm{m} = 683\,\mathrm{lm/W}$ initially was chosen in the Système International d'Unités (SI) to fit the old illumination quantity 'Hefnerkerze' [40].

The brightness L is now defined as the *luminous flux per unit solid angle* Ω_1 *and per unit projected emitting area* A_1. For the observation normal to the emitting surface, it reads:

$$\textbf{Brightness } \boldsymbol{L} = \frac{\mathrm{d}^2\Phi_\mathrm{ph}}{\mathrm{d}\Omega_1 \mathrm{d}A_1} \left[\frac{\mathrm{lm}}{\mathrm{sr\,m^2}} = \frac{\mathrm{cd}}{\mathrm{m^2}}\right], \tag{2.2}$$

involving the definition for the SI unit of the *luminous intensity*: Candela = cd. If the emitting area A_1 is observed under an oblique angle ϕ, the projected area $A_1 \cos\phi$ needs to be considered.

At this stage, a definition for the range of high brightness for organic phosphorescent systems is available. In general, there are two approaches to specify the transition from low to high luminance. First, one can link this definition to the human perception, i.e. high brightness corresponds to values where the human eye is glared. Based on various experimental series, $L_\mathrm{crit} = 730\,\mathrm{cd/m^2}$ is derived as critical luminance; beyond this value, an uncomfortable glare sets in [41]. It is worth noting that this value is determined for eyes adapted to the darkness. Above $10^4\,\mathrm{cd/m^2}$, human eyes are permanently glared, so that they cannot adapt to this brightness anymore. A different and more physical approach is to define high brightness for luminescent systems based on their photophysical properties. Here, high luminance is reached when the emission efficiency of the system starts to decline as a consequence of the high excitation levels applied to the system. As it will be shown in subsequent chapters, for organic LEDs, these two definitions roughly fall together. Thus, even state-of-the-art OLEDs, with efficiencies close to the internal limit, show a noticeable drop of efficiency between 100 and $1{,}000\,\mathrm{cd/m^2}$ [42].

In Figure 2.3, different OLED applications are sorted depending on their expected operating brightness. OLED-based computer displays and television screens, operat-

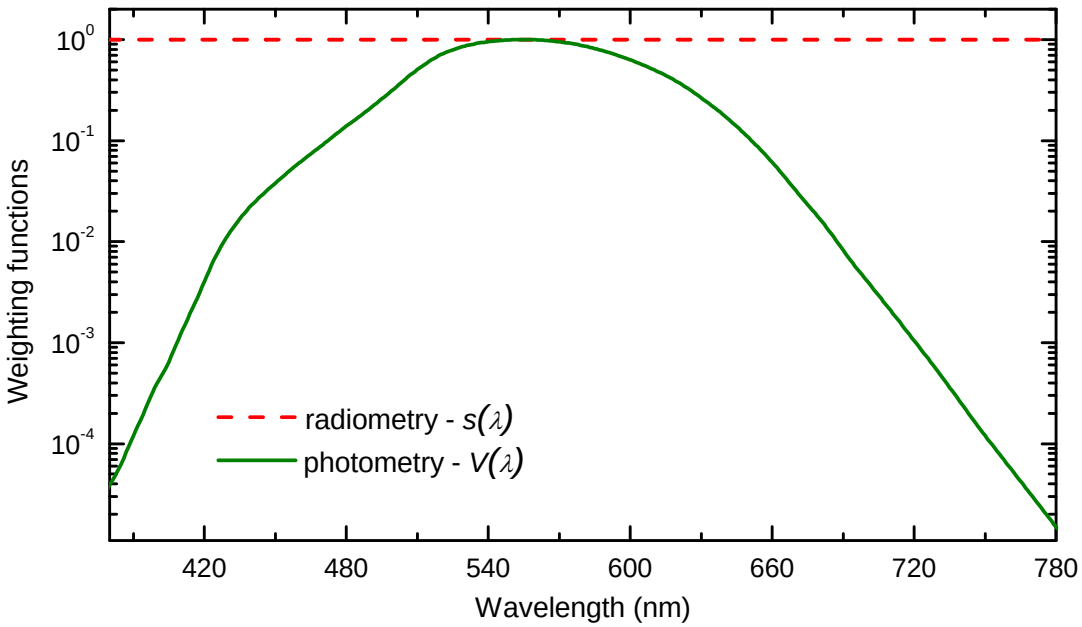

Figure 2.2: The functions $s(\lambda)$ and $V(\lambda)$ are plotted as a function of wavelength. They are used to weight the radiation emitted from a light source, depending on the set of quantities chosen (radiometric or photometric). The function $V(\lambda)$ resembles the sensitivity of the human eye, while the absolute values of the radiation are used in the radiometry.

ing at a few hundred candela per meter square, are still considered as low luminance applications. Researchers around the globe consider a luminance of 1,000 cd/m^2 to be 'illumination relevant'. Ideally, lighting tiles based on white OLEDs will have a brightness of a few thousand cd/m^2, in order to replace existing technologies. Organic LEDs for outdoor signage and traffic lights (including exterior car lights) are still at a conceptual stage but are expected to operate mainly under high brightness conditions. Among applications with high device brightness, the research and development of white organic LEDs for general lighting is seriously pushed to industrial levels. In 2004 the European Commission started to fund a large R&D project 'OLLA' within the Sixth Framework Programme (FWP) to develop high brightness OLEDs for next generation lighting applications. This project was superseded in 2008 by a follow-up, 'OLED100.EU', within the seventh FWP.

In contrast to many point-like light sources, the area-emitting OLEDs can be virtually scaled to any size. To use them as an indoor light source, white organic LEDs have to create a total luminance flux as comparable to existing technologies. A mid-size room is well illuminated with an incandescent lamp with a nominal power of 100 W. Considering their average power efficiency of 10 lm/W and, for the ease of this estimation, assuming that all its radiated power can be used for illumination by attaching a suited reflector, it produces a total luminance flux of 1,000 lumen. This is to be compared to an OLED-based lighting solution, as it is expected to be available in the coming years. Data sourced from a white organic LED, which

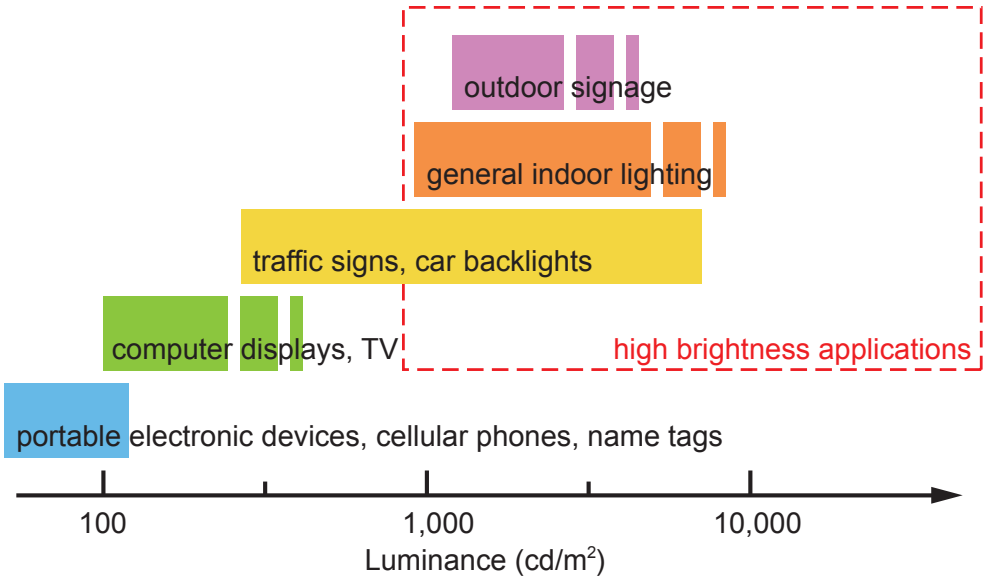

Figure 2.3: Different potential OLED applications are given with respect to their targeted operating brightness. The dashed box indicates the range of high brightness applications [41]. Depending on the specific design and customer needs, the upper limit for some categories is not distinct. Large size LCD-panels for outdoor signage and advertisement have been recently introduced by Sharp (1.83 m^2) and Samsung (1.55 m^2). These devices operate at 1,500 and 2,000 cd/m^2, respectively.

is developed within this work, serve as the calculation basis (cf. Chapter 7).[1] For OLEDs, the absolute current and, consequently, the total power consumption scales with the device area – the larger the area, the more power will be consumed. Figure 2.4 connects the lighting panel size with the corresponding estimated brightness that is required to produce a luminance flux of 1,000 lumen. Hence, for a wide range of panel size, operation at high luminance levels is required, e.g. a squared panel with an edge length of 30 cm would have a brightness of 1,900 cd/m^2. For other applications, where the panel size cannot simple be scaled up, even higher values are expected. If one aims to replace an existing 20 W halogen desktop lamp with a typical power efficiency of $\sim$ 25 lm/W by a 5 by 20 cm^2 OLED lighting tile, its brightness would need to be as high as 8,600 cd/m^2.

An additional argument for the need of high device brightness is the production cost for such lighting tiles. Roughly, the costs per emitted lumen is inversely proportional to the device brightness. For instance, the OLED100.EU project targets a production cost of €100/m^2. This would result in much different tile costs of €9 and €25 for squared tiles with 30 and 50 cm edge length, respectively.

[1] The mentioned white OLED has a power efficiency of 59.4 lm/W at 1,000 cd/m^2, which changes as a function of the current density, flowing through the device.

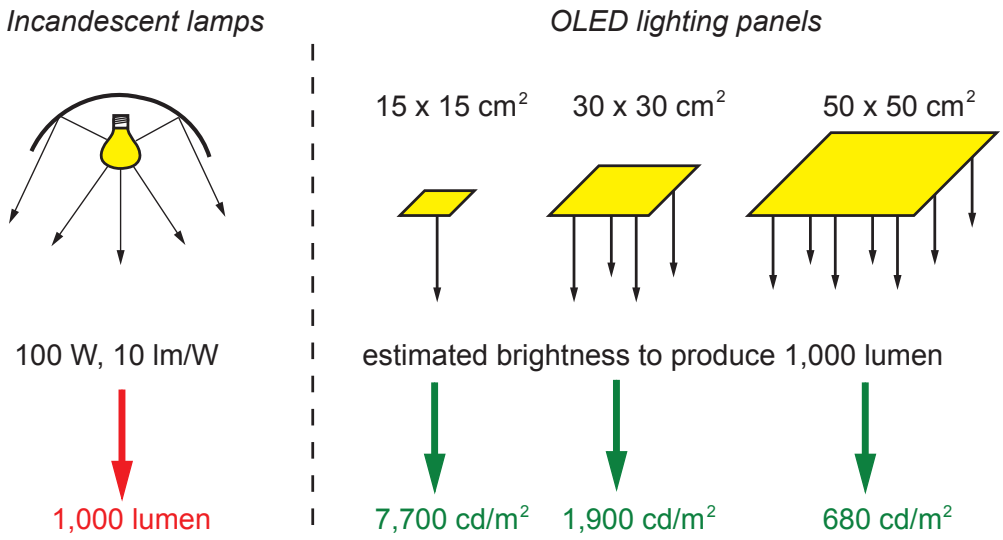

Figure 2.4: To estimate size and device brightness for future OLED lighting panels, they are schematically compared with incandescent lamps. The different light distributions of both technologies are not considered. To produce similar luminance flux like a 100 W incandescent lamp, OLEDs need to operate at high brightness, e.g. a reasonably sized 30 by 30 cm^2 panel would need a brightness of 1,900 cd/m^2.

2.3 Electrophosphorescence

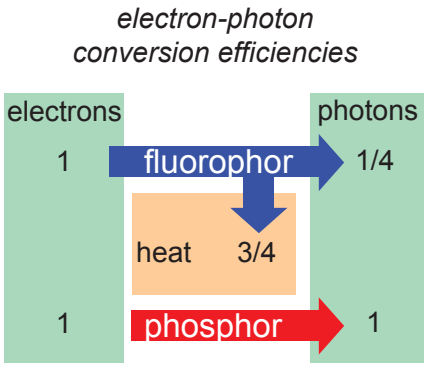

As mentioned earlier, light emission in organic LEDs is achieved by injection of charges from the electrode materials into the organic layers. Once injected, they move under the applied electric field to the emission layer, located in the center of the organic layers, where they meet and form excited molecular states – i.e. 'excitons'. In organic amorphous materials, the charges carry a spin-polarization, which in the end also influences the generation of excitonic states with different spin configurations. A state can either be spin antisymmetric – i.e. a singlet state, which fluoresces – or spin symmetric. The latter is called triplet state, the corresponding triplet emission is referred to as *phosphorescence* [43]. As a consequence of the state multiplicity, triplets are generated in a ratio of 3:1 with respect to singlet excitons [5]. Fluorescent emitter materials, for instance highly efficient laser dyes, do not allow radiative emission from their triplet state. These non-radiative triplets will be internally disactivated, e.g. via phonons, ultimately producing heat. Consequently, OLEDs comprising fluorophors as emission centers are limited to internal electron-photon conversion

efficiencies of 25 %, which is not sufficient for many of the applications mentioned above. Particularly tailored phosphorescent materials can overcome this problem, as they can both efficiently emit from and additionally redirect created singlets to their triplet states, resulting in internal efficiencies of unity, which is a fourfold increase compared to electrofluorescence [6].

2.4 The Downside of Phosphorescence

Relating to the previous section, it is evident that highly phosphorescent molecules need to be incorporated in OLEDs to maximize the device efficiency. Phosphorescence, which is known from 'glow in the dark' toys, actually involves a quantum mechanically forbidden transition from an excited triplet state to the ground state, as it undergoes a spin flip of the excited electron [43]. Intensive research effort has led to a new class of materials – organometallic complexes – which can emit very efficiently from their triplet state with time constants comparable to the *RC*-time of organic LEDs. If the excited state lifetime would be much longer than the device *RC*-time (ranging from ns to µs), the emitting molecules would saturate quickly, resulting in poor device efficiencies [6, 44]. Even though state-of-the-art phosphors have excited state lifetimes down to 1 µs, they are still about two orders of magnitude longer than their fluorescent counterparts, which is the main reason for different electroluminescent properties of fluorescence and phosphorescence.

The following calculation illustrates this difference without going further into details of resulting microscopic photophysical properties. These issues will be discussed in the following chapters. Representative fluorescent and phosphorescent excited state lifetimes are set to 10 ns and 1 µs, respectively, for simplification of this calculation [17, 20]. The brightness L, achieved within a device, is proportional to the excited state density n and inversely to the excited state lifetime τ [20]. It reads:

$$L \sim \frac{n}{\tau}. \tag{2.3}$$

Considering the spin statistics discussed in the preceding section, one derives for a fluorescent (fl) and a phosphorescent (ph) system, respectively:

$$L \sim \frac{n_{\mathrm{fl}}}{4 \cdot \tau_{\mathrm{fl}}} \quad \text{and} \quad L \sim \frac{n_{\mathrm{ph}}}{\tau_{\mathrm{ph}}}, \tag{2.4}$$

with corresponding subscripts. This leads to an expression for the ratio between the excited state densities $n_{\mathrm{ph}}/n_{\mathrm{fl}}$:

$$\frac{n_{\mathrm{ph}}}{n_{\mathrm{fl}}} \sim \frac{\tau_{\mathrm{ph}}}{4 \cdot \tau_{\mathrm{fl}}} = \left[\frac{1\,\mu\mathrm{s}}{4 \cdot 10\,\mathrm{ns}} = \mathbf{\frac{25}{1}} \right]. \tag{2.5}$$

The values in brackets are taken from above. To obtain the same luminance from phosphorescence and fluorescence, respectively, it is necessary to pump the phosphorescent system 25 times as high. For these considerations it is assumed that each emitting system consists solely of one material species, which can be different in real

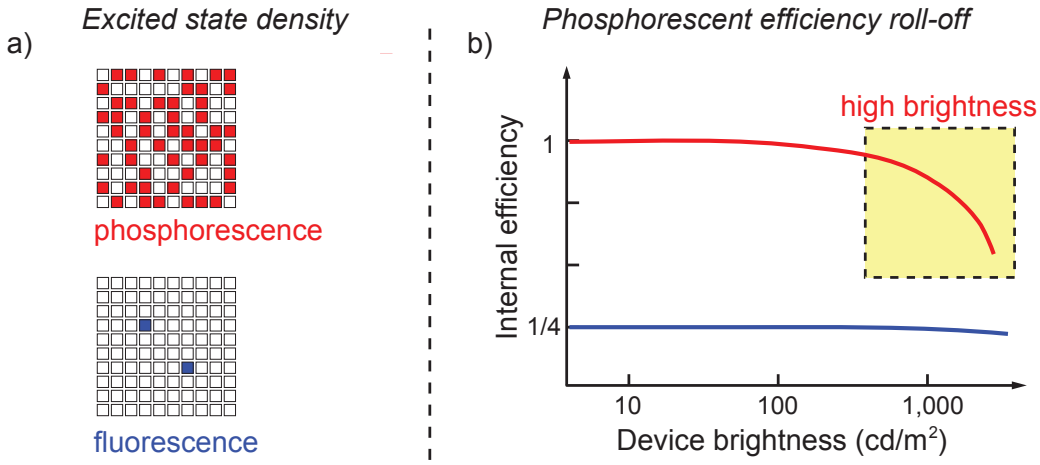

Figure 2.5: a) Excited state density for a given luminance is illustrated for both phosphorescent and fluorescent systems. Each box represents one molecule, the coloured ones excited states. Compared to fluorescence, the phosphorescence counterpart needs to be pumped more than one order of magnitude higher. b) The internal efficiencies of phosphorescent and fluorescent OLEDs are schematically plotted as a function of luminance. A pronounced reduction of efficiency is observed for phosphorescent OLEDs which typically fall into the region of high brightness applications.

device set-ups for singlet and triplet centered emission.[2] This difference in the excited state densities n_i is illustrated in Figure 2.5 a). For electrophosphorescence, the excited states apparently become very dense compared to fluorescence, where the majority of molecular states are in their ground state configuration. Without knowing the details of underlying processes, this highly dense system clearly holds a much higher probability of exciton annihilation by intra- and intermolecular interactions, such as the interaction with charges, with other excited states, or external impacts like the applied electric field. These interactions will reduce the total number of excited states, which ultimately reduces the efficiency at high excited state densities. The consequence for the performance of phosphorescent organic LEDs is depicted schematically in Figure 2.5 b). Despite its potentially four times higher electron-photon conversion efficiency, a phosphorescent OLED is accompanied with a pronounced reduction of efficiency at high brightness – the so-called efficiency roll-off.

In Figure 2.5 b), a range of future high brightness applications is depicted, accentuating the need for improvements. Extensive research is spent on the high brightness performance of organic phosphorescent LEDs, to benefit from their intrinsically high efficiency even at high luminance. It is the scope of this work to investigate microscopic, linear and non-linear effects which are important to understand this efficiency roll-off in detail. Based upon a profound understanding of highly excited phosphorescent systems, concepts will be introduced that improve the efficiency of state-of-the-

[2]Generally, phosphors, and to some extent fluorophors, have to be diluted into a host material to obtain high luminescence quantum yields.

art organic LEDs at high brightness. These approaches address both, monochrome and white organic LEDs. Just to highlight one result of this work, white organic LEDs with fluorescent tube efficiencies (reaching a power efficiency of 90 lm/W) are developed and discussed – the highest values reported so far.

Chapter 3

Organic Semiconductors

This chapter provides the fundamental theory of organic semiconductors. Initially, the electronic structure of organic molecules is developed, which is necessary to understand the essential material properties. Intermolecular energy transfer mechanisms, especially those determining processes at high excitation levels, are discussed in detail. The basic charge transport properties of organic semiconductors will be mentioned, as they are important to understand the working principle of organic devices. This chapter closes with an introduction to the fundamentals of organic LEDs. Since state-of-the-art OLEDs consist of multiple layers, the corresponding functionality will be stated. Throughout this discussion, the actual materials used in this work, will be introduced.

3.1 Molecular Orbitals

The ability of organic molecules to absorb and emit light, desirably in the ultraviolet and visible range of the electromagnetic spectrum, respectively, makes them highly attractive for the use in optoelectronic devices. Electromagnetic radiation, i.e. light, can be treated as oscillating electric and magnetic fields $\vec{E}(x,t)$ and $\vec{B}(x,t)$ which are perpendicular with respect to each other and to the propagation direction [45, 46]. The quantum mechanical description of light shows that absorption and emission are quantized, represented by *photons*. The energy E of these photons is inversely proportional to the corresponding wavelength λ:

$$E = \frac{hc}{\lambda}. \tag{3.1}$$

Here, h denotes *Planck's constant* having a value of $h = 6.626 \cdot 10^{-34}\,\mathrm{Js}$ and c the speed of light in vacuum ($c = 2.9979 \cdot 10^{8}\,\mathrm{m/s}$). This quantization determines the interaction of light with matter. Light can only be absorbed or emitted, if the energy difference between two states (i - initial and f - final) of the incorporated molecule equals the energy of the photon:

$$|E_\mathrm{i} - E_\mathrm{f}| = \frac{hc}{\lambda}. \tag{3.2}$$

It is therefore essential to gain knowledge about the electronic states of a system to understand the photo-physical properties in detail. The most important states of an organic compound are the *highest occupied* (HOMO) and *lowest unfilled molecular orbitals* (LUMO), which jointly form the frontier orbitals of the molecule. These frontier orbitals are important because they are largely responsible for many of the chemical and photo-physical properties of the molecule. According to the *Koopmans' theorem*, which ignores reorganization processes of the molecule, the HOMO energy of a molecule is equal to its ionization potential I_p and the LUMO energy corresponds to the electron affinity E_a of the molecule [47]. Their energetic difference defines the energy gap of a material, which is a very selective parameter for functional materials used in organic electronics. Taking exciton binding energies up to 1 eV into account,[1] organic compounds for the use in OLEDs, which shall emit in the visible range of the electromagnetic spectrum, should have an energy gap spanning from 2 to 4 eV.

Born-Oppenheimer Approximation

For organic molecules, the *Schrödinger equation* needs to be solved in order to determine their basic electronic properties. Considering the number of atoms of a typical organic molecule, it is easy to notice that these systems are highly complex, where approximations – even in the days of powerful computers – are inevitable. For instance pentacene, a rather small representative, comprising five linearly-fused benzene rings is made of 36 atoms.

The Schrödinger equation for a single molecule, which is completely described by its *total wavefunction* ψ^T, reads:

$$\mathcal{H}\psi^\mathrm{T} = E\psi^\mathrm{T}, \tag{3.3}$$

where $\mathcal{H}$ is the Hamiltonian and E the corresponding energy eigenvalue. To describe a stationary state of a system, it is sufficient to reduce the problem to the time-independent part of the wavefunction, which is the solution of the time-independent Schrödinger equation. This wavefunction ψ^T is a function of the electron coordinates $\vec{r} = r_1, r_2, \ldots$ and the inner coordinates $\vec{R} = R_1, R_2, \ldots$ of the nuclei. The *Born-Oppenheimer* approximation [45, 48] separates the electronic and vibrational parts of the total wavefunction,

$$\psi^\mathrm{T}_{j,v}(\vec{r}, \vec{R}) = \psi^{\vec{R}}_j(\vec{r}) \cdot \chi^j_v(\vec{R}). \tag{3.4}$$

This is indeed a reasonable approach, since the mass of a proton and an electron differ by a factor of 1836 and, therefore, the nuclei can be treated as fixed [49]. Here, j indicates the electronic and v the vibrational states, respectively. For a given geometry $\vec{R}$ of the system, $\psi^{\vec{R}}_j(\vec{r})$ is the eigenfunction to the corresponding electronic Hamilton operator $\mathcal{H}^{\vec{R}}_\mathrm{el}(\vec{r})$. Consequently, there are eigenfunctions $\chi^j_v(\vec{R})$ of the vibrational operator $\mathcal{H}_\mathrm{vib}(\vec{r}, \vec{R})$ for a certain electronic state j. The product ansatz of the total wavefunction ψ^T leads to a total energy of a certain molecular state, which can be

[1] This value differs for excited states in their electronic singlet and triplet configuration, with higher values for triplet states. This energy difference is discussed later in this section.

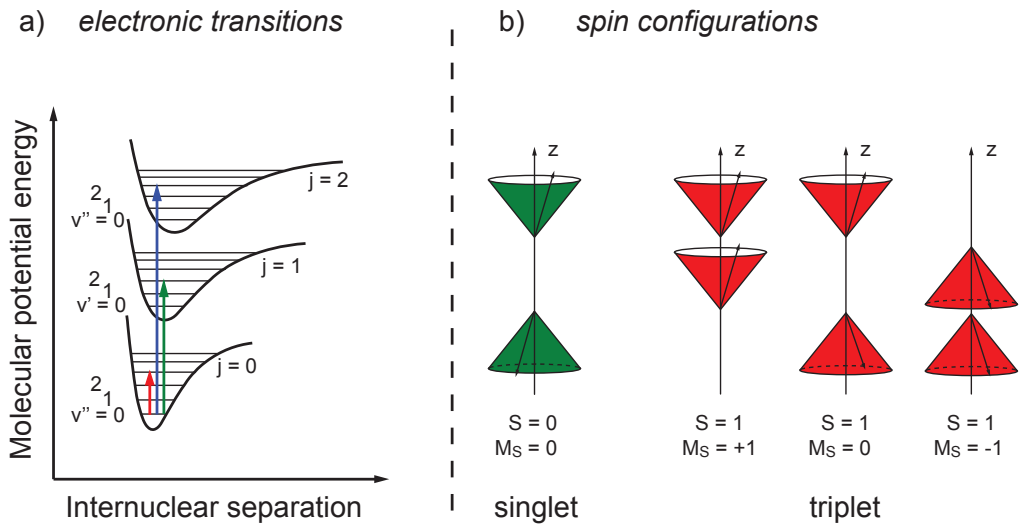

Figure 3.1: a) Illustration of the electronic states j with their corresponding vibrational substates v of an organic molecule. b) Spin configurations of an organic molecule. For a singlet state, the electrons spins have opposite orientation, so that they add up to zero. For $S = 1$, there are three possible configurations, which differ in the quantum number M_S for the projection of the spin on the z-axis (taken from [50]).

written as the sum of electronic and vibrational contributions:

$$E^{\mathrm{T}} = E^{\mathrm{el}} + E^{\mathrm{vib}}. \tag{3.5}$$

Figure 3.1 a) schematically shows the state distribution of a molecule in this approximation, where every electronic state is superposed by vibrational states. This also implies that the excitation energies of a system can be separated into electronic and vibrational contributions.

LCAO Method

To determine energies of molecular states and transition moments between different molecular states, it is necessary to access the corresponding wavefunctions $\psi_j^{\vec{R}}(\vec{r})$. Here, a common approach is the LCAO (Linear Combination of Atomic Orbitals) method in which the *molecular orbitals* (MOs) ϕ_i are produced from a combination of atomic orbitals (AOs) ξ_μ [50]. This can be expressed as:

$$\phi_i = \sum_\mu c_{\mu i} \xi_\mu, \tag{3.6}$$

with the coefficients $c_{\mu i}$. This method is exact as long as the basis functions ξ_μ for this linear combination is complete. Of course this would require an infinite basis set, which cannot be used in reality, where, for the ease of the calculation, approximations

must be made. Often, this basis contains only a few atomic orbitals. For illustration, this concept is applied to the hydrogen molecule (H_2). Here, the smallest set of basis functions are two AOs ξ_α and ξ_β, one for each of the hydrogen atoms α and β,[2] which creates two MOs:

$$\phi_+(\vec{r}) = N_+[\xi_\alpha(\vec{r}) + \xi_\beta(\vec{r})] \tag{3.7}$$

and

$$\phi_-(\vec{r}) = N_-[\xi_\alpha(\vec{r}) - \xi_\beta(\vec{r})], \tag{3.8}$$

with scaling factors N_+ and N_- that assure the normalization of the orbitals ($\langle\phi_i|\phi_i\rangle = 1$). The corresponding orbital densities for these wavefunctions read:

$$P_{+/-}(\vec{r}) = N^2_{+/-}[\xi^2_\alpha(\vec{r}) + \xi^2_\beta(\vec{r}) \pm 2\xi_\alpha(\vec{r})\xi_\beta(\vec{r})], \tag{3.9}$$

which apparently differ in the *overlap density* $\xi_\alpha(\vec{r})\xi_\beta(\vec{r})$. With respect to the isolated atom configuration, it is energetically favourable for electrons to occupy the state with a positive contribution of the overlap density, i.e. $\phi_+(\vec{r})$. This is crucial, because it represents an enhancement of the probability of finding an electron in the internuclear region, which makes this configuration a *bonding* state. In contrary, for $\phi_-(\vec{r})$ the orbital density between the hydrogen atoms is smaller compared to the densities of the isolated AOs, which is therefore an *antibonding* configuration [47, 50].

Spin Orbitals

According to the *Pauli principle*, each orbital can be occupied by two electrons with opposite spin, so that each linear combination produces two orbitals, which are referred to as *spin orbitals*. Introducing spin functions α and β, these spin orbitals can be written as $\Psi_k(j) = \phi_i(j)\alpha(j) =: \phi^i$ and $\Psi_l(j) = \phi_i(j)\beta(j) =: \bar{\phi}^i$ with the MOs ϕ_i from above [45]. Here, the electron coordinates (including spin coordinates) are represented by the electron number j. Each distribution of electrons to these spin orbitals is referred to as a *configuration*, represented by Φ. According to the Pauli principle, only electronic wavefunctions *antisymmetric* under an exchange of coordinates of two electrons are allowed:

$$\Phi(1,\ldots,i,j,\ldots,n) = -\Phi(1,\ldots,j,i,\ldots,n), \tag{3.10}$$

which can be best written as a *Slater determinant*:

$$\Phi(1,\ldots,i,j,\ldots,n) = |\,\Psi_1(1)\,\Psi_2(2)\ldots\Psi_n(n)| = \frac{1}{\sqrt{n!}}\begin{vmatrix} \Psi_1(1)\,\Psi_1(2)\ldots\Psi_1(n) \\ \Psi_2(1)\,\Psi_2(2)\ldots\Psi_2(n) \\ \vdots \\ \Psi_n(1)\,\Psi_n(2)\ldots\Psi_n(n) \end{vmatrix}. \tag{3.11}$$

The configuration with closed shells for the $n/2$ lowest MOs is the ground-state of a system [50]:

$$^1\Phi(1,\ldots n) = |\phi^1(1)\bar{\phi}^1(2)\phi^2(3)\ldots\phi^{n/2}(n-1)\bar{\phi}^{n/2}(n)|. \tag{3.12}$$

[2] These AOs are the well known 1s-orbitals of the hydrogen atom.

This wavefunction is an eigenfunction to both spin operators $\mathcal{L}^2$ and $\mathcal{L}_z$ with corresponding eigenvalues of $S = 0$ and $M_S = 0$, therefore it is referred to as *singlet state*, which is indicated by the preceding superscript '1' in ${}^1\Phi(1, \dots n)$. This picture changes for an excited system, where two orbitals are only occupied by one electron each. Now there are four possibilities to form products with the spin functions α and β, which ultimately results in four different Slater determinants of the type $|\phi^1(1)\bar{\phi}^1(2)\dots\phi^i(k)\bar{\phi}^i(k+1)\dots|$ etc. These wavefunctions still must be eigenfunctions to $\mathcal{L}^2$ and $\mathcal{L}_z$. The wavefunction with $S = 0$ and $M_S = 0$ is, similar to the ground state, a singlet state. The remaining three solutions correspond to $S = 1$, are therefore called *triplet state*, and are distinguished by their eigenvalue to $\mathcal{L}_z$ of $M_S = +1, 0, -1$. Accordingly, these configurations are denoted as ${}^3\Phi(1, \dots n)$. The possible spin configurations of an excited molecular system are schematically shown in Figure 3.1 b). Without external fields and in the non-relativistic limit, these triplet states are degenerate so that they have identical energies [45]. States of a certain multiplicity $M = 2S + 1$ can now be expressed as a linear combination of configurations of the same multiplicity and symmetry:

$$ {}^M\Psi_j^{\vec{R}}(1, \dots n) = \sum_K C_K {}^M\Phi_K(1, \dots n), \tag{3.13}$$

where Φ_K denotes any ground or excited configuration. The corresponding coefficients C_K can be obtained from a variational principle [50]. If the wavefunctions of Equation (3.13) are known, it is possible to calculate the electronic excitation energies between ground state 0 and excited state a:

$$\Delta E_{0\to\mathrm{a}}^{\mathrm{el}} = {}^{M'}E_{\mathrm{a}} - {}^{M}E_0 = \langle {}^{M'}\Psi_{\mathrm{a}}^{\vec{R}}|\mathcal{H}|{}^{M'}\Psi_{\mathrm{a}}^{\vec{R}}\rangle - \langle {}^{M}\Psi_0^{\vec{R}}|\mathcal{H}|{}^{M}\Psi_0^{\vec{R}}\rangle. \tag{3.14}$$

The transition moment $\vec{U}_{0\to\mathrm{a}}$ for such an excitation is calculated as:

$$\vec{U}_{0\to\mathrm{a}} = \langle {}^{M'}\Psi_0^{\vec{R}}|\mathcal{U}|{}^{M}\Psi_{\mathrm{a}}^{\vec{R}}\rangle, \tag{3.15}$$

where the operator $\mathcal{U}$ can be the operator of the electric dipole moment, the magnetic dipole moment or the electric quadrupole moment, depending on the transition.

Singlet-Triplet Splitting

The electronic wavefunction $\psi_j^{\vec{R}}(\vec{r})$ of an n-electron system is a function of $3n$ space coordinates of all electrons. Within the orbital approximation, this problem is reduced to a product wavefunction, called *Hartree-product*, where each orbital $\varphi_i(\vec{r}_i)$ is only a function of coordinates of one single electron:

$$\psi_j^{\vec{R}}(\vec{r}) \equiv \psi_j^{\vec{R}}(\vec{r}_1, \vec{r}_2, \dots) = \left[\prod_{i=1}^{n} \varphi_i(\vec{r}_i)\right]_j^{\vec{R}}. \tag{3.16}$$

This product wavefunction would be exact, if the Hamilton operator $\mathcal{H}_{\mathrm{el}}^{\vec{R}}(\vec{r})$ of the system could expressed as a sum of single electron operators $\hat{h}_{\mathrm{el}}^{\vec{R}}(\vec{r}_i)$ that only affect

the corresponding single electron coordinates $\vec{r}_i$. It would result in a total energy E that is the sum of eigenvalues of all n single electron Schrödinger equations [50]. Nevertheless, the product ansatz of the electronic wavefunction is not exact, as the Hamilton operator contains terms that depend on coordinates of two electrons, which takes the *electron interaction*, i.e. the Coulomb repulsion between electrons, into account. The resulting Hamiltonian, containing electron interactions, can be written as:

$$\mathcal{H}_{\mathrm{el}}^{\vec{R}}(\vec{r}) \equiv \mathcal{H}(\vec{r}) = \sum_k \hat{h}(k) + \sum_{i<k}\sum \hat{g}(i,k), \tag{3.17}$$

where $\hat{h}(k)$ is the single electron operator, describing the kinetic and potential energy of electron k and $\hat{g}(i,k)$ is the operator that takes the Coulomb interaction between the electrons i and k into account. Within this approximation, the excitation energies from state i to k for singlet and triplet states transform to:

$${}^1\Delta E_{\mathrm{i}\to\mathrm{k}} = \langle {}^1\Phi_{\mathrm{i}\to\mathrm{k}}|\mathcal{H}|{}^1\Phi_{\mathrm{i}\to\mathrm{k}}\rangle - \langle {}^1\Phi_0|\mathcal{H}|{}^1\Phi_0\rangle = \varepsilon_{\mathrm{k}} - \varepsilon_{\mathrm{i}} - J_{\mathrm{ik}} + 2K_{\mathrm{ik}} \tag{3.18}$$

for a transition in a singlet configuration, whereas the corresponding triplet excitation energy reads:

$${}^3\Delta E_{\mathrm{i}\to\mathrm{k}} = \langle {}^3\Phi_{\mathrm{i}\to\mathrm{k}}|\mathcal{H}|{}^3\Phi_{\mathrm{i}\to\mathrm{k}}\rangle - \langle {}^3\Phi_0|\mathcal{H}|{}^3\Phi_0\rangle = \varepsilon_{\mathrm{k}} - \varepsilon_{\mathrm{i}} - J_{\mathrm{ik}}. \tag{3.19}$$

Here, ε_{i} and ε_{k} are the energies of the orbitals, J_{ik} is the Coulomb integral, describing the electron interactions, and K_{ik} is the exchange integral that stems from the electrostatic interaction of the overlapping orbitals. They read:

$$J_{\mathrm{ik}} = \frac{e^2}{4\pi\varepsilon_0}\iint |\phi_{\mathrm{i}}(1)|^2 \frac{1}{r_{12}} |\phi_{\mathrm{k}}(2)|^2 \mathrm{d}\vec{r}_1 \mathrm{d}\vec{r}_2 \tag{3.20}$$

and

$$K_{\mathrm{ik}} = \frac{e^2}{4\pi\varepsilon_0}\iint \phi_{\mathrm{i}}^*(1)\phi_{\mathrm{k}}^*(2) \frac{1}{r_{12}} \phi_{\mathrm{k}}(1)\phi_{\mathrm{i}}(2) \mathrm{d}\vec{r}_1 \mathrm{d}\vec{r}_2. \tag{3.21}$$

The exchange integral K_{ik} is only non-zero when the involved orbitals carry the same spin factor, i.e. for singlet configurations [50]. This implies that the singlet state has a higher energy compared to the corresponding triplet state. Here, the effective repulsive interaction between electrons with the same spin is smaller, because the Pauli principle does not allow to have these electrons to be closely together. In this approximation, the energy difference ΔE_{ST} between singlet and triplet state energies, E_{S} and E_{T}, is:

$$\Delta E_{\mathrm{ST}} = E_{\mathrm{S}} - E_{\mathrm{T}} = {}^1\Delta E_{\mathrm{i}\to\mathrm{k}} - {}^3\Delta E_{\mathrm{i}\to\mathrm{k}} = 2K_{\mathrm{ik}}, \tag{3.22}$$

which is commonly referred to as *singlet-triplet splitting*.

3.2 Optical Properties of Organic Molecules

Monochromatic light absorption in an isotropic and homogeneous medium is described by the *Lambert-Beer law*:

$$A = \log(I_0/I) = \varepsilon c d, \tag{3.23}$$

in which A is a dimensionless quantity referred to as *extinction*, c the concentration of the solved compound, d the thickness of the the sample, and ε is the molar extinction coefficient, which is a function of the wave number $\varepsilon = \varepsilon(\tilde{\nu})$. The wave number $\tilde{\nu}$ is equal to the inverse of the wavelength $1/\lambda$ and is, mostly in the field of optical spectroscopy, given in units of cm^{-1}. Following an exponential law, absorption reduces the incoming light intensity I_0 to $I \equiv I(d)$ at a certain sample thickness d [45].

Oscillator Strength

As discussed in the preceding section, an electronic transition occurs between different states of a molecule. The intensity of a certain transition is now proportional to the intensity of the corresponding absorption band, which itself is defined as the integral $\int_{\mathrm{band}} \varepsilon(\tilde{\nu})\mathrm{d}\tilde{\nu}$. To quantify an electronic transition, this integral is compared to an equivalent model described by classical oscillators, which leads to the dimensionless *oscillator strength* f:

$$f = 4.319 \cdot 10^{-9} \int\limits_{\mathrm{band}} \varepsilon(\tilde{\nu})\mathrm{d}\tilde{\nu}. \tag{3.24}$$

Its value is in the order of 1 for an allowed transition. Theoretically, this oscillator strength can be derived from the time-dependent perturbation theory, which needs to be applied to describe the interaction of light with matter. Here, the Hamiltonian reads $\mathcal{H} = \mathcal{H}_0 + \mathcal{H}_{\mathrm{pert}}(t)$, the second term represents the interaction between an oscillating electromagnetic field and the molecule [45].

Selection Rules

The transition moment $\vec{U}_{0\to\mathrm{a}}$ (cf. Eqn. (3.15)) can be used to distinguish between quantum mechanically *allowed* and *forbidden* transitions. The transition moments of the electronic and the magnetic dipole moment as well as of the electric quadrupole moment operator typically are in the ratio of $10^7 : 10^2 : 1$, hence, the electric dipole moment transitions are of greater importance [45]. For dipole transitions ($\vec{U}_{0\to\mathrm{a}} \equiv \vec{M}_{0\to\mathrm{a}}$), the corresponding dipole moment operator reads:

$$\mathcal{M} = -|e| \sum_j \vec{r}_j + |e| \sum_\mu Z_\mu \vec{R}_\mu, \tag{3.25}$$

where j and μ indicate the incorporated electrons and nuclei, respectively. A transition is forbidden strictly when $\vec{M}_{0\to\mathrm{a}} = 0$, i.e. when its intensity vanishes. Moreover, these forbidden transitions can be accompanied by a finite intensity, if the forbiddance is weakened by a suitable perturbation. In the following, the spin selection rule

will be highlighted, to clarify its importance for fluorescence and phosphorescence in connection with the working principle of organic LEDs.

Apparently, the operator for the transition moment $\mathcal{M}$ does not contain spin contributions (cf. Eqn. (3.25)).[3] Consequently, the integration over spin variables transforms $\vec{M}_{0\to a}$ to zero,

$$\vec{M}_{0\to a} = \langle {}^{M'}\Psi_0^{\vec{R}} | \mathcal{M} | {}^{M}\Psi_a^{\vec{R}} \rangle = 0, \tag{3.26}$$

whenever the spin functions of initial and final states are different, i.e. $\langle \phi_i | \phi_f \rangle = 0$. Following these considerations, transitions are only allowed if the multiplicity M of initial and final state are equal. Because of this spin selection rule, singlet-triplet transfers are usually not observed for aromatic hydrocarbon systems.

However, in reality, especially for all non-linear molecules, the spin angular momentum and its components are not constant, so that the spin configurations are mixed to some extent. The interaction between the spin angular momentum of an electron and the orbital angular momentum of the same electron is the most important coupling – the *spin-orbit coupling*. It is part of the total Hamiltonian and its contribution $\mathcal{H}_{SO}$ reads:

$$\mathcal{H}_{SO} \sim \sum_j \sum_\mu \frac{Z_\mu}{|\vec{r}_\mu|^3} \hat{l}_j \cdot \hat{s}_j, \quad \text{with} \quad \hat{l}_j = \vec{r}_j \times \hat{p}_j. \tag{3.27}$$

In this notation, $\hat{l}_j$ is the orbital angular momentum of the electron. The scalar product $\hat{l}_j \cdot \hat{s}_j$ of two operators, one affecting the coordinates in space, the other one the spin coordinates, causes the mixing of the pure spin states. The contribution of $\mathcal{H}_{SO}$ linearly increases with increasing atomic number Z, so that the spin-orbit coupling mainly becomes important for incorporated heavy metals [51]. As it will be discussed later, it is this heavy metal induced spin-orbit coupling that makes the triplet states of organic compounds accessible for efficient emission in phosphorescent OLEDs.

If $\mathcal{H}_{SO}$ is part of the electronic Hamiltonian $\mathcal{H}_{el}$, then the electronic eigenfunctions will consist of wavefunctions with different multiplicity. However, since the mixing is weak, the resulting function will have either predominantly singlet or triplet character, so that these states are still referred to as singlet and triplet state, respectively.

Apart from spin selection rules, a transition can be forbidden because of the symmetry of the molecule. In general, the transition moment $\vec{U}_{0\to a}$ equals to zero whenever its integrand is not totally symmetric.

Franck-Condon Principle

Because the atomic nuclei are much heavier than the electrons, an electronic transition proceeds much faster than a possible response of the nuclei. As previously discussed, this justifies the Born-Oppenheimer approximation, in which the wavefunction is

[3] This also holds for both the magnetic dipole moment and the electric quadrupole moment operator.

factorized into contributions of the electrons and nuclei. In general, ground and excited state configurations will have different internuclear separations with higher average bond length for the excited system, as it carries more antibonding character. An electronic transition will be most intense for similar vibrational wavefunctions, i.e. for minimal changes in the internuclear separations – the so-called *vertical transition* (cf. Fig. 3.1). Transitions to other vibrational states of the excited configuration also occur, but with lower intensity I, which is proportional to the square of the transition moment $\vec{M}_{0\to\mathrm{a}}$ [45]:

$$I \sim |\vec{M}_{0\to\mathrm{a}}|^2 = |\vec{M}^{\mathrm{el}}_{0\to\mathrm{a}}|^2 \quad \cdot \quad \underbrace{|\langle\chi^{\mathrm{a}}_{v'}|\chi^0_v\rangle|^2}_{\text{Franck-Condon factor}} \quad , \tag{3.28}$$

with (cf. Eqns. (3.15) and (3.25))

$$\vec{M}^{\mathrm{el}}_{0\to\mathrm{a}} = -|e|\langle\,\Psi^{\vec{R}}_{\mathrm{a}}|\sum_j \vec{r}_j|\,\Psi^{\vec{R}}_0\rangle. \tag{3.29}$$

The electronic transition moment $\vec{M}^{\mathrm{el}}_{0\to\mathrm{a}}$ determines the intensity of the total transition $0 \to \mathrm{a}$, whereas the overlap integral of the vibrational wavefunctions, $\langle\chi^{\mathrm{a}}_{v'}|\chi^0_v\rangle$, describes the distribution of the latter intensity to the various vibrational sublevels. The square of these overlap integrals is called *Franck-Condon factors* (cf. Eqn. (3.28)). The summation of these Franck-Condon factors for all possible vibronic substates yields [45]:

$$\sum_{v'} |\langle\chi^{\mathrm{a}}_{v'}|\chi^0_v\rangle|^2 = 1. \tag{3.30}$$

Excited State Relaxation

In the preceding sections, mainly electronic transitions into excited states have been discussed. However, it is also of great importance to have a closer look at processes that can reverse the absorption. The relaxation under emission of photons is one of these processes and essential for light-emitting devices. Generally, there is a separation into monomolecular and bimolecular processes, the latter involving the interaction with the environment. This chapter focusses on monomolecular processes; bimolecular interactions will be introduced in subsequent sections.

In Figure 3.2 the *Jablonski diagram* is shown, which can be used best to illustrate all competing monomolecular photo-physical processes within an organic molecule [45, 48]. Upon absorption, the molecule is, within the singlet manifold, excited to a higher singlet state (S_n). As shown in Figure 3.2, absorption can also take place from T_1 to a higher triplet level, as it is an allowed transition. Nevertheless, the molecule has to be in this T_1 state beforehand. For the majority of organic complexes, the internal relaxation from higher excited to the corresponding lowest excited state is much faster than radiative processes. Thus, emissive recombination, i.e. fluorescence and phosphorescence, originates solely from the lowest excited states, S_1 and T_1, respectively. This property is referred to as *Kasha's rule* [48, 51], which can be explained by the Franck-Condon factors (cf. Eqn. (3.28)) for transitions between

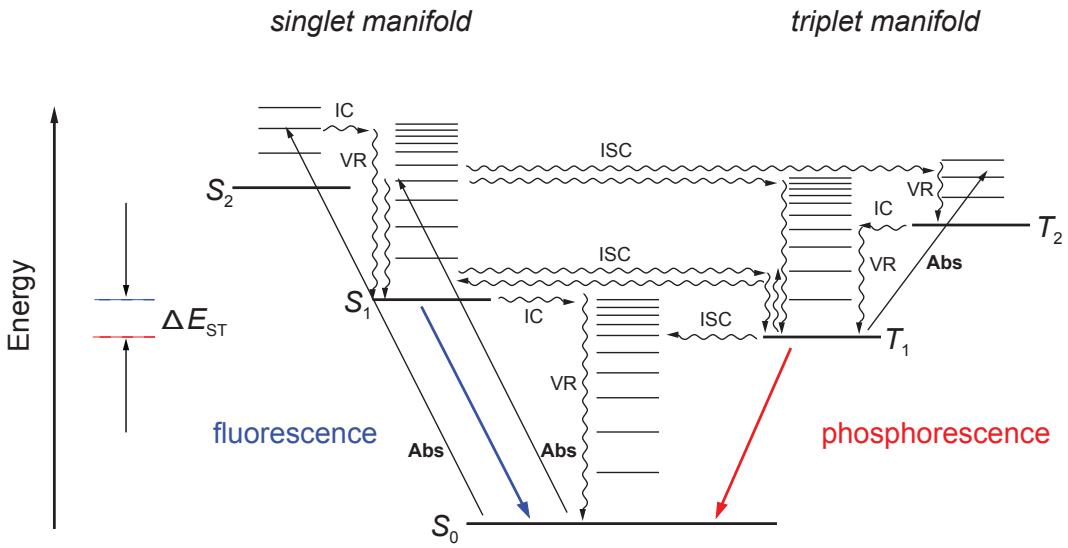

Figure 3.2: The Jablonski diagram to illustrate all competing monomolecular deactivation processes. Singlet and triplet manifold correspond to states with a multiplicity of 1 and 3, respectively. 'Abs' denotes absorption. Thick straight lines indicate emissive processes, i.e. fluorescence and phosphorescence. All wavy lines represent non-radiative processes – ISC = intersystem crossing, VR = vibrational relaxation and IC = internal conversion. (taken from [50]). Additionally, the singlet-triplet splitting ΔE_{ST} is depicted (cf. Eqn. (3.22)).

excited states k and k', which are highest for fast transitions. The vibrational orbital overlap $\langle \chi_{v'}^{k'} | \chi_{v}^{k} \rangle$ is largest between electronic states whose lowest vibrational levels are close in energy. In most molecules, the lowest vibrational levels of the excited states lie close together, so that molecules in higher states quickly reach the lowest excited state, before they have time to fluoresce or phosphoresce. However, the energy gap between S_1 (or T_1) and S_0 is greater, and fluorescence (or phosphorescence) occurs rather than internal relaxation (cf. below: energy gap law).

The internal relaxation itself is a two-step process. It involves the *internal conversion* (IC) from higher to lower electronic states, e.g. from S_2 to S_1, and the subsequent vibrational relaxation (VR) to the corresponding vibrational ground state ($v = 0$) of a certain configuration. In addition, there can be conversions between states of different multiplicity, the so-called *intersystem crossing* (ISC), which involves a spin flip of the excited electron. The rate constants for these various channels strongly depend on the special molecular structure. For instance, the introduction of a heavy metal atom to the core of a molecule, which induces strong spin-orbit coupling, will increase the rate of ISC and of phosphorescence itself to levels that can compete with fluorescence.

Excited State Lifetime

Without competing non-radiative decay channels, the deactivation of an excited state can only occur by spontaneous emission. The *natural lifetime* of a state is defined by the mean time the molecule remains in this excited state. For an ensemble of molecules, represented by an excited state density n, this emission follows a first order rate equation [45]:

$$\frac{\mathrm{d}n}{\mathrm{d}t} = -k_0 n, \tag{3.31}$$

in which k_0 is the rate constant for the emission, defined as the inverse of the natural lifetime τ_0. Simple integration of Equation (3.31) results in:

$$n(t) = n_0 e^{-k_0 t} \xrightarrow{I \sim n(t)/\tau_0} I(t) = I_0 e^{-k_0 t}, \tag{3.32}$$

with the initial excited state density n_0 and intensity I_0. The natural lifetime τ_0 can be correlated to the oscillator strength f via [45]:

$$\tau_0 \approx \frac{1.5}{\tilde{\nu}_{\max}^2 f}. \tag{3.33}$$

Here, $\tilde{\nu}_{\max}$ is the wavenumber of the absorption maximum of the corresponding electronic transition. Due to the fact that absorption and emission have the same dependence from the transition moment $\vec{U}_{0\to\mathrm{a}}$, the excited state lifetime is inversely proportional to the integral of the absorption band $\int_{\mathrm{band}} \varepsilon(\tilde{\nu})\mathrm{d}\tilde{\nu}$.

Referring to Figure 3.2, the emission from an excited state is not the only channel for deactivation, but various pathways, competing with the radiative decay, ultimately lead to vibrational relaxation. These processes, represented by rate constants k_i, will shorten the natural lifetime τ_0 according to [45, 48]:

$$\tau = \frac{1}{k_0 + \sum_i k_i}. \tag{3.34}$$

In contrast to the natural lifetime, τ is simply referred to as excited state lifetime.

Quantum Yield and Efficiency

To quantify the deactivation channels of an excited molecular system, the *quantum yield* Φ is introduced [45]. Its differential definition for a certain process j reads:

$$\Phi_j = \frac{d\mathrm{n}_j}{\mathrm{d}t} \cdot \left[\frac{\mathrm{d}n_\mathrm{A}}{\mathrm{d}t}\right]^{-1}, \tag{3.35}$$

where n_j is the number of excited states that undergo process j and n_A represents the total number of absorbed photons. In contrast to the alternative definition which describes a ratio between the number of molecules that contribute to the process j and the total number of absorbed photons, this expression is more precise as it also

correctly describes processes, for which the quantum yield is not constant throughout the reaction. In addition, the *efficiency* η of a certain transition j is defined as:

$$\eta_j = \frac{\mathrm{d}n_j}{\mathrm{d}t} \cdot \left[\frac{\mathrm{d}n_\mathrm{I}}{\mathrm{d}t}\right]^{-1} = \frac{k_j}{\sum_i k_i}. \tag{3.36}$$

In contrast to the quantum yield, n_I denotes the number of states that enter the initial state of the process j. Both definitions, i.e. quantum yield and efficiency, fall together when $n_\mathrm{I} = n_\mathrm{A}$. One has to be aware that these quantities are often wrongly used as synonyms. The right side of Equation (3.36) shows that the efficiency of a transition j can also be expressed as the ratio of its rate constant k_j and the sum of all rate constants.

Energy Gap Law

Probably the most important quantities of organic molecules are the fluorescence and phosphorescence quantum yields. According to the definitions made above, they can be expressed as:

$$\Phi_\mathrm{F} = \eta_\mathrm{abs} \cdot \eta_\mathrm{F} \quad \text{and} \quad \Phi_\mathrm{P} = \eta_\mathrm{abs} \cdot \eta_\mathrm{ST} \cdot \eta_\mathrm{P} \tag{3.37}$$

Here, the subscripts refer to absorption, fluorescence, and phosphorescence, respectively. Moreover, η_ST represents the efficiency of the triplet state formation. It has been shown for the fluorescence of aromatic hydrocarbons that the rate of non-radiative relaxation k_nr, can be correlated to the energy gap between ground and lowest excited state ΔE [45, 47]. Here, non-radiative relaxation combines the processes of internal conversion and subsequent vibrational relaxation (cf. Figure 3.2). It reads:

$$k_\mathrm{nr} = 10^{13} \cdot e^{-\alpha \Delta E} \quad \text{with} \quad \alpha = 4.5\,(\mathrm{eV})^{-1}, \tag{3.38}$$

which transforms the fluorescence quantum yield Φ_F to:

$$\Phi_\mathrm{F} = \eta_\mathrm{abs} \cdot \eta_\mathrm{F} = \eta_\mathrm{abs} \frac{k_\mathrm{F}}{k_\mathrm{F} + k_\mathrm{ST} + 10^{13} \cdot e^{-\alpha \Delta E}}. \tag{3.39}$$

In consequence, Φ_F decreases as the energy gap ΔE is reduced. Qualitatively, this effect is also observed for highly phosphorescent materials, comprising the transition metal iridium in the core of the molecular structure [52]. Here, a proportionality constant of $\tilde{\alpha} = 8.1\,(\mathrm{eV})^{-1}$ is found for a series of iridium complexes with different substituents.

Stokes Shift of Absorption and Emission

One important photo-physical property of organic molecules is the *Stokes shift* between the absorption and emission spectra of a molecule. This property is essential for organic LEDs, because otherwise a large fraction of emitted light would be absorbed within the organic layers. In Figure 3.3, absorption and emission transitions between the ground and lowest excited singlet state are schematically depicted. Simplified potential energy curves with their corresponding vibrational sublevels are

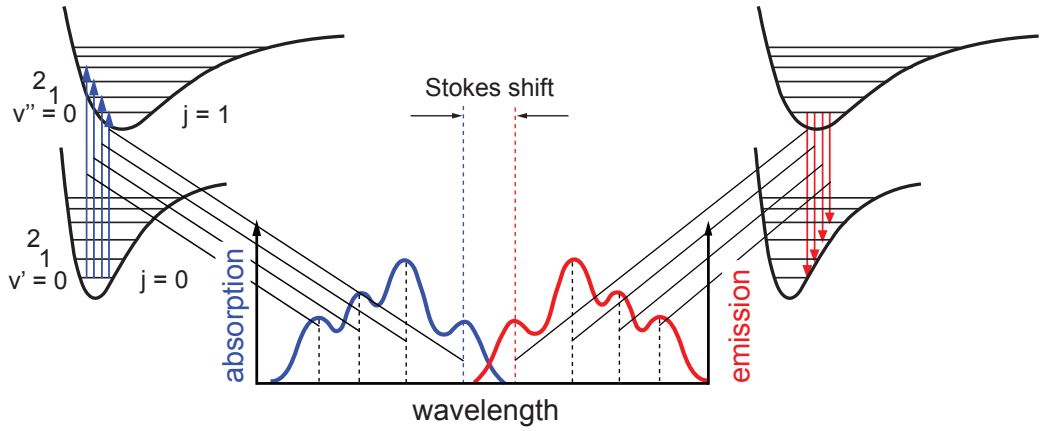

Figure 3.3: Schematic absorption and emission spectra are shown as a function of the wavelength. The emission spectra is red shifted with respect to the absorption bands – this shift is called Stokes shift. Furthermore, the mirror image relation between absorption and emission bands is illustrated, which has its origin in the Franck-Condon principle (according to [48]).

used to understand this effect. Upon energy absorption, electrons can be lifted from the vibrationless S_0 state to all vibrational levels of the S_1 state, according to the Franck-Condon principle. Here, the nuclear coordinates are not in their equilibrium configuration in respect to the new electronic state, so that vibrational relaxation to the vibrationless sublevel occurs. This process is very fast, even compared to fluorescence[4], with typical rate constants of $\sim 10^{13}\,\mathrm{s}^{-1}$ [48]. After this relaxation, fluorescence takes place; now from the vibrationless level of S_1 to all vibrational sublevels of the molecular ground state, again corresponding to the Franck-Condon factors for each transition. As a result, the red shift of the emission spectrum and the mirror image symmetry between absorption and fluorescence arise (cf. Fig. 3.3). This spectral feature is qualitatively similar for phosphorescent emission, with the lowest excited triplet state having a different equilibrium configuration, which results from different Franck-Condon factors. Additionally, the phosphorescence is red shifted according to the singlet-triplet splitting [51].

The Stokes shift depends on the equilibrium geometry of ground and excited states, respectively – the larger the difference of their internuclear separation, the larger the Stokes shift, as the energy difference of the transitions with largest Franck-Condon factors are related the difference in the configuration coordinate $\vec{R}$ of the molecule [45].

Efficient Phosphorescence

As mentioned in the Chapter 2, organic molecules that efficiently emit from their triplet state are inevitable to realize internal electron-photon conversion efficiencies of unity. In the mid-1990s, Thompson and co-workers promoted a new class of ma-

[4]Typical values for fluorescence are $\sim 10^6 - 10^9\,\mathrm{s}^{-1}$ [45].

terials as emitting molecules in organic LEDs: organometallic complexes [6]. These materials incorporate transition metals like platinum [53–55], osmium [56], iridium [57, 58], etc. in the core of the organic molecule, which introduce strong spin-orbit coupling due to their high atomic number Z (cf. Eqn. (3.27)). A direct consequence of this coupling is its strong impact on the selection rules. Conventional fluorescent organic molecules have, according to the Jablonski diagram, two channels for relaxation. Either they depopulate in the singlet manifold by fluorescence or internal non-radiative relaxation or they convert their spin configuration via ISC to the triplet manifold, where further deactivation is possible. Since fluorescence with time constants of $\sim 1\,\mathrm{ns}$ has much higher rates than the ISC to the triplet states ($\sim 10\,\mathrm{ns}$), the latter can not efficiently quench the singlet excitation [59]. Upon incorporation of transition metals, the electronic wavefunctions extend over a larger spatial region of the molecule. This reduces the electron-electron and exchange interactions as a consequence of an on average larger spatial separation of the interacting electrons. This, in turn, reduces the singlet-triplet splitting ΔE_{ST} [59]. Similar to the energy gap law of the fluorescence quantum yield (cf. Eqn. (3.39)), the rate of intersystem crossing k_{ISC} increases with decreasing ΔE_{ST} [60]. For organometallic complexes, strongly reduced time constants for k_{ISC} are observed due to this energy gap law and to the mixing of singlet and triplet states, induced by the spin-orbit coupling. For instance, for materials comprising either palladium (Pd) or platinum (Pt), the ISC rate is reduced to corresponding values of $k_{\mathrm{ISC}}(\mathrm{Pd}) = 800\,\mathrm{fs}$ and $k_{\mathrm{ISC}}(\mathrm{Pt}) = 50\,\mathrm{fs}$ [61]. In such molecules, since the ISC rate is drastically increased, the triplet states can be efficiently occupied when fed by singlet states.

As previously discussed, the $T_1 \rightarrow S_0$ transition in organic compounds is quantum mechanically forbidden. Therefore, if once populated, the triplet state is mainly deactivated by internal non-radiative relaxation. Again, the spin-orbit coupling in organometallic compounds weakens the selection rules and reduces the time constants for radiative triplet relaxation by several orders of magnitude [59, 61], down to microseconds for state-of-the-art phosphors [6]. In summary, the very high rates for intersystem crossing and radiative $T_1 \rightarrow S_0$ transition make these organometallic compounds to promising OLED emitter materials, as they can harvest excited states from both spin manifolds. This opens the door to internal phosphorescence quantum yields of unity.

Excitons

At this stage, it is time to introduce the concept of *excitons* as quasiparticles in a solid, describing an excited state. These elementary excitations provide a transport of energy without transporting net charge. Mainly depending on the dielectric constant κ of the surrounding matter, which influences the screening of electron and hole, these excitons can be delocalized (*Wannier-Mott* excitons) or localized (*Frenkel* excitons) [62]. A scheme of these different types of excitons is given in Figure 3.4. If electron and hole are separated by many inter-atomic spacings, for instance in inorganic semiconductors, one can apply the effective mass approximation, which leads to an effective radius for the electron-hole pair [62]:

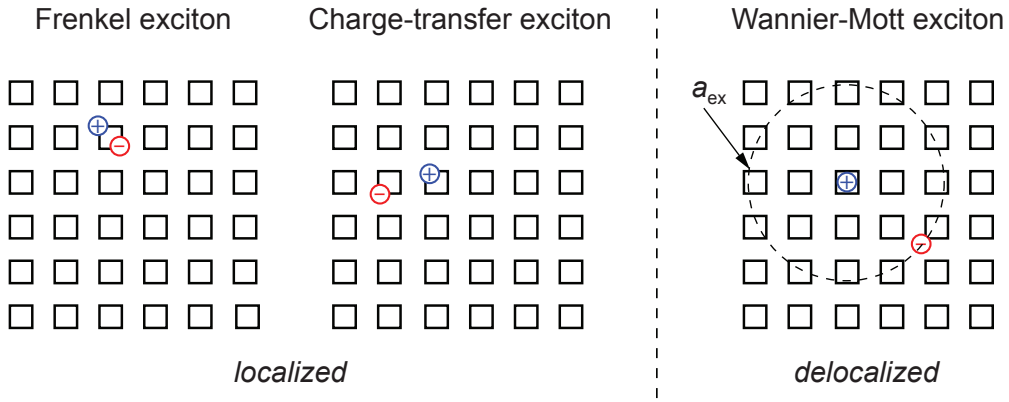

Figure 3.4: Different types of excitons. For the delocalized Wannier-Mott exciton, the effective radius a_{ex} is additionally depicted.

$$a_{ex} = \hbar^2 \kappa / \mu e^2, \tag{3.40}$$

in which μ^{-1} is the sum of the inverse effective masses of electron and hole, and e is the elementary charge. For GaAs, the effective electron-hole separation can be calculated to $a_{ex} = 10 - 12\,\text{nm}$ [63], which is roughly one order of magnitude larger than the atomic spacing.

Excitons in organic semiconductors are Frenkel excitons [5, 64], with electron and hole localized in the same molecule (cf. Fig. 3.4). Here, the electron is lifted from the HOMO level of the molecule to a higher, previously unoccupied level (LUMO), leaving a single occupied HOMO. These excitons are strongly Coulomb-correlated with binding energies in the order of $0.5 - 1.5\,\text{eV}$ [65]. In addition to these intramolecular excitations, another class of excitons is often observed in organic materials, where the electron is transferred to a nearest neighbour molecule. These configurations, as shown in Figure 3.4, are called *charge-transfer (CT)* excitons. They are still localized and Coulomb-correlated, however, because the charge separation is increased, the CT exciton binding energy is reduced. These states are considered to be degenerate due to the short-range nature of the splitting term K_{ik} in Equation (3.21) [5]. For electrical excitation, i.e. injection of electrons and holes to an organic solid, CT states are precursor states to the formation of intramolecular excitons.

3.3 Intermolecular Energy Transfer

Once a molecule is in an excited state, the monomolecular deactivation is not the only way to the relax to the molecular ground state. Rather, the energy of an excitation can be transferred from one molecule to another. For this reason, throughout this section, molecules are referred to as *donor D* or *acceptor A* whenever they give away or accept energy, respectively. Furthermore, the multiplicities of a certain molecular state will be denoted with preceding superscripts, i.e. 1 or 3 for singlet and triplet states, respectively. Excited states are marked with an asterisk, levels higher than the lowest possible electronic excitation with a double asterisk, correspondingly.

Trivially, energy can be transferred as a two-step process that involves the emission and absorption of a photon $h\nu$:

$$D^* \rightarrow D \quad + \quad h\nu \tag{3.41}$$

$$h\nu \quad + \quad A \rightarrow A^*. \tag{3.42}$$

Therefore, it is an energy transfer via radiation, often referred to as *reabsorption*. Here, it is not necessary to distinguish between singlet and triplet states, as the two steps are completely decoupled and solely depend on the specific properties of D and A. If D and A are of the same material, where a reasonable spectral overlap of emission and absorption bands is needed, this process can substantially increase the excited state lifetime of the system (*radiation trapping*). Naturally, this process is not very efficient as both, the molecular efficiency of luminescence η_{lum} and of absorption η_{abs}, reduce the transfer yield. This type of transfer can overcome large distances, which mainly depends on η_{abs}, as it does not involve a coupling of initial and final states.

Non-Radiative Energy Transfers

In contrast to reabsorption, the energy can also be transferred in a single-step process based on direct coupling between donor and acceptor. Such transfers conserve the initial donor energy. They are proportional to the number of transitions in the emission band of the donor $I_D(\tilde{\nu})$ and in the absorption band of the acceptor $\varepsilon_A(\tilde{\nu})$ that are equal in energy. This is quantified in the spectral overlap integral which reads:

$$J = \int_0^\infty \bar{I}_D(\tilde{\nu})\bar{\varepsilon}_A(\tilde{\nu})\mathrm{d}\tilde{\nu}, \tag{3.43}$$

where $\bar{I}_D$ and $\bar{\varepsilon}_A$ represent normalized intensities with respect to the integrated band. Within time dependent perturbation theory, an expression for the rate of a non-radiative transition $k_{D^*\rightarrow A}$ known as *Fermis golden rule* is derived. It reads:

$$k_{D^*\rightarrow A} = \frac{2\pi}{\hbar} \underbrace{\langle \Psi_{\mathrm{i}} | \mathcal{H}' | \Psi_{\mathrm{e}} \rangle}_{=:\beta}{}^2 \rho_E. \tag{3.44}$$

Here, $\mathcal{H}'$ is the operator characterizing all electrostatic interactions between electrons and nuclei of donor and acceptor and ρ_E is the density of states of the acceptor vibrational levels. The integral β describes the coupling of the transitions between the wavefunctions of donor and acceptor. In this equation, Ψ_i and Ψ_e are antisymmetric product wavefunctions of initial and final state.[5] The integral can be split into a Coulomb and an exchange term: $\beta = \beta^\mathrm{c} - \beta^\mathrm{e}$ [45]. The Coulomb term β^c is the classical interaction of the ground and excited state charge densities for donor and acceptor, which can be separated into dipole-dipole, dipole-quadrupole interaction, etc. using a multipole expansion. In contrast to the Coulomb term, the exchange interaction – only understood in the quantum mechanics framework – determines the integral β^e.

Förster Transfer

The energy transfer that is based on the Coulomb interaction with the coupling integral β^c has been investigated by Förster [66]. For the dominating dipole-dipole interaction in the multipole expansion and for intermolecular distances that are not too small (so that strong orbital overlap is present), the Coulomb term of β shows the following dependence [45]:

$$\beta^\mathrm{c} \sim \frac{\vec{M}_D \vec{M}_A}{R_{DA}^3}, \tag{3.45}$$

in which $\vec{M}_i$ are the corresponding transition moments and R_{DA} is the intermolecular distance between donor and acceptor. Based on this relation, Förster showed that the energy transfer rate constant (cf. Eqns. (3.43) and (3.44)) can be written as [67]:

$$k_\mathrm{Coulomb} \equiv k_\mathrm{F} = k_D \frac{9(\ln 10)\kappa^2 \Phi_D}{128\pi^5 N_\mathrm{A} n^4} \cdot J \cdot \frac{1}{R_{DA}^6} = k_D \left[\frac{R_0}{R_{DA}}\right]^6, \tag{3.46}$$

with the rate constant k_D of the excited donor in absence of an acceptor, an orientation factor κ, the refractive index n of the medium in the range of spectral overlap, the Avodadro constant N_A, and the luminescence quantum yield Φ_D of the donor.

Apparently, this transfer can only occur if both donor and acceptor transitions are allowed. In other words, the integration over spin variables in β^c is non-zero only when the spins of D and A are conserved. Here, because the operators for the transition moment do not contain the spin, the integration over spin variables for the transition moment equals to zero, whenever the spin functions of initial and final state differ. This leads to the following allowed energy transfer reactions:

$$^1D^* + {}^1A \longrightarrow {}^1D + {}^1A^* \tag{3.47}$$

$$^1D^* + {}^3A \longrightarrow {}^1D + {}^3A^*. \tag{3.48}$$

Note that there are examples of molecules having a triplet ground state configuration [68, 69], giving rise to ^3A on the left side of the second equation. A singlet-triplet

[5] For a two-electron case, these product functions would read: $\Psi_\mathrm{i} = [\Psi_{D^*}(1)\Psi_A(2) - \Psi_{D^*}(2)\Psi_A(1)]/\sqrt{2}$ and $\Psi_\mathrm{e} = [\Psi_D(1)\Psi_{A^*}(2) - \Psi_D(2)\Psi_{A^*}(1)]/\sqrt{2}$. Here, the functions Ψ_D and Ψ_A are spin functions.

transfer, ${}^3D^* + {}^1A \rightarrow {}^1D + {}^3A^*$, is strictly forbidden in the Förster theory as it would require two simultaneous intersystem crossing steps. In case a phosphorescent donor is incorporated, the recombination in the triplet manifold is enhanced due to spin-orbit coupling. Here, the following additional transfers are possible [45, 69]:

$$ {}^3D^* + {}^1A \longrightarrow {}^1D + {}^1A^* \tag{3.49} $$
$$ {}^3D^* + {}^3A \longrightarrow {}^1D + {}^3A^*. \tag{3.50} $$

Even though the ${}^3D^* \rightarrow {}^1D$ step requires intersystem crossing and thus has a lower rate constant than the transitions starting from ${}^1D^*$, they may have a similar probability as the transfer process starting from singlet states since the lifetime of the triplets is correspondingly longer. However, for the process in Equation (3.49), two different types of molecules have to be involved in order to excite the energetically higher singlet state of the acceptor with the triplet donor state energy. The Förster energy transfer can efficiently overcome distances of up to 10 nm, which is much larger than typical molecular dimensions.

Dexter Transfer

In contrast to the dipole-dipole coupling of Förster mechanism, Dexter energy transfer is mediated by exchange interactions with the corresponding transition coupling integral β^{e}. Its strength strongly depends on the orbital overlap of donor and acceptor, resulting in a decrease of this interaction with increasing intermolecular distance. Dexter-type transfers obey the *Wigner-Witmer* rules for spin conservation, requiring the total spin of the configuration to be conserved throughout the reaction [70]. According to the rules of vector addition, this requirement reads:

$$ \begin{aligned} (\mathrm{S}_{D^*} + \mathrm{S}_A), (\mathrm{S}_{D^*} + \mathrm{S}_A - 1) \ldots |\mathrm{S}_{D^*} - \mathrm{S}_A| \ni & \\ \mathrm{S}_{(D^*\ldots A)} \stackrel{!}{=} \mathrm{S}_{(D\ldots A^*)} & \\ \in (\mathrm{S}_D + \mathrm{S}_{A^*}), (\mathrm{S}_D + \mathrm{S}_{A^*} - 1) \ldots |\mathrm{S}_D - \mathrm{S}_{A^*}|. & \end{aligned} \tag{3.51} $$

Here, $\mathrm{S}_{(D^*\ldots A)}$ and $\mathrm{S}_{(D\ldots A^*)}$ refer to the total spin of the donor-acceptor complex before and after the interaction, respectively, and S_i to the spin of the corresponding state. Hence, allowed reactions of the Dexter mechanism are:

$$ {}^1D^* + {}^1A \longrightarrow {}^1D + {}^1A^* \tag{3.52} $$
$$ {}^3D^* + {}^1A \longrightarrow {}^1D + {}^3A^*. \tag{3.53} $$

Moreover, triplet-triplet annihilation, with two excited triplet states interacting, is allowed:

$$ {}^3D^* + {}^3A^* \longrightarrow {}^1D + {}^{1,3,5}A^*. \tag{3.54} $$

In this case the acceptor can be in its singlet, triplet, or quintet configuration. As mentioned before, the singlet-singlet interaction is a very efficient Förster-type transfer as well, so that it is rarely observed based on exchange interactions. In contrast,

the triplet-triplet energy transfer is of great importance for it provides the basis for efficient triplet excited state migration in organic materials.

In 1953, Dexter derived an expression for the rate constant of this exchange interaction based energy transfer [71], which reads:

$$k_{\text{exchange}} \equiv k_{\text{D}} = \frac{2\pi}{\hbar} K^2 e^{-2R_{DA}/L} \cdot J, \tag{3.55}$$

where K is a constant in units of energy [72]. The exponential dependence on the intermolecular distance R_{DA} accounts for the necessity of orbital overlap of the involved molecules. The Dexter transfer is accordingly a short distance interaction, typically reaching up to 1 nm, which is much shorter than the interaction radius of the Förster mechanism.

Exciton Diffusion

Even though excitons do not carry a charge, they can migrate throughout organic solids. The driving force of this exciton motion is a gradient in the exciton concentration $\nabla n(\vec{r}, t)$. Both energy transfer mechanisms, Förster- and Dexter-type, can contribute to this exciton migration, which itself is a series of uncorrelated hopping steps from one molecule to another. Such movement is often referred to as a *random walk* process. The theory of particle diffusion in general has been introduced by Fick. *Fick's* 2^{nd} *law*, the diffusion equation, describes the the development of the exciton density $n(\vec{r}, t)$ in space and time [73]. Ignoring quenching processes, it reads:

$$\frac{\partial n(\vec{r}, t)}{\partial t} = G(\vec{r}, t) - \frac{n(\vec{r}, t)}{\tau} + D\nabla^2 n(\vec{r}, t). \tag{3.56}$$

$G(\vec{r}, t)$ represents the exciton generation, τ the excited state lifetime, and D the diffusion constant. Because thin films and complete organic LEDs are planar structures and most organic materials are isotropic, the diffusion problem can often be reduced to one direction of space.

In many cases, especially under electroluminescence operation of OLEDs, the excitons are generated in the layer of interest in the very proximity of an interface. Here, a delta-like generation profile $G(x, t) = G \cdot \delta(x = x_0, t)$ is assumed. Under these boundary conditions, the steady-state ($\partial n/\partial t = 0$) solution of Fick's 2^{nd} law can be derived to [74–76]:

$$n(x) = n_0 \cdot \mathrm{e}^{-x/L_x} \quad \text{with} \quad L_x = \sqrt{D\tau}, \tag{3.57}$$

where n_0 is the exciton density at the interface of generation and L_x is the corresponding diffusion length.

3.4 High Brightness Non-Linearities in Phosphorescent OLEDs

In this section, processes which lead to a decrease of the electron-photon conversion efficiency of organic phosphorescent LEDs at high brightness will be discussed. Here, the focus will solely be on triplet excited states since they are the origin of phosphorescence – a very efficient type of recombination utilized in OLEDs.

Whenever a certain density of triplet excitons n is present, the interaction with the environment possibly introduces quenching pathways that reduce n non-radiatively. The most prominent processes are the interaction of triplet excitons with charges, referred to as *triplet-polaron quenching* (TPQ), the impact of the applied external field to the triplet excited states that leads to a *field-induced excited state dissociation* and the interaction among each other, i.e. *triplet-triplet annihilation* (TTA). Such processes can be expressed by the following reactions:

triplet-polaron quenching: $$^3D^* + A^\pm \longrightarrow {}^1D + A^{\pm *} \tag{3.58}$$

field-induced triplet dissociation: $$^3D^* \xrightarrow{F_{\text{ext}}} M^+ + M^- \tag{3.59}$$

triplet-triplet annihilation: $$^3D^* + {}^3A^* \longrightarrow {}^1D + {}^{1,3,5}A^{**}. \tag{3.60}$$

Here, M^+ and M^- represent a positive $(+)$ and a negative $(-)$ charged molecule, respectively, which is summarized in $M^\pm$. Further, F_{ext} denotes the applied external electric field. Each individual process can be expressed as a second order term in a rate equation that describes the time development of the triplet exciton density n:

$$\frac{\mathrm{d}n}{\mathrm{d}t} \sim -k_{\text{TPQ}} n q^\pm - k_{\text{Field}} n - k_{\text{TTA}} n^2, \tag{3.61}$$

where $n \equiv n(t)$, k_{TPQ} is the rate constant for TPQ, $q^\pm$ the charge carrier density, and k_{Field} and k_{TTA} are the rate constants for field-induced dissociation and TTA, respectively. TTA is the only processes that scales quadratically with the exciton density n; the others show a linear dependence. Hence, triplet-triplet annihilation is the dominating process that ultimately limits the efficiency of phosphorescent systems at high excitation levels (high n) [19].

Triplet-polaron quenching has been investigated in earlier studies for various phosphorescent emitter systems of state-of-the-art OLEDs [20]. In contrast to TTA, which is insignificant at low brightness, its contribution to the efficiency roll-off continuously increases with increasing current density j that flows through the device, starting at very low intensities. Nonetheless, the efficiency reduction due to TPQ is rather moderate over a wide range of j and is clearly surpassed by the TTA contribution, whenever the device is optimized for a charge balance factor close to one. Here, the number of excess charges, which can not contribute to the recombination but still act as a quenching site in the TPQ framework, is minimized.

According to literature, the efficiency roll-off in phosphorescent OLEDs is dominated by electric field-induced exciton dissociation [21, 77], a presumption that is investigated in this work. It is approved that, at least for established phosphorescent

OLEDs, the triplet state dissociation can be ruled out as a significant process under typical operation conditions. This is a very reasonable assertion, because the large exciton binding energy of a triplet state in organic materials will make dissociation unlikely. The results of this study will be presented in Appendix A for completeness, however they are not essential for the main scope of this work.

As mentioned above, it is the quadratic dependence on the triplet exciton density n that results in a TTA-dominated efficiency roll-off at high brightness. In the remaining part of this section, the physics of triplet-triplet annihilation will be given in detail. Here, different mechanisms that lead to TTA are introduced. Moreover, possible energetic configurations of the emissive systems will be discussed with respect to these mechanisms.

Host-Guest Systems

Referring to Section 3.2, efficient phosphorescence can be obtained from organometallic complexes that strongly enhance the spin-orbit coupling. One common property of phosphorescent emitters is their quantum yield Φ_P, which is noticeably reduced for bulk layers [53, 78]. On the other hand, strongly improved quantum yield values are obtained, whenever the phosphor is diluted into another material – the *host* material. The phosphorescent dopant is accordingly referred to as *guest* material.[6] This effect is called *concentration* or *aggregation* quenching [79, 80]. High quantum yields are typically achieved with a concentration of the phosphor in the host-guest system in the range of $1 - 10\,\mathrm{wt}\%$. If such a system is excited, mainly the host material will initially carry the excitation, simply because of its high concentration in the mixture.

For the host material itself, certain properties are required to make it suitable for phosphorescent emitters. Most importantly, the excitation that is created on host sites must be transferred to the phosphor, i.e. the site of emissive recombination, unless emission from the host is desired. Here, singlet excitons are mainly transferred via the Förster mechanism while triplet excitons migrate from site to site, ultimately reaching a phosphorescent molecule, based on Dexter-type transfer steps (cf. Sec. 3.3). Both energy transfers require a spectral overlap J between donor and acceptor, i.e. host and guest molecules.

Once the excitation is transferred from the host to guest sites, it is necessary to confine the excitation on the phosphor so that radiative recombination can occur efficiently [39, 81]. In case the phosphorescent emitter is in its lowest excited triplet level, migration to other molecules proceeds highly efficient via Dexter-type triplet-triplet energy exchange steps. Therefore, the relative position of the matrix triplet level with respect to the phosphor T_1 state is important as non-radiative transfers conserve the transferred energy (cf. Sec. 3.3). In Figure 3.5, different configurations of host and guest triplet levels are depicted; the transfer from host to guest and vice versa are denoted as k_HG and k_GH, respectively. The highest phosphorescence quantum yield Φ_P of the mixed system can be expected for an exothermic system, i.e. the T_1 level of the matrix is higher in energy compared to the phosphor, which

[6] Another very common term for the host material is *matrix*. Accordingly, the guest molecules are referred to as *dopant* material in conjunction with the use of *matrix*.

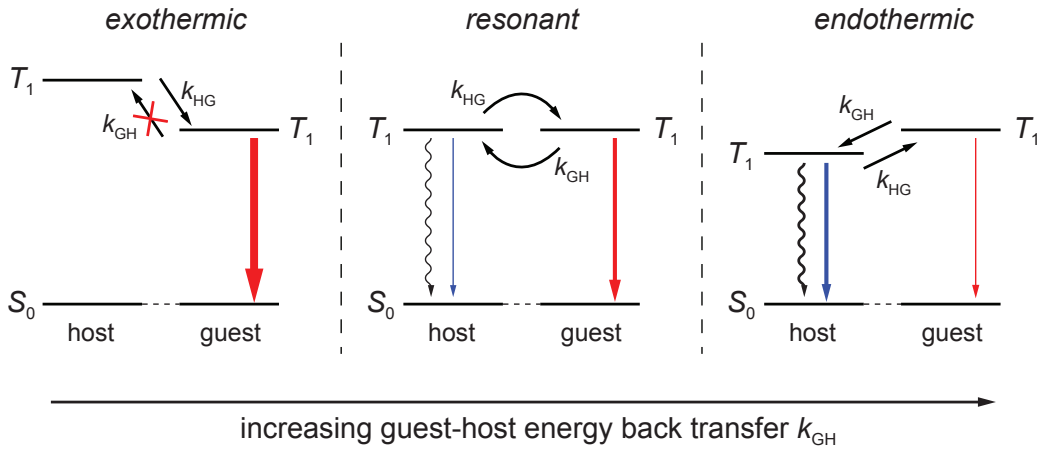

Figure 3.5: Different triplet energy configurations of host and guest materials for phosphorescent emitter systems. The thickness of the arrows qualitatively indicates the strength of the corresponding recombination (red: phosphorescence, blue: fluorescence, wavy black: vibrational relaxation). For simplicity, this picture assumes a radiative efficiency $\eta_P = 1$ from the guest T_1 level. From left to right, the back-transfer rate k_{GH} increases, which increases the probability that excitation is disactivated on host sites, ultimately reducing the phosphorescence quantum yield of the mixed system.

reads for a mixed system:

$$\Phi_P = \eta_{abs} \cdot \eta_{HG} \cdot \eta_{ST} \cdot \eta_P \quad \text{with:} \quad \eta_{HG} = k_{HG}/(k_{HG} + k_{GH}). \tag{3.62}$$

This is a simplified picture, because both the phosphor absorption and the singlet-singlet Förster-type transfer from host to guest are not taken into account. Still, it can be used best to illustrate how Φ_P changes when an additional loss channel k_{GH} is introduced. For the latter, only the Dexter-type triplet-triplet energy transfer is possible. In the case of an exothermic system, the rate k_{GH} vanishes so that the efficiency of host-guest energy transfer η_{HG} can be unity. Depending on the strength of the energy back-transfer, the overall phosphorescence quantum yield is reduced – the lower the triplet energy of the matrix, the higher k_{GH} [82]. Resonant triplet energies of matrix and dopant mark an intermediate configuration (cf. Fig. 3.5).

Single-Step Long Range TTA

The process of triplet-triplet annihilation in solid mixed films can have different underlying mechanisms. One of them is a single-step longe range interaction, based on a Förster-type energy exchange. It is the limiting mechanism for every phosphorescent mixed system as it solely depends on the spectral properties of the emitting guest. Interestingly, this mechanism has been introduced just recently by Staroske *et al.* [83]. Referring to Equation (3.60), triplet-triplet annihilation mediated by the Förster-type energy transfer is possible, if the donor is a phosphorescent material, because then the

transition moment for $T_1 \rightarrow S_0$ is non-zero. Moreover, the transition of the acceptor molecule, i.e. $T_1 \rightarrow T_n$, lies within the triplet manifold and is therefore an allowed transition. Referring to Equation (3.46), it is proportional to the spectral overlap of phosphorescent emission of the donor and the excited triplet state absorption of the acceptor.

Generally, and not only for this mechanism, the time development of the guest triplet exciton density n (with $n \equiv n(t)$) following a short pulsed excitation can be expressed by the following rate equation:

$$\frac{\mathrm{d}n}{\mathrm{d}t} = -\frac{n}{\tau} - f k_{\mathrm{TTA}}(t) n^2, \tag{3.63}$$

where f accounts for the number of triplet states that are deactivated in the TTA interaction; consequently, it can have values of 1/2 or 1. In this work, $f = 1/2$ is always assumed, i.e. the acceptor state will ultimately keep its excited configuration. The first term represents the monomolecular deactivation of the triplet exciton density n that is inversely proportional to the excited state lifetime τ. To distinguish different TTA mechanisms, the rate constants will be defined as:

$$\gamma_{\mathrm{TT}}(t) := k_{\mathrm{TTA,\ F\ddot{o}rster\text{-}type}}(t) \tag{3.64}$$

$$k_{\mathrm{TT}}(t) := k_{\mathrm{TTA,\ Dexter\text{-}type}}(t), \tag{3.65}$$

where $k_{\mathrm{TT}}(t)$ hereinafter refers to TTA that occurs as a consequence of Dexter-type energy transfers. Within the Förster framework, the rate constant $\gamma_{\mathrm{TT}}(t)$ can be approximated to [84]:

$$\gamma_{\mathrm{TT}}(t) = \frac{2}{3}\pi R_{\mathrm{F}}^3 \sqrt{\frac{\pi}{\tau t}}, \tag{3.66}$$

with the Förster radius R_F for the transfer to an excited guest molecule. There is no regime for which this transfer rate is time independent. Taking this expression into account, the rate equation (3.63) can be solved to:

$$n(t) = \frac{n_0 e^{-t/\tau}}{1 + \frac{2}{3}\pi^2 f n_0 R_{\mathrm{F}}^3 \mathrm{erf}\left(\sqrt{\frac{t}{\tau}}\right)} \quad \text{with} \quad n_0 := n(t=0). \tag{3.67}$$

This one step mechanism clearly suggests that the rate for TTA does not depend on the concentration of the phosphorescent emitter c_{dopant} in the mixed solid film, i.e. $\gamma_{\mathrm{TT}}(t) \not\propto c_{\mathrm{dopant}}$. Furthermore, it suggests that TTA should not be observed in this framework when the average guest-guest distance exceeds the Förster radius R_{F}. Staroske *et al.* showed that a constant Förster radius R_{F} is obtained from experiments, not depending on the number of guest molecules in the intermolecular space between donor and acceptor [83]. This is a major difference to other TTA mechanisms. This mechanism is illustrated in Figure 3.6 a) for an exothermic host-guest system, i.e. in case the excitation is efficiently confined on phosphor sites ($k_{\mathrm{GH}} = 0$).

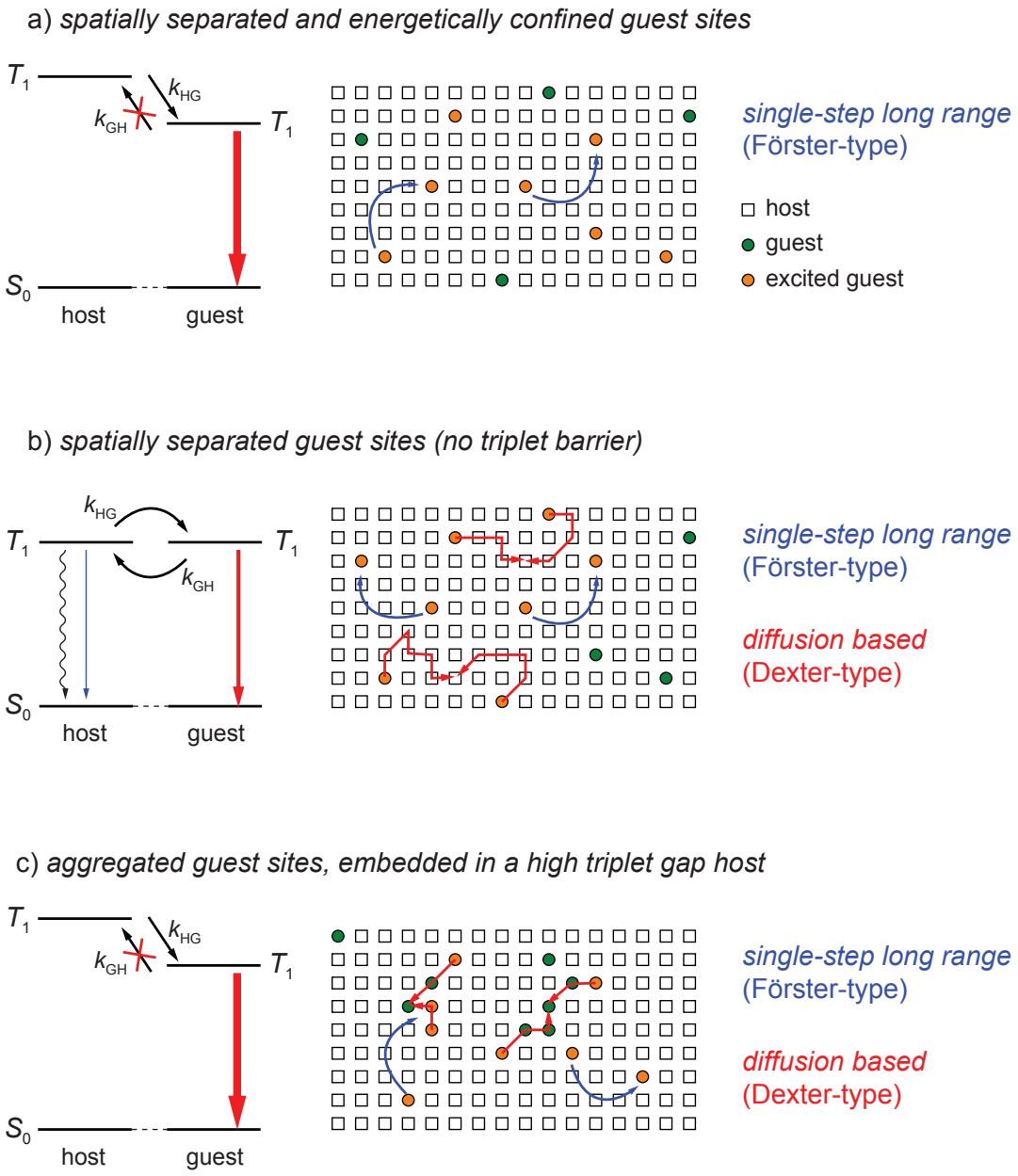

Figure 3.6: Different configurations of the host-guest system in respect to both their relative triplet energies and to the microscopic structure of the mixed film. Host and guests are roughly shown in a molecular ratio of 10:1. Similar to Figure 3.5, the strength of the arrows indicates the emission efficiency of the corresponding host-guest system. a) Excitons are confined on guest sites. The emitter molecules are spatially well separated. In this case, only Förster-type TTA is possible. b) When the triplet energies of host and guest are in resonance, additionally to the single-step process, exciton migration on the grid of host and guest molecules is possible, leading to diffusion based TTA. c) Even though exciton confinement is given, Dexter-type TTA is observed, whenever the guest molecules form aggregates in the mixed film. Hence, it is possible for an exciton to migrate on the locally dense grid of emitter molecules.

Moreover, it depicts the case of spatially well separated molecules in the mixed film, which assures that no other mechanism leading to TTA is possible. Single-step Förster-type TTA will occur in every system, with a strength that solely depends on the spectral properties of the guest, so that it is referred to as *intrinsic limit* [83].

Diffusion based TTA

In the preceding section it has been discussed that excitons can migrate in organic solids, driven by the concentration gradient $\nabla n(\vec{r}, t)$. Consequently, two excited states that diffuse towards each other as a result of random walks in the system can efficiently annihilate, mainly due to exchange interactions. As mentioned above and shown in Figure 3.6 a), the exciton motion in mixed films of host and emitting guest can be efficiently suppressed due to spatial separation and energetic confinement. Such systems are free of diffusion based TTA. However, there are two cases where additional TTA as a result of exciton diffusion is expected – they are depicted in Figure 3.6 b) and c). In b), the triplet energies of matrix and dopant are depicted in resonance so that the excitons are free to move within the mixed film. Hence, compared to good energetic confinement, it is possible for two excited states to reach a critical distance $\bar{a}$, where TTA is possible as a result of exchange interactions. This distance $\bar{a}$ can be expected to have values of the 3D lattice constant of the system [84]. Of course, systems are possible where the triplet energy of the matrix material is even lower compared to the corresponding level of the emitter. However, these systems are not considered here, as they do not provide efficient phosphorescence because the excitation mainly gets quenched on host triplet sites.

In order to prevent this motion of excited states, and hence diffusion based TTA, it is necessary to find suitable mixed systems, where the triplet energy of the host material is higher than the phosphor triplet level. However, experimental results often show that the single-step Förster limit is by far not reached. This can only be explained by a strong tendency of the emitting phosphor to form aggregates during the sample preparation. This scenario is depicted in Figure 3.6 c). Densely packed guest molecules within the mixed host-guest system enable triplet exciton motion between guest sites, even though energetic confinement by host molecules is given. Once again, diffusion based TTA is expected in such a configuration.

The rate constant for TTA originating from exciton motion on the molecular grid is given by [85]:

$$k_{\mathrm{TT}}(t) = 8\pi D\bar{a}\left(1 + \frac{\bar{a}}{\sqrt{2\pi Dt}}\right). \tag{3.68}$$

For times much larger than the nearest neighbour hopping time $t_{\mathrm{hop}} = \bar{a}^2/6D$, the time dependent term in Equation (3.68) can be neglected [86]. This turns $k_{\mathrm{TT}}(t)$ into a simple time-independent form:

$$k_{\mathrm{TT}} = 8\pi D\bar{a}. \tag{3.69}$$

Using this relation, the solution to the general rate equation (3.63) can be written as:

$$n(t) = \frac{n_0}{\left(1 + n_0 \frac{8\pi D\bar{a}\tau}{2}\right) \mathrm{e}^{t/\tau} - n_0 \frac{8\pi D\bar{a}\tau}{2}} \quad \text{with} \quad n_0 := n(t=0). \tag{3.70}$$

One distinct difference to the single-step long range Förster mechanism is its dependence on the guest concentration c_{dopant}, which is taken into account by the diffusion constant D. For systems with energetic confinement, regardless whether the guest molecules are spatially separated or arranged in aggregates, a higher concentration of guest molecules increases the probability for exciton migration between guest sites. Only the special case of host and guest resonant triplet energies (cf. 3.6 b)) does not suggest a dependence on the guest concentration at first glance. Here, for all possible concentrations of the guest molecule, diffusion should be possible with the same average probability. However, since the hopping rate between two host, two guest, or one host and one guest molecule can be different, such systems might still carry a concentration dependence.

It is worth mentioning that diffusive transport and, consequently, bimolecular reactions strongly depend on the dimensionality of the organic solid [87]. All preceding considerations are made for an isotropic three-dimensional case without preferential direction. Engel *et al.* derived a solution for the case of 1D stacking of the organic molecules, where the lattice constant in one direction of space is by far smaller than the ones of the remaining two directions [84]. In such a system, preferentially one-dimensional diffusion is expected. However, the functional dependence of an 1D rate constant $k_{\mathrm{TT,1D}}$ for diffusive TTA falls together with the solution of the single-step long range mechanism, so that is not possible to distinguish between these mechanisms. A lower dimensionality, caused by microscopic ordering of the molecules, is not expected for the materials used in this work.

3.5 Charge Transport Properties

In the preceding sections, only the physics of neutral molecular excitations – the excitons – were discussed. Of course, molecules can also be charged. Carrying an additional *electron* on the LUMO level provides a negative charge, whereas a positive charge is caused, if the HOMO is singly occupied by one electron (a *hole*). These charge carriers are able to move under an applied electric field $\vec{F}$. In a first approximation, the drift velocity $\vec{v}$ of a charge carrier is linearly proportional to $\vec{F}$:

$$\vec{v} = \bar{\mu}\vec{F}, \tag{3.71}$$

when $\bar{\mu} \neq \bar{\mu}(\vec{F})$. This introduces the charge carrier mobility $\bar{\mu}$, which generally is a tensor. Once again, for typical amorphous organic materials it is assumed that they are isotropic in respect to their charge transport properties. Furthermore, the transport is commonly reduced to a one-dimensional problem as organic devices are treated to have infinite extension in two directions turning the mobility into a scalar μ. It is noteworthy that the mobility cannot be seen as a fixed intrinsic material property that comes along with each organic compound. It rather is a material parameter which must be determined for each specific case. Here, the sample preparation conditions, the morphology of the substrate, the material purity, and the method of mobility measurement strongly influence the quantitative result of μ.

Frequently used experimental methods of determining the mobility for electrons and holes, respectively, are the time-of-flight method [88], field-effect-mobility measurements [89, 90] and the analysis of space-charge-limited-currents [91–93].

Hopping Transport in Organic Solids

In contrast to conventional inorganic semiconductors, where the charge transport proceeds in widely delocalized states, a series of individual hopping steps between localized states determines the current flow in organic materials [89]. These hopping steps are thermally activated, so that the mobility in organic semiconductors increases with increasing temperature, which is in direct contrast to the limiting phonon scattering in inorganic materials. Quantitatively, compared to the conventional band transport, the hopping transport is accompanied with much lower mobilities. Bässler introduced a model, the *Gaussian disorder model* (GDM), where the hopping transport occurs between Gaussian distributed density of states (DOS) [94], the latter being expressed as:

$$\rho(\hat{\varepsilon}) = (2\pi\sigma^2)^{-1/2}\mathrm{e}^{-\hat{\varepsilon}^2/2\sigma^2}. \tag{3.72}$$

Here, σ is the width of the DOS and $\hat{\varepsilon}$ the energy measured from the center of the DOS. Modeling the density of states by Gaussian distributions is justified by the Gaussian shape of absorption and fluorescence bands. For the state distribution of charge carriers, a similar shape is expected [94].

Space Charge Limited Currents

For organic molecular solids within devices, one has to distinguish between ohmic and space charge limited currents (SCLCs). In the ohmic current regime, the sample is free of space-charge. This is the case when the dielectric relaxation time t_r is shorter than the transit time t_t of the charge through the material. The criterion for ohmic conduction thus reads,

$$t_\mathrm{r} = \frac{\varepsilon}{\sigma} = \frac{\varepsilon}{en_\mathrm{c}\mu} < t_\mathrm{t} = \frac{d^2}{\mu V} \Rightarrow V_\mathrm{crit} \approx \frac{en_\mathrm{c}d^2}{\varepsilon}, \tag{3.73}$$

in which σ is the conductivity, ε the dielectric constant, V the applied voltage, n_c the charge carrier density, and d the thickness of the sample [95]. For voltages exceeding V_crit ($V > V_\mathrm{crit}$), steady state conditions with additional space-charge arise. Due to the limited mobility, the charges accumulate at the electrode hindering further injection of carriers. In this space-charge-limited regime, the current density obeys the *Mott-Gurney law*,

$$j_\mathrm{MG} = \frac{9}{8}\mu\varepsilon_\mathrm{r}\varepsilon_0\frac{V^2}{d^3}, \tag{3.74}$$

where j is the current density, V the applied voltage, d the thickness of the sample, ε_r the relative permittivity, and ε_0 the permittivity of free space. For this equation, ohmic contacts and unipolar transport are assumed. Furthermore, trap states within the material are not considered by this equation, which makes it the most ideal case of SCLC-theory. Nevertheless, it explains the relationship between current density and voltage, $j \sim V^2$, which is fundamental for the understanding of j-V-characteristics of devices, composed of organic compounds.

Additional trap states that might be present in an organic solid are taken into account in the extension of the SCLC theory, the so-called *trap filled limited current* (TFLC) theory. These traps are gradually filled with increasing applied voltage V until the trap filled limit is reached. Currents above this limit are described by the following equation [92, 93]:

$$j = e\mu N_\mathrm{c}\left(\frac{2l+1}{l+1}\right)^{l+1}\left(\frac{l}{l+1}\frac{\varepsilon_\mathrm{r}\varepsilon_0}{eN_\mathrm{t}}\right)^{l}\frac{V^{l+1}}{d^{2l+1}}. \tag{3.75}$$

Here, N_c is the density of states at the transport level, N_t the total density of trap states, and $l = E_\mathrm{t}/kT$ (E_t depth of trap states). This equation is assuming an exponential distribution of trap states $n_\mathrm{t}(E)$ [92]. This is in agreement with the approximation of traps to be distributed in the energy tail of the Gaussian density of states [94]:

$$n_\mathrm{t}(E) = \left(\frac{N_\mathrm{t}}{kT_\mathrm{t}}\right)\mathrm{e}^{-(E-E_\mathrm{c})/k_\mathrm{B}T_\mathrm{t}} \quad \text{with} \quad E_\mathrm{c} > E > 0, \tag{3.76}$$

with E_c being the energy of the conduction level and $k_\mathrm{B}T_\mathrm{t}$ the energy characterizing the trap distribution.

Functional Dependence of the Mobility

Apart from the temperature dependence that is tightly connected to phonons of the system [89], the mobility further depends on the applied electric field F and the charge carrier density n_c. At high applied fields, an enhancement of the SCL current can be observed, which is attributed to a field-dependent mobility. It reads:

$$\mu(F,T) = \mu(0,T)\mathrm{e}^{\gamma(T)\sqrt{F}}, \tag{3.77}$$

where $\mu(0,T)$ is the zero-field mobility and $\gamma(T)$ the so-called field enhancement factor [96]. The latter describes the barrier lowering for hopping in direction of F. With this Poole-Frenkel type mobility $\mu(F,T)$, the current density can be approximated to [97]:

$$j_\mathrm{PF} = \frac{9}{8}\varepsilon_\mathrm{r}\varepsilon_0\mu(0,T)\frac{V^2}{d^3}\mathrm{e}^{0.89\gamma(T)\sqrt{V/d}}. \tag{3.78}$$

Furthermore, an increase of local carrier concentration n_c leads to a pronounced carrier density dependence of the mobility. Typically, these effects are observed for carrier concentrations of $n_\mathrm{c} > 10^{16}\,\mathrm{cm}^{-3}$ [98]. Referring to numerical simulation results of multilayer organic LEDs, typical carrier concentrations in transport materials range between $10^{16} - 10^{18}\,\mathrm{cm}^{-3}$ for both trapped and free charges [99]. However, in emissive layers the average carrier density can be in the order of $n_\mathrm{c} \sim 10^{15}\,\mathrm{cm}^{-3}$ for holes and electrons. Only in case of strong carrier accumulation in the emission layer at interfaces to adjacent layers, the concentration can noticeably exceed $10^{15}\,\mathrm{cm}^{-3}$. The carrier dependence is especially important for organic field-effect transistors, where the highest carrier densities reach values in the range of $10^{20}\,\mathrm{cm}^{-3}$ (approximately 0.01 carriers per site) [100, 101]. The mobility enhancement due to the presence of charge carriers is described by an empirical relation:

$$\mu(n_\mathrm{c},T) = \mu(0,T) + \frac{\sigma_0}{e}\left(\frac{\left(\frac{T_0}{T}\right)^4 \sin\left(\pi\frac{T}{T_0}\right)}{(2\alpha)^3 B_\mathrm{c}}\right)^{T_0/T} n_\mathrm{c}^{T_0-1/T}, \tag{3.79}$$

in which σ_0 is a prefactor for the conductivity, α^{-1} the effective overlap parameter between localized states, T_0 a measure of the width of the exponential DOS, and B_c a critical number for the onset of percolation [96]. Using an approximation for the current density contribution that stems from the carrier concentration [98], the total current density can be written as [96]:

$$j_{n_\mathrm{c}} = j_\mathrm{MG} + c\frac{V^{T_0/T+1}}{L^{2(T_0/T)+1}}, \tag{3.80}$$

with a proportionality constant c.

3.6 Organic Light-Emitting Diodes

Originally, electroluminescence (EL) was referred to luminescence that occurs by application of an electric field to a phosphor [102]. In this case, no net current passes through the device and only the applied field lifts atomic electrons into the conduction band. Nowadays, luminescence is termed electroluminescence as it is seen as a consequence of injection and flow of charge carriers through a material.

This work focusses on a very promising candidate of electroluminescent devices for many applications: the organic LED. In this section, the various processes that need to take place for such a device to luminesce will be discussed. Most importantly, the corresponding efficiencies are highlighted to point out the great potential of phosphorescent OLEDs and the strong efficiency limitation due to poor light outcoupling. This section will be followed by an introduction to state-of-the-art OLEDs, including a discussion of their various functional layers in the multilayer architecture.

The Efficiency of an OLED

The overall electron-photon conversion efficiency, which is referred to as *external quantum efficiency* (η_{ext}, EQE), can be expressed as [43]:

$$\eta_{\mathrm{ext}} = \gamma_{\mathrm{bal}} \cdot \Phi_{\mathrm{em}} \cdot \left\{ \begin{array}{ll} r_{\mathrm{ST}} & \text{fluorescence} \\ 1 - r_{\mathrm{ST}}(1 - \eta_{\mathrm{ISC}}) & \text{phosphorescence} \end{array} \right\} \cdot \eta_{\mathrm{out}}. \tag{3.81}$$

Here, γ_{bal} is the charge balance factor, r_{ST} the fraction of created singlet excitons, η_{ISC} the intersystem crossing efficiency, Φ_{em} the quantum yield of the emitting molecule, and finally η_{out} the light outcoupling efficiency. To illustrate each contribution to η_{ext}, the flowchart in Figure 3.7 quantifies each process leading to electroluminescence, including the very important differentiation between fluorescent and phosphorescent OLEDs.

Upon application of an external electric field, holes and electrons are injected and forced to move to the center of the organic materials. When reaching their corresponding capture radius, these charges form Coulomb-correlated electron-hole pairs which ultimately collapse to singlet and triplet excited states. At large separation distances, these states are degenerate in a ratio of 1:3 [5]. Since the carrier transport in amorphous organic systems is mediated by uncorrelated hopping steps, the carriers undergo a recombination of the *Langevin* type [103, 104]. The steady-state current density of an OLED is a combination of hole j_{p} and electron j_{n} current densities, which generally can differ in their value. Efficient EL is only observed if an electron is provided for each hole to recombine (or vice versa). This is expressed by the charge balance factor γ_{bal}:

$$\gamma_{\mathrm{bal}} = \frac{j_{\mathrm{low}}}{j_{\mathrm{high}}} \leqslant 1, \tag{3.82}$$

in which j_{low} is the lower and j_{high} the higher of the two (hole and electron) current densities. Here, it needs to be assumed that j_{low} completely contributes to exciton formation. It can be unity for $j_{\mathrm{p}} = j_{\mathrm{n}}$. As it will be discussed in detail in Section 3.7,

state-of-the-art organic LEDs work close to $\gamma_{\mathrm{bal}} = 1$ as a consequence of electrically doped transport layers and carrier blocking layers within the OLED stack.

In organic LEDs, the excited states, i.e. singlets and triplets, are created with a one to three ratio. This is a consequence of the multiplicity of both states, which is one for singlets and three for triplets [4–7]. Hence, whenever fluorescent emitters are used as emitting molecules in an OLED, about 75 % of the excitation is lost in their triplet manifold, even if their fluorescent quantum yield reaches 100 % (cf. Fig. 3.7). To account for the singlet and triplet formation in organic devices, the fraction of created singlets r_{ST} is introduced, which is consequently considered to be $r_{\mathrm{ST}} = 0.25$ [43]. Hence, for fluorescent OLEDs, the process of exciton generation in conjunction with the corresponding fluorescent quantum yield Φ_{F} contributes to η_{ext} with $r_{\mathrm{ST}} \cdot \Phi_{\mathrm{F}} \leqslant 0.25$. This picture drastically changes in case of phosphorescent OLEDs. Referring to the discussion of efficient phosphorescence in Section 3.2, the heavy metal effect changes the intermolecular energy transfers. The spin-orbit coupling strongly increases the transition moments for the recombination in the triplet state configuration, so that triplet emission from state-of-the-art phosphors can be observed with very high yields Φ_{P} close to one [78]. Moreover, these phosphorescent emitters show very high intersystem crossing efficiencies from singlet to triplet states. Hence, the fraction of created singlets r_{ST} can be efficiently harvested for triplet state emission with an efficiency of $r_{\mathrm{ST}} \cdot \eta_{\mathrm{ISC}}$ (cf. Eqn. (3.81)). Referring to Figure 3.7, the use of phosphorescent emitters can lead to internal efficiencies of 100 %, which is a fourfold increase compared to fluorescence.

At first glance, phosphorescent emitter molecules seem to be the ideal candidate for high efficiency OLEDs, but their excited state lifetime in the range of microseconds causes a negative effect on the high brightness performance (cf. Section 3.4). Here, bimolecular annihilation processes strongly reduce the EQE at high brightness. Therefore, many researchers try to improve η_{ext} of fluorescent OLEDs by increasing the fraction of created singlet excitons r_{ST}. Recently, Okumoto *et al.* reported on green fluorescent OLEDs with nearly 10 % EQE, which clearly contradicts the above statements, as it would translate in a singlet fraction of approximately $r_{\mathrm{ST}} = 0.5$. The underlying mechanism is not fully understood, however, the most reasonable explanation is the creation of additional singlet states via TTA (cf. Eqn. (3.60)) [105].

Another concept to increase r_{ST} is referred to as *extrafluorescence* [106]. In general, prior to exciton formation, charge-transfer (CT) states are formed, which also carry a certain spin configuration [5]. Investigations by Segal *et al.* proved that incorporation of a mixing material, for which the energetic order of singlet and triplet charge-transfer states ($E_{\mathrm{CT},S} < E_{\mathrm{CT},T}$) is inversed, increases the rate to form singlet CT states strongly, resulting in a higher singlet fraction in the fluorescent emitting layer [106]. Compared to a reference device, an EQE improvement of a factor of 2.8 is observed. However, as this mixing only proceeds in the region of the interface between mixing and emitting layer and demands special material properties, it is not yet clear if this concept can be widely adopted to state-of-the-art fluorescent OLEDs.

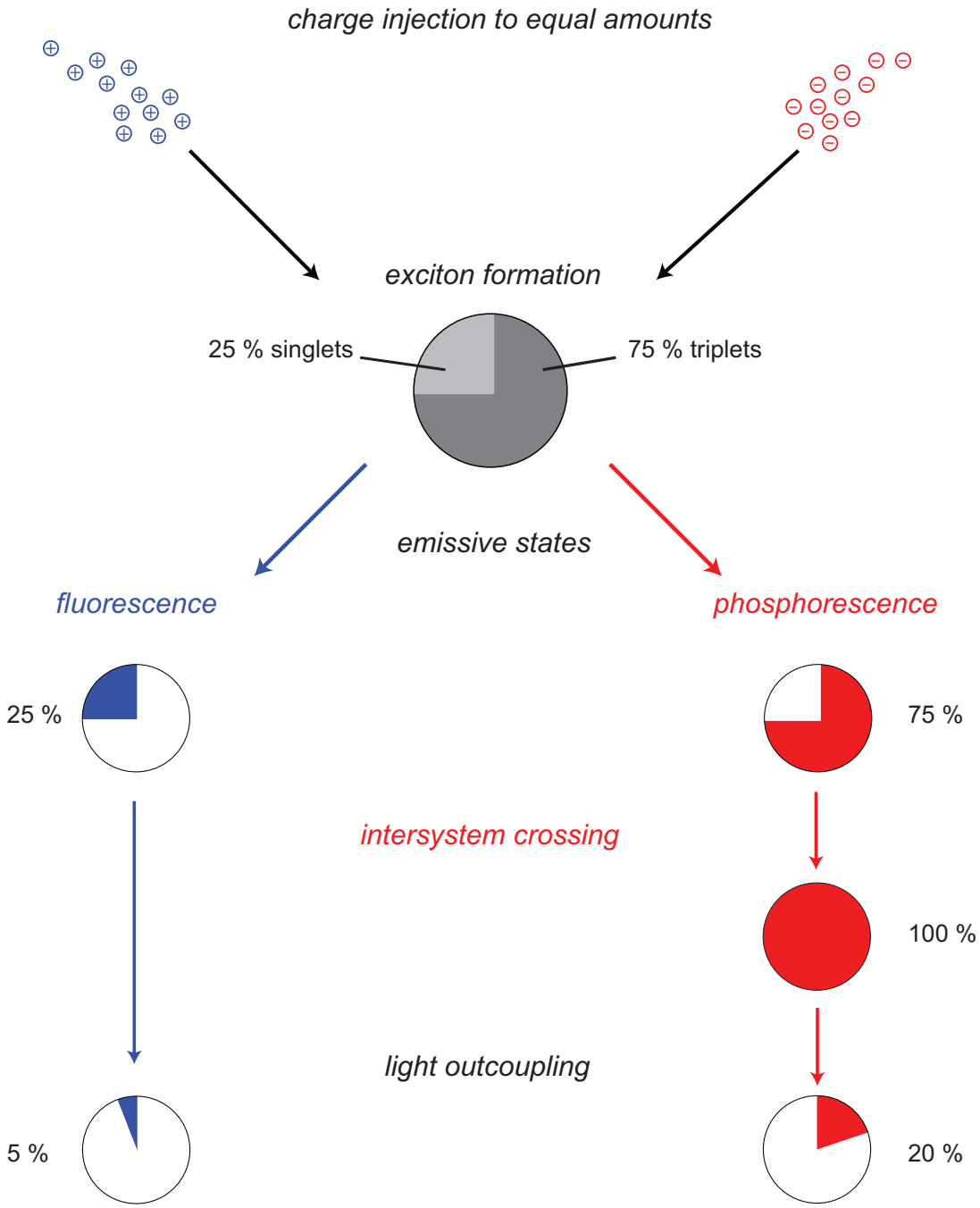

Figure 3.7: This flowchart illustrates the all important processes that contribute to electroluminescence of OLEDs for the important cases of a fluorescent and phosphorescent device. The highest possible efficiencies are assumed for each process. The light outcoupling efficiency refers to bottom-emitting OLEDs on standard flat glass substrates.

Critical Current Density

In order to discuss the efficiency roll-off of OLEDs at high brightness, Baldo *et al.* introduced the critical current density j_c [19]. It is defined as:

$$\eta_{ext}(j_c) = \frac{1}{2}\eta_{ext,j\to 0}, \tag{3.83}$$

where $\eta_{ext,j\to 0}$ is the external quantum efficiency of the OLED at very low current density, where no bimolecular quenching is expected. Thus, j_c defines the current density, where the device efficiency drops to half of its initial value at low brightness. In general, this value can either be directly calculated from OLED data or estimated from model calculations [20]. Its worth noting that the experimental determination of j_c is in many cases affected by severe device degradation, resulting in lower values.

It is very universal to state the EQE versus current density, because it does not take the spectral response of the human eye into account. Thus, efficiency data of OLEDs with different spectra can be compared with respect to their roll-off characteristics directly. Furthermore, it is easier to implement the current density into model calculations. However, it is then hard to judge wether the roll-off affects a certain application (with a given brightness) or not. Therefore, as long as it is not necessary to compare OLEDs with much different spectra or model calculations are included, the EQE versus brightness data will be discussed in this work.

Light Outcoupling

Due to its thin film layered architecture, a large fraction of the light created in the center of the organic stack can not to escape to air. However, it is desired to couple out as much light to the forward hemisphere, where the observer is typically located. In a very simple model, omitting microcavity effects and differences in the refractive indices of different functional materials, the efficiency to couple out light that is isotropically emitted in the OLED center can be approximated to [107–109]:

$$\eta_{out} = \frac{1}{2n^2}, \tag{3.84}$$

in which n refers to the refractive index of the glass substrate.[7] Hence, for a standard glass with $n = 1.51$, the outcoupling efficiency roughly amounts to 20 %. It is necessary to note that this discussion of the light extraction efficiency η_{out} only holds for OLEDs in the standard device configuration, i.e. the bottom-emitting layout. For different device architectures (e.g. top-emitting OLEDs), these considerations might differ. Figure 3.7 clearly shows that the light outcoupling in standard OLED configurations is the largest loss channel. Even if phosphors yield internal efficiencies of 100 %, the optics of the OLED only allow every fifth photon to escape the device.

Figure 3.8 illustrates the different light modes that propagate within the OLED after emission in the EML. They are formed as a consequence of different interfaces

[7] It is most common to use n for refractive indices, which is similar to the definition of the exciton density in this work. The context however will be sufficient to avoid misunderstandings.

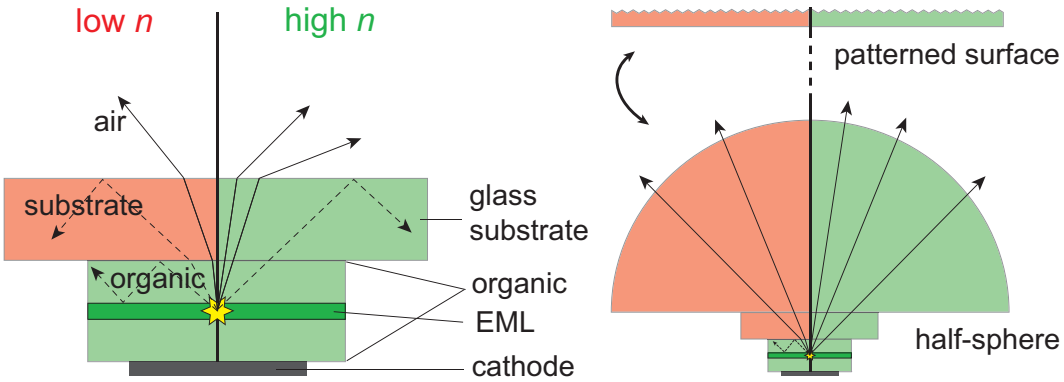

Figure 3.8: The possible paths of light progagation in an OLED. Two cases are distinguished: low (red) and high (green) refractive index n. Left: Cross-section of an OLED. Dashed lines indicate modes that cannot escape the device (organic and substrate modes), solid lines indicate outcoupled air modes. Right: Possible set-ups for improved light outcoupling. All substrate modes are coupled out, by applying a large index matched half-sphere. For practical applications, the half-sphere is replaced by a patterned surface.

within the architecture that show a step in the refractive indices n_i of the involved materials. Organic materials and the commonly used transparent conductor ITO have refractive indices of $n_{\text{org}} = 1.6-1.8$ in the visible part of the electromagnetic spectrum [109–111]. Using conventional glass substrates with a refractive index of $n_{\text{sub}} = 1.51$, the first optical interface is the organic stack (incl. ITO)/glass substrate interface. Total internal reflection traps part of the emitted light to the organic layer stack, forming *organic modes*, while the remaining light is coupled into the glass substrate. In the simplest picture, these organic modes form waveguide modes between the glass and the highly reflective bottom electrode.

The critical angle θ_{g} for total internal reflection is given by [40]:

$$\sin\theta_{\text{g}} = \frac{n'}{n}, \tag{3.85}$$

where n' describes the optically less dense medium compared to n. Having reached the substrate glass, the light faces the glass substrate/air interface with a step in the refractive indices of $\Delta n = 0.51$ for standard glass. Here, the critical angle for total internal reflection is $\theta_{\text{g}} = 41.5\,^{\circ}$. Hence, light of higher angles will form zig-zag modes within the glass substrates, which are called *glass* or *substrate modes*. Finally, the light that is coupled from the glass to air is referred to as *air* or *outcoupled modes* (cf. Fig. 3.8). For standard glass substrates, the organic and glass modes are calculated to have roughly equal amounts of 40 % each [107, 108].

Thus, extensive research efforts are spent on the improvement of light outcoupling, as it bears a fivefold increase of the OLED efficiency η_{ext}. These efforts can be divided into two separate tasks, the outcoupling of glass and organic modes. Coupling out substrate modes is comparably simple to achieve, because the interface of interest is the outermost one between the rigid glass and air, where various modifications are possible. First of all, using a glass half-sphere of equal refractive index as the substrate with much larger dimensions than the OLED pixel, all glass modes can be coupled out [112]. Here, each ray that enters the substrate reaches the glass/air interface with a 90 ° angle of incidence to the surface normal. This set-up, illustrated in Figure 3.8, is used to quantify the total amount of light that enters the glass substrate. However, due to their bulky shape, these macro-extractors have no practical relevance. This can be easily circumvented by patterned substrate surfaces, e.g. periodic pyramidal [109] or microlens [113, 114] arrays, which typically yield improvement factors of $1.2 - 1.5$. Similar improvements can be obtained by surface attached scattering layers [109].

In contrast, improving the outcoupling of organic modes is much harder to achieve, because it involves changes of the OLED architecture. One very sophisticated approach is the integration of low refractive index grids between organic materials and the ITO anode [115]. Its low n is used to redirect rays in the organic material to higher angles of incidence to the glass or reflective cathode surface, respectively. Hence, a larger fraction of light can leave the device. This concept is further improved by applying a microlens array to the substrate surface, leading to improvement factors up to 2.3 [115]. For monochrome OLEDs, Meerheim *et al.* reported an improved light outcoupling using strong microcavity resonators [116]. By optically optimizing the cavity, the emission affinity of the OLED can be tuned to fit the emission spectrum of the emitter, which leads to improvements up to a factor of 1.5. This approach results in narrowband emission with strong colour shifts for higher viewing angles which is detrimental to improve the outcoupling efficiency of broad/white emitting OLEDs.

Another approach to improve the outcoupling of organic modes is to match the refractive index of the glass substrate to the values of the underlying organic materials in the range of $n_{\text{sub}} \sim 1.8$ [117]. This approach is applied in Chapter 7 to improve the efficiency of white OLEDs [27]. The concept is schematically depicted in Figure 3.8l. Here, the emitted light does not face an optical interface until it reaches the glass/air interface. However, the critical angle for TIR strongly decreases to $\theta_{\text{g}} = 33.7\,^{\circ}$, if the glass index is $n_{\text{sub}} = 1.8$. Thus, this approach easily realizes very efficient light coupling to the glass substrate, but at the same time requires even better light outcoupling at the glass/air interface. Importantly, in this architecture, no real glass modes are formed anymore, because trapped light will uniformly travel as zig-zag modes between highly reflective cathode and the glass/air interface.

Plasmonic Losses

Another effect that strongly influences the efficiency of an OLED is the coupling of the emitting dipoles to the surface plasmons of the highly reflective metal, i.e. the cathode in the bottom-emitting OLED layout. Their impact is very strong for distances between the emitter and the cathode up to 60-80 nm and steadily decreases

for larger distances [118, 119]. This coupling can be strongly reduced by placing the emission layer into the second or higher field antinode of the optical system [112, 120]. A negligible level of these losses is obtained for distances larger than 200 nm.

Gärtner and Greiner have theoretically addressed this issue by calculating the complete mode spectrum of different OLED configurations, using standard microcavity theory [121, 122]. By expanding the field of the emitting dipoles into plane waves, which are parameterized by the horizontal wave vector k_{hor}, they calculated total radiant power F as an integral of the contributions $F(k_{\mathrm{hor}})$:

$$F = \int_0^\infty F(k_{\mathrm{hor}}) k_{\mathrm{hor}} \mathrm{d}k_{\mathrm{hor}}. \tag{3.86}$$

Further introducing a normalized horizontal wavevector $\bar{k}_{\mathrm{hor}} = k_{\mathrm{hor}}/k_{\mathrm{air}}$ resulted in the following classification of modes [121]:

- $\bar{k}_{\mathrm{hor}} \leqslant 1$: power emitted to air,
- $1 \leqslant \bar{k}_{\mathrm{hor}} \leqslant n_{\mathrm{sub}}$: power into substrate modes, and
- $\bar{k}_{\mathrm{hor}} \geqslant n_{\mathrm{sub}}$: power into organic and plasmonic modes.

By increasing the emitter-cathode distance from 60 to 250 nm, which corresponds to the first and second field antinode of their model system, the main changes in the mode power spectra are observed for $\bar{k}_{\mathrm{hor}} \geqslant 1.51 = n_{\mathrm{sub,low}}$. Apparently, a large fraction of the power that is originally coupled to surface plasmons (small emitter-cathode distance) is only converted into organic modes (large emitter-cathode distance). Thus, for conventional substrates, the overall gain in light output is low, because the increase in organic mode power cannot be extracted by means of substrate surface modification.

The suppressed coupling to the surface plasmons can be utilized by incorporation of high index substrates (in their calculation with $n_{\mathrm{sub,high}} = 1.85$), which match the refractive indices of the incorporated organic materials. Here, most of the emitted power is coupled into modes with $\bar{k}_{\mathrm{hor}} \leqslant 1.85 = n_{\mathrm{sub,high}}$, i.e. either into air or substrate modes. Calculations show that up to 90 % of the generated light can be coupled into the substrate, of which about 1/3 is leaving the substrate without additional outcoupling concepts [121]. The remaining power in the substrate can potentially be extracted using conventional techniques, e.g. microlens arrays.

A helpful side effect, especially when used in combination with high index glass substrates, is the angular emission pattern of OLEDs optimized for the second or higher field antinode. Here, the OLEDs exhibit a more direct emission so that light outcoupling at the glass/air interface becomes easier, since high angle light is suppressed. The latter is difficult to couple out due to the small critical angle of $\theta_{\mathrm{g}} = 33.7\,^\circ$ for TIR.

3.7 Functional Layers and Materials Used

In contrast to the very early work of Tang and VanSlyke, where the OLED consisted of two organic layers sandwiched between the electrodes [2], the state-of-the-art organic LEDs comprise various layers with different functionality. This section provides a description of these different layers in the multilayer OLED architecture. Furthermore, this discussion is supplemented with a brief introduction of the specific material systems used in this work.

Electrically Doped Organic Semiconductors

Before holes and electrons can meet in the emission layer (EML) of an organic LED in the center of the layer stack, they have to be injected from the electrodes and transported through the outer organic layers. In this work, all OLEDs comprise electrically doped transport layers, which is commonly referred to as *p-i-n concept* (see below). Here, the 'i' denotes 'intrinsic', summarizing electrically undoped organic layers in the center of the OLED stack. The doping can be achieved by mixing the organic semiconductor with strong acceptor and donor materials for p-type and n-type doping, respectively. Here, an acceptor material removes an electron from the HOMO level of the organic compound, creating a free hole, while a donor transfers an electron to the LUMO level of the matrix [123].[8]

In general, reactive metals such as lithium or cesium can be used for efficient electrical doping [124], but since these atoms are very small, their tendency to diffuse in the organic compound is very high. This generally results in a poor device stability. Therefore, it is desired to incorporate larger, rigid organic materials as dopants for the use in OLEDs. Various studies have shown that the conductivity can be increased orders of magnitude for p-type [125–129] and n-type doping [130, 131], because the presence of the dopant strongly increases the free carrier density. In some cases it was shown that the conductivity of the doped layer increases super linearly with the corresponding molar concentration of the dopant material [123]. This is a result of subsequent filling of energetically distributed, localized states upon charge release upon doping [128]. Most impressively, the concept of molecular doping is shown for organic homojunction diodes by Harada *et al.*, where the well known zinc-phthalocyanine (ZnPc) is both p- and n-type doped, using organic dopants [132].

As the concept of electrical doping is not the scope of this work, the interested reader is referred to a recent review article by Walzer *et al.* [133]. It covers both the fundamentals of doping as well as its impact to organic devices such as OLEDs or organic solar cells.

[8] Similar to mixed systems in efficient phosphorescent emission layers, the organic semiconductor that is electrically doped is referred to as 'matrix'.

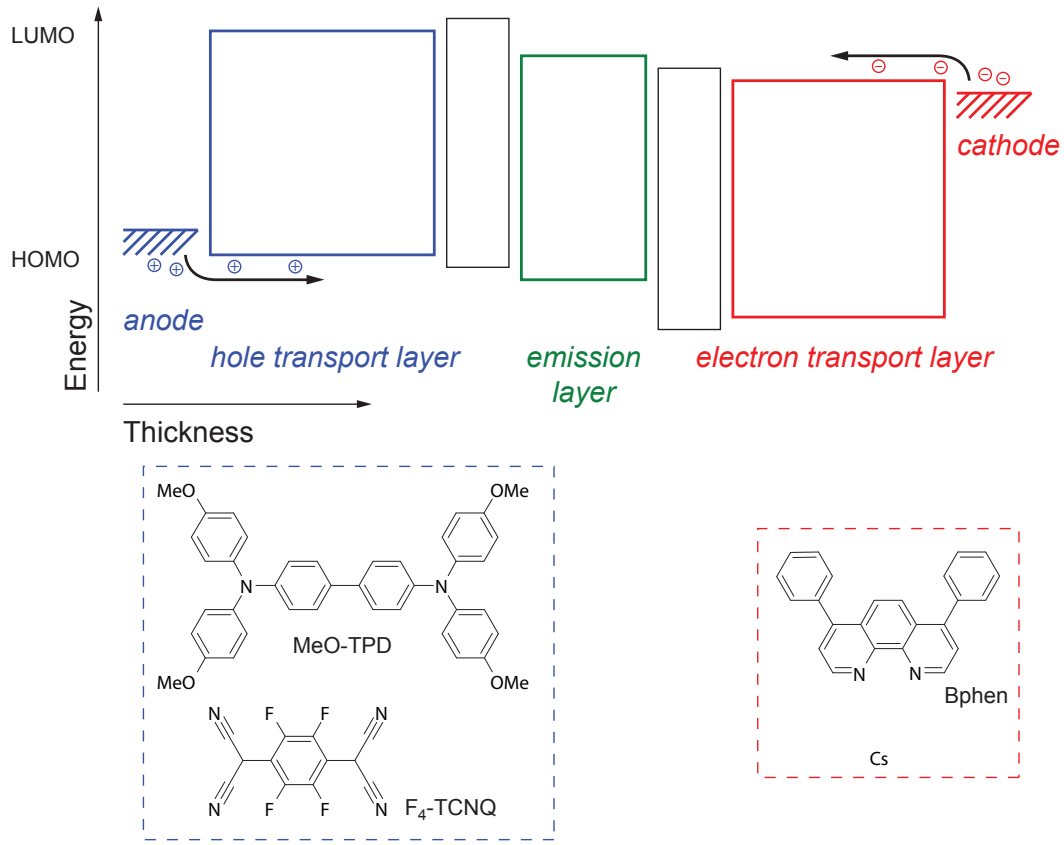

Figure 3.9: The energy diagram of a typical multilayer OLED is shown, highlighting the hole and electron transport layers in contact to the electrodes. In this work, the p-doped HTL is a mixture of MeO-TPD and F_4-TCNQ (dopant), typically with a molar concentration of 4 mol% of the dopant. The ETL is cesium doped Bphen, prepared in a ratio of roughly 1:1.

The p-i-n Concept

In p-i-n OLEDs, doped transport layers are used as charge transport layers, adjacent to the anode and cathode. The complete schematic energy diagram is shown in Figure 3.9. These mixed layers exhibit three distinct improvements compared to conventional, undoped devices:

- Compared to the intrinsic material, the conductivity of doped transport layer can be several orders of magnitude higher, hence, ohmic losses as a consequence of charge transport drop to a negligible level. This can strongly reduce the OLED operating voltage, therefore enabling higher device power efficiencies.

- Generally, if a metal and a semiconductor are in contact, the Fermi level aligns. In case of a doped organic semiconductor, the Fermi level shifts towards the corresponding transport level of the semiconductor. Hence, at the interface to the metal, the transport level of the organic doped system moves closer to the

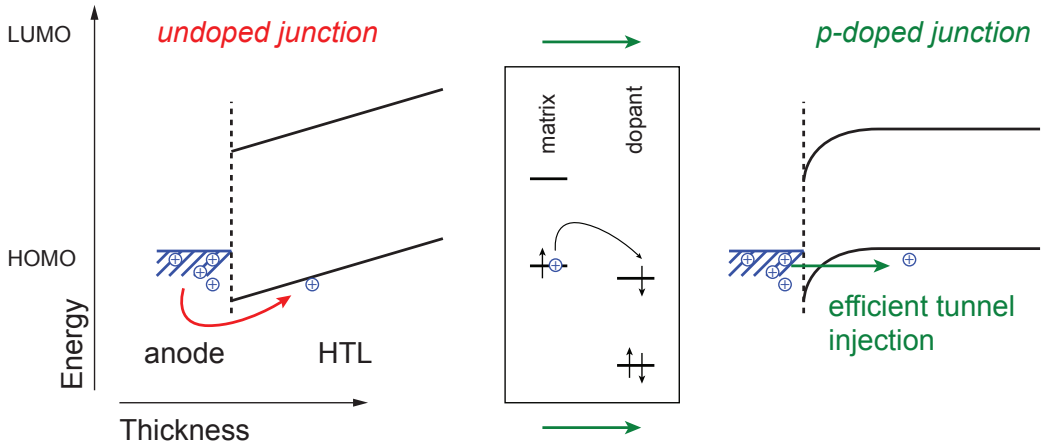

Figure 3.10: Interface between a metal and an organic semiconductor for the cases of undoped and doped hole transport layers. In the undoped case, the holes need to overcome the hole injection barrier formed between metal and HOMO level of the organic material. By incorporation of a suitable acceptor material with a low lying LUMO, an electron from the matrix HOMO is transferred to the dopant LUMO. In the p-doped case, holes can efficiently be injected via tunneling through a thin space charge region.

metal work function. Furthermore, the doping results in a very strong level bending, forming a very thin space charge region, which can easily be tunneled through [126]. In consequence, similar to inorganic materials, a Schottky contact is formed, assuring quasi ohmic injection via efficient tunnel injection into the organic material [43]. This is schematically shown in Figure 3.10 for the case of p-type doping.

- The design flexibility of the OLEDs is greatly increased due to the above properties. The formation of the Schottky contact allows a great variability in the choice of the contact materials, as the electrical properties of the devices remain nearly unchanged. Furthermore, as the resistive losses in the transport layers are negligible, the thicknesses of these layers can be adjusted to realize optimal optical properties of the devices without changing the OLED operating voltage.

In this work, the p-doped hole transport layer (HTL) comprises *N,N,N',N'*–tetrakis(4-methoxyphenyl)-benzidine (MeO-TPD) as the matrix, which is doped with 2,3,5,6-tetrafluoro-7,7,8,8-tetracyanoquino-dimethane (F_4-TCNQ) at a concentration of 4 mol%. In Chapter 7, instead of using F_4-TCNQ, a proprietary molecular dopant NDP-2, purchased from Novaled AG, Dresden, is used with the same molar ratio. Compared to F_4-TCNQ, it allows more stable device processing in the single chamber deposition tool. Here, the standard dopant F_4-TCNQ causes severe cross contamination of the deposition crucibles.

Even though an entirely molecular system would be more desirable, cesium (Cs) doped 4,7-diphenyl-1,10-phenanthroline (Bphen) is used as doped electron transport layer (ETL). Here, Cs is mixed with Bphen in an approximate ratio of 1:1. The molecular structures of the transport layer materials are shown in Figure 3.9.

Transparent conductive oxides, typically indium tin oxide, are used as transparent anodes [134]. For the highly reflective cathode, aluminum (Al) is used as a standard material, having a work function of 4.3 eV [20]. In Chapter 7, silver (Ag, work function: 4.1 eV [135]) is used as the cathode, due to its slightly higher reflectivity compared to Al.

Charge Carrier Blocking Layers

Within the p-i-n layer sequence, in addition to the EML, two thin functional layers sandwiching the EML are introduced. This is schematically shown in Figure 3.11. Primarily, they serve as hole (HBL) and electron (EBL) blocking layers, confining the injected charge carriers to the emission layer. Their various desired properties are exemplarily discussed for the EBL. The HBL shall have equivalent properties for the opposite charge carrier type.

To prevent electron leakage, the LUMO level of the EBL must be noticeably higher than the corresponding EML levels, introducing a large energy barrier that the electrons can not overcome easily (cf. Fig 3.11). The HOMO level of this blocker material should level in between the transport levels of the HTL and the EML to support the charge injection into the latter. For the same reason, the EBL should not have a very low hole mobility, because it would hinder charge transport and injection.

It is important to have an intrinsic layer between the doped transport layers and the EML, because otherwise the dopant molecules would act as strong exciton quenching sites. Here, the blocking layers with a typical thickness of 10 nm are sufficient to prevent this quenching.

Especially for phosphorescent OLEDs, where the triplet exciton diffusion length is of the same order as of the typical thicknesses of the EML [74, 136], the excitons must be confined to the latter. This is similar to the discussion of the ideal host-guest system for phosphorescent emitters (cf. Fig. 3.5). Hence, the triplet energy of the blocking layers should be higher than the phosphor and even higher than the corresponding energy of the EML matrix material [81].

For the OLEDs discussed in this work, *N,N'*-di(naphthalen-1-yl)-*N,N'*-diphenyl-benzidine (NPB) and 2,2',2" (1,3,5-benzenetriyl) tris-(1-phenyl-1H-benzimidazole) (TPBi) are used as EBL and HBL, respectively. Their corresponding chemical structures are shown in Figure 3.11. The triplet energy of NPB has been determined to be 2.29 eV [81], which indicates that only excitons generating light in the low energy region (photon wavelength below 540 nm) can be in its proximity without severe losses. TPBi, as it will be shown the Chapter 7, has a triplet energy of 2.6 eV that roughly corresponds to a critical wavelength of 480 nm. At this wavelength, the triplet levels of phosphorescent emitter and blocker material have the same energy.

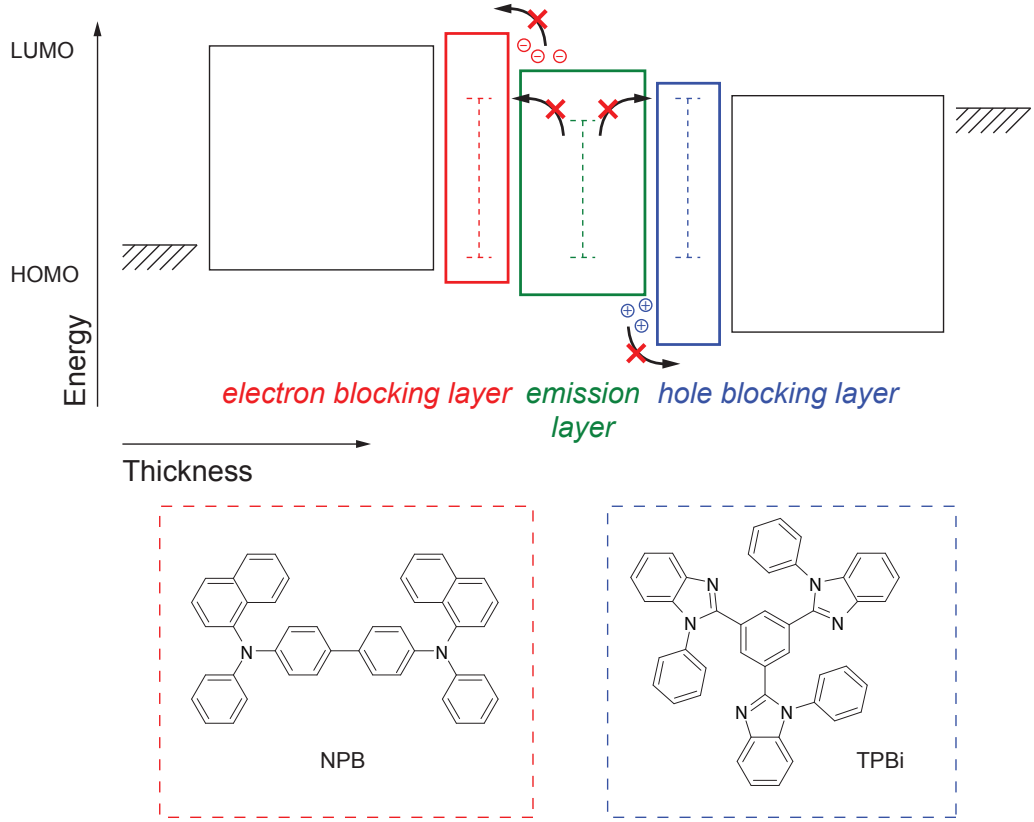

Figure 3.11: The energy diagram of a typical multilayer OLED, highlighting the charge carrier blocking layers. In p-i-n OLEDs, these layers are introduced to efficiently confine the injected charges to the EML, to suppress quenching of excitons at the doped transport layers, and, in case of phosphorescent OLEDs, to avoid exciton leakage from the EML. The arrows indicate undesired processes. In this work, NPB and TPBi are used as electron and hole blocking layers, respectively.

Emission Layer

As discussed in Section 3.4, highly efficient phosphorescence from organic molecules can only be obtained if the phosphor is diluted in a host material. As these emission systems are discussed in very detail in the following chapters, the materials used will only be briefly introduced at this stage. Chapters 5 and 6 deal with the exciton dynamics at high brightness of various EML systems comprising the green phosphors $Ir(ppy)_3$ and $Ir(ppy)_2(acac)$. In Chapter 7, a novel EML concept for white light emission is introduced, comprising FIrpic, $Ir(ppy)_3$ and $Ir(MDQ)_2(acac)$ (cf. Fig. 3.12).

All used phosphorescent emitter molecules are organometallic complexes with a centered iridium atom. Solely a change of the ligand structure allows a great variability in the photophysical properties of such compounds [6, 52, 137–140]. In Figure

3.12, the chemical structures of all phosphors and, additionally, their photoluminescence (PL) spectra, as obtained from a TCTA:phosphor mixed layer of 2 wt%, are shown.

The chemical structures of the host materials of the emission layer – TPBi, 4,4'-*N,N'*-dicarbazole-biphenyl (CBP), and 4,4',4"-tris (*N*-carbazolyl)-triphenylamine (TCTA) – are also depicted in Figure 3.12. TCTA has the highest triplet energy of 2.83 eV, while CBP and TPBi have almost identical T_1 energies of 2.6 eV.

Compilation of Important Energy Levels

As the discussion of Section 3.4 and the present section indicate, the electronic structure of molecules is of great importance for the development of highly efficient organic LEDs. Appropriate transport levels, i.e. HOMO and LUMO levels, are required to ultimately realize efficient carrier recombination in the centered EML of an OLED. Especially important for phosphorescent emitters are the triplet levels of matrix and surrounding materials to achieve good exciton confinement on emitter sites. Therefore, Figure 3.13 provides an overview of these energy levels for all used materials except for the p-dopant F_4-TCNQ. The values of the latter are only important to realize a p-doped HTL, which has been shown in detail before [133].

The HOMO and LUMO levels were determined from UPS and the optical gap, respectively [20, 42, 141, 142]. In Figure 3.13, they are arranged similar to their position in an OLED stack. However, the values of the emitters are exclusively plotted on the right, because their contribution to the electrical function of a device strongly depends on their concentration and relative position to the corresponding matrix materials.

The triplet levels of the materials are depicted on the bottom of Figure 3.13. The T_1-level of MeO-TPD is not known in literature. However, it is not of great importance, because the p-doped HTL will always be separated from the EML by a 10 nm thick electron blocking layer that also prevents possible exciton quenching by the MeO-TPD triplet level. The values of NPB [81] and Bphen [143], which were measured at 5 K and 77 K, respectively, are taken from literature as indicated. The triplet levels of TCTA, CBP and TPBi are determined in this work using a gated phosphorescence set-up (cf. Ch. 4). The triplet levels of the emitter materials are calculated from their RT emission peaks, as obtained from TCTA:emitter samples with roughly 2 wt% emitter concentration (cf. Fig. 3.12).

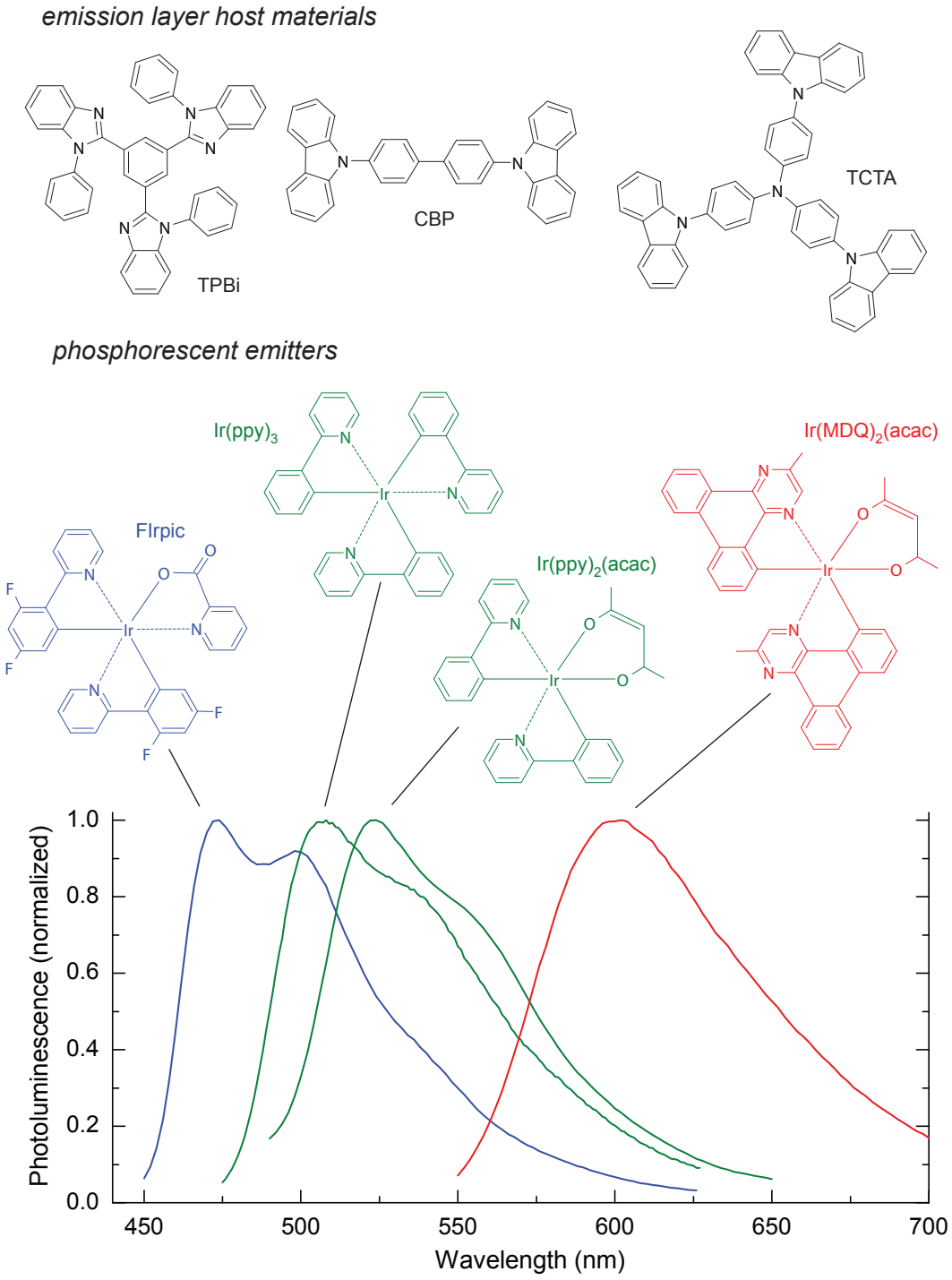

Figure 3.12: Top: Chemical structures of all host and phosphorescent emitter materials used in this work. Bottom: Photoluminescence spectra of all phosphors, obtained from a mixed film, where the emitters are diluted into TCTA with approximately 2 wt% (sample thickness: 20 nm).

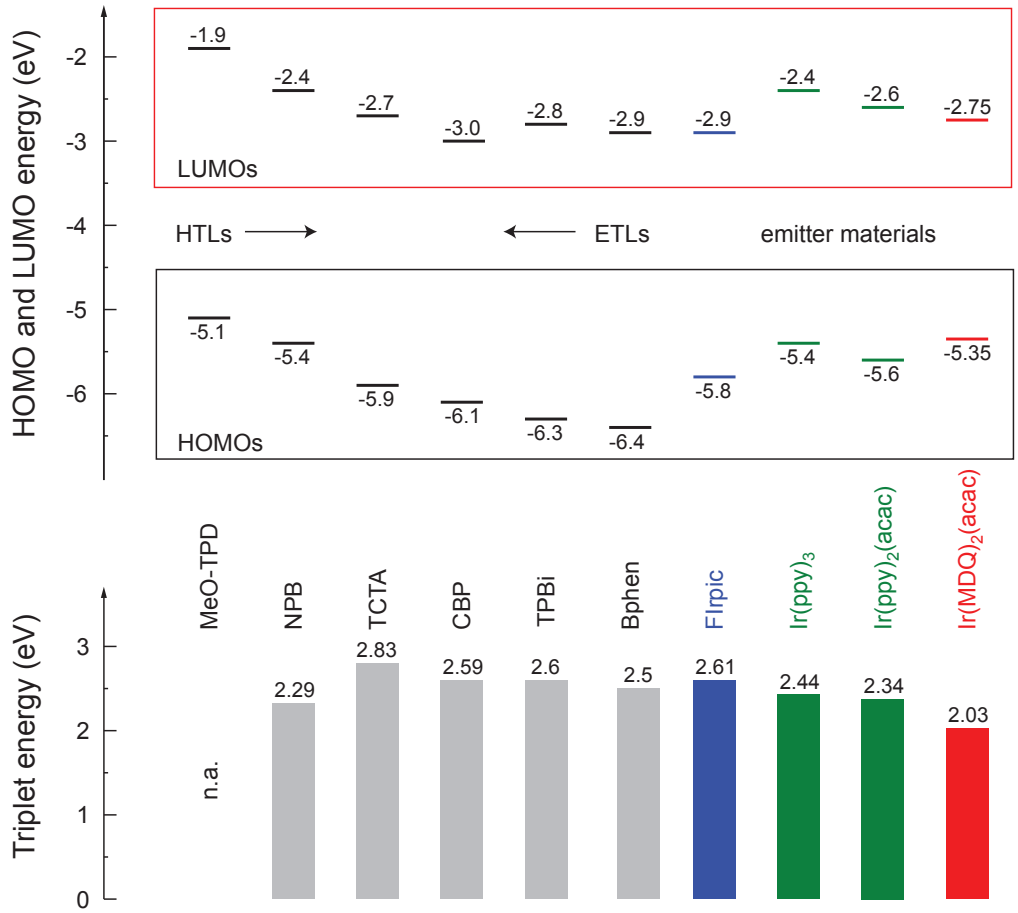

Figure 3.13: Top: HOMO and LUMO values of the materials used in this work. They are ordered in respect to their functionality within an OLED (HTLs to the left, ETLs to the right). Bottom: Triplet energy levels of used materials. For the emitters, the triplet level is the energy of their emission peak. The values for the matrix materials are determined at low temperature.

Chapter 4

Experimental

In this chapter, the methods of this work will be discussed. The methods of device evaluation will be described to understand the interpretation of the experimental data. This chapter closes with a detailed discussion of a time-resolved luminescence set-up that is capable to detect either photo- or electroluminescence signals.

4.1 Sample Preparation

All samples discussed in this work are prepared by thermal evaporation of the corresponding materials under high vacuum conditions. Depending on the specific experiment, different types of glass plates – made of regular, high refractive index, or quartz glass – with an approximate thickness of 1 mm are used as substrates. All glass substrates are cleaned in an ultrasonic bath with acetone, ethanol, and iso-propanol prior to material deposition. Throughout this work, indium tin oxide (ITO) is used as a transparent anode material of the investigated OLEDs to couple out the generated light through the glass substrate. This ITO is commercially pre-coated and structured on top of the corresponding glass substrates. If not otherwise specified, standard glass and 90 nm thick ITO are used for the OLEDs. These anodes have a sheet resistance of $(25 \pm 5)\,\Omega$/square.

For the sample preparation, two different vacuum systems are used. The first system is a ten chamber cluster tool (base pressure 10^{-9} mbar) that is directly attached to a glovebox under nitrogen atmosphere and a flowbox. Its layout allows highest flexibility in time and user demands. Substrate sizes are typically up to 1 inch square substrates. The second system is a semi-automatic single chamber tool (base pressure 10^{-8} mbar) with an attached nitrogen glovebox that has combinatorial capabilities. It is possible to have a variation in up to 36 small test devices on one glass wafer in a rectangular layout. Using movable shutters, it is possible to individually address each row and column. It handles glass wafers with a size of 15 by 15 cm^2 that allow various device layouts.

Layer Deposition

In both systems, the organic materials are evaporated by resistive heating of ceramic crucibles under high vacuum. The temperature of the crucible is measured in contact mode. The evaporation rate of the organic compounds is monitored by a quartz crystal microbalance (QCM) operated at approximately 6 MHz. Using a proportional–integral–derivative (PID) controller, the evaporation rate is regulated by the feedback of heating current and crucible temperature. The metals used as contacts of devices are also evaporated by thermal evaporation. While for the evaporation of aluminum, a ceramic crucible is used, some materials like silver are handled in a tungsten boat. All devices, which are typically finalized by a metal contact, are prepared without breaking the vacuum during the complete process.

Both organic materials and metals are evaporated through shadow masks, situated directly below the sample substrate. Different mask layouts are used to obtain the desired device set-up. In case of the single chamber system with the large glass wafers, the substrate mount in the chamber is continuously rotated to improve the film homogeneity. The cluster tool can have up to six organic sources in a chamber while the single chamber system holds up to 12 organic sources (plus up to three metal sources). Mixed layers can easily be fabricated by co-evaporation, where the control of the evaporation rates of more than one organic source is achieved by individual QCMs. The conductivity of the n-doped ETL is controlled with a test layer on top of the substrate covered with ITO stripes, where the lateral current is measured upon ETL deposition.

Sample Encapsulation

Due to their sensitivity towards moisture and air, the samples and devices comprising organic material are encapsulated in the above mentioned gloveboxes under nitrogen atmosphere. For this purpose, glass plates with a 250 µm cavity are used for the case of regular and quartz glass. This cavity assures that the samples are not scratched or contaminated with particle dust. Furthermore, this avoids thin film interference effects between the glass plates. These cavity glasses are attached and sealed to the sample substrate using an epoxy resin. All measurements throughout this work are either performed under nitrogen atmosphere or carried out with encapsulated samples.

4.2 Device Evaluation

Two different evaluation routines are employed to determine the device performance of organic LEDs. They mainly differ in the measurement speed and accuracy. The standard evaluation is suitable for the majority of all experiments. However, to precisely determine the absolute device efficiency, an integration sphere is used, correctly accounting for the angular emission pattern of a specific OLED. Both set-ups are discussed subsequently.

Typically, three device efficiencies are discussed in literature: the *current efficiency* η_C, the *power efficiency* η_P, and the *external quantum efficiency* η_{ext} [60, 144]. While the latter is a measure of the number of photons that are created per injected electrons, the other two efficiencies are photometric quantities that take the sensitivity of the human eye into account (cf. Fig. 2.2).

The current efficiency is calculated from the luminance $L_{0°}$, obtained in forward direction, and the current density j_{meas} passing through the device:

$$\eta_C = \frac{L_{0°}}{j_{meas}} \quad [\mathrm{cd/A}]. \tag{4.1}$$

Knowing the operating voltage at the measurement point $V(j_{meas})$, the power efficiency for the light emitted to the forward hemisphere can be calculated. It reads:

$$\eta_P = \eta_C \frac{f_D \pi}{V(j_{meas})} \quad [\mathrm{lm/W}], \tag{4.2}$$

with

$$f_D = \frac{1}{\pi I_0} \int_0^{\pi/2} \int_{-\pi}^{+\pi} I(\theta, \phi) \sin\theta \, \mathrm{d}\phi \, \mathrm{d}\theta. \tag{4.3}$$

Here, f_D accounts for the angular distribution of the emitted light $I(\theta, \phi)$ in the forward hemisphere, which is a function of the azimuth (ϕ) and zenith (θ) angle. Furthermore, I_0 represents the light intensity measured in forward direction. Finally, the radiometric external quantum efficiency is calculated using:

$$\eta_{ext} = \eta_C \frac{f_D \pi e}{K_r E_{ph}} \quad \left[\frac{\%}{100}\right], \tag{4.4}$$

where E_{ph} is the average photon energy of the emitted device spectrum. The transformation from the photometric to the radiometric quantities is achieved by the introduction of the luminous efficiacy K_r that is calculated by:

$$K_r = 683 \frac{\int_{380\,\mathrm{nm}}^{780\,\mathrm{nm}} \Phi_r(\lambda) V(\lambda) \, \mathrm{d}\lambda}{\int_0^\infty \Phi_r(\lambda) \, \mathrm{d}\lambda} \quad [\mathrm{lm/W}], \tag{4.5}$$

where Φ_r is the radiant flux and $V(\lambda)$ the weighting function, accounting for the sensitivity of the human eye (cf. Sec. 2.2).

Measuring in Forward Direction

The current-voltage characteristics of the devices is measured with a Keithley SM2400 source-measure unit. The emitted EL intensity is measured in forward direction with a fast photodiode that is calibrated with a CAS 140 CT spectrometer (Instrument Systems Optische Messtechnik).[1] For the evaluation of this data, a Lambertian emission pattern of the angular distribution $I(\theta, \phi)$ is assumed, i.e. $I(\theta, \phi) = I_0 \cos\theta$. With this assumption, f_D equals to 1.

This procedure is applied when comparing different devices to investigate their relative differences. Here, it is assured that the layer structure is similar (so that $I(\theta, \phi)$ is similar for all devices), that these devices have similar spectra, and that they are prepared under equal conditions (at best in one process run). The high speed of measurement of this evaluation is important for a precise measurement of the efficiency roll-off, i.e. η_ext versus j or L, to assure that device degradation during the measurement sweep is negligible.

Integrating Sphere Measurements

To precisely determine the efficiency of an organic LED, they are measured with an integrating sphere (Instrument Systems Optische Messtechnik) that is connected to the calibrated CAS 140 CT spectrometer. This system allows the determination of the power and external quantum efficiency directly without any assumptions because it accounts for all light emitted to the forward hemisphere. Again, using the SM2400 to drive the device, the efficiencies can be detected at a certain current density j passing through the device. From the measurement in forward direction with the above described set-up, this current density can be correlated to the corresponding device brightness L_{0° in forward direction. However, due to the large size of the sphere (20 inch), the device brightness must be rather high ($> 1,000\,\mathrm{cd/m^2}$) and still long integration times ($> 15\,\mathrm{s}$) need to be applied. This makes it inapplicable for standard device evaluation. Furthermore, problems arise for samples that degrade during measurement. Here, a complete device characteristics cannot be recorded without errors.

In Chapter 7, both measurements are combined. Here, the efficiencies determined in the integrating sphere are used to calibrate the current-voltage-luminance characteristics, itself being determined with the fast photodiode based set-up. All measurements carried out with this integrating sphere will be marked with an asterisk (e.g. EQE*).

[1] This spectrometer itself is commercially calibrated, so that it is used as the reference device for absolute, wavelength-dependent measurements.

4.3 Time-Resolved Luminescence

Before the technique to measure luminescence in time- and spectrum-resolved fashion is introduced, standard set-ups for the photophysical characterization of solid films will be stated.

Photoluminescence spectra of organic bulk and mixed solid films are measured with a luminescence spectrometer Fluoromax (HORIBA Jobin Yvon). Monochromatic light is used for the sample excitation, which is selected with a monochromator from a xenon arc lamp. The detector comprises a second monochromator and a photomultiplier tube. Colour filters in the detector pathway can be integated. Transmission, reflection, and absorbance of the sample films are measured with the spectral photometer UV-3101 (Shimadzu Deutschland). It is a two beam difference spectrometer with an additional extension unit MPC-3101 for reflection measurements. It covers the UV-VIS-IR spectral range ($190 - 3200\,\mathrm{nm}$).

Transient Photoluminescence

The general set-up to measure time-resolved photoluminescence of organic solid films is shown in Figure 4.1. Samples are excited with a pulsed nitrogen laser MNL 200 (Lasertechnik Berlin) that directly couples the light into a glass fibre. It operates at a wavelength of 337.1 nm with a typical pulse duration of 1.3 ns. The exciting light intensity can be varied with a set of neutral filters. The initial pulse energy is determined by a power meter 1835-C, featuring a suitable detector head 318J09B (both Newport). The emitted light of the sample is coupled into a glass fibre that guides the light to the active area of a fast photodiode (PD) PDA10A-EC (Thorlabs), itself directly connected to a fast multichannel oscilloscope infinium 54815A (Hewlett Packard) for data read-out (cf. bottom of Fig. 4.1).

In order to calculate exciton densities that are created on the guest molecules upon PL excitation, this set-up has to be calibrated. For an estimation of the initial guest triplet exciton density n_G, samples with a high guest concentration ($\geqslant 1\,\mathrm{mol\%}$) are analyzed. It is checked that the host emission of such samples is completely quenched by the guest molecules, so that the host-guest energy transfer is complete ($k_{\mathrm{H}\to\mathrm{G}} = 1$). It is assumed that the intersystem crossing rate k_ISC to the guest triplet (T_1) state is unity [145]. n_G is calculated for minimal pump exciton density n_p by assuming $k_{\mathrm{H}\to\mathrm{G}} = 1$, thus, $n_\mathrm{G} = k_{\mathrm{H}\to\mathrm{G}} k_\mathrm{ISC} n_\mathrm{p}$. This results in a calibration factor C between photodiode (PD) signal, i.e. phosphorescence, and n_G, i.e. $n_\mathrm{G} = C(U - U_0)_\mathrm{PD}$. Here, U is the measured PD voltage and U_0 the corresponding dark signal.

In additional continuous wave (cw) experiments, a HeCd gas laser IK5351R (Kimmon Electric) is used as excitation source. Here, its 325 nm line is chosen to match the absorption band of the organic compounds. Neutral filters are used to vary the excitation power, which is directly determined using the 1935-C power meter with an 883-UV detector head (Newport). In this case, the corresponding sample spectra is measured with a CCD-based compact fibre spectrometer USB2000 (OceanOptics).

Spectrum- and Time-Resolved Electroluminescence

To investigate the exciton dynamics in multicolour white organic LEDs, a set-up is realized to measure the time decay of the emission layer under EL operation. Instead of using a laser for excitation, the complete OLED is excited with a voltage pulse, generated by a pulse generator 8114A (Hewlett Packard). To determine applied voltage and the corresponding current density flowing through the device, two voltages U_1 and U_2 are recorded with the oscilloscope over the OLED and a $50\,\Omega$ resistance (in series), respectively. The corresponding driving circuit is depicted in Figure 4.1 (bottom) [146, 147].

In general, the light detection is similar to the transient PL set-up, discussed above. However, to additionally achieve a spectral resolution of the time decay, different colour filters are inserted between the OLED and the PD. This introduces the possibility to vary the transmission of the multicolour white spectra, emitted from such OLEDs. Subsequently, for a given transmission, both the time decay and the EL spectra are measured. The latter are recorded with the USB2000 spectrometer.

As an example of a possible application of this set-up, the effective charge carrier mobility of the EML material combination is determined in the multilayer OLED device, similar to a time-of-flight (TOF) experiment, which is described in Appendix B. Here, the measurements are carried out without the spectral variation.

Gated Phosphorescence at 77 K

For the determination of triplet levels of fluorescent host materials, a gated phosphorescence set-up is used that was realized by N. Seidler [148]. The samples are cooled to liquid nitrogen temperature (77 K) using a glass dewar vessel. The pulsed nitrogen laser MNL 200 provides the excitation source. Using a delay generator DG 535 (Stanford Rresearch Systems, Inc.), which is triggered by the laser pulse, a delayed detection in a spectrometer LS 50 B (Perkin Elmer) is realized. By an appropriate choice of the time delay between excitation and detection, the slow and weak phosphorescence signal can be separated from the intensive prompt fluorescence.

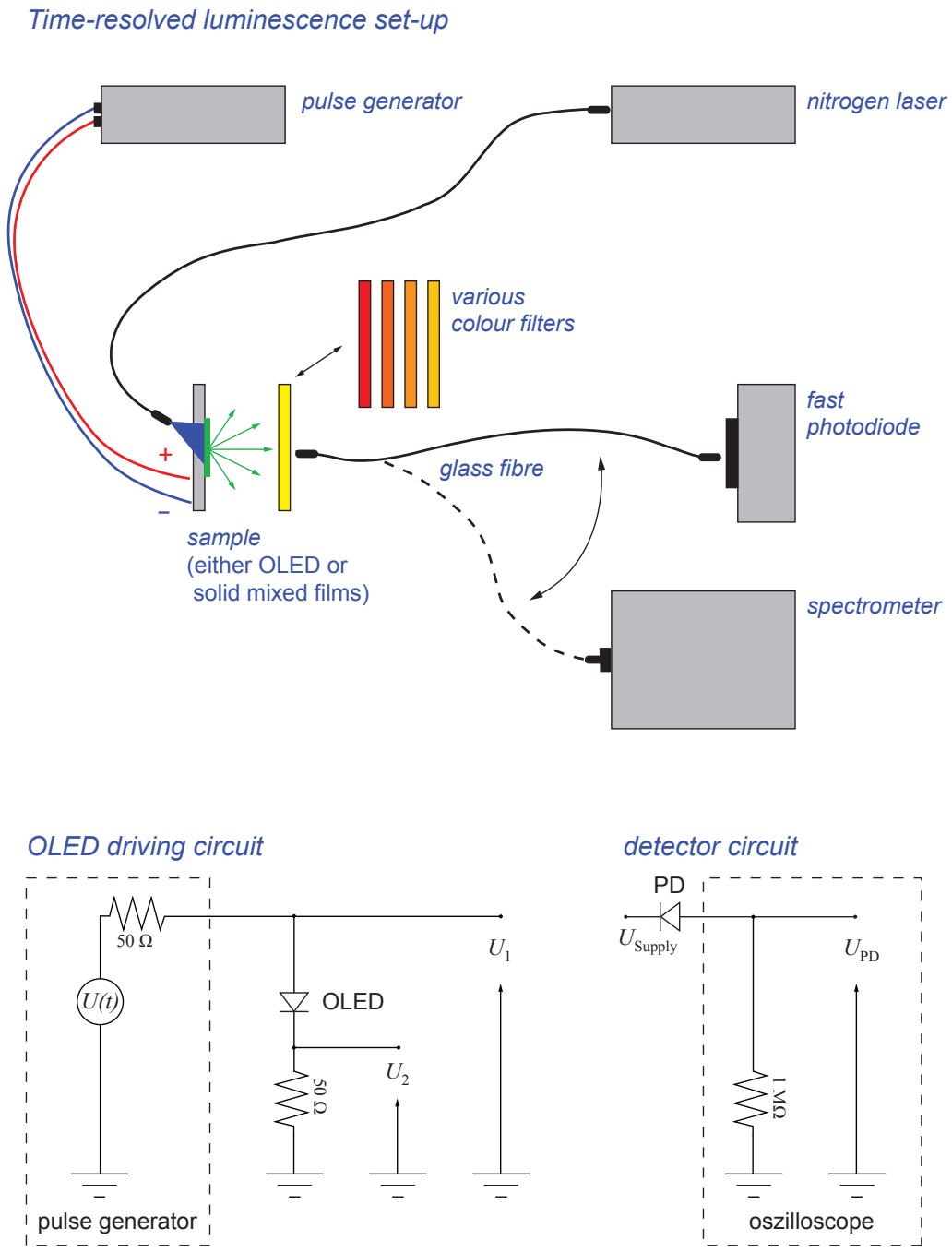

Figure 4.1: Time-resolved luminescence set-up. Top: The sample is either a complete OLED or a solid film of the system of interest. It can be excited by a short laser pulse (PL) or by a voltage pulse (EL). The emitted light is coupled into a glass fibre that connects to the available detectors (photodiode and spectrometer). Bottom: Electrical circuits for the OLED driving and the photodiode read-out.

Chapter 5

Host-Guest Triplet-Triplet Annihilation

In this chapter, triplet-triplet annihilation between host and guest excitons will be discussed. Focussing on highly efficient exothermic systems, they provide a contrast to systems with a matrix triplet level below the corresponding level of the phosphor. At high excitation levels, the phosphorescent emitter starts to saturate and unexpected host-guest TTA sets in, interestingly for a widely used system with a confining triplet-state configuration. This annihilation is directly observed in time-resolved photoluminescence experiments.

5.1 Systems with Host-Guest Interactions

According to Section 3.4, discussing high brightness phenomena, TTA was solely assumed to take place between guest molecules. This is a valid picture for state-of-the-art emitter systems, which are energetically designed to efficiently direct and confine all excitons to guest molecules. Nonetheless, this chapter will show that this is an assumption that needs to be reconsidered. Since the triplet lifetime of host materials is in most cases orders of magnitude longer compared to the corresponding guest time constant, the high host triplet density will accumulate easily. For instance, CBP has a triplet lifetime of 14 ms [75], which differs in approximately four orders of magnitude compared to the $Ir(ppy)_3$ excited state lifetime. Hence, whenever host triplets are populated, the intermolecular processes at high excitation levels might change noticeably.

Host-guest triplet-triplet annihilation has been discussed in literature before. Research was especially focussed on mixed organic systems, where the triplet energy of the host material is equal or even lower than the corresponding guest T_1 energy. One of these systems is N,N'-diphenyl-N,N'-bis(3-methylphenyl)-(1,1'-biphenyl)-4,4'-diamine (TPD) doped with the well-known phosphor $Ir(ppy)_3$ [21]. Its energy configuration is shown in Figure 5.1. TPD has a triplet level that lies approximately 150 meV below the $Ir(ppy)_3$ triplet state, therefore such mixed films are endothermic

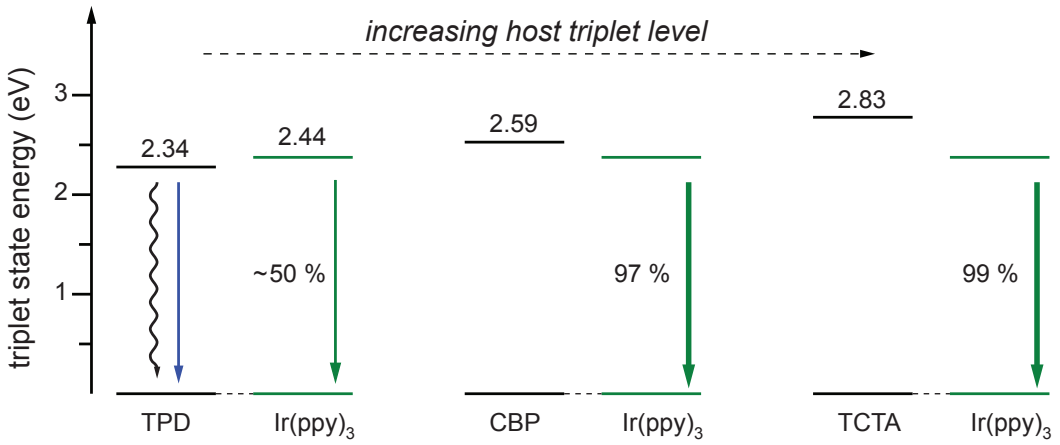

Figure 5.1: Triplet levels of different host-guest systems comprising the $Ir(ppy)_3$. From left to right, the T_1 level of the host increases. For TPD, the mixed system is endothermic as its triplet level is about 100 meV below the $Ir(ppy)_3$ state. Additionally given are the PL quantum yields, illustrated by the strength of the arrows, for highly diluted samples (2 and 1 wt% for CBP [78] and TCTA [149], respectively). The value for TPD is estimated from OLED data (6 wt%) [21]. The wavy line indicates non-radiative recombination on TPD.

systems (cf. Sec. 3.4). Having strong guest-host energy back-transfer rates k_{GH}, systems like this will be accompanied with a high host triplet exciton density. Therefore, the host exciton dynamics need to be included in the discussion of the overall TTA. As indicated in Figure 5.1, the PL quantum yield is much lower[1] than the potential limit of 100 % for phosphorescent emitters as a consequence of noticeable triplet energy losses on the host material.

Baldo *et al.* investigated the probably most prominent phosphorescent host-guest system so far, CBP:$Ir(ppy)_3$ by time-resolved experiments [19, 76]. In contrast to their observations, this system with the host material T_1 level higher than the corresponding emitter energy (cf. Fig. 5.1), is expected to decay following a monoexponential law with a certain excited state lifetime τ. However, both EL transient signals and OLED efficiency data could not be described with a single time constant. Rather, Baldo *et al.* used a weighted biexponential function with two time constants τ_1 and τ_2 to fit the data. Without evidence, they appointed this unexpected behaviour to host-guest interactions [19]. This experimental observation has not attracted further interest, even though high brightness applications more and more move into the main focus of OLED research, presumably because the PL quantum yield of CBP:$Ir(ppy)_3$ (2 wt%) $\Phi_P = 97\,\%$ is close to the theoretical limit [78, 150]. In the following, the photophysical properties of CBP:$Ir(ppy)_3$ especially at high brightness will be discussed, directly addressing this open issue [23].

[1] In literature, no PL quantum yield data is available for TPD:$Ir(ppy)_3$. Therefore, an internal quantum efficiency is estimated of $\sim 50\,\%$, using the EL data of Ref. [21].

5.2 Population of Host Triplet States

All data in this chapter are the result of PL experiments, with two gas lasers as excitation sources, i.e. a N_2 laser for time-resolved measurements and a HeCd laser for cw investigations. Before triplet interactions between host and guest species can be discussed, it is necessary to explain how triplet states of the matrix material can efficiently be populated, as light absorption only generates singlet states.

Prepared Samples

In this study, two samples are prepared on top of quartz glass substrates. These samples are encapsulated under a nitrogen atmosphere with another quartz glass.

Sample 5-1: CBP:$Ir(ppy)_3$ (20 nm, 0.9 mol%)

Sample 5-2: TCTA:$Ir(ppy)_3$ (20 nm, 1.1 mol%)

In Figure 5.2 a), absorbance and PL intensity of Sample 5-1 and 5-2 are plotted. The strong emission at approximately 510 nm is the phosphorescence of $Ir(ppy)_3$, the weak high energy feature is the host fluorescence of the corresponding material. Strong differences are obtained for the two host materials CBP and TCTA. Referring to Chapter 4, the chemical structures of both materials are very similar. Both comprise carbazole units as building blocks, CBP having two and TCTA having three such elements. This is mainly reflected by the similar absorbance spectra of both samples, with most of the contribution originating from the matrix because the dopant is highly diluted. While their singlet energies, determined by the fluorescence peak of these matrices, are both at 3.1 eV, they show different triplet energy levels. The phosphorescence spectra of CBP and TCTA are plotted in Figure 5.2 a) as dashed lines. In measures of energy, the triplet levels of CBP and TCTA are at 2.59 eV and 2.83 eV (cf. Fig. 5.1), respectively. This yields different singlet-triplet splittings [151] of $\Delta E_{\mathrm{ST,CBP}} = 0.51\,\mathrm{eV}$ and $\Delta E_{\mathrm{ST,TCTA}} = 0.27\,\mathrm{eV}$. Thus, the value of TCTA, compared to CBP, is only half as large.

Reaching Guest Site Saturation

In Figure 5.2 b), the phosphorescence output, represented by the $Ir(ppy)_3$ triplet density n_{Ir}, of both samples is plotted versus the pump exciton density n_{p}. The latter is a measure of the singlet exciton density created on the host material upon laser absorption. Details discussing the determination of n_{Ir} were given in Section 4.3.

In the lower pump regime, a linear behaviour between n_{p} and n_{Ir} is observed for both samples. With increasing laser intensity, this linear behaviour vanishes. It is followed by a regime where the $Ir(ppy)_3$ triplet density does not increase anymore upon increasing n_{p}. Neither material degradation nor bleaching[2] of the mixed films are observed in the measurements. The first is checked by recording the input-output curves in Figure 5.2 b) a second time, showing complete coincidence. Bleaching is

[2]Here, bleaching is referred to a decreasing absorption of the samples with increasing pump power.

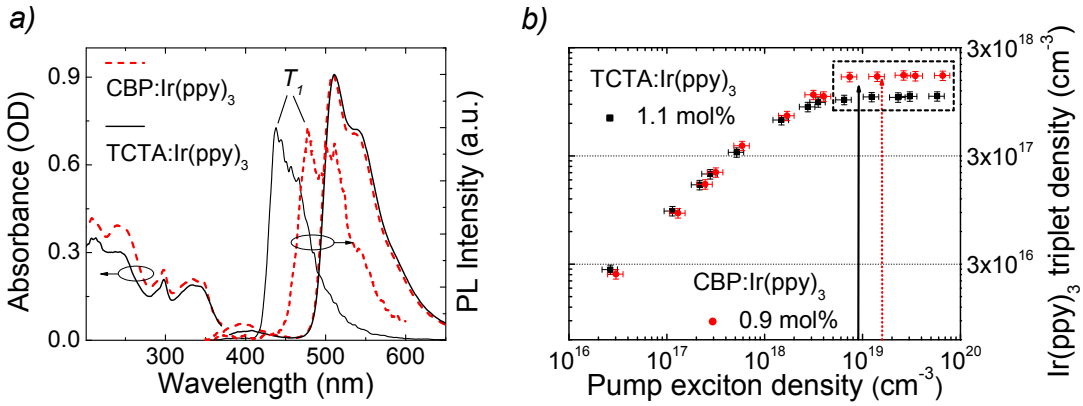

Figure 5.2: a) Absorbance and photoluminescence of Samples 5-1 and 5-2. T_1 marks the phosphorescence spectra of the host materials measured in a polystyrene matrix (2 wt%) at 77 K. b) The triplet density on guest sites is plotted as a function of the pump exciton density, i.e. the singlet exciton density created upon laser absorption. The arrows indicate the calculated guest densities in the mixed film. The dashed box marks the saturation regime of the phosphor.

excluded by measuring the transmission of the mixed film as a function of the laser intensity. By assuming cubic closed packing of the molecules in the mixed film and a homogeneous $Ir(ppy)_3$ distribution, the guest densities of Samples 5-1 and 5-2 are calculated, which are indicated by the dashed lines in Figure 5.2 b). These densities are similar to the onset of the plateau in the n_{Ir} versus n_p plot. Hence, this regime of constant n_{Ir} can be attributed to the saturation of the phosphor. In other words, in this regime it is not possible to transfer all the created singlet excitons of the host material to the emitting triplet states of the phosphor because they are all occupied.

Possible Pathways for the Excess Singlets

With increasing pump intensity in the saturation regime of the host-guest system, where all guest sites are excited, a density of excess singlets is built up on the matrix material. These singlets only have a few possible decay channels, which are schematically shown in Figure 5.3 for the case of Sample 5-1, i.e. comprising CBP as matrix. Obviously, the host fluorescence (pathway (a) in Fig. 5.3) is one decay channel. However, if the singlets could not be deactivated otherwise, a strong increase of fluorescence in the guest saturation regime would be expected.

Another channel for the residual singlets is the energy transfer to the excited guest molecules. Here, the guest would undergo a $T_1 \rightarrow T_n$ transition. This energy transfer can have very high oscillator strength because the transition in the triplet manifold of the guest is spin-allowed. Hence, both Förster- and Dexter-type energy transfer can contribute to this energy exchange.

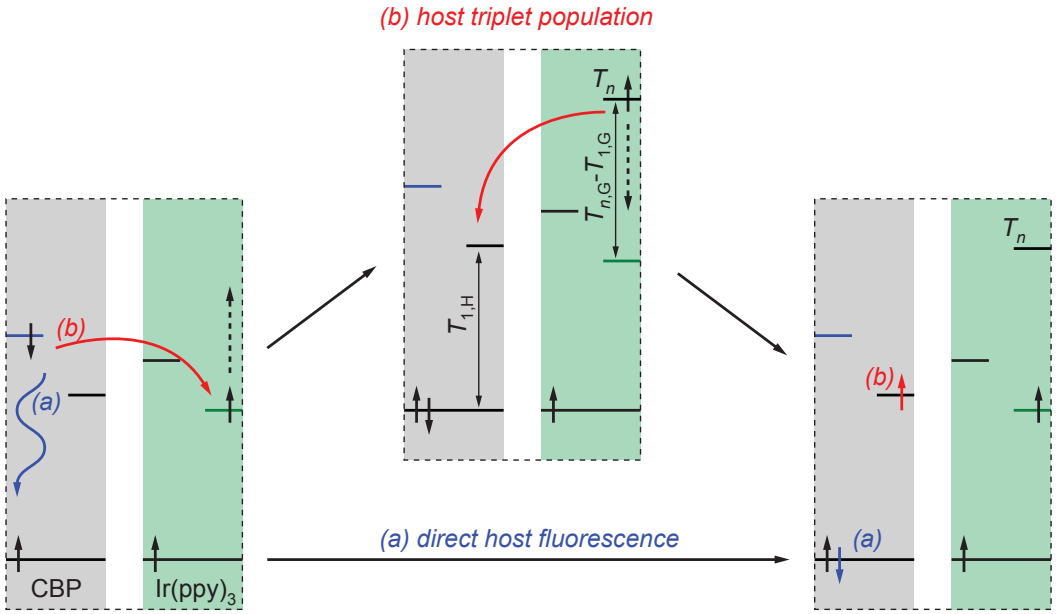

Figure 5.3: The possible pathways of created singlet host excitons upon laser absorption are illustrated for the case of guest site saturation. This is schematically shown for CBP:Ir(ppy)$_3$. As the guest sites are already in the excited state, the host singlet states can either directly relax [pathway (a)] or they can lift the guest triplet states to higher levels (T_n) [pathway (b)]. The latter states can either internally relax to their corresponding T_1 state or transfer this excess energy $T_{n,\mathrm{G}} - T_{1,\mathrm{G}}$ by Dexter transfer to the host triplet state $T_{1,\mathrm{H}}$.

After this step, the host molecule is relaxed while the guest now appears in a higher excited triplet state T_n. This transfer, which is shown as the first step of pathway (b) in Figure 5.3, can be expressed as:

$$ {}^1H^* + {}^3G^* \xrightarrow{-\Delta E_1} {}^1H + {}^3G^{**}, \tag{5.1} $$

where H and G indicate host and guest sites, and the double asterisk marks a higher excited state. A possible loss of energy during this conversion is indicated as $-\Delta E_1$, for example stemming from an internal vibrational relaxation of the final state: ${}^3G_{n,j} \rightarrow {}^3G_{n,0}$ (cf. Fig. 3.2). This ${}^3G^{**}$ state can either internally relax to the lowest triplet level ${}^3G^*$ obeying Kasha's rule (cf. Sec. 3.2) or transfer its energy back to the triplet state of the host molecule.

The energy back-transfer that ultimately results in a population of the host triplet states reads:

$$ {}^3G^{**} + {}^1H \xrightarrow{-\Delta E_2} {}^3G^* + {}^3H^*. \tag{5.2} $$

Again, $-\Delta E_2$ denotes a possible loss of energy. This transfer is illustrated in the second step of pathway (b) of Figure 5.3. Referring to Equation (3.51), this step conserves to total spin of the configuration obeying the Wigner-Witmer selection rules. Obviously, this is a Dexter-type transfer, so that it is only efficient on nearest

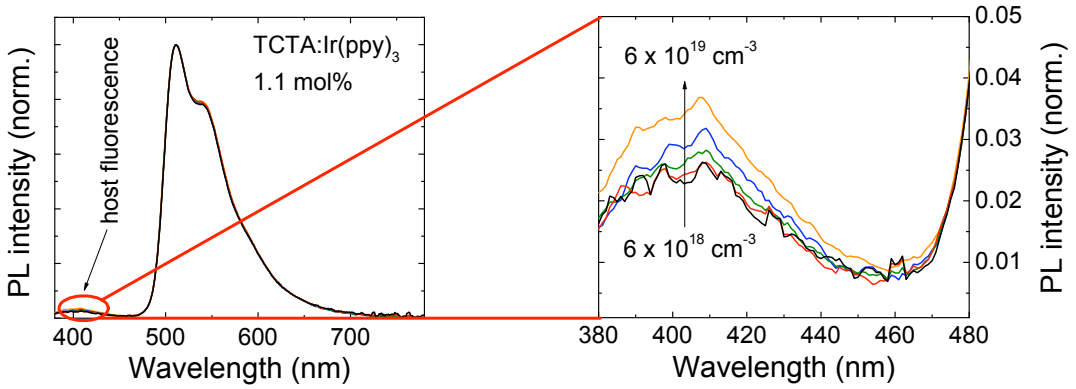

Figure 5.4: Normalized PL of the TCTA:Ir(ppy)$_3$ sample under a variation of the pump exciton density n_p. The sample is excited with a cw HeCd laser at 325 nm. Left: Complete spectra with indication of the host fluorescence. Right: Zoom in of the host emission. The arrow indicates the increase of n_p from $6 \times 10^{18}\,\mathrm{cm}^{-3}$ to $6 \times 10^{19}\,\mathrm{cm}^{-3}$.

neighbour distances. Apparently, this energy exchange is only possible when the following relation is fulfilled:

$$T_{n,\mathrm{G}} - T_{1,\mathrm{G}} \geqslant T_{1,\mathrm{H}}, \tag{5.3}$$

otherwise additional energy is required for its occurrence. However, this aspect is difficult to verify because most of all the energy of the intermediate, higher excited state T_n is experimentally not accessible.

In general, a third possible decay channel for CBP singlets is not included in the scheme of Figure 5.3: the direct intersystem crossing to the CBP triplet state. Giebink *et al.* have studied exciton dynamics of CBP in detail [75]. From their data it is possible to deduce that only $2-3\,\%$ of the created singlet excitons are transferred to the CBP T_1 state. Furthermore, referring to Figure 5.3, pathway (b) and this direct intersystem crossing have the same final result, i.e. the population of CBP triplet states.

Host Fluorescence

As discussed above, host fluorescence is one of three possible deactivation channels for the excess singlet excitons. To investigate this channel, both samples are excited with a cw laser with variable intensity in the saturation regime, i.e. from $n_\mathrm{p} = 6 \times 10^{18}\,\mathrm{cm}^{-3}$ to $n_\mathrm{p} = 6 \times 10^{19}\,\mathrm{cm}^{-3}$. The spectra are plotted exemplarily for Sample 5-2 comprising TCTA in Figure 5.4. On the left, the complete spectra with TCTA fluorescence and Ir(ppy)$_3$ phosphorescence features are shown. These spectra are normalized to the peak guest phosphorescence. The host emission is zoomed in on the right hand side of Figure 5.4. An increase of host fluorescence can be observed with increasing pump exciton density n_p. Nonetheless, by integrating this spectral region for lowest and highest n_p, it turns out that the fluorescence is only increased by $28\,\%$ for Sample

5-2. The same analysis for Sample 5-1, comprising CBP, results in a fluorescence increase of 23 %.

Hence, pathway (b) of Figure 5.3, i.e. the transfer to the excited guest triplet state, must contribute to the deactivation of the singlet states of the host material. However, at this stage it is hard to decide whether this energy is further transferred to the host triplet level $T_{1,\mathrm{H}}$ or the internal relaxation to $T_{1,\mathrm{G}}$ is the dominating channel. This issue strongly depends on the specific host material, as it will be discussed in the following section.

5.3 Direct Observation of Host-Guest TTA

The saturation regime, as indicated in Figure 5.2 b), allows to study the decay of a constant $\mathrm{Ir(ppy)_3}$ triplet exciton density n_{Ir} under a variation of the pump density n_{p}. Time-resolved experiments are carried out to investigate triplet-triplet annihilation of these samples. The corresponding PL transients are plotted in Figure 5.5 b) and c) for Sample 5-1 and 5-2, respectively. These decay curves are split in time for better visibility. From left to right, the pump exciton density n_{p} is increased. The left black transient of both samples corresponds to a pump level that still lies in the linear regime of the input-output plot (cf. Fig. 5.2 b)). The thin solid lines correspond to calculated fits according to Equations (3.70) and (5.4).

Triplet-triplet annihilation in PL transients is observed as the deviation from the monoexponential decay that is expected in the absence of bimolecular interactions. Comparing the transients of Sample 5-1 and 5-2 in the linear regime, very similar decay shapes are observed. Upon a further increase of n_{p} in the CBP:$\mathrm{Ir(ppy)_3}$ sample, the deviation from the monoexponential decay steadily increases, despite the fact that the initial guest intensity remains unchanged. The latter indicates the $\mathrm{Ir(ppy)_3}$ saturation regime, i.e. the number of excited states that contribute to the emission is constant. Additionally, a new feature of the PL transients of Sample 5-1 arises solely in the saturation regime. The long-living part of the transient does not describe the decay according to the guest triplet lifetime $\tau_{\mathrm{G}} = 2\,\mu\mathrm{s}$, but rather shows a longer time constant. This feature can be ascribed to energy back-transfer from CBP host triplet excitons that are transferred to $\mathrm{Ir(ppy)_3}$ sites at a weak rate $1/\tau_{\mathrm{BT}}$ [152]. This long-living feature will be discussed in detail at the end of this section.

The given picture strongly differs for Sample 5-2 comprising TCTA as host material. Here, the shape of the PL transients in the saturation regime (cf. Fig. 5.5 c)) do not change at all; neither in initial intensity nor in the curvature of the transient. This indicates that the strength of TTA between excited $\mathrm{Ir(ppy)_3}$ sites, which are monitored in the PL set-up, are not affected by an increase of n_{p} for Sample 5-2. The decay of the TCTA sample, excited with the highest intensity, is plotted as crossed symbols in Figure 5.5 b) to compare with the corresponding CBP:$\mathrm{Ir(ppy)_3}$ transient. Clearly, the latter shows stronger overall TTA.

Host-Guest TTA for CBP:Ir(ppy)$_3$

Presumably an additional TTA mechanism must be present since n_{Ir} is constant in the saturation regime and still an increasing curvature in the transients is observed for Sample 5-1 comprising CBP. However, this requires additional species to annihilate with. As discussed in the preceding section, the population of host triplets, building up a density $n_{\mathrm{h,T}}$, is expected in the saturation regime. Consequently, the mechanism that leads to the observed increase in TTA proceeds between host and guest excited states.

Here, guest excitons are able to diffuse to host sites, because of the close lying triplet levels of CBP and Ir(ppy)$_3$ of 2.59 eV and 2.44 eV, respectively. Excitons leaving the grid of guest molecules face the high triplet density $n_{\mathrm{h,T}}$, which is a consequence of the long triplet lifetime of the CBP host of $\tau_{\mathrm{T,CBP}} = 14\,\mathrm{ms}$ [75]. Thus, TTA on the host grid is efficient. Furthermore, direct TTA interactions might occur between host and guest sites.

This increasing TTA contribution will be analyzed with the 3D diffusion model. In order to take the slow component in the PL transients of CBP:Ir(ppy)$_3$ into account, Equation (3.70) is extended to:

$$n(t) = \frac{n_0}{\left(1 + n_0 \frac{k_{\mathrm{TT}}\tau}{2}\right) \mathrm{e}^{t/\tau} - n_0 \frac{k_{\mathrm{TT}}\tau}{2}} + n_{\mathrm{BT}} \cdot e^{(-t/\tau_{\mathrm{BT}})}, \tag{5.4}$$

with n_{BT} being the effective triplet density that contributes to the energy back-transfer, itself having a time constant of τ_{BT}. Without forestalling the discussion of the slow component at the end of this section, its lifetime is deduced from the long-living tail of the PL transient to $\tau_{\mathrm{BT}} = 18\,\mu\mathrm{s}$, which is used in the calculations. The effective triplet density n_{BT} will be used as a free parameter to fit the onset and strength of the delayed emission. For the PL transients 2 and 5, additionally calculated fits are shown in Figure 5.5 b), where the slow component in not taken into account by setting $n_{\mathrm{BT}} = 0$ in Equation (5.4).

The product of the rate constant for TTA based on 3D exciton motion k_{TT} and the initial triplet density n_0 is used as fit parameter. However, for the discussion of the monitored guest emission, which has a constant intensity in the saturation regime, n_0 is assumed to be constant. The calculated fits are plotted as solid lines in Figure 5.5 b). These calculations are only carried out to quantify the additional TTA contribution. In general, this host-guest TTA would require a significant extension of the rate equation set (cf. Eq. (3.63)) by introducing host (n_{H}) and guest (n_{G}) exciton densities and the corresponding rate constants [77, 153]. The results are displayed in Figure 5.5 a) as a function of the pump exciton density n_{p}. While the TTA rate constant for Sample 5-2 (TCTA) remains unchanged at a value of $(2.9 \pm 0.3) \times 10^{-12}\,\mathrm{cm^3 s^{-1}}$ throughout the saturation regime, an increase in k_{TT} of CBP:Ir(ppy)$_3$ by more than a factor of three with increasing n_{p} is observed.

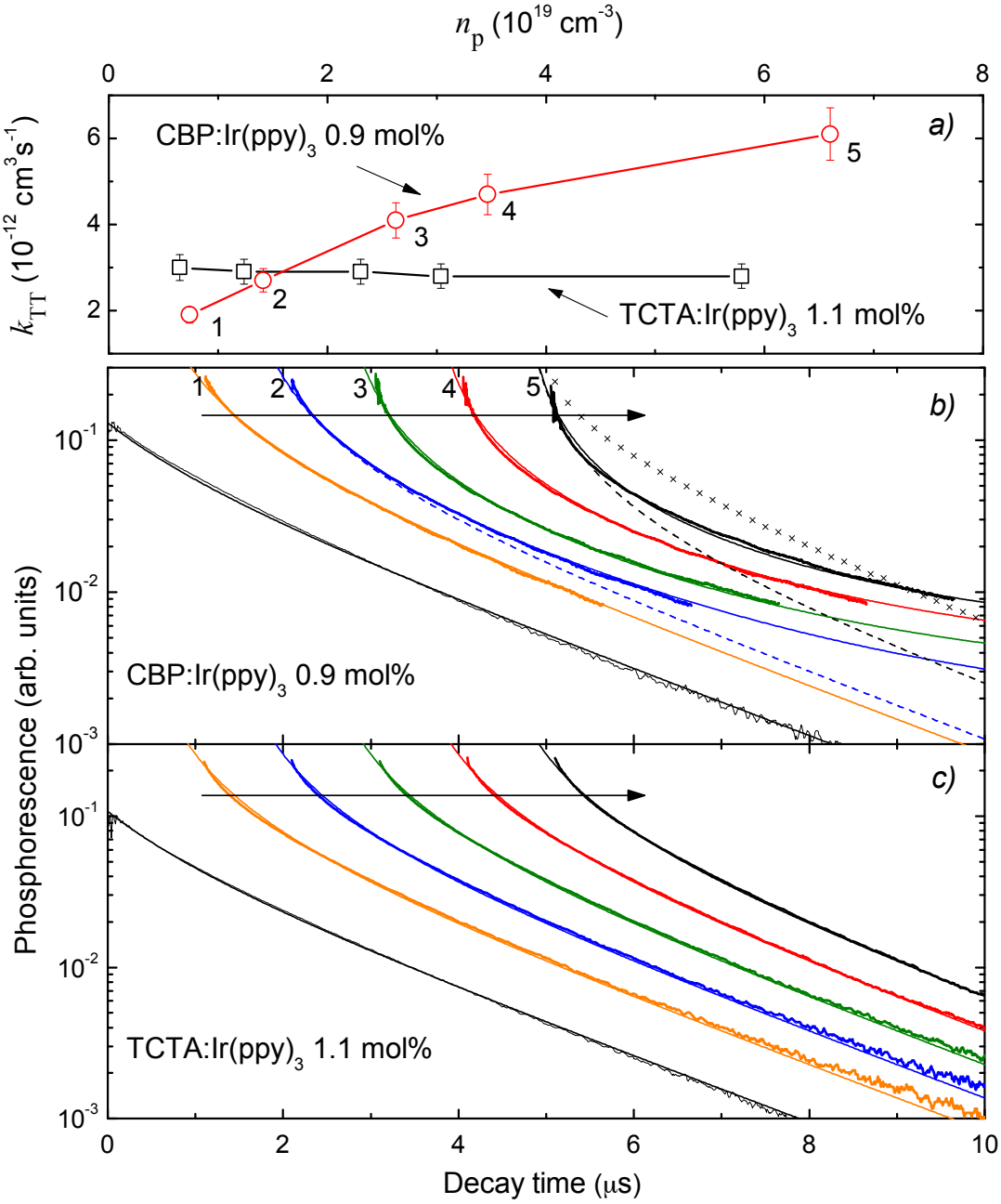

Figure 5.5: a) k_{TT} as derived from fits (solid lines) in b) and c) as a function of n_p according to Equations (5.4) and (3.70), respectively. For the CBP:Ir(ppy)$_3$, the transients are numbered and cross-linked to the k_{TT} values in a). – b) and c): PL transients of host:Ir(ppy)$_3$ films. From left to right, n_p is increased in the saturation regime, indicated by the arrows. Crossed symbols in b) depict the corresponding transient of the TCTA:Ir(ppy)$_3$ sample. CBP is accompanied with additional TTA contributions, as the deviation from monoexponential decay is more pronounced when compared with TCTA. The stars in b) represent the data of TCTA:Ir(ppy)$_3$ from c) for comparison. The dashed lines in b) correspond to calculations that do not take the slow component into account (transients 2 and 5).

The triplet density n_{BT}, as derived from the calculated fits of the CBP:Ir(ppy)$_3$ data, scales linearly with the pump density ($n_{\mathrm{BT}} \sim n_{\mathrm{p}}$), clearly indicating that the delayed component is a result of a host triplet density building up. This agrees with the fact that the slow component in the CBP:Ir(ppy)$_3$ transients sets in only in the saturation regime. Comparing the photoluminescence transients 1 and 2 in Figure 5.5 b), the calculated fit of transient 1 shows good agreement with $n_{\mathrm{BT}} = 0$, however a deviation (onset of the slow component) from the simple 3D diffusion model (dashed blue line) is observed for transient 2.

The host triplet density $n_{\mathrm{h,T}}$ in CBP can be estimated at the highest pump level to $4 \times 10^{19}\,\mathrm{cm}^{-3}$ as the amount of excitons which do not contribute to the increase of host fluorescence (77 %, cf. Sec. 5.2). Because of the long CBP triplet lifetime of $\tau_{\mathrm{T,CBP}} = 14\,\mathrm{ms}$, $n_{\mathrm{h,T}}$ is constant throughout the depopulation of the guest excitons. Reversing the above assumption n_0 being constant in the product $n_0 k_{\mathrm{TT}}$ in Equation (3.70), the estimation of $n_{\mathrm{h,T}}$ can be verified. By assuming that the increase of TTA is solely due to an increase of n_0 ($k_{\mathrm{TT}} = \mathrm{const.}$), qualitatively considering the build-up of $n_{\mathrm{h,T}}$, an initial triplet density of $n_0 = 2.3 \times 10^{19}\,\mathrm{cm}^{-3}$ is derived, roughly half of the value determined above for $n_{\mathrm{h,T}}$.

For two reasons, host-guest triplet-triplet annihilation is not observed for the TCTA:Ir(ppy)$_3$ system:

- The small singlet-triplet splitting of TCTA (0.27 eV) reduces the population rate of $n_{\mathrm{h,T}}$, because the intermediate state $^3G^{**}$ must have higher energy compared to the case of CBP, in order to populate the TCTA triplet state. Here, the possible energetic loss $-\Delta E_1$ might reduce the energy of $^3G^{**}$ too much, so that the condition of Equation 5.3 is not fulfilled. This, in turn, suggests that the internal relaxation to the $T_{1,\mathrm{G}}$ is the dominant process.

- If the T_1-level of TCTA is populated, the high T_1-level of TCTA (2.83 eV) efficiently suppresses guest triplet motion to host sites and, therefore, annihilation of guest excitons with corresponding host species.

Long-Living Feature in the CBP:Ir(ppy)$_3$ Transients

As discussed above, a long-living feature (cf. Fig. 5.5 b)) arises in the PL transients of the CBP:Ir(ppy)$_3$ sample (Sample 5-1) solely in the saturation regime. In Figure 5.6, the PL decay of Sample 5-1 is recorded in a larger time window to fully detect this feature. For the room temperature measurement (295 K), the dashed red and solid black data correspond to the first and last pump exciton density n_{p} in the saturation regime (cf. Fig. 5.2 b)). Again, with increasing n_{p}, an increasing curvature is observed at short times, indicating increased TTA due to host-guest interactions. On longer time scales, the long-living feature describes a monoexponential decay with a time constant of 18 µs, which is independent of the excitation intensity. However, the onset of this delayed component in the transients shifts to shorter times and increases in intensity. With its time constant about one order of magnitude longer than the natural lifetime of Ir(ppy)$_3$ (1-2 µs), this component can be ascribed to a energy back-transfer from long-living CBP triplet states to the emitting phosphor

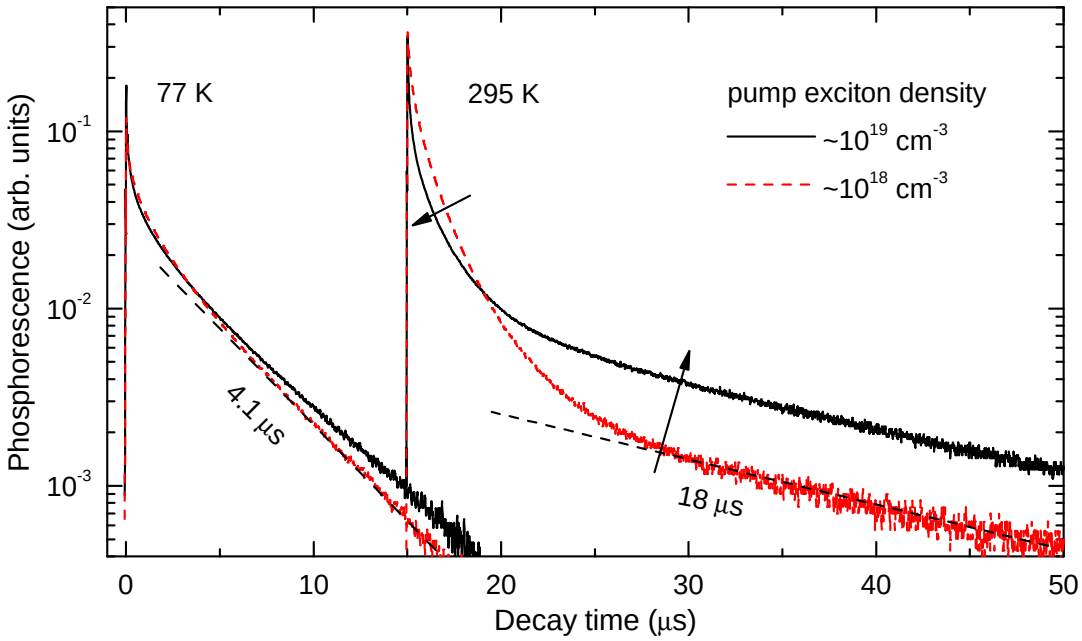

Figure 5.6: Photoluminescence transients of Sample 5-1 comprising CBP as host at different temperatures in the saturation regime of the phosphor (split in time by 15 µs for better visibility). For the transients at lower excitation intensities, the dashed lines indicate the monoexponential decay of the long-living tail.

[78, 81, 152]. With CBP triplets being the origin of this delayed decay, the observed intensity increase with increasing pump exciton density n_p is very reasonable.

In addition to the room temperature measurements, PL transients are recorded at liquid nitrogen temperature (77 K) to gain a better understanding of the population scheme in the CBP:Ir(ppy)$_3$ system. The corresponding data are plotted in Figure 5.6. For this experiment, identical sample (Sample 5-1) and excitation intensity are used. However, as the glass dewar vessel holding the sample changes the set-up geometry, the absolute intensities are not comparable. Furthermore, the sample can not be completely fixed in space, rather the bubbles of the liquid nitrogen randomly shake it, so that slight variations in the intensity cannot be avoided. The two transients, differing in n_p in one order of magnitude, almost show identical shape. The initial curvature originates from guest-guest TTA, similar to the results in the linear pump regime or to the TCTA:Ir(ppy)$_3$ at all n_p. This curvature develops into a monoexponential decay with a time constant of 4.1 µs. The time constant is slightly longer for the highly excited measurement (4.5 µs). Presumably, this is an extrinsic temperature effect, because the measurement sequence proceeds from low to high pump intensities. Possibly, the sample has not completely reached the thermal equilibrium of 77 K at the time of the measurement and, therefore, the longer time constant is detected as a result of a 'cooler' sample. However, this time constant agrees with earlier reports of temperature dependent time-resolved measurements of CBP:Ir(ppy)$_3$ solid mixed films, where (3 ± 1) µs were obtained at 77 K [154]. In conclusion, no pronounced host-guest interactions are observed at liquid nitrogen temperature.

This suggests that the triplet population in CBP:Ir(ppy)$_3$ (cf. Sec. 5.2), the origin for host-guest TTA in the first place, is thermally activated. According to the above discussion, TTA of guest triplets with host species will require the guest excited states to jump onto the grid of host molecules.[3] This requires an additional energy of roughly 150 meV, exhibiting the difference of CBP and Ir(ppy)$_3$ T_1 states. Here, the Boltzmann factors [$W(E,T) = \exp(-E/k_\mathrm{B}T)$] at 295 K and 77 K for this energy are 2.7×10^{-2} and 1.3×10^{-10}, respectively. Especially at room temperature, the Boltzmann factor seems to be small. However, this calculation does not consider the energetic broadening of the CBP and Ir(ppy)$_3$ T_1 levels, which might strongly affect the absolute values. The ratio of $W(E, 295\,\mathrm{K})/W(E, 77\,\mathrm{K})$ though is roughly 2×10^7, which indicates that it is very unlikely for guest states to transfer to host sites at low temperature.

Referring to Figure 5.6, no delayed component is observed in the PL transients of Sample 5-1 at 77 K. Apparently, no detectable energy back-transfer from CBP host triplets to the emitting Ir(ppy)$_3$ molecules occurs. This, however, suggests that at 77 K either the motion of host triplets is strongly suppressed so that they relax non-radiatively rather than reaching guest sites, or that the host triplet population is not efficient in first place. The latter can only be explained if the transfer from the T_n guest state to the CBP triplet state (cf. Eq. (5.2)) is also thermally activated, changing the relation of Equation (5.3) to:

$$T_{n,\mathrm{G}} - T_{1,\mathrm{G}} \leqslant T_{1,\mathrm{H}}. \tag{5.5}$$

[3] An alternative mechanism for host-guest TTA describes the direct interaction between host and guest molecules.

Chapter 6

Improving the High Brightness Performance of Organic LEDs

In contrast to the preceding chapter, focussing on host-guest TTA, this chapter discusses universally observed guest-guest TTA, for which it is only an open issue at which OLED brightness and how strong it sets in. Here, a closer look is taken on the archetype phosphorescent emitter Ir(ppy)$_3$. It will be shown that this emitter has strong tendencies to aggregate in mixed solid films, which is detrimental for high brightness OLED performance, because it opens an efficient TTA channel. Subsequently, two approaches are discussed that improve the device performance by reducing TTA. The first concept introduces sub-structured emission layers to suppress exciton motion in the bulk. In contrast, the other concept, which reduces the emitter aggregation, solely addresses the emitter material properties. This chapter closes with a short conclusive remark on the universality of morphologically induced TTA.

6.1 Triplet-Triplet Annihilation: Open Question

As mentioned in Section 3.4, triplet-triplet annihilation dominates the efficiency reduction of phosphorescent OLEDs at high brightness, an effect that is generally referred to as efficiency roll-off (cf. Ch. 2). Hence, one of the greatest challenges in the development of highly efficient phosphorescent organic LEDs will be to push the roll-off to highest possible brightness values so that the applications desired do not suffer from lower device efficiencies.

In order to quantify the efficiency roll-off of OLEDs, which is necessary to compare different devices, Baldo *et al.* introduced the critical current density j_c (cf. Sec. 3.6). It defines the current density at which the EQE of the OLED drops to half of its initial value. The latter is obtained at very low brightness or current density, respectively, where no bimolecular quenching processes are expected [19]. Here, by switching from brightness to current density, it is possible to compare differently emitting systems and devices, because the spectral response of the human eye is not taken into account.

PtOEP Defines the Benchmark for all Phosphorescent Systems

The first phosphorescent OLEDs that paved the way to reach internal efficiencies of 100 % used 2,3,7,8,12,13,17,18-octaethylporpine platinum (PtOEP) as emitter [7] - one of the best studied phosphorescent emitter molecule so far. In a detailed study of the transient properties of PtOEP doped in a CBP matrix, Staroske *et al.* showed that TTA in this system is best described solely by the single-step long range model [83]. As discussed in Section 3.4, this mechanism limits every phosphorescent system because it only depends on the spectral properties of the emitter itself, i.e. its overlap J_{phos} between $T_1 \rightarrow S_0$ emission and $T_1 \rightarrow T_n$ absorption. Here, the emitter molecules are spatially well separated in a matrix material with strong confining properties (high T_1 level), assuring that the exciton motion, leading to additional TTA channels, is sufficiently suppressed (cf. Fig 3.6 a)). Using their model, they proved that an estimation of $j_{\mathrm{c}} = 5\,\mathrm{mA/cm^2}$, solely based on photoluminescence data, agreed with experimental OLED data for CBP:PtOEP. In summary: (i) PtOEP is an emitter, showing single-step long range TTA as the only mechanism and (ii) single-step long range TTA is the intrinsic limit and further improvement can only be achieved if the spectral overlap J_{phos} is reduced by molecular engineering.

However, in practice, PtOEP is outdated because of its long excited state lifetime of 95 µs [83], which also increases TTA to an undesirable level. State-of-the-art phosphorescent emitter molecules, almost completely spanning the visible spectrum, have lifetimes that are roughly two orders of magnitude shorter compared to PtOEP [6].

Model Predicts Better $Ir(ppy)_3$ Performance

Using the single-step long range model, Staroske *et al.* estimated the critical current density for $Ir(ppy)_3$ [83], which is the archetype phosphorescent emitter of present OLED research with a triplet lifetime in the range of 1-2 µs [19, 20, 81, 154]. The calculation yields $j_{\mathrm{c}} = 6\,\mathrm{A/cm^2}$, which is about three orders of magnitude larger than the PtOEP value. However, experimental data are reported between 0.1 to $0.6\,\mathrm{A/cm^2}$ [19, 20], indicating that there is at least one order of magnitude room for improvement. Staroske *et al.* expected emitter molecule aggregation during the film preparation to be the reason for the increasing strength of TTA in $Ir(ppy)_3$-based organic LEDs.

This issue has also been addressed by other researchers. Namdas *et al.* investigated solution-processed $Ir(ppy)_3$-cored dendrimers in PL experiments under a variation of the dendron size from 2 to 10 nm [155, 156]. With this approach, they could very precisely control the core-to-core distance. Based on time-resolved data, they obtained critical current densities j_{c} up to $18\,\mathrm{A/cm^2}$. Namdas *et al.* actually determined a value of $j_{\mathrm{c}} = 44\,\mathrm{A/cm^2}$, however assuming an exciton recombination zone of 25 nm that is very unlikely to be found in a small molecule-based OLED. Staroske *et al.* therefore rescaled j_{c} to a 10 nm thick recombination zone.

If the calculated critical current densities of $6\,\mathrm{A/cm^2}$ or higher can be reached by future emitter molecules, most of the OLED applications could be operated at higher brightness levels without suffering from the efficiency roll-off. However, most

of these arguments only consider TTA as the origin of efficiency reduction at high brightness: at higher currents and consequently to higher external fields, the impact of triplet-polaron quenching and field-induced exciton dissociation [20] will gain in strength, so that they have to be re-addressed.

The discrepancy in j_c for $Ir(ppy)_3$ between model prediction and experimental results is the motivation for the work presented in this chapter. The question 'Why do $Ir(ppy)_3$-based OLEDs perform so poorly at high brightness?' will be addressed and solutions for a reduced efficiency roll-off will be provided.

6.2 Emitter Dopant Aggregation

The discussion of the previous section suggests that $Ir(ppy)_3$ has a strong tendency to aggregate in the mixed host:guest layer. This has a negative effect on TTA in such systems, as diffusion based annihilation becomes possible. Triplet-triplet annihilation of $Ir(ppy)_3$-based emission layers is investigated in this section with a focus on the microscopic composition of these films.

Prepared Samples

To thoroughly investigate TTA, single mixed layers of TCTA doped with $Ir(ppy)_3$ at different concentrations are prepared on quartz substrates.

Sample 6.2-1: TCTA:$Ir(ppy)_3$ (20 nm, 0.1 mol%)

Sample 6.2-2: TCTA:$Ir(ppy)_3$ (20 nm, 1.1 mol%)[1]

Sample 6.2-3: TCTA:$Ir(ppy)_3$ (20 nm, 9.3 mol%)

Here, TCTA is chosen as matrix material to assure optimum triplet exciton confinement to guest sites due to its high triplet state of $T_1 = 2.83\,\text{eV}$ (cf. Ch. 5). The very low concentration of Sample 6.2-1 assures that, even at high tendency of aggregate formation, most of the highly diluted emitter molecules are spatially separated. Sample 6.2-3, with a concentration of 9.3 mol%, on the other hand represents the reference sample, because typical phosphorescent OLEDs have emitter concentrations in that range.

Part of the investigation about emitter aggregation are transmission electron microscopy (TEM) experiments to determine the Ir-atom distribution within the mixed film. Therefore, an additional sample is prepared.

Sample 6.2-4: 2-micron hole carbon film (TEM substrate) / TCTA:$Ir(ppy)_3$ (50 nm, ∼10 mol%)

[1] This sample has already been introduced in Chapter 5 as Sample 5-2. However, to avoid confusion, it is re-labelled for the use in this new context.

It is sealed in nitrogen atmosphere and only briefly exposed to air during transfer to the microscope. Before measurement, it is degassed for 24 h in vacuum.

Finally, one heterolayer sample is prepared that is referred to as sub-structured emission layer. It is compared to two reference samples, which are prepared at the same day. Here, very thin layers of TCTA:$Ir(ppy)_3$ mixed films with a high nominal concentration of 11.4 mol% are intermitted by intrinsic 2 nm thin layers of TCTA. In total, this heterosystem comprises six interlayers, adding up to a layer thickness of 19 nm.

Sample 6.2-5: TCTA:$Ir(ppy)_3$ (20 nm, 1.1 mol%)[2]

Sample 6.2-6: TCTA:$Ir(ppy)_3$ (20 nm, 9.6 mol%)

Sample 6.2-7: [TCTA:$Ir(ppy)_3$ (1 nm, 11.4 mol%) / TCTA (2 nm)]$_6$ / TCTA: $Ir(ppy)_3$ (1 nm, 11.4 mol%) (19 nm in total)

Determination of an Upper Limit for the Förster Radius R_F

In Section 3.4, two different models to describe TTA were discussed in detail. Both completely differ in the underlying physical mechanism. However, from the experimental point of view, it is not possible to distinguish between their contribution to the overall TTA.

Commonly, triplet-triplet annihilation is investigated in time-resolved luminescence experiments. At low triplet densities, where no bimolecular quenching processes occur, the transient signal follows a monoexponential decay law with the phosphorescence lifetime of the emitter τ. At higher triplet densities, TTA sets in and the transient signal plotted in a semi-logarithmic scale deviates from the monoexponential law. This curvature transforms into the monoexponential decay at long times, where the exciton density is low again. By analyzing the two models of Equations (3.67) and (3.70), it is apparent that both can describe such a curvature in the transient, only depending on the characteristic quantities. These models do not fully coincide, however the determination of the mechanism for the origin of the observed TTA is not possible by simply going for the 'better' fit. The parameters to be determined are R_F and k_{TT} for the single-step long range and the diffusion-based model, respectively.

The three films with varying $Ir(ppy)_3$ concentration (Sample 6.2-1, -2, and -3) are investigated in a time-resolved manner as a function of the pump exciton density n_p. They comprise TCTA as a matrix material. The corresponding input-output characteristics are plotted in Figure 6.1 a). First, at low pump levels, the initial $Ir(ppy)_3$ triplet density n_{Ir} increases linearly with n_p to finally reach a level with constant n_{Ir} upon further increasing n_p. For Sample 6.2-3, the saturation is not fully reached with the applied pump intensity. The arrows in Figure 6.1 a) indicate the calculated guest densities for Samples 6.2-1 and -2, which coincide with the onset of the saturation regime.

[2]This sample coincides with Sample 6.2-2, however it is prepared at a completely different time. Later results will show, that some properties slightly change under a day-to-day variation.

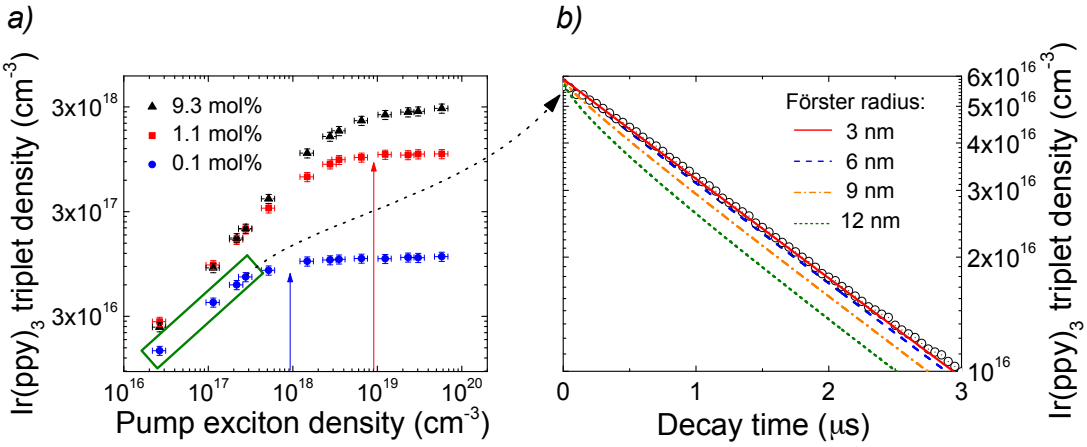

Figure 6.1: a) The $Ir(ppy)_3$ triplet exciton density n_{Ir} is plotted as a function of the pump exciton density n_p, which is created on the TCTA host, for Samples 6.2-1, -2, and -3. Solid arrows indicate the calculated guest density of the samples at lower concentration. For each data point, a PL transient is recorded. The green box indicates the observation of complete monoexponential decay. b) PL transient of Sample 6.2-1 (0.1 mol %) from the green box in a) with maximum pump density n_p. Solid lines: Calculated fits according to the single-step long range model (cf. Eq. (3.67)) with a variation in R_F.

As a first step, the data analysis determines an upper limit for the Förster radius R_F. In order to suppress possible emitter molecule aggregates, a highly diluted sample with a concentration of 0.1 mol% is chosen. The green box in Figure 6.1 a) indicates the PL transients that follow a completely monoexponential law at any time. The PL transient is plotted in Figure 6.1 b) as circles. It is fitted with the single-step long range model according to Equation (3.67) under a variation of R_F. Here, the highest value for the Förster radius that starts to deviate from the monoexponential decay of the experimental data is derived as the upper limit for R_F.

As discussed earlier, Staroske *et al.* determined a Förster radius of $R_F = 2.9\,nm$ from basic photophysical properties of $Ir(ppy)_3$ [83]. Therefore, under variation of R_F starting at 3 nm, calculated fits according to the single-step long range model (cf. Eq. (3.67)) are plotted in Figure 6.1 b). An increasing deviation from the experimental data is observed when the Förster radius is increased, while the fit with $R_F = 3\,nm$ resembles the PL transient. With a Förster radius of 6 nm, the differences become distinct, which is therefore derived as an upper limit for the Förster radius for TTA in the TCTA:$Ir(ppy)_3$ system [24]. For comparison, Kawamura *et al.* could determine the Förster radius of various Ir-based phosphorescent emitters for the triplet energy transfer to a ground state acceptor, which are all below 2 nm [79]. For $Ir(ppy)_3$ they determined a value of 1.4 nm in a CBP matrix.

Knowing that the Förster radius for single-step TTA cannot exceed 6 nm for TCTA:$Ir(ppy)_3$, the samples with the higher $Ir(ppy)_3$ concentration (Sample 6.2-2 and -3) are analyzed with the Förster model. Representative PL transients of each sample (cf. Fig. 6.1 a)) at high n_p are plotted in Figure 6.2. In addition to exper-

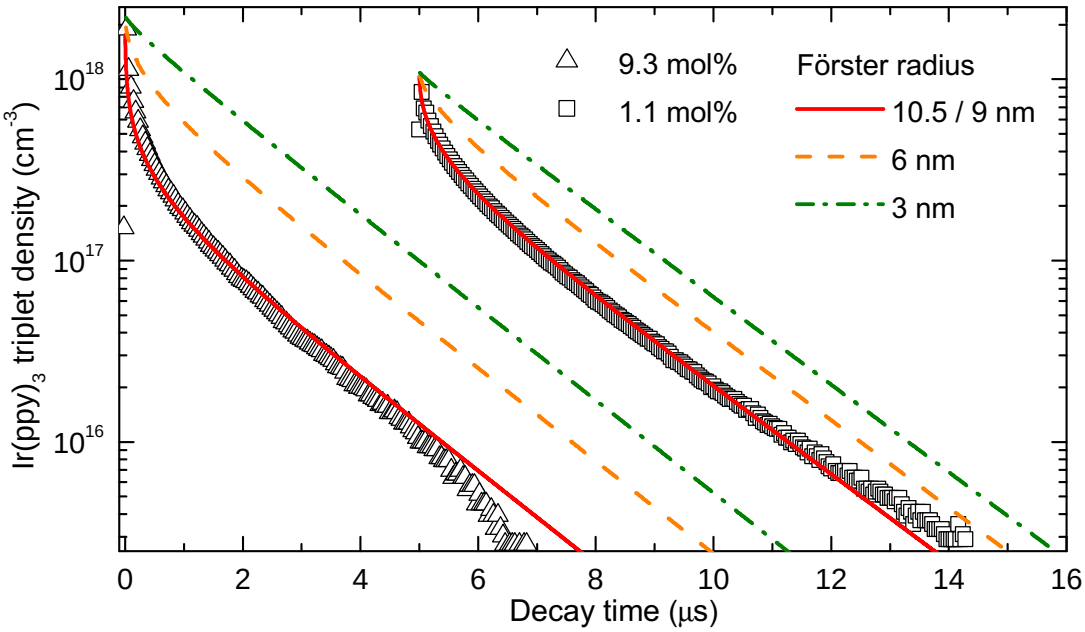

Figure 6.2: Two selected PL transients of Samples 6.2-2 and 6.2-3 (cf. Fig. 6.1). Experimental data is split in time (5 µs) for better visibility. Additionally, calculated fits according to the single-step long range model are included. Red: best fit, orange: upper limit for R_F and green: R_F as determined from Staroske *et al.* [83].

imental data, three calculated fits for each sample are included in Figure 6.2. The red lines indicate the best fits of the transients. They are obtained at $R_F = 9\,\text{nm}$ and $R_F = 10.5\,\text{nm}$ for the 1.1 mol% and 9.3 mol% sample, respectively. However, in contrast to these findings, the model suggests that R_F is independent from the emitter concentration [83]. The orange lines corresponds to $R_F = 6\,\text{nm}$, indicating the Förster limit as determined above. Finally, the green lines correspond to a Förster radius of 3 nm, which represents the prediction of Staroske *et al.* for R_F of $Ir(ppy)_3$ based on the single-step model [83]. Clearly, the strength of the experimentally observed TTA is by far higher than predicted by the single-step long range model. Most impressively, the model suggests almost no TTA contribution at such high pump levels (calculated green lines). Apparently, another channel for TTA must be present in $Ir(ppy)_3$-based systems that gives rise to the experimentally observed annihilation.

Another interesting feature of the transient signals is the decreasing excited state lifetime for increasing emitter concentration. In addition to the Förster radius, the fits according to Equation (3.67) include the excited state lifetime τ as another free parameter. Here, it is determined from the monoexponential long-living tail of transients at low n_p, decreasing from 1.8 µs to 1.7 µs for 1.1 mol% and 9.3 mol%, respectively. For the highly diluted Sample 6.2-1 with a concentration of 0.1 mol%, the lifetime is $\tau = 1.8\,\mu\text{s}$, similar to the 1.1 mol% sample. This indicates the saturation of this effect at very low emitter concentrations [78]. Kawamura *et al.* investigated this effect for different phosphorescent emitter molecules in detail. They observe a decrease of

the photoluminescence quantum yield and the excited state lifetime of mixed films with increasing concentration. Interestingly, this so-called concentration quenching mechanism is mediated through a Förster-type transfer [79].

Finally, the calculated fits (red lines in Fig. 6.2) do not yield a perfect agreement with the experimental transient. At different timescales, visible deviations from the data are observed. Having only R_F as a free parameter at hand (because τ can be precisely determined), the single-step model provides no better fits. This, again, suggests that the single-step mechanism is not the dominating channel for TTA this phosphorescent system.

Aggregation of Ir(ppy)$_3$ Molecules in the Mixed Film

The results of the PL transients in conjunction with the single-step model clearly suggest that mixed films of TCTA:Ir(ppy)$_3$ have a certain property that strongly increases TTA. Again referring to Staroske *et al.*, one possible explanation is the strong tendency to form aggregates or at least locally highly dense clusters of emitter molecules [83]. Indeed, Noh *et al.* reported strong differences in the energy transfer from matrix to the emitter for Ir(ppy)$_3$ doped in different polymer matrices. The latter was very weak for poly[9,9'-di-*n*-hexyl-2,7-fluorene-alt-1,4-(2,5-di-*n*-hexyloxy)phenylene] (PFHP) [157]. Studying the film composition with optical and transmission electron microscopy (TEM) proved a strong tendency of the emitter molecules to form aggregates in the PFHP matrix. This occurred up to a level with the emitter molecules being so well separated from the matrix that the distances between matrix and emitter prevented energy transfer processes. However, there is a large difference between the study of Noh *et al.* and the mixed films of this work. Doped polymer films are prepared by spin-coating or equivalent wet processes that will most likely yield very different microscopic compositions of the mixed film compared to thermally evaporated small molecule based systems. Namdas *el al.* investigated neat evaporated films of Ir(ppy)$_3$ by atomic force microscopy (AFM) [155]. Their AFM images show that the Ir(ppy)$_3$ molecules arrange in needle-like structures instead of forming a structureless amorphous film. These studies give rise to the question, to what extend aggregation of Ir(ppy)$_3$ molecules affects the high brightness performance of phosphorescent solid mixed films.

In order to discuss a possible aggregation in the present system, i.e. TCTA doped with Ir(ppy)$_3$, its PL properties must be previously considered. In Figure 6.3 a), the PL spectra of all three samples with different emitter concentrations of 0.1, 1.1 and 9.3 mol% (Samples 6.2-1,-2, and -3) are plotted. In the blue spectral region, the TCTA host fluorescence is observed, which decreases with increasing Ir(ppy)$_3$ content. This can be clearly attributed to a host-guest energy transfer that is not complete for Samples 6.2-1 and -2, because the few, highly diluted emitter molecules simply cannot capture all matrix excitation by any type of energy transfer – either Förster- or Dexter-type. The phosphorescence spectrum of Ir(ppy)$_3$ is located in the green spectral region with a maximum at roughly 510 nm. With increasing concentration, a distinct red-shift of the emitter peak wavelength is observed from 507 nm of the 0.1 mol% sample to 509 nm (1.1 mol%) and, finally, to 515 nm of the highly concentrated sample.

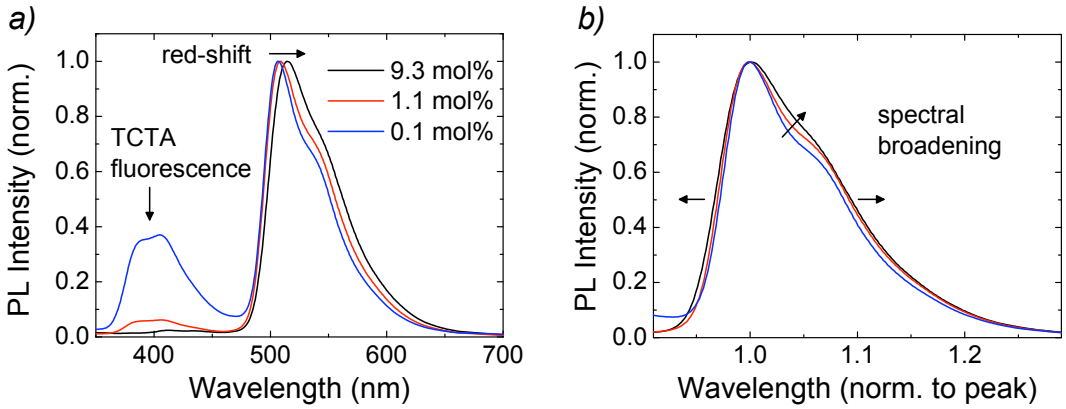

Figure 6.3: Photoluminescence spectra of TCTA:Ir(ppy)$_3$ mixed films with different emitter concentrations. a) Normalized spectra. b) PL spectra from a) normalized to the peak intensity (y-axis) and, additionally, to the peak wavelength (x-axis) to compare the spectral shape. Arrows indicate increasing emitter concentration.

In Figure 6.3 b), the emission spectra of Ir(ppy)$_3$ of all three samples are normalized to its respective emission peak wavelength. Hence, it is possible to directly compare the spectral changes upon an increase of the emitter concentration. Spectral broadening is observed upon increasing emitter concentration. By analyzing the spectra of Figure 6.3 a), the full width at half maximum (FWHM) steadily increases from 58 nm to 62 nm and, finally, 66 nm with increasing emitter content. Furthermore, the shape of the phosphorescent emission changes. For high concentrations, the spectral features (the emission shoulder at a normalized wavelength of ~ 1.05) are weaker.

Both of these observations, i.e. the red-shift and the spectral broadening, clearly indicate molecular aggregation [78]. The decrease of PL quantum yield of such mixed films at increasing emitter content is well known. This is explained by the concentration quenching effect [79, 158]. This same effect makes bulk layers of Ir(ppy)$_3$ and most other phosphorescent materials useless for efficient OLEDs [80].

To investigate possible aggregation, a 50 nm thick mixed film of TCTA:Ir(ppy)$_3$ with an approximate concentration of 10 mol% (Sample 6.2-4) is prepared for the imaging by aberration (Cs) corrected scanning TEM.[3] STEM 1 at Daresbury Laboratory equipped with a Nion Mark II Cs-corrector is operated at 100 kV accelerating voltage with a probe size of about 0.1 nm [159]. To study the Iridium distribution in the film, a high angle annular dark field (HAADF) signal is used. It increases monotoneously with the atomic number of the scattering atoms if the sample thickness is suitable and not changing rapidly on the length scale of interest [160]. Thus, since no other heavy element is included into the film composition, Ir-atoms and agglomerates appear brighter in HAADF contrast. The HAADF image of the Ir-distribution represents a projection through a 50 nm thick sample where only the first few nanometers

[3]The measurements are performed by Dr. Meiken Falke. Current affiliation: Institut für Physik, Technische Universität Chemnitz, D-09107 Chemnitz, Germany.

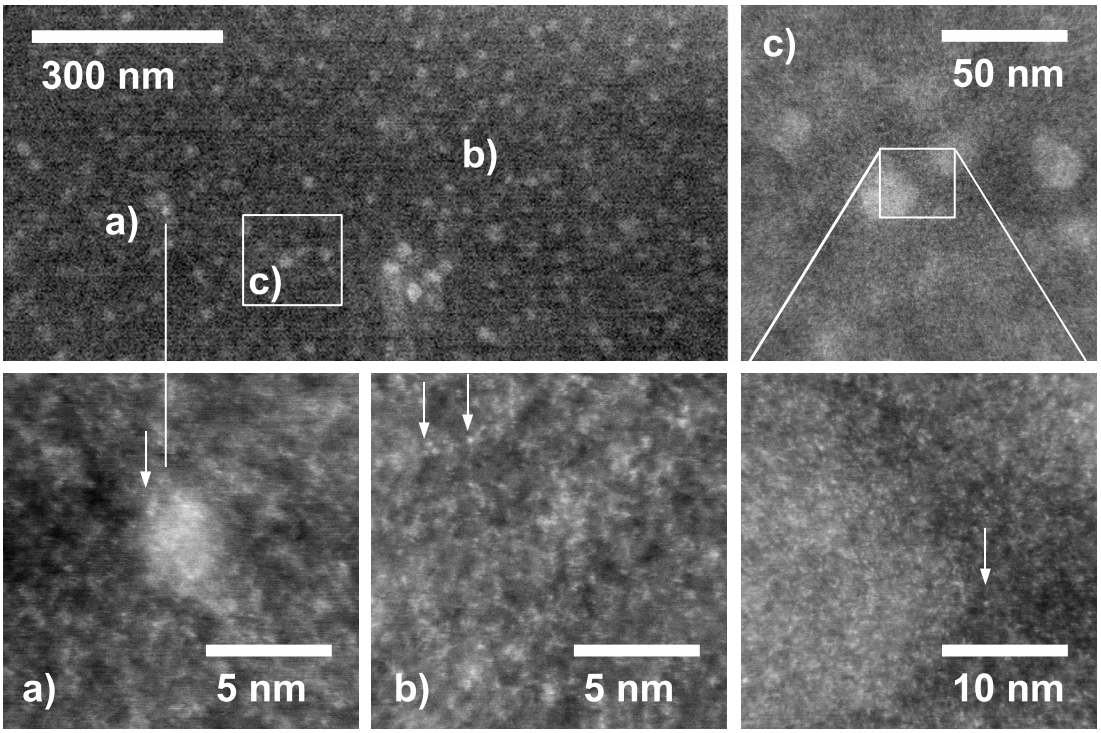

Figure 6.4: HAADF images of the 50 nm TCTA:Ir(ppy)$_3$ film. Higher resolution images are taken for the indicated regions a), b) and c). Image c) is shown with a further zoom-in (bottom right).

are focussed. Electron energy loss spectroscopy is used to prove that the bright areas are not caused by fluctuations in the amount of carbon content. Figure 6.4 shows the HAADF signal of a large film area. Images a), b) and c) are taken at higher resolution. Iridium aggregates of 3-4 nm (Fig. 6.4 a)) and a few larger ones with a diameter of about 30 nm diameter (Fig. 6.4 c)) are observed. They appear particularly bright amongst the otherwise evenly dust-like spread Ir (Fig. 6.4 b)) in the film. The small sharp bright dots in the high resolution images, marked by arrows for four examples, represent the HAADF signal of single Ir atoms in the slice of the film where the electron beam is focussed. The left arrow in Figure Fig. 6.4 b) points to a group of three Ir atoms.

These TEM images together with the results of the spectral analysis provide direct proof that the phosphorescent emitter material Ir(ppy)$_3$ aggregates when embedded in an organic matrix material such as TCTA. This is particularly obtained for the conventional sample preparation using thermal co-evaporation in vacuum to deposit on substrates at room temperature. These findings make it essential to re-address the picture of the microscopic composition of the mixed film and its influence on possible TTA channels in such films.

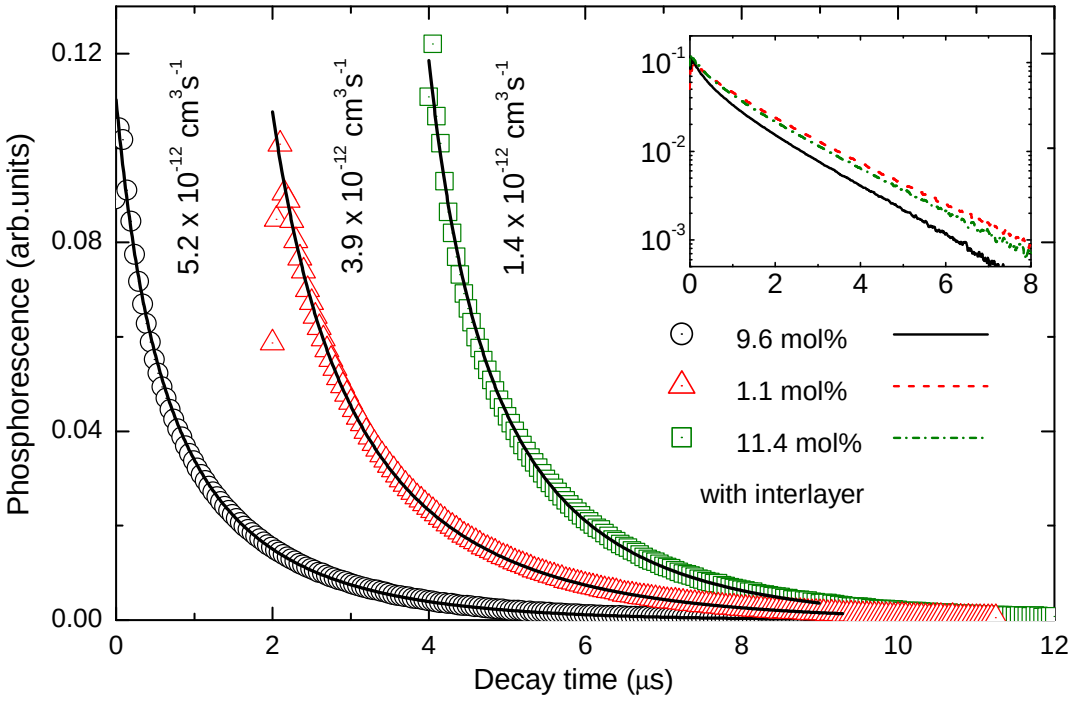

Figure 6.5: Photoluminescence transients of TCTA:Ir(ppy)$_3$ mixed films with different composition (Samples 6.2-5, -6, and -7). Transients are split in time for better visibility (2 µs each). Solid lines: Calculated fits according to the diffusion based model (cf. Eq. (3.70)), the derived values for k_{TT} are displayed. The sub-structured sample shows the smallest TTA rate constant. Inset: data in semi-logarithmic plot.

Open Channel for Diffusion Based TTA

Even though excitons are efficiently confined to guest molecules in the TCTA:Ir(ppy)$_3$ system, the strong tendency to form clustered structures in the matrix material completely changes the picture. Now excitons can easily migrate on the grid of guest molecules through individual hopping steps. At high excitation density, two triplet excitons can reach the critical distance $\bar{a}$, where they can annihilate (cf. Section 3.4). This scenario is shown in Figure 3.6.

Consequently, the PL transients are now analyzed using the diffusion based TTA model. Selected PL transients of two mixed films with different emitter concentration (Sample 6.2-5 and 6.2-6) of 1.1 mol% and 9.6 mol%, respectively, are plotted in Figure 6.5. They are selected to reach similar Ir(ppy)$_3$ triplet densities n_{Ir}. The best fits according to Equation (3.70) are plotted as solid black lines, the corresponding fit parameter k_{TT} is displayed for each case. Compared to the calculated fits according to the single-step long range model as plotted in Figure 6.2, the diffusion based fits agree with the experimental data at any time scale. Hence, the diffusion model is more appropriate to describe TTA in the present system.

As mentioned above, the PL transients have similar n_{Ir}, so that, qualitatively, the TTA contribution can be derived from the curvature of the transient in a semi-logaritmic plot (inset of Fig. 6.5). For Sample 6.2-6 comprising a high emitter concentration of 9.6 mol%, much stronger TTA is observed compared to the 1.1 mol% sample. This agrees with the diffusion based model, which predicts increasing TTA with increasing emitter concentration, because exciton motion becomes easier. The triplet-triplet rate constant k_{TT}, which accounts for the TTA strength in this model, can be directly derived from the fits. Here, k_{TT} increases from $3.9 \times 10^{-12}\,\mathrm{cm^3 s^{-1}}$ to $5.2 \times 10^{-12}\,\mathrm{cm^3 s^{-1}}$ when increasing the emitter concentration from 1.1 to 9.6 mol%. This, again, confirms the concentration dependence and, consequently, the correctness of applying the diffusion based model.

Suppressing Exciton Motion in Layers with Emitter Aggregates

According to the TEM images of Figure 6.4, the $\mathrm{Ir(ppy)_3}$ clusters have various diameters ranging from 3 to 30 nm. It should therefore be possible to manipulate the microscopic composition of these clusters using a complex sequential sample preparation.

A scheme of the proposed EML design is shown in Figure 6.6. The idea is to deposit a very thin mixed film of TCTA:$\mathrm{Ir(ppy)_3}$ of only 1 nm. Knowing that the emitter tends to form aggregates, this layer is followed by a layer of intrinsic matrix material, i.e. TCTA. The preparation of this heterosystem is repeated several times to reach a typical EML thickness. The interlayer must fulfill opposing conditions: (i) It must be fairly thin so that all the excited host states can be transferred to emitter molecules and, at the same time, (ii) it must be thick enough to suppress Dexter-type triplet transfers between guest molecules from different sub-EMLs. It is further desirable to make the interlayer as thin as possible to increase the number of emitting, doped sub-EMLs, to use this architecture as an OLED emission layer. This results in a sub-structured EML that possesses 1D exciton confinement. Excited triplet states are hindered to move in one direction of space, because they can not overcome the triplet barrier of the interlayer (cf. Fig. 6.6).

A good compromise for the above criteria is provided by a thickness of 2 nm for the TCTA interlayer. This agrees with the results from Schwartz *et al.* using an intrinsic interlayer in white OLEDs to suppress triplet energy transfer between a fluorescent and a phosphorescent EML. They proved the sufficiency of an interlayer of 2 nm thickness [37]. In order to reach a typical total thickness of an emission layer, Sample 6.2-7 is prepared, containing 6 TCTA interlayers. The sample has a doped sub-EML on either side, resulting in a total thickness of 19 nm [24].

In addition to the previously discussed homogeneous samples, this sample is analysed in cw and time-resolved manner. First, PL transients of this sample are recorded. A transient with similar initial intensity (equal n_{Ir}) is additionally plotted in Figure 6.5. Comparing the transients plotted in semi-logaritmic manner (inset), a weaker TTA contribution is observed for the sub-structured sample, even though the emitter concentration in the sub-layers is slightly higher (11.4 mol%). When calculating a fit according to the diffusion model, a triplet-triplet rate constant of

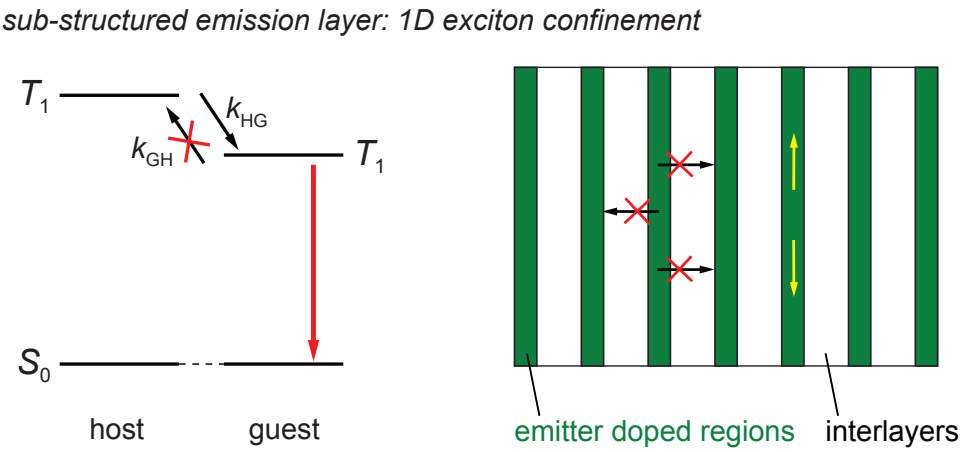

Figure 6.6: Scheme of the sub-structured EML (Sample 6.2-7) comprising intrinsic interlayers of the matrix material. Owing to its high triplet energy, the interlayers prevent excitons from diffusing in one direction of space. Hence, only diffusion in the plane of the thin sub-layers is possible (yellow arrows).

$1.4 \times 10^{-12}\,\mathrm{cm^3 s^{-1}}$ is derived. This is only 27 % of the value of Sample 6.2-6 with a concentration of 9.6 mol%. Here, it is taken into account that the active volume of the sub-structured sample is roughly 1/3 of Sample 6.2-6. This results in a higher n_{Ir} necessary to obtain equal photoluminescence intensity. This decrease in k_{TT} can only be attributed to an overall reduction of diffusion. By introduction of the thin intrinsic TCTA interlayers, the excited states are efficiently hindered to migrate in one direction of space, reducing the random-walk process of diffusion.

3D Confinement versus Aggregation

The suppression of diffusion should also be realized by reduction of the emitter concentration in a single mixed film down to values at which the guest distance reaches values of the TCTA interlayer thickness. Assuming cubic closed packing with every guest molecule occupying the space of a TCTA molecule (density $\rho = 1.139\,\mathrm{g/cm^3}$), and molar mass $M = 740.9\,\mathrm{g/mol}$) and further no emitter aggregation, one can compute the guest distance to 1.4 and 2.9 nm for 9.6 and 1.1 mol% emitter concentration, respectively. Hence, for the 1.1 mol% sample, the guest distance is even greater than the thickness of the undoped interlayers ($\sim 2\,\mathrm{nm}$) of the sub-structured sample.

From this point of view, the homogenous sample with 1.1 mol% should have a very low k_{TT} since it should efficiently suppress exciton diffusion in all directions. However, the contrary is true. The rate constant k_{TT} of the sub-structured sample is only 36 % of the value of the 1.1 mol% mixed film (Sample 6.2-5). Since the estimation of the guest distance is based on a homogeneous distribution of $\mathrm{Ir(ppy)_3}$ molecules in the film, these results give further evidence for the preparation of mixed films comprising $\mathrm{Ir(ppy)_3}$ being accompanied by formation of aggregates, i.e. regions of short guest-guest distance which enhance diffusion-based TTA.

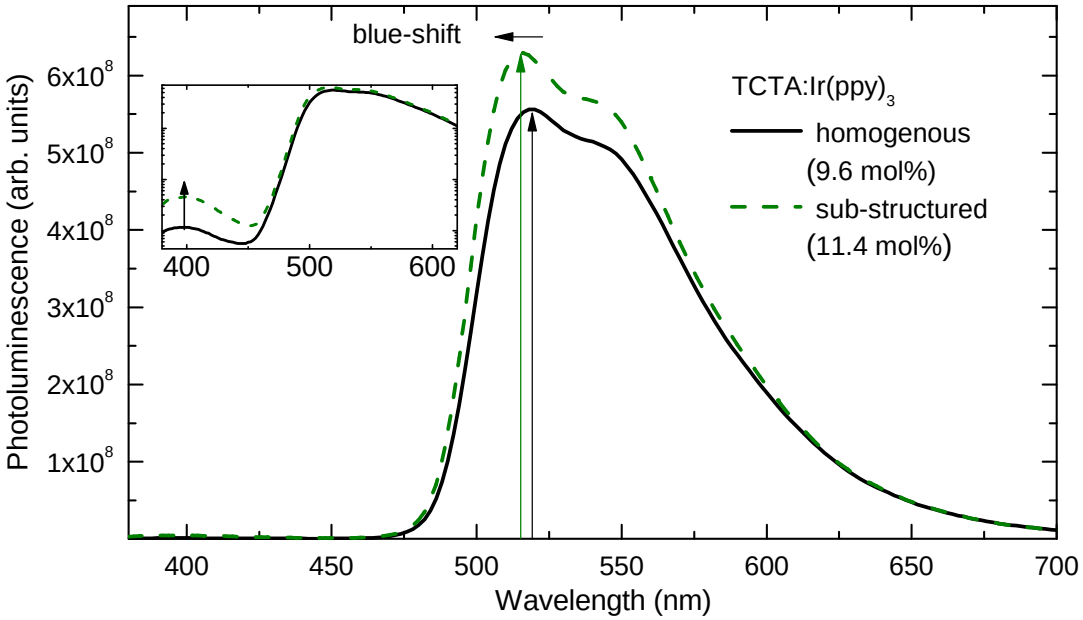

Figure 6.7: Photoluminescence of Sample 6.2-6 and 6.2-7. The arrows indicate the corresponding emission maximum. Compared with the homogeneous reference sample, the sub-structured system shows a slightly higher intensity and a blue-shift of the peak wavelength. Inset: data in semi-logarithmic scale with a focus on the TCTA fluorescence (arrow).

Excited State Lifetime and Photoluminescence Intensity

At this stage, the effect of the TCTA interlayers on the general photophysical properties will be discussed. In Figure 6.5, the PL transients are plotted for Samples 6.2-5, -6, and -7, where differences in the excited state lifetime τ (see inset) are observed. The lifetimes are 1.65 µs for the highly doped sample, 1.95 µs for the 1.1 mol% sample, and 1.81 µs for the sub-structured sample.[4] This decrease in τ from 1.1 mol% to 9.6 mol% agrees with the earlier cited work of Kawamura *et al.* that discusses the concentration quenching mechanism [79]. At this stage, it is highly plausible to assume that the emitter aggregation even amplifies the concentration quenching effect. Thus, by preventing the aggregation, it should also be possible to increase the PL quantum yield of such mixed films at concentrations in the range of 10 mol%, which is a typical doping ratio used in phosphorescent OLEDs.

Interestingly, compared to the highly doped sample with 9.6 mol% ($\tau = 1.65$ µs), the excited state lifetime of the sub-structured sample increases to 1.81 µs. This suggests that the photoluminescence properties of the sub-structured sample are improved compared to the homogeneously doped reference sample. Figure 6.7 shows

[4]This sample series (Samples 6.2-5 and -6) has slightly higher excited state lifetimes compared to Samples 6.2-2 and -3, even though the structures are virtually identical. The lifetime τ is very sensitive to the preparation conditions, e.g. the oxygen content in the nitrogen glovebox during the encapsulation. A temperature effect can be excluded by comparing lifetime versus temperature data of Ref. [154].

the PL intensity of the sub-structured and the highly doped reference sample. As expected, the PL intensity is higher for the sub-structured sample. These spectra are absorption corrected and measured in the same geometry. Hence, their absolute values can be compared similarly to PL quantum yield values. This is only possible because the thin-film optics of the two samples are nearly identical comprising the same materials with the same total thickness. Here, the sub-structured sample shows a (12 ± 3) % increase in the PL intensity. Furthermore, the TCTA fluorescence in the sub-structured sample increases (cf. inset of Fig. 6.7), indicating that the host-guest energy transfer is not as efficient as for the reference sample. This effect originates from the six TCTA interlayers, which cannot fully transfer their excitation to the phosphor-doped regions.

Referring to Figure 6.3 that illustrates the PL spectrum of mixed films with different emitter concentrations, aggregates in the mixed film are accompanied with a red-shift in the emitted spectrum. However, as indicated by the arrows in Figure 6.7, the peak wavelength of the sub-structured sample spectrum shifts about 4 nm to the blue. This is further evidence that the sub-structured sample reduces the formation of emitter aggregates in the mixed film.

6.3 OLEDs with a Sub-Structured Emission Layer

In the preceding section, a sub-structured emission layer that comprises thin intrinsic matrix interlayers was discussed. Time-resolved PL experiments showed that this architecture has improved properties at high excitation levels, i.e. weaker triplet-triplet annihilation. In this section, the EML concept will be integrated into an OLED structure. The prepared OLEDs will be discussed in respect to their high brightness performance.

Prepared Organic LEDs

Three OLEDs comprising the green phosphorescent emitter $Ir(ppy)_3$ are prepared with the following layer sequence. The EML is displayed boldface for clarity. Device 6.3-1 serves as the reference device with a commonly used doping ratio of 10 mol% [150, 161]. Compared to this high concentration device, the results of the preceding section suggest another OLED that has a reduced emitter concentration of 1 mol% (6.3-2). Finally, Device 6.3-3 comprises the sub-structured EML similar to Sample 6.2-7 of Section 6.2. Only the first mixed sub-EML is chosen to be 2 nm thick in order to have a total EML thickness of 20 nm, equal to the other two devices.

Device 6.3-1: MeO-TPD:F_4-TCNQ (25 nm, 4 wt%) / NPB (10 nm) / **TCTA: $Ir(ppy)_3$ (20 nm, 10 mol%)** / TPBi (10 nm) / Bphen:Cs (55 nm) / Al (100 nm)

Device 6.3-2: MeO-TPD:F_4-TCNQ (25 nm, 4 wt%) / NPB (10 nm) / **TCTA: $Ir(ppy)_3$ (20 nm, 1 mol%)** / TPBi (10 nm) / Bphen:Cs (55 nm) / Al (100 nm)

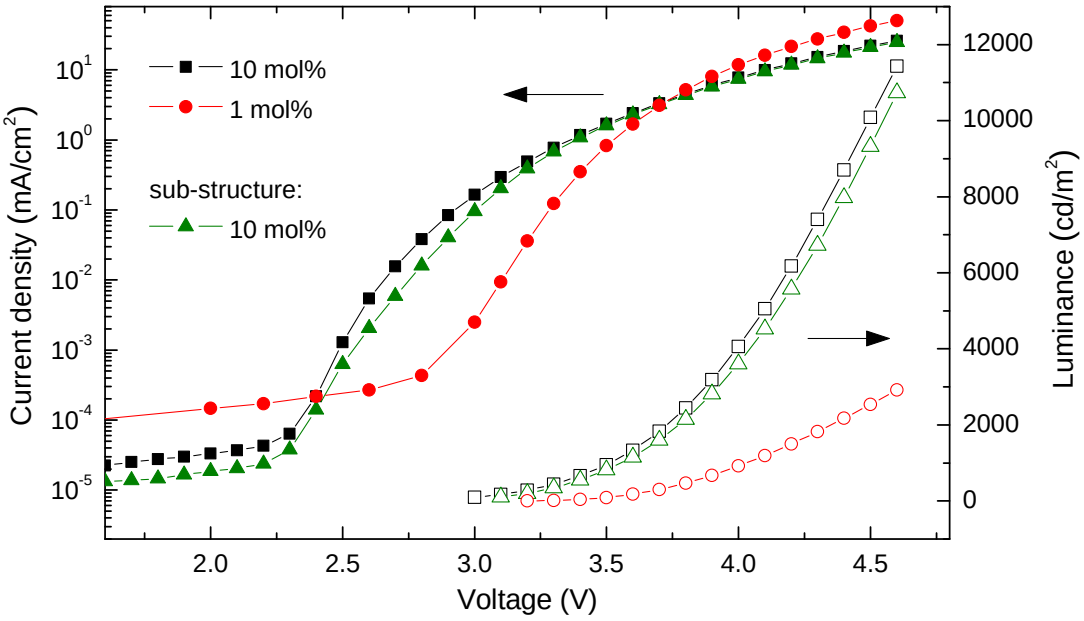

Figure 6.8: Current density-voltage-luminance characteristics of Devices 6.3-1, -2, and -3. Closed symbols represent the current density, open symbols the luminance data.

Device 6.3-3: MeO-TPD:F_4-TCNQ (25 nm, 4 wt%) / NPB (10 nm) / **TCTA: Ir(ppy)$_3$ (2 nm) / [TCTA (2 nm) / TCTA:Ir(ppy)$_3$ (1 nm)]$_6$ (10 mol%)** / TPBi (10 nm) / Bphen:Cs (55 nm) / Al (100 nm)

Current Density-Voltage-Luminance Characteristics

In Figure 6.8, the current density and luminance are plotted versus voltage for all three OLEDs. Compared to the reference device (Device 6.3-1) with high Ir(ppy)$_3$ concentration, the 1 mol% device shows worse j-V properties. While the onset voltage for the reference device is located between 2.2 and 2.3 V, the onset voltage of the low concentration device lies at approximately 2.8 V. The latter value cannot be precisely determined because this device additionally has higher leakage currents. However, the increased voltage that is necessary for the 1 mol% device agrees with the discussion of He *et al.*, where it is suggested that the hole injection and transport in the TCTA:Ir(ppy)$_3$ EML is mediated through the HOMO level of the dopant [8, 162]. Thus, by strongly reducing the emitter molecules, the concentration falls below the percolation limit so that no efficient transport is possible. The reason for the current density exceeding the values of the reference device above 3.6 V of the OLED with 1 mol % concentration is still unclear.

On the other hand, the OLED comprising the sub-structured EML shows nearly identical j-V characteristics compared to the reference device. This is surprising, because the energy difference of the HOMO levels of TCTA and Ir(ppy)$_3$ is 0.5 eV (cf. Fig. 3.13). Therefore, one would expect that holes, located in the sub-EMLs on the Ir(ppy)$_3$ HOMO, need to overcome the energy barrier to the TCTA HOMO level.

Referring to Figure 6.8, a difference in the characteristics below 3 V is visible, where the current density is lower for the sub-structured device. However the differences are small and even vanish above 3 V, where both sets of data fall together. Presumably, holes can tunnel through such thin layers [163] and hop from layer to layer, because the sub-structured layers are not perfectly closed.

Figure 6.8 illustrates that the light emission of Device 6.3-2 with the low $Ir(ppy)_3$ concentration of 1 mol% is by far not as efficient as the reference and the sub-structured devices. While the latter two reach luminance values of approximately 11,000 cd/m^2 at 4.6 V, the 1 mol% device only reaches 3,000 cd/m^2 at the same voltage. The differences are even larger considering the higher current density of the 1 mol% device at 4.6 V.

Electroluminescence

Referring to the work of Kawamura *et al.*, the emission efficiency of a phosphorescent mixed film increases with decreasing emitter concentration [78]. In their data of $Ir(ppy)_3$ doped in CBP, the PL quantum yield increases from 85 % (10 mol%) to 97 % (1 mol%). This suggests that the highest OLED quantum efficiency should be observed for emitter concentrations in the range of 1 mol%. However, typical doping ratios in phosphorescent OLED emission layers are much higher [58]. The electroluminescence spectra of the present devices, plotted in Figure 6.9, can be used as further evidence for the need of emitter concentrations > 1 mol%. In contrast to Devices 6.3-1 and -3, the 1 mol% device shows a pronounced high energy feature in the EL spectra with no distinct peak wavelength. Therefore, the light emitted from Device 6.3-2 does not solely originate from the highly efficient triplet states of $Ir(ppy)_3$, which has detrimental influence on the device EQE. The latter will be discussed later, together with the EQE data of the other OLEDs.

This high energy emission most likely originates from a charge-transfer state, referred to as *exciplex*, and not from TCTA fluorescence, as the TCTA emission is centered at 400 nm (cf. Fig. 5.4 b) and Fig. 6.7). Because the EML is preferentially hole transporting [20], the exciplex is formed between the HOMO (5.9 eV) of TCTA and the LUMO (3.0 eV) of TPBi. The energy difference of 2.9 eV corresponds to a wavelength of approximately 430 nm. This value is determined without considering the exciton binding energy of this interfacial state. It is in general smaller than the on-site exciton binding energy ($\lesssim$ 0.5 eV [164]), because the charges are spatially further separated [165, 166]. Hence, the blue shoulder in the EL spectrum agrees with the spectral region where the TCTA/TPBi exciplex is expected. It is the low emitter concentration that gives rise to this emission, because there are not enough $Ir(ppy)_3$ sites to capture all the excitation.

The previous Section 6.2 discussed the photoluminescence properties of the various emission layers in detail. In Figure 6.7, the PL spectra of the homogeneously doped (9.6 mol%) and the sub-structured (11.4 mol%) EMLs both showed a distinct contribution from the TCTA fluorescence. This mainly stems from the optical excitation where only singlet excitons are generated. The sub-structured sample showed an increased TCTA fluorescence. Interestingly, as plotted in Figure 6.9, neither the EL

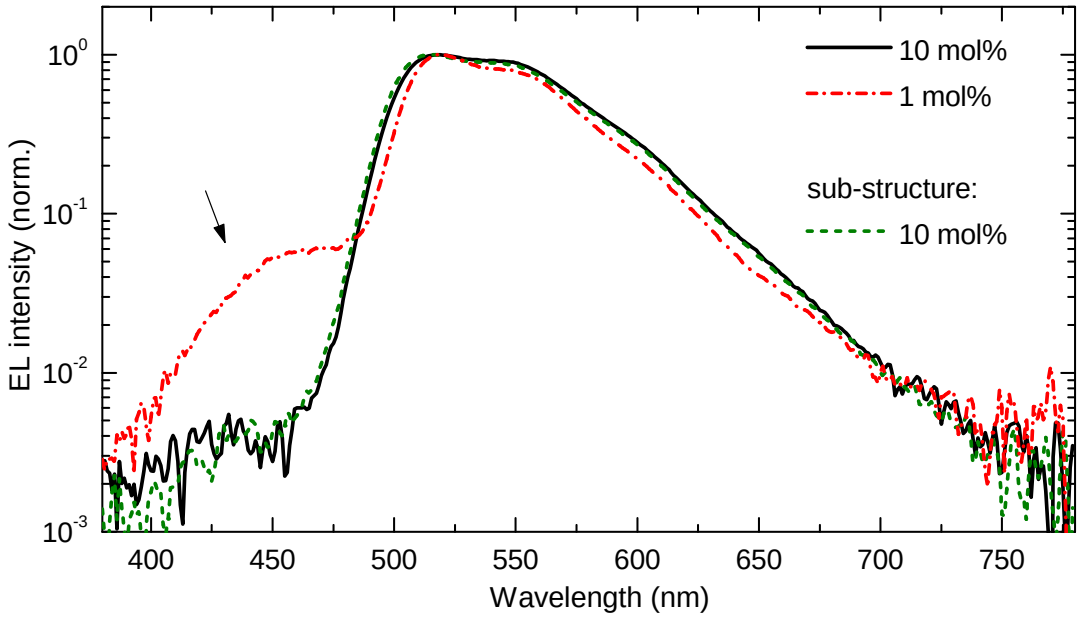

Figure 6.9: Electroluminescence spectra of Devices 6.3-1, -2, and -3. The arrow points to an exciplex emission of the OLED with 1 mol% emitter concentration that is formed between the EML and the hole blocking layer.

spectrum of the reference OLED nor the one of the device with the sub-structured EML show any host emission. In the blue spectral region, both spectra have only signals on the noise level of the spectrometer. This clearly indicates that the excitons, regardless whether they are created on matrix or emitter molecules, can efficiently be harvested by the phosphor, which is essential for high efficiency.

Comparing the spectral shape of the $Ir(ppy)_3$ emission of the 1 mol% Device with the other OLED spectra in Figure 6.9, its spectrum is more narrow and slightly red-shifted. The smaller FWHM value, similar to the PL samples of Figure 6.3, can be easily ascribed to the lower emitter concentration and, hence, to less aggregation. However, the unexpected red-shift with decreasing doping ratio is most likely an artifact of the narrowed spectrum of the 1 mol% Device.

External Quantum Efficiency

The EQE versus current density is plotted in Figure 6.10. The OLEDs with highly concentrated emitters reach high values of 15.8 % (reference) and 14.4 % (sub-structured EML) at low brightness, where bimolecular quenching is negligible. In contrast, the EQE of the 1 mol% device is lower than 4 % even at low current density. This low efficiency is directly correlated with the exciplex emission formed at the TCTA/TPBi interface. Despite highly efficient exciplex based OLEDs being reported [167], the prerequisites for efficiently emitting interface states are challenging to be met. Furthermore, similar to conventional OLEDs, internal efficiencies can only be lifted above 25 %, if the interfacial triplet states can be additionally used for radiative recombination. This, however, requires the incorporation of heavy metal atoms in at least one

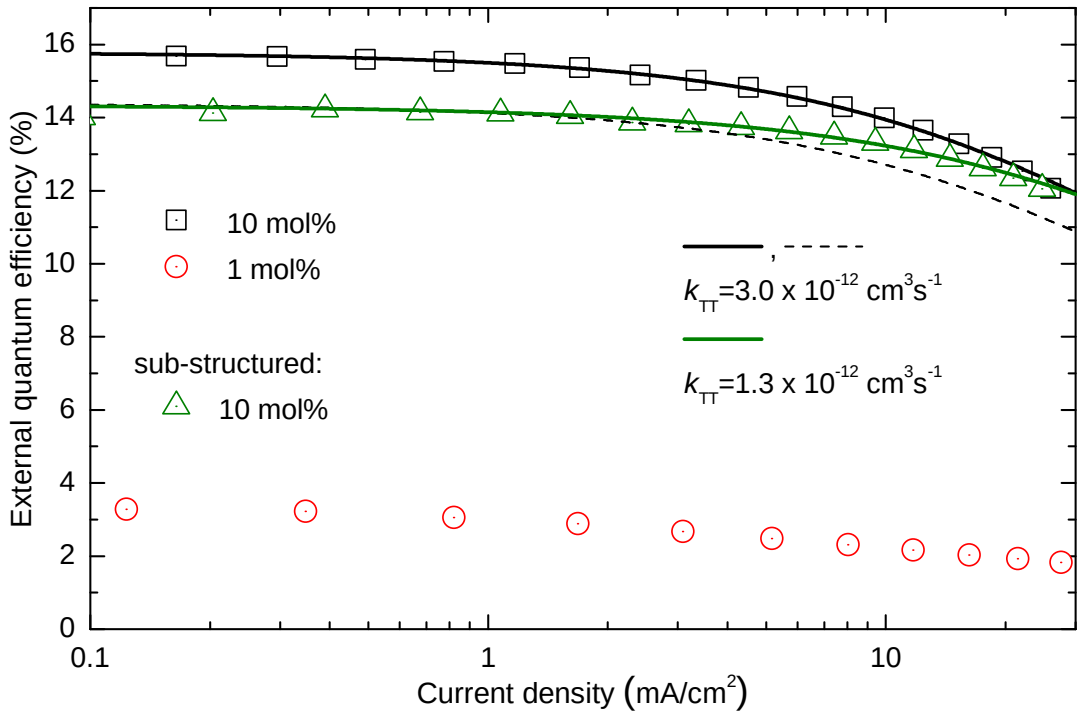

Figure 6.10: EQE versus current density for Devices 6.3-1, -2 and -3 (open symbols). The lines correspond to calculated fits according to the EQE roll-off model from Ref. [20]. To fit the data, only k_{TT} is varied. The dashed line is a rescaled fit of the 10 mol% device. Data exceeding 30 mA/cm^2 could not be obtained due to a strong superposition with the device degradation.

of the materials to enhance the spin-orbit coupling [168]. Because of the low EQE of Device 6.3-2 (1 mol%), which is not sufficient for applications, it will not be included in the following discussion of the EQE roll-off.

For increased current density in Figure 6.10, the reference device shows a stronger EQE roll-off, despite the fact that it yields a higher absolute EQE value. The differences in the OLED roll-off can be best compared using a model that describes the EQE as a function of the current density j that encounters both TTA and TPQ [20]. In Reference [20], this model was applied to a phosphorescent OLED comprising TCTA:Ir(ppy)$_3$ which is almost identical to the present reference device. Hence, the values of the triplet-triplet ($k_{\mathrm{TT}} = 3.0 \times 10^{-12}\,\mathrm{cm^3 s^{-1}}$) and triplet-polaron ($k_{\mathrm{P}} = 0.3 \times 10^{-12}\,\mathrm{cm^3 s^{-1}}$) annihilation rate constants are kept fixed while using the thickness of the recombination zone (RZ) w as fit parameter for slight adjustments. More precisely, it is used as a fit parameter for the reference device and then used to fit the sub-structured device without further variation. The influence of w will be discussed later.

For the excited state lifetime, a value of $\tau = 1.64\,\mu\mathrm{s}$ is used for the reference device as derived from Reference [20]. As discussed earlier, τ increases by introducing the sub-structure EML. The analysis of Samples 6.2-5 and 6.2-7 resulted in values of 1.65 µs and 1.81 µs for reference and sub-structure sample, respectively, providing an

increase of 10 %. Hence, for the calculation of the fit for the sub-structured device, a 10 % longer lifetime is used (1.80 µs).

Because the j-V characteristics are almost identical for the reference and sub-structured device (cf. Fig. 6.8), k_P is not expected to differ strongly for the sub-structured EML. Additionally, the results of Reference [20] show that the EQE roll-off in $Ir(ppy)_3$-based OLEDs is dominated by TTA. The used value of k_{TT} is confirmed by independent analysis of PL transients of a corresponding EML sample [25].

Figure 6.10 shows the fit based on the model of Reference [20] for the reference device as a black solid line. This fit is rescaled to initial values of the sub-structure device (dotted black line). It clearly shows that the interlayer device has a lower efficiency roll-off than the normalized reference device, indicating that TTA is reduced. As next modeling step, the derived value for w for the RZ is kept fixed to fit the interlayer data by varying k_{TT}. Good agreement with experimental data is found with $k_{TT} = 1.3 \times 10^{-12}\,\mathrm{cm^3 s^{-1}}$ that is only 43 % of the value for the reference device.

Influence of the Recombination Zone *w*

In general, the impact of triplet-triplet annihilation scales with the triplet exciton density n_{Ir}, which itself depends on the active luminescent volume. In OLEDs, the lateral dimensions of this volume area defined by the active area of the device pixel. In vertical direction it is the actual exciton recombination profile in the EML which contributes to the active volume rather than the thickness of the EML. In most cases, this profile is much narrower than the EML thickness. In Reference [20], the thickness of the recombination zone has been estimated to $w = 5\,\mathrm{nm}$ for the TCTA:$Ir(ppy)_3$ OLED, where it is located at the interface to the hole blocking layer.

Because the EML of the sub-structured device contains 6 intrinsic TCTA interlayers with a total thickness of 12 nm, the effective luminescent EML is shrinked to 8 nm already. This is the upper limit of w_{sub} for the sub-structured device. However, if the recombination zone would reach the electron blocking layer NPB, a strong drop in the EQE would be expected. Here, as shown by Goushi *et al.*, NPB has a triplet level of $T_1 = 2.3\,\mathrm{eV}$ which is lower than the emissive state of $Ir(ppy)_3$ so that the phosphorescence would be effectively quenched [81]. In contrast, the EQEs of the reference and sub-structured device are at equally high levels, ranging between initial values of $14 - 16$ % EQE (cf. Fig. 6.10). This becomes apparent if one assumes an equal n_{Ir} in all sub-EMLs of the sub-structured device and, further, that the emission of the 2 nm sub-EML (close to the EBL) is quenched by the NPB triplet state. This yields a luminescence of only 75 % which would be reflected in an EQE value in the range of 11 % – far less than the observed 14.4 %. This leads to the conclusion that the created exciton density does not reach the 2 nm thick sub-EML that is adjacent to the EBL. Hence, it is reasonable to assume the recombination zone w_{sub} being comparable to the value of the reference device (5 nm). Consequently, the broadening of the RZ in the sub-structured device can be excluded to be the reason for the reduced EQE roll-off.

Increased Critical Current Density j_c

Using the applied EQE model of Reference [20], the critical current density j_c of the corresponding OLEDs can be estimated. By extrapolating to $\eta_{ext}(j_c)$ (cf. Sec. 3.6), the reference and sub-structured device yield critical current densities of 140 and 270 mA/cm^2, respectively, which is nearly a twofold improvement [25]. This is more appropriate than using the expression for j_c as derived from Baldo *et al.*, which only takes TTA into account [19]. Consequently, it would overestimate j_c, because it ignores triplet-polaron quenching. For instance, calculating j_c for the reference sample accounting only for TTA results in a higher critical current density of 159 mA/cm^2.

For a practical high brightness level of 5,000 cd/m^2, which corresponds to a current density of approximately 10 mA/cm^2 in the present devices, the EQE model is used to determine the relative performance. Here, the normalized EQE $\bar{\eta}_{ext} := \eta_{ext}(j)/\eta_{ext,0}$ yields values of 0.88 and 0.92 for the reference and sub-structured device, respectively. This clearly indicates that real applications can benefit from the sub-structured EML concept.

6.4 Suppressing Emitter Aggregation by Molecular Engineering

In the previous section, the emission layer of a green phosphorescent OLED comprising Ir(ppy)$_3$ as emitter was sub-structured by insertion of intrinsic TCTA layers. It was used to introduce exciton confinement within the EML because the emitter shows a strong tendency to form aggregates that enhance TTA. Even though the concept showed improved high brightness performance, the fabrication of such sub-structured EMLs is complicated. Furthermore, this concept is only a workaround as it does not address the origin of the emitter aggregation.

This section focusses on the emitter material itself, because it is most likely that its molecular properties give rise to the observed aggregation. Therefore, Ir(ppy)$_3$ will be compared to another Ir-based green emitter that has very similar properties, i.e. Ir(ppy)$_2$(acac) [26]. They slightly differ in their chemical structure (cf. Fig. 3.12). In contrast to the homoleptic Ir(ppy)$_3$, one of the phenylpyridine ligands is exchanged by acetylacetonate to form Ir(ppy)$_2$(acac). The change in the molecular structure results in a noticeable difference in the molecular dipole moment [169], which give rise to the assumption that these molecules show differences in the strength of aggregation. Even though Ir(ppy)$_2$(acac) has sucessfully been used as OLED emitter serveral years ago [58], its high brightness performance has not yet been addressed.

Prepared Organic LEDs

In order to best compare the two different phosphorescent emitters, either Ir(ppy)$_3$ or Ir(ppy)$_2$(acac) are incorporated into the EMLs of a defined OLED stack without changing any other parameters. Furthermore, to achieve a higher amount of data, two different OLED stack designs are used. Again, the EMLs of the devices are displayed

boldface for clarity. A high concentration of 8 wt% of the emitter is chosen to assure aggregate formation in the reference devices comprising $Ir(ppy)_3$.

First, similar to the architecture of Device 6.3-1 of Section 6.3, single EML (SEML) OLEDs are prepared. Here, the emitters are diluted into TCTA, a hole transporting matrix material, at a concentration of 8 wt%, forming a 20 nm thick EML. The complete layer sequences of these devices are given below.

Device 6.4-1: MeO-TPD:NDP-2 (25 nm, 4 wt%) / NPB (10 nm) / **TCTA: $Ir(ppy)_3$ (20 nm, 8 wt%)** / TPBi (10 nm) / Bphen:Cs (55 nm) / Al (100 nm)

Device 6.4-2: MeO-TPD:NDP-2 (25 nm, 4 wt%) / NPB (10 nm) / **TCTA: $Ir(ppy)_2(acac)$ (20 nm, 8 wt%)** / TPBi (10 nm) / Bphen:Cs (55 nm) / Al (100 nm)

Furthermore, the double emission layer (DEML) concept is used to prepare an additional set of OLEDs where the emitters are compared. The DEML is designed to locate the exciton recombination zone in the center of the complete EML [170]. This is achieved by using TCTA as a hole transporting matrix and TPBi as the electron transporting counterpart, both being doped with the respective emitter with equal concentration of 8 wt%. The corresponding OLED stacks are displayed below.

Device 6.4-3: MeO-TPD:NDP-2 (25 nm, 4 wt%) / NPB (10 nm) / **TCTA: $Ir(ppy)_3$ (8 nm, 8 wt%) / TPBi:$Ir(ppy)_3$ (12 nm, 8 wt%)** / TPBi (10 nm) / Bphen:Cs (55 nm) / Al (100 nm)

Device 6.4-4: MeO-TPD:NDP-2 (25 nm, 4 wt%) / NPB (10 nm) / **TCTA: $Ir(ppy)_2(acac)$ (8 nm, 8 wt%) / TPBi:$Ir(ppy)_2(acac)$ (12 nm, 8 wt%)** / TPBi (10 nm) / Bphen:Cs (55 nm) / Al (100 nm)

In contrast to the OLEDs of Section 6.3, the p-dopant of the HTL is exchanged from F_4:TCNQ to NDP-2. In the single chamber tool, where these devices are fabricated, solely NDP-2 is used to avoid possible vacuum tool contamination issues, possibly occurring if F_4:TCNQ would be evaporated instead. It has been shown earlier that no significant difference is observed using one or the other p-dopant [171].

Current Density-Voltage Characteristics and EL Spectra

The j-V characteristics of all four devices are plotted in Figure 6.11 a). Compared to the SEML devices, the DEML counterparts for both emitter molecules show steeper characteristics. This has been observed previously [170] and stems from the incorporation of hole and electron transporting matrices (here TCTA and TPBi, respectively), which lowers the driving voltage. Comparing the electrical performance of devices comprising $Ir(ppy)_3$ and $Ir(ppy)_2(acac)$, lower voltages are observed for the latter. While the onset voltage of all devices is nearly identical at 2.3 V, the operating voltage at a current density of 10 mA/cm^2 is reduced by 0.2 V from the $Ir(ppy)_3$ to the $Ir(ppy)_2(acac)$ devices, similar for SEMLs and DEMLs. This clearly indicates that

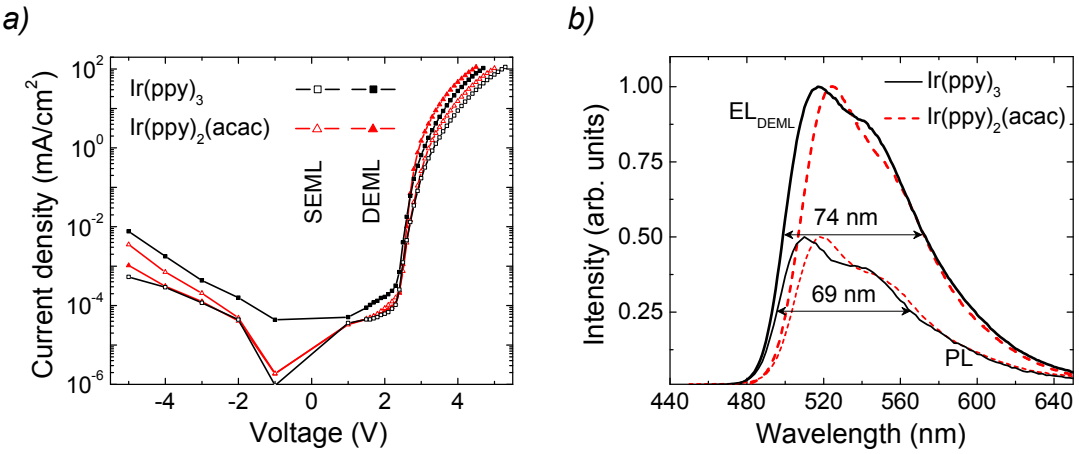

Figure 6.11: a) Current density-voltage characteristics of all devices (Devices 6.4-1, -2, -3, and -4). b) EL spectra (thick lines normalized to 1) of the DEML devices, measured at 1,000 cd/m^2 in forward direction. Additionally, PL spectra (thin lines normalized to 0.5) of liquid solutions of both emitters diluted in toluene (6.5×10^{-3} mg/ml) are plotted. The horizontal dashed lines indicate the FWHM of Ir(ppy)$_3$ in the mixed film and solution with the corresponding value.

the emitter itself contributes to the charge transport, an effect that has been proposed many times before [8, 36, 42, 162, 172].

The electroluminescence spectra of both DEML devices are plotted in Figure 6.11 b), as measured at 1,000 cd/m^2 in forward direction. The spectra of the SEML devices are nearly identical, so that they are not shown here. Compared with the Ir(ppy)$_3$ emission, the Ir(ppy)$_2$(acac) peak is 8 nm red-shifted to 525 nm. Furthermore, its spectrum has a smaller FWHM value of 66 nm (Ir(ppy)$_3$: 74 nm).

External Quantum Efficiency

Figure 6.12 plots the EQE as a function of current density for all four OLEDs prepared in this study. The y-axis is chosen to start at a value of 10 % EQE to better visualize the differences. First of all, the DEML devices reach much higher EQE values than their corresponding SEML counterparts, i.e. approximately 18 and 15 % EQE at low brightness for DEML and SEML, respectively. For both OLED structures, the absolute EQE values of the corresponding emitter molecule are nearly identical. This simplifies the discussion of the efficiency roll-off, as their EQE characteristics can be directly compared. For both SEML devices, especially for the the Ir(ppy)$_2$(acac) OLED, an initial increase of EQE with increasing current density is observed. High leakage currents, which in general could be the reason for the low EQE at low currents, can be excluded as a reason, because all current densities at negative bias are in the same order of magnitude (cf. Fig. 6.11). It is most likely, that, especially for the SEML architecture, the charge balance γ_{bal} (cf. Eq. (3.81)) within the EML is not at its optimum at low voltages, because the energy levels of the OLEDs are not fully

symmetric. By using the DEML concept, this imbalance can be minimized.

Starting at similar absolute values, the DEML devices comprising $Ir(ppy)_3$ and $Ir(ppy)_2(acac)$ show different roll-off characteristics. The efficiency of the $Ir(ppy)_3$ OLED steadily decreases, starting at very low current densities. In contrast, indicated by the diverging green lines, the $Ir(ppy)_2(acac)$ device maintains higher EQE values at high brightness. For instance, a 10 % drop of the EQE at 100 cd/m^2 is reached at 8,000 and 11,000 cd/m^2 for $Ir(ppy)_3$ and $Ir(ppy)_2(acac)$, respectively. The discussion of the SEML devices is not straightforward because, as discussed above, the absolute efficiencies at low brightness cannot be determined with certainty. Still, comparing with the results of the DEML devices, the internal efficiencies of the SEMLs comprising $Ir(ppy)_3$ and $Ir(ppy)_2(acac)$, respectively, are similar, provided that no electrical effects lower the efficiency. Additionally, the SEML $Ir(ppy)_2(acac)$ device reaches higher EQEs at high brightness or current density, respectively (cf. Fig. 6.12).

In summary, the devices comprising $Ir(ppy)_2(acac)$ show an improvement in the EQE roll-off, hence, the corresponding EMLs show a weaker TTA contribution than their $Ir(ppy)_3$ containing counterparts. Despite the fact that the photophysical properties of both emitters differ due to the ancillary ligand in $Ir(ppy)_2(acac)$ [58, 138, 140, 173], presumably affecting the Förster radius R_F for single-step long range TTA, the subsequent discussion will show that the differences can be found in diffusion based TTA.

Superposition of Efficiency Roll-Off and Device Aging

Before discussing triplet-triplet annihilation of these devices in detail, the undesired effect of device aging during the measurement sweep will be addressed. In general, the long term stability of an OLED scales with the current density or, respectively, the luminance [9, 42]. Especially at high brightness, where the roll-off becomes dominant, the EQE of an OLED significantly drops even on timescales of the measurement sweep. This results in the fact that, if two subsequent sweeps are measured, the second value of the EQE at very low brightness is noticeably decreased. Hence, the device aging during the measurement sweep even accelerates the roll-off.

In Figure 6.12, the blue solid lines indicate that EQE characteristics of the DEML devices of both emitters seem to converge slightly. Thus, at such high current densities, the $Ir(ppy)_2(acac)$ devices show a slightly stronger roll-off. Because the compared devices differ only in the emitter molecule itself, it is very likely that they age differently, which might be the reason for the altered roll-off characteristics. In order to check this influence of the emitter degradation, the long term stability of all devices is measured. The normalized luminance as a function of operation time is plotted in Figure 6.13 as measured at a constant current density of 10 mA/cm^2. Here, the trend is clear: For both EML architectures, the devices comprising $Ir(ppy)_2(acac)$ show shorter lifetimes than their corresponding $Ir(ppy)_3$ counterpart.

By carefully analyzing several consecutive measurement sweeps of such devices, using previously determined measurement parameters to minimize the sweep time, a threshold current density for a noticeable device aging on timescales of the sweep

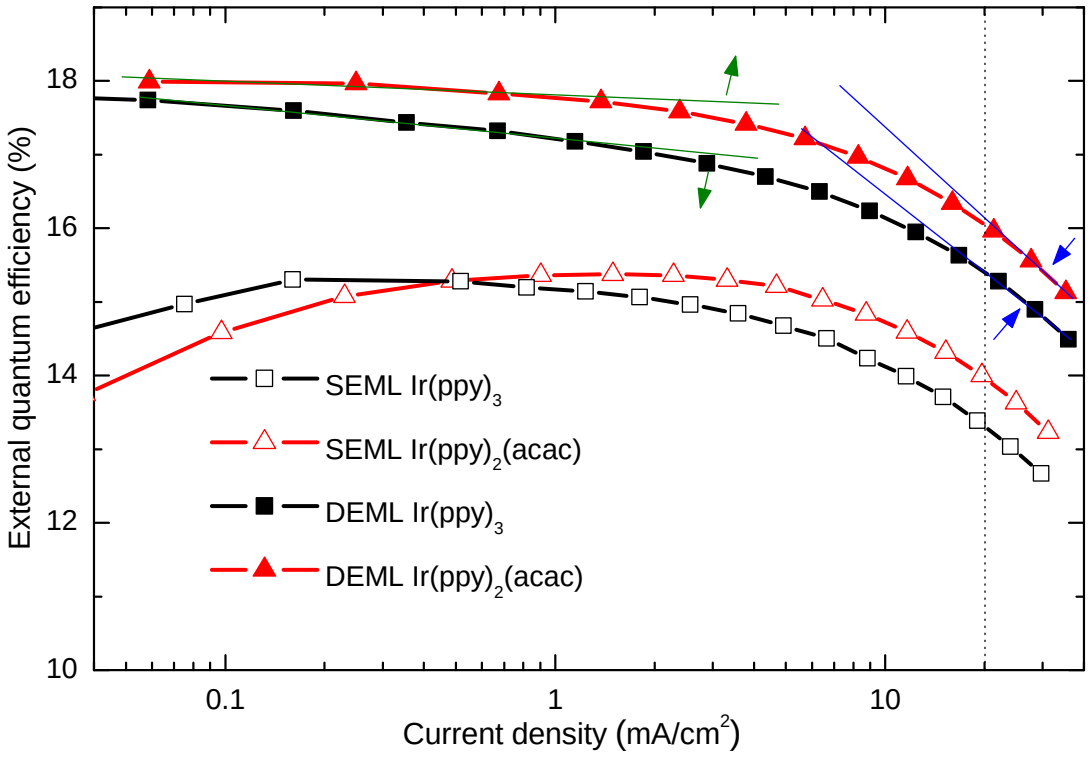

Figure 6.12: External quantum efficiencies of all devices are plotted as a function of current density. The DEML devices yield higher EQE values than the SEML counterparts. Thin lines (green and blue) indicate the differences in the roll-off for the $Ir(ppy)_3$ and $Ir(ppy)_2(acac)$ DEML devices.

(2-5 s) is determined to be:

$$j_{\text{aging}} \geqslant (20 \pm 5)\,\text{mA/cm}^2 \qquad \text{with} \qquad \frac{\eta_{\text{ext},n+1}(j_{\text{aging}})}{\eta_{\text{ext},n}(j_{\text{aging}})} \leqslant 0.98, \tag{6.1}$$

with n representing a counter for consecutive sweeps. This threshold current density j_{aging} is determined for the shorter living emitter material, i.e. $Ir(ppy)_2(acac)$. It is marked by the vertical dashed line in Figure 6.12. It indicates that the stronger roll-off for the $Ir(ppy)_2(acac)$ devices at very high current densities is most likely due to their faster degradation. However, it is not straightforward to deconvolve the EQE data with respect to the device aging, because the error bars in lifetime determination are larger than the expected differences in the efficiency data.

Photoluminescence Transients of the OLEDs

In order to directly determine the difference in TTA for the two emitter materials, the complete OLEDs are investigated in a time-resolved photoluminescence experiment. Therefore, the complete devices are excited with a pulsed, high-intensity laser with 337.1 nm. The active area is covered with a black shadow mask to realize a defined excitation area. Because the Ir-emitters with excited state lifetimes in the microsecond

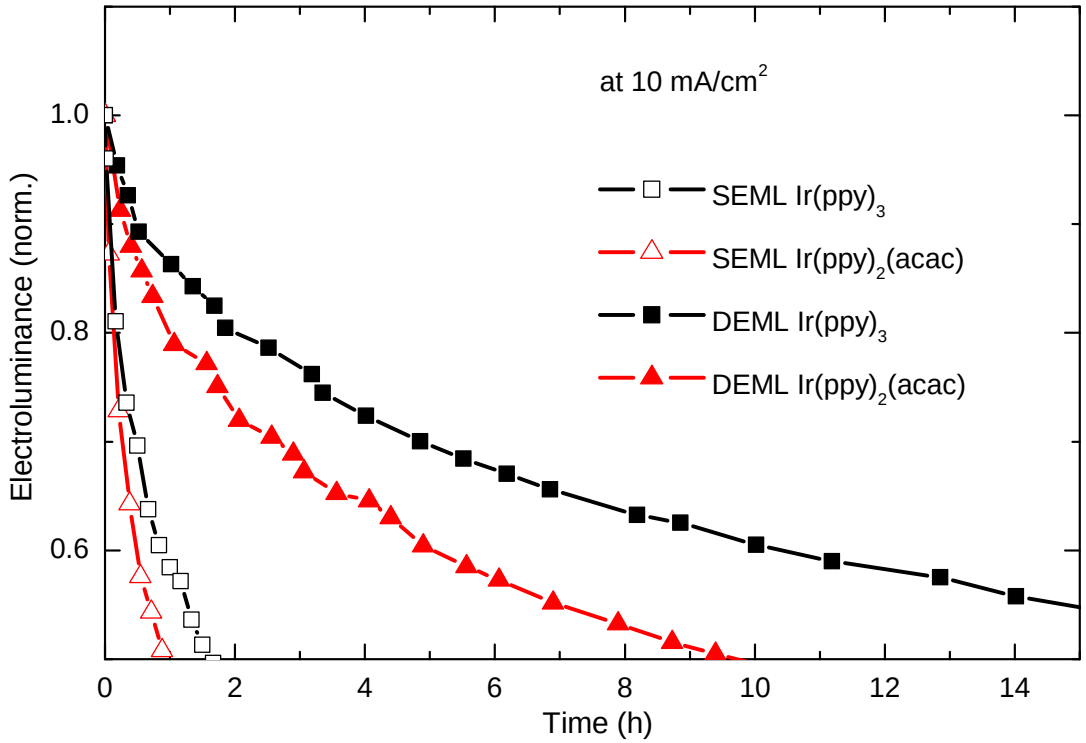

Figure 6.13: Device lifetime data down to 0.5 initial intensity of all devices, measured at a constant current density of $j = 10\,\mathrm{mA/cm^2}$. This corresponds to high brightness values in the range of 5,000–7,000 $\mathrm{cd/m^2}$. The homoleptic $\mathrm{Ir(ppy)_3}$ shows a higher device stability for both SEML and DEML architecture.

range show the longest radiative lifetime τ in the layer stack, all other contributions from emitting layers do not influence the recorded signal. For this experiment, the SEML devices of the corresponding emitter are chosen, because they solely comprise TCTA as matrix material, which has good exciton confining properties due to its high triplet level of 2.83 eV. Thus, in a PL experiment, a monoexponential decay at low excitation levels can be expected, which is essential for later fit calculations. In contrast, TPBi in the DEML devices has a triplet level of 2.6 eV, similar to CBP for which a long-living component was observed in Chapter 5. Furthermore, possible energy transfers between the two sub EMLs of the DEML devices can be excluded.

As mentioned before, an excitation laser pulse with a high pulse energy (30 µJ) is chosen to have a strong TTA contribution that can be reliably analyzed. Furthermore, it compensates excitation losses at the glass substrate (reflection and absorption) and at other organic layers. The geometry of the set-up and the optical environment (which is given by the identical organic layer stack) are kept identical for both emitters. The PL transients of the SEML devices are plotted in Figure 6.14. Both devices yield comparable initial intensities. In the inset, with the transients being plotted in double linear scale, the stronger TTA contribution is observed for the $\mathrm{Ir(ppy)_3}$ device, as it reveals a stronger curvature. From the EQE data of Figure 6.12, the phosphorescence quantum yield Φ_P of both emitters can be assumed to be similar.

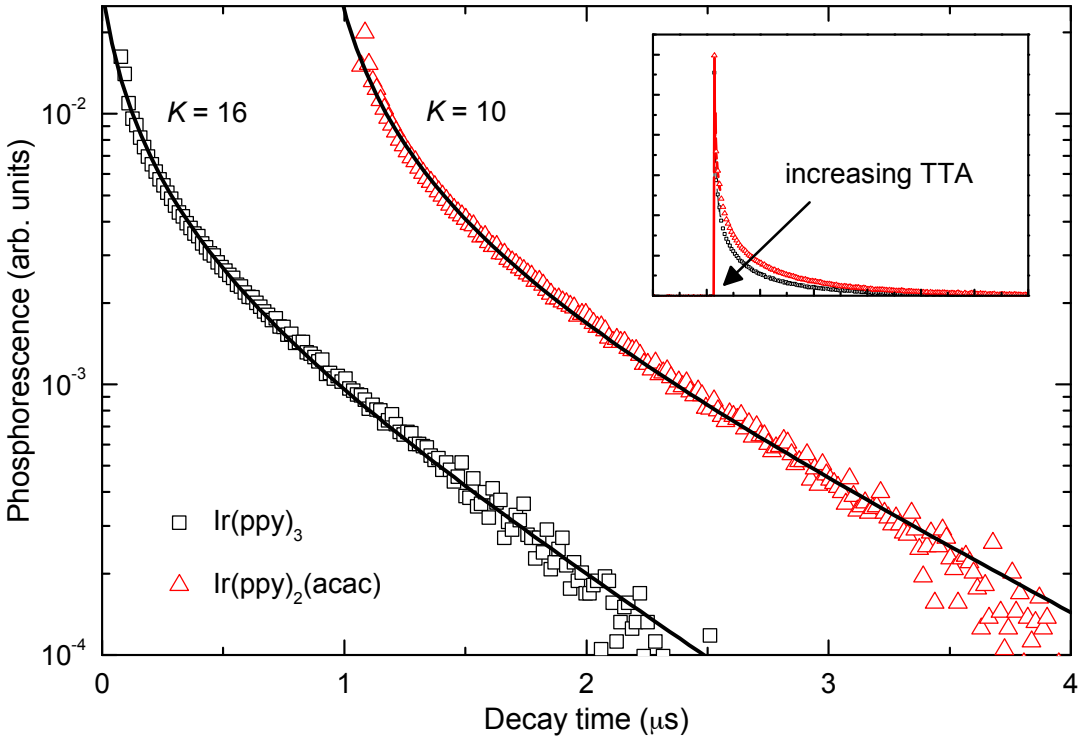

Figure 6.14: PL decay curves of both SEML devices after excitation with a strong pulsed laser (337.1 nm nitrogen laser with 1.3 ns duration). The data are split in time (1 µs) for better visibility. Additionally, calculated fits according to the diffusion based TTA model (Eq. (3.70)) are plotted together with the fit parameter K. Inset: The same data plotted in double linear scale. The arrow indicates increasing TTA contribution.

With these facts it is possible to derive that the exciton density created upon laser absorption $n_0 = n(t = 0)$ is equal for both devices.

Equation (3.70) is used to calculate fits of the PL transients displayed in Figure 6.14 with two free fit parameters: τ and K. The latter is defined as:

$$K = \frac{1}{2} n_0 k_{\mathrm{TT}}. \tag{6.2}$$

The excited state lifetime τ is derived from the monoexponential decay of the long-living transient tail, so that K remains as only free parameter, accounting for the TTA contribution.

For the following discussion, the subscripts 'Ir3' and 'Ir2' are introduced for $\mathrm{Ir(ppy)_3}$ and $\mathrm{Ir(ppy)_2(acac)}$, respectively. The resulting values of the calculated fits are summarized in Table 6.1. Because of the complex multilayer system of the OLED devices, it is not feasible to calculate the absolute value of n_0 and, consequently, no absolute value of k_{TT} can be determined. However, because it is valid to set $n_{0,\mathrm{Ir3}} = n_{0,\mathrm{Ir2}}$, the relative strength of TTA can be calculated to: $k_{\mathrm{TT,Ir2}} = 0.625 \cdot k_{\mathrm{TT,Ir3}}$. Thus, TTA is reduced by approximately 40 % for the heteroleptic emitter $\mathrm{Ir(ppy)_2(acac)}$ [26].

fit parameter	$Ir(ppy)_3$	$Ir(ppy)_2(acac)$	ratio (Ir3/Ir2)
τ (ns)	730	930	0.79
K (s^{-1})	16	10	1.60

Table 6.1: Fit parameters of the SEML device PL transients, as displayed in Figure 6.14. For both parameters, their respective ratio between the $Ir(ppy)_3$ and $Ir(ppy)_2(acac)$ value is determined in the last column.

On the other hand, the radiative lifetime is shorter for the $Ir(ppy)_3$ ($\tau = 730\,ns$), compared to 930 ns of the $Ir(ppy)_2(acac)$ device. Here, the roll-off is reduced for shorter lifetimes [20]. The absolute values of the lifetime τ are shorter because the emission takes place in an optical resonator that increases the decay rate [174, 175]. Overall, the reduced triplet-triplet annihilation for $Ir(ppy)_2(acac)$, represented by the rate constant k_{TT} weights more than the detrimental increase in its excited state lifetime τ. The inset of Figure 6.14 plots the transient signal in a linear scale. Here, the time integral of the phosphorescence is larger for $Ir(ppy)_2(acac)$ system, indicating a higher emission efficiency at that excitation level.

These changes between the two systems in the PL transients, and correspondingly in the strength of TTA, are small compared to the difference in strength of TTA, as predicted by the single-step long range model. Referring to Figure 6.2, similar transients could only be fitted with a value of R_F that by far exceeds the upper limit determined to $R_F = 6\,nm$. Hence, the observed differences cannot be explained by a change in R_F for the two emitters. However, because distinct differences in the ground state extinction coefficients for $Ir(ppy)_3$ and $Ir(ppy)_2(acac)$ are observed [58, 138, 140, 173], it is reasonable to assume that these emitters are accompanied with different spectral overlap of their triplet emission and excited state absorption [83]. Therefore, if diffusion based TTA for the present emitters could be completely suppressed, differences in TTA due to the single-step mechanism would still be possible.

Reduced Aggregation for $Ir(ppy)_2(acac)$

Because the emission layers for the different emitters are completely identical, involving the same thickness, doping concentration, matrix material, and surrounding optical environment, the differences in triplet-triplet annihilation should be an intrinsic property of the mixed EMLs. Furthermore, these differences can only be induced by the emitter itself. The discussion of Section 6.2 showed that these iridium complexes have a strong tendency to form emitter aggregates.

Hence, it is reasonable to assume that both emitters, $Ir(ppy)_3$ and $Ir(ppy)_2(acac)$, show differences in the cluster formation during film preparation. Neither of these complexes are charged, so that a Coulomb coupling of these molecules, leading to such clusters, can only be induced by their respective dipole moment. Park *et al.* carried out density functional theory calculations (B3LYP) of the molecular ground state of both emitters [169]. The dipole moments derived from their calculations are

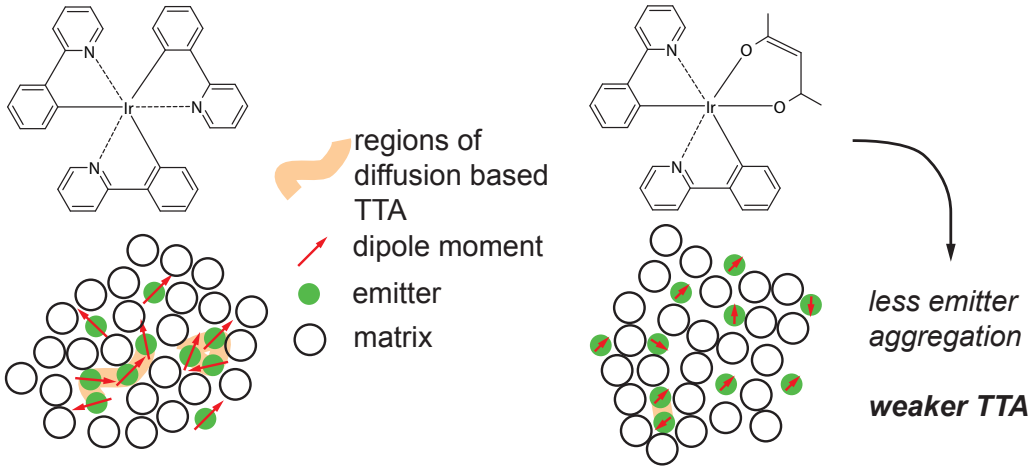

Figure 6.15: Scheme illustrating the proposed influence of the molecular ground state dipole moment on the emitter aggregation in the mixed film. The dipole moments of $Ir(ppy)_3$ and $Ir(ppy)_2(acac)$ are 6.26 and 1.91 D (debye), respectively, as calculated using density functional theory [169]. The larger dipole moment of $Ir(ppy)_3$ increases aggregate formation, resulting in locally densely packed emitter clusters in which diffusion based TTA can occur.

6.26 D (debye) and 1.91 D for $Ir(ppy)_3$ and $Ir(ppy)_2(acac)$, respectively.

A scheme of the proposed microscopic arrangement is given in Figure 6.15. The strongly reduced dipole moment of $Ir(ppy)_2(acac)$ (only 31 % of the $Ir(ppy)_3$ value) leads to a weaker coupling of individual molecules due to Coulomb attraction [26]. On the other hand, this coupling is more effective for $Ir(ppy)_3$, leading to locally dense emitter regions. These regions provide the only efficient channel for diffusion based TTA, i.e. triplet exciton migration between emitter molecules in such clusters. Other diffusion is efficiently suppressed by the choice of the matrix material TCTA that has a very high triplet level of 2.83 eV, so that excitons can not hop on host sites. Consequently, TTA is stronger for the $Ir(ppy)_3$ emitter because it shows a higher degree of aggregation as a result of a comparably high dipole moment.

In order to give further evidence for this interpretation, the luminescent properties of both emitters will be analysed in detail in the following. A general feature of emitter aggregation is the spectral broadening of the luminescence, which has been reported for fluorescent [176] and phosphorescent [79, 158] emitters. Therefore, highly diluted toluene:emitter solutions with a concentration of approximately 6.5×10^{-3} mg/ml for each emitter are prepared to have the majority of the molecules in an isolated form. The photoluminescence spectra of these solutions, in addition to the EL spectra of the DEML devices, are plotted in Figure 6.11 b). In solution, the FWHM of $Ir(ppy)_3$ and $Ir(ppy)_2(acac)$ are 69 nm and 66 nm, respectively. For $Ir(ppy)_2(acac)$, the FWHM remains unchanged at 66 nm for the transition from solution to the solid mixed film emission of the OLED. In contrast, a spectral broadening is observed for $Ir(ppy)_3$. Here, the FWHM shows an increase of 5 nm to 74 nm (cf. Fig. 6.11 b)). The broadening of the $Ir(ppy)_3$ emission agrees with the spectral development of Samples 6.2-1, -2,

and -3 of Section 6.2, where the $Ir(ppy)_3$ concentration was varied in a solid matrix. There, the FWHM of the phosphorescence steadily increased to higher concentrations in a similar fashion. Note, that the absolute FWHM values of the spectra shown in Section 6.2 are systematically smaller than the results presented here, due to the use of different spectrometers. In Section 6.2, a compact fibre spectrometer (USB2000) is used without a correction file leading to an underestimation of the red spectral region.

The consistency of the calculated dipole moment, being much larger for $Ir(ppy)_3$, and the observed spectral broadening which is only seen for $Ir(ppy)_3$ strongly supports the proposed microscopic arrangement of the emitters in the mixed film. As it is one of the easiest ways to obtain an improved OLED roll-off by switching to another emitter molecule with superior high brightness properties, these results provide new design strategies for future emitter engineering. By taking the emitter dipole moment into consideration at the stage of material synthesis, phosphorescent emitter molecules can be developed to close the gap to the single-step long range limit.

6.5 Aggregation in Other Emitter Systems

In the preceding sections, a detailed investigation of triplet-triplet annihilation in organic phosphorescent systems comprising $Ir(ppy)_3$ – the archetype phosphorescent compound of present literature – was presented. However, one might argue that all the results, especially the emitter aggregation, are specifically related to $Ir(ppy)_3$ with weak general importance. Therefore, this brief section is intended to give examples of the universality of this problem.

The Red Emitter $Ir(MDQ)_2(acac)$

Similar to the sample series of Section 6.2, three samples of the orange emitting phosphorescent EML comprising $Ir(MDQ)_2(acac)$ are prepared with different emitter concentrations.

Sample 6.5-1: NPB:$Ir(MDQ)_2(acac)$ (20 nm, 0.5 wt%)

Sample 6.5-2: NPB:$Ir(MDQ)_2(acac)$ (20 nm, 2 wt%)

Sample 6.5-3: NPB:$Ir(MDQ)_2(acac)$ (20 nm, 20 wt%)

The photoluminescence of these samples are plotted in Figure 6.16. In a), their normalized spectra are shown. With increasing emitter concentration, a red-shift of the peak wavelength is observed, similar to the results of $Ir(ppy)_3$. Figure 6.16 b) plots the phosphorescence spectra normalized with respect to the corresponding peak wavelength. Even though the differences are smaller than observed for $Ir(ppy)_3$, a continuous spectral broadening of the emission is observed with increasing $Ir(MDQ)_2(acac)$ concentration. Hence, $Ir(MDQ)_2(acac)$ molecules presumably form aggregates in the mixed film in a similar fashion.

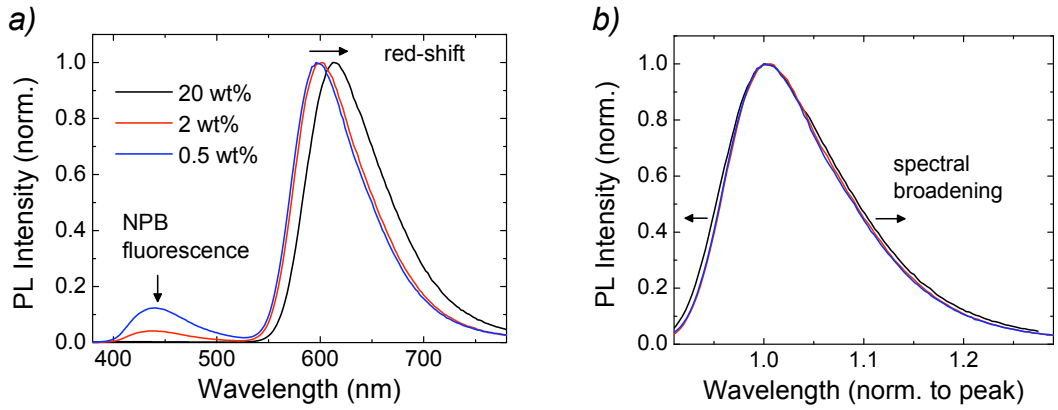

Figure 6.16: Photoluminescence spectra of NPB:Ir(MDQ)$_2$(acac) mixed films with different emitter concentrations. a) Normalized spectra. b) PL spectra from a) normalized to the peak intensity (y-axis) and, additionally, to the peak wavelength (x-axis) to compare the spectral shape. Arrows indicate increasing emitter concentration.

In the report of Meerheim *et al.*, various OLEDs comprising Ir(MDQ)$_2$(acac) as emitter were discussed, mainly with respect to optimize the EQE, which reached very high values up to 20 % EQE [42]. However, the critical current density j_c for such devices only yield approximately 60-70 mA/cm^2, which is even lower than the data determined for Ir(ppy)$_3$ in Section 6.3. Note that j_c can be directly determined from the experimental data for Ir(MDQ)$_2$(acac)-based systems, because OLEDs comprising this emitter are highly stable (up to 1,000 h lifetime at a brightness of 10,000 cd/m^2) [42]. The excited lifetime of Ir(MDQ)$_2$(acac) with $\tau = 1.4\,\mu s$ is similar to the values of Ir(ppy)$_3$ [27]. Assuming that the photophysical properties (especially the oscillator strength of the molecular transitions) of these Ir(III) complexes do not differ by orders of magnitude [79], it is reasonable to conclude that the single-step long range limit for j_c should be in the same range as predicted for Ir(ppy)$_3$, i.e. $\sim 1\,A/cm^2$. This suggests that diffusion based TTA is an issue for Ir(MDQ)$_2$(acac) as well. The triplet levels of the EML materials (NPB and Ir(MDQ)$_2$(acac)) of the OLEDs in Reference [42] are 2.3 and 2.0 eV, respectively, so that exciton confinement should be given similar to TCTA:Ir(ppy)$_3$. Hence, emitter aggregation in the mixed film, opening the channel for diffusive TTA, is expected to be present.

The Blue Emitter FIrpic

Within this work, no experiments to investigate a possible aggregation of FIrpic in a solid state matrix are carried out, however, the data in literature suggest that this blue emitter suffers from the same effect as Ir(ppy)$_3$. Kawamura *et al.* prepared mixed films of FIrpic doped into CBP at various concentrations up to 50 mol% emitter content [78]. Similar to Ir(ppy)$_3$ and Ir(MDQ)$_2$(acac), they observed both a red-shift of the emission peak and a transition to a broader, featureless spectrum at high concentration.

In a very recent publication of Su *et al.*, FIrpic was used to realize highly efficient blue and white phosphorescent OLEDs [39]. Their devices, utilizing a carrier- and exciton-confining structure, were optimized to reduce the efficiency roll-off and reach remarkably high values of 25 % EQE at 1,000 $\mathrm{cd/m^2}$. Still, for the monochrome blue OLED they only obtained a critical current density of $j_\mathrm{c} = 82\,\mathrm{mA/cm^2}$. However, the authors did not discuss the influence of device aging during the sweep, which should in general be an issue for the low-stability FIrpic. Again, similar to the discussion of the roll-off data of the $\mathrm{Ir(MDQ)_2(acac)}$ OLEDs, this value suggests that the device is far away from its single-step limit, where aggregation is the most evident reason for strong TTA.

Summary

For Ir(III) complexes, being the phosphorescent emitter class with highest potential to date, the formation of aggregates in the mixed film seems to be a general feature. This property is detrimental for the high brightness performance of OLEDs, because it opens the door for unwanted, but very efficient diffusion based triplet-triplet annihilation. In this respect, these emitters still bear great potential for improvement of their efficiency at very high brightness. Therefore, among lifetime and colour quality issues, pushing the efficiency roll-off of phosphorescent OLEDs to even higher luminance levels remains one of the active research fields of state-of-the-art OLEDs.

Chapter 7

White Organic LEDs with Fluorescent Tube Efficiency

One of the main results discussed in Chapter 6 is the strong emitter aggregation. Using a novel emission layer concept, the triplet-triplet annihilation is reduced due to improved exciton confinement by introducing thin interlayers. In this chapter, the sub-structured approach is extended to multicoloured emission layers. The first section of this chapter will address the 'bottom-up' approach. This is followed by a detailed discussion of the final emission layer design for white OLEDs, including a concept of weakly doped blocking layers as a tool to optimize the device efficiency. The discussion of the EML is finished with an analysis of the roll-off of these devices. To further improve the white OLED efficiency, the device stack is adapted to high refractive index substrates, promising a boost in light outcoupling. Finally, by placing the EML in the second field antinode from the cathode, plasmonic losses are suppressed, which leads to an additional increase in efficiency.

7.1 OLEDs with Sub-Structured EMLs Comprising Different Emitters

In Chapter 6, the concept of a sub-structured emission layer was introduced to improve the high brightness performance of monochrome devices comprising the green emitter $Ir(ppy)_3$. The insertion of thin intrinsic layers of the matrix material with a high triplet level resulted in strong exciton confinement on guest sites. Hence, excitons that are located in one specific sub-EML are forced to remain in this thin layer until they ultimately recombine. This leads to a strong reduction of the Dexter-type energy transfer rates between adjacent sub-EMLs.

In the following step, differently emitting phosphorescent molecules in the sub-EMLs are to be incorporated with the goal to achieve white light emission. Figure 7.1 shows a scheme of this concept. It is obvious that the exciton confinement must be given for all emitters, i.e. the triplet level of the host material must be higher

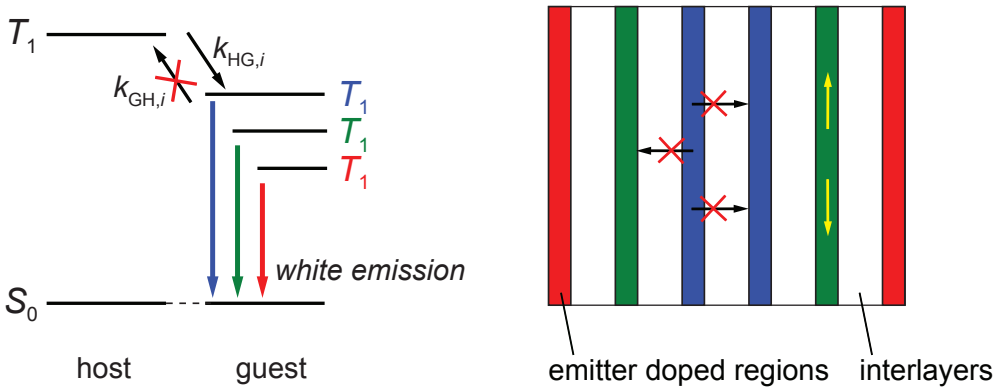

Figure 7.1: The sub-structured concept comprising different phosphorescent emitters to achieve white light emission. To assure that all emitters can efficiently convert the local excitation in the corresponding sub-layer, the confining condition of the host material ($k_{\mathrm{GH},i} = 0$) must be fulfilled for each emitter. Hence, the T_1 level of the host must be higher than the triplet level of the high energy blue emitter.

than all corresponding emitter T_1 levels. Otherwise, there would be a back-transfer rate $k_{\mathrm{GH},i}$ that would prevent the decoupling of the sub-EMLs. In order to obtain simultaneous emission from all phosphors, it is not sufficient to suppress Dexter-type transfers from sub-EML to sub-EML, rather Förster-type transfer rates must also be controlled. Kawamura *et al.* have determined the Förster radius R_{F} for blue, green, and red emitting phosphorescent materials in photoluminescence experiments to be below 2 nm [79]. Even though, in contrast to their work, the Förster-type transfers in the present concept are between different emitters, the values of R_{F} for such transfers will be comparable. At first, this concept will be investigated in photoluminescence experiments.

Prepared Samples

To simplify the notation of the multilayer systems discussed in the following, a convention will be introduced, which is valid throughout this Chapter 7:

- If not stated differently, the emitter concentration is 10 wt %.
- The emitters FIrpic, $\mathrm{Ir(ppy)_3}$ and $\mathrm{Ir(MDQ)_2(acac)}$ are abbreviated B, G, and R, respectively, which will be given in parenthesis for doped layers.
- The thicknesses of the sub-layers are denoted as subscripts in units of nm.
- The interlayer is denoted as 'i' and is made of the matrix material to the left.

Furthermore, the emitter materials will be given in colour. To give an example, a heterostructure like TCTA:$\mathrm{Ir(ppy)_3}$ (4 nm, 10 wt%) / TCTA / TCTA:FIrpic (2 nm, 10 wt%) will be written as: $\mathrm{TCTA_4(G)\ /\ i_2\ /\ TCTA_2(B)}$.

TCTA is chosen as the only available host material with high enough triplet level to confine FIrpic excitons. Here, the energy difference of their T_1 levels is still 0.2 eV (cf. Fig. 3.13). Three samples are prepared with a variation in the interlayer thickness, to check whether the intrinsic interlayers of TCTA can efficiently decouple the different sub-EMLs, leading to a broad spectrum.

Sample 8.1-1: $\mathrm{TCTA_1(R)}$ / $\mathbf{i_2}$ / $\mathrm{TCTA_1(G)}$ / $\mathbf{i_2}$ / $\mathrm{TCTA_1(B)}$ / $\mathbf{i_2}$ / $\mathrm{TCTA_1(B)}$ / $\mathbf{i_2}$ / $\mathrm{TCTA_1(G)}$ / $\mathbf{i_2}$ / $\mathrm{TCTA_1(R)}$

Sample 8.1-2: $\mathrm{TCTA_1(R)}$ / $\mathbf{i_3}$ / $\mathrm{TCTA_1(G)}$ / $\mathbf{i_3}$ / $\mathrm{TCTA_1(B)}$ / $\mathbf{i_3}$ / $\mathrm{TCTA_1(B)}$ / $\mathbf{i_3}$ / $\mathrm{TCTA_1(G)}$ / $\mathbf{i_3}$ / $\mathrm{TCTA_1(R)}$

Sample 8.1-3: $\mathrm{TCTA_1(R)}$ / $\mathbf{i_4}$ / $\mathrm{TCTA_1(G)}$ / $\mathbf{i_4}$ / $\mathrm{TCTA_1(B)}$ / $\mathbf{i_4}$ / $\mathrm{TCTA_1(B)}$ / $\mathbf{i_4}$ / $\mathrm{TCTA_1(G)}$ / $\mathbf{i_4}$ / $\mathrm{TCTA_1(R)}$

Photoluminescence of Multicolour Sub-Structured EMLs

In Figure 7.2, the photoluminescence spectra of the three samples from above are plotted. From bottom to top, the intrinsic TCTA interlayer thickness increases by 1 nm for each spectrum, starting at 2 nm. First of all, the spectral feature at high energies (400 nm) corresponds to the TCTA fluorescence, mostly originating from intrinsic interlayers. In the mixed sub-layers, it will be efficiently quenched due to the high emitter concentration of 10 wt%. Clearly, emission from all emitters is observed, even for the thinnest interlayer thickness of 2 nm. The arrows in Figure 7.2 indicate the corresponding spectral features of the phosphors.

Obviously, the relative intensities of the peaks change under the thickness variation of the interlayer. With decreasing interlayer thickness, the interlayer energy transfers increase, causing these differences. However, the analysis of these changes is highly complex in such a cascading system. Still, the results obtained from these samples are very promising. Down to interlayer thicknesses of 2 nm, it is possible to have simultaneous emission from all three emitters. Therefore, this multicolour sub-structured EML is a promising concept for white organic LEDs.

Integration in Organic LEDs

In photoluminescence experiments, the excitation is nearly constant throughout the layer stack owing to the much longer absorption length in such layers [20]. This picture completely changes for electrical excitation. Here, the exciton generation and recombination takes place in a narrow zone close to an interface between two materials in most of the cases. Therefore, it is still unclear, whether all sub-EMLs with different emitters can be sufficiently electrically excited to produce white light. First attempts to incorporate the multicolour sub-structured EML to an OLED are very similar to the devices of Chapter 6.

Because the general OLED structure beyond the EML does not change from device to device, it is only shown at the beginning. Thus, for the different devices, simply the EML and, if varied, blocking layers are stated.

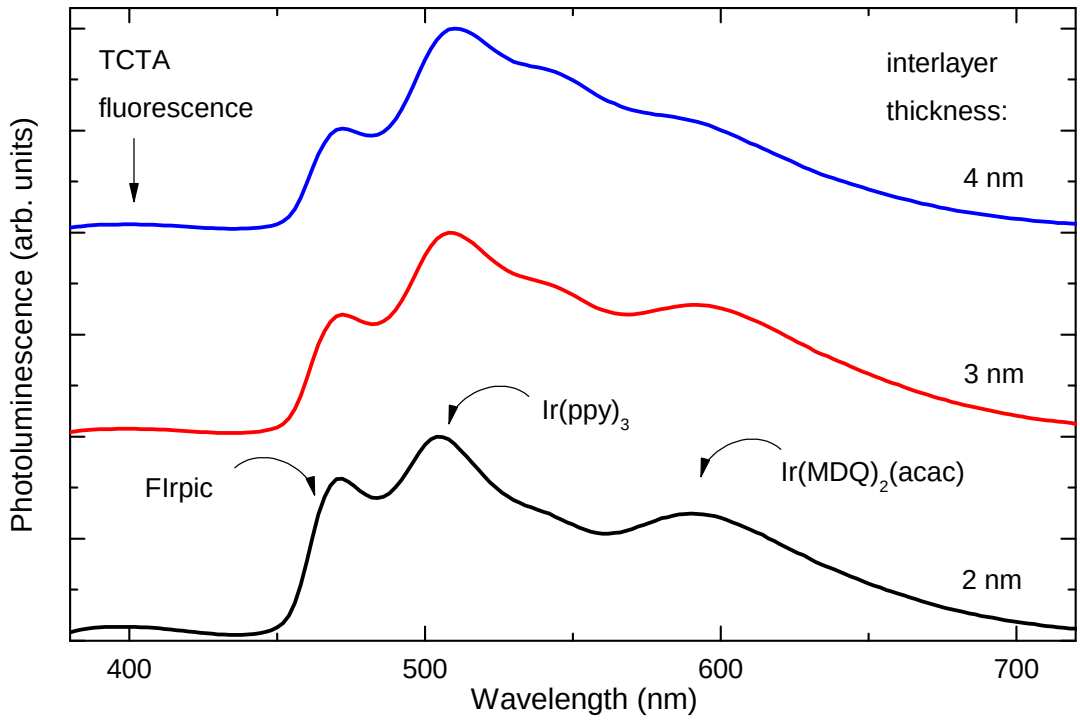

Figure 7.2: Photoluminescence spectra of Samples 8.1-1, -2, and -3 comprising three differently emitting phosphors (one per sub-EML). These samples vary in the TCTA interlayer thickness in between the sub-EMLs. The spectra are vertically split for better visibility. The different peaks in the broad spectrum can clearly be attributed to the emission of FIrpic, $Ir(ppy)_3$, and $Ir(MDQ)_2(acac)$, respectively.

OLED stack: MeO-TPD:F_4-TCNQ (60 nm, 4 wt%) / NPB (10 nm) / **emission layer** / HBL (10 nm) / Bphen:Cs (40 nm) / Al (100 nm)

Device 8.1-4: $TCTA_1$(R) / i_2 / $TCTA_1$(G) / i_2 / $TCTA_1$(B) / i_2 / $TCTA_1$(B) / i_2 / $TCTA_1$(R) / Bphen (HBL)

Device 8.1-5: $TCTA_1$(R) / i_2 / $TCTA_1$(B) / i_2 / $TCTA_1$(B) / $TPBi_2$ / $TPBi_1$(G) / TPBi (HBL)

The layer sequence of Device 8.1-4 is very similar to the PL samples. The only difference is the missing right $Ir(ppy)_3$ doped sub-EML, which is left out to enhance the blue emission in the preferentially hole transporting TCTA matrix. TCTA is known to have a very thin recombination zone close to the HBL [20, 162]. Bphen is chosen as HBL, because the adjacent sub-EML contains the red emitter $Ir(MDQ)_2(acac)$ for which it is the standard blocking material [42]. The overall performance of this device is plotted in Figure 7.4 (black symbols). The device has steep j-V characteristics similar to the green monochrome devices of the previous chapter. It reaches an EQE of nearly 10 % at low brightness. However, by analysing the EL spectrum in Figure 7.4 b), almost pure red emission is observed. FIrpic contributes very weakly

to the spectrum, despite the fact that the first blue sub-EML is only 3 nm separated from the HBL interface, where the generation occurs. This provides an interesting result for the discussion of Section 6.3, dealing with the recombination zone in the sub-structured EML device. It gives further evidence that the recombination zone w in the sub-structure device is comparable to the reference structure. However, it represents a significant drawback for achieving white light emission.

Device 8.1-5 is prepared to improve the balance between all emitters. Here, TPBi is used as a standard HBL for $Ir(ppy)_3$ – the outermost emitter in this device. TPBi is introduced as second matrix material to slightly extend the recombination zone, similar to the DEML approach [170], with the difference that the overall TPBi layer is very thin (3 nm). The OLED data are given in Figure 7.4. The device even shows slightly lower voltages compared to Device 8.1-4. Similar improvements were discussed in Section 6.2 for monochrome DEML OLEDs. The external quantum efficiency reaches approximately 13 % EQE at 100 cd/m^2 – much more than for Device 8.1-4. However, no real improvement with respect to a balanced multicolour spectrum is obtained. In this device, the main emission stems from $Ir(ppy)_3$, showing slight shoulders to the left (FIrpic) and right ($Ir(MDQ)_2(acac)$). Hence, further broadening of the recombination zone is required in order to realize a white OLED based on the sub-structured EML concept.

Sub-Structured Double Emission Layer OLEDs

The results of Device 8.1-5 show that an EML with a thin, additional second matrix material can produce emission from all emitters, despite the fact that their relative emission intensities are not sufficiently balanced for white emission. Therefore, the concept of double emission layers is followed to further broaden the recombination zone in order to achieve white emission. These experiments are based on a TCTA/TPBi DEML matrix combination [170]. In addition to the following layer sequences, the sub-structured EMLs are schematically shown in Figure 7.3.

OLED stack: MeO-TPD:F_4-TCNQ (60 nm, 4 wt%) / NPB (10 nm) / **emission layer** / HBL (10 nm) / Bphen:Cs (40 nm) / Al (100 nm)

Device 8.1-6: $TCTA_1$(R) / i_2 / $TCTA_1$(G) / i_2 / $TCTA_1$(B) / i_2 / $TCTA_1$(B) / $TPBi_1$(B) / i_2 / $TPBi_1$(B) / i_2 / $TPBi_1$(G) / i_2 / $TPBi_1$(R) / Bphen (HBL)

Device 8.1-7: $TCTA_1$(R) / i_2 / $TCTA_1$(G) / i_2 / $TCTA_1$(B) / i_2 / $TCTA_1$(B) / $TPBi_1$(B) / i_2 / $TPBi_1$(B) / i_2 / $TPBi_1$(R) / i_2 / $TPBi_1$(R) / Bphen (HBL)

Device 8.1-8: $TCTA_3$(R) / i_2 / $TCTA_1$(G) / i_2 / $TCTA_1$(B) / $TPBi_1$(B) / i_2 / $TPBi_1$(R) / i_2 / $TPBi_3$(R) / TPBi (HBL)

Device 8.1-9: $TPBi_2$(B) / i_2 / $TPBi_1$(R) / i_2 / $TPBi_1$(G) / i_2 / $TPBi_3$(R) / TPBi (HBL)

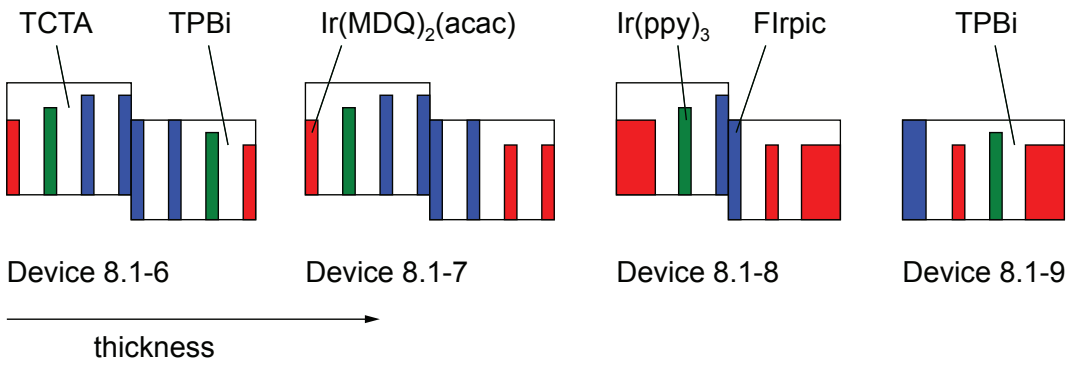

Figure 7.3: Layer design of the sub-structured EMLs of Devices 8.1-6 to 8.1-9. The offset between TCTA and TPBi illustrates the HOMO and LUMO offset, characteristic for a DEML. The thicknesses are according to the layer sequence given in the text. The relative heights of the emitters correspond to their triplet energy.

The first device (Device 8.1-6) has a completely symmetric EML, i.e. both matrices contain four sub-EMLs with one red, one green, and two blue layers. The blue sub-EMLs are located at the TCTA/TPBi interface to reduce losses of FIrpic to the blocking materials that have lower triplet levels (cf. Fig. 3.13). The EL spectrum of this device is plotted in Figure 7.4 b). Emissions from both FIrpic and $Ir(ppy)_3$ are observed, however only a very weak shoulder at 600 nm can be attributed to the red emission from $Ir(MDQ)_2(acac)$. This is plausible, because the red sub-EMLs are the outermost ones in the DEML structure – far away from the interface of exciton generation (TCTA/TPBi). Therefore, in Device 8.1-7, the green sub-EML in the TPBi matrix is exchanged by an additional red sub-EML (cf. Fig. 7.3). The EL spectrum of this device is shown in Figure 7.4 b). In contrast to the previous Device 8.1-6, an increased red emission is observed while at the same time the green emission drops to a negligible level. The comparison of these two devices leads to a very important conclusion: In the hole transporting EML part containing TCTA as matrix, only noticeable blue emission is generated, because already the green sub-EML in Device 8.1-7 does not emit sufficiently. Hence, it will be very problematic to address different emitters on the TCTA side of the EML.

An additional device is prepared to determine the number of sub-EMLs in the TCTA system that can be excited electrically. In Device 8.1-8, one of the two blue sub-EMLs in both DEML parts is removed, so that the general distribution of the emitters is similar to Device 8.1-7. Still, the EL spectrum of this device does not show a distinct emission from the green emitter $Ir(ppy)_3$. In general it is not easy to quantify an $Ir(ppy)_3$ emission in such spectra, because its main emission peak coincides with the shoulder of the FIrpic emission caused by its vibronic progression. However, the lower intensity of the peak at 510 nm compared to the main peak of FIrpic suggests that the green emission is very weak. Hence, emission from the second sub-EML (seen from the TCTA/TPBi interface) in the TCTA system is hardly visible.

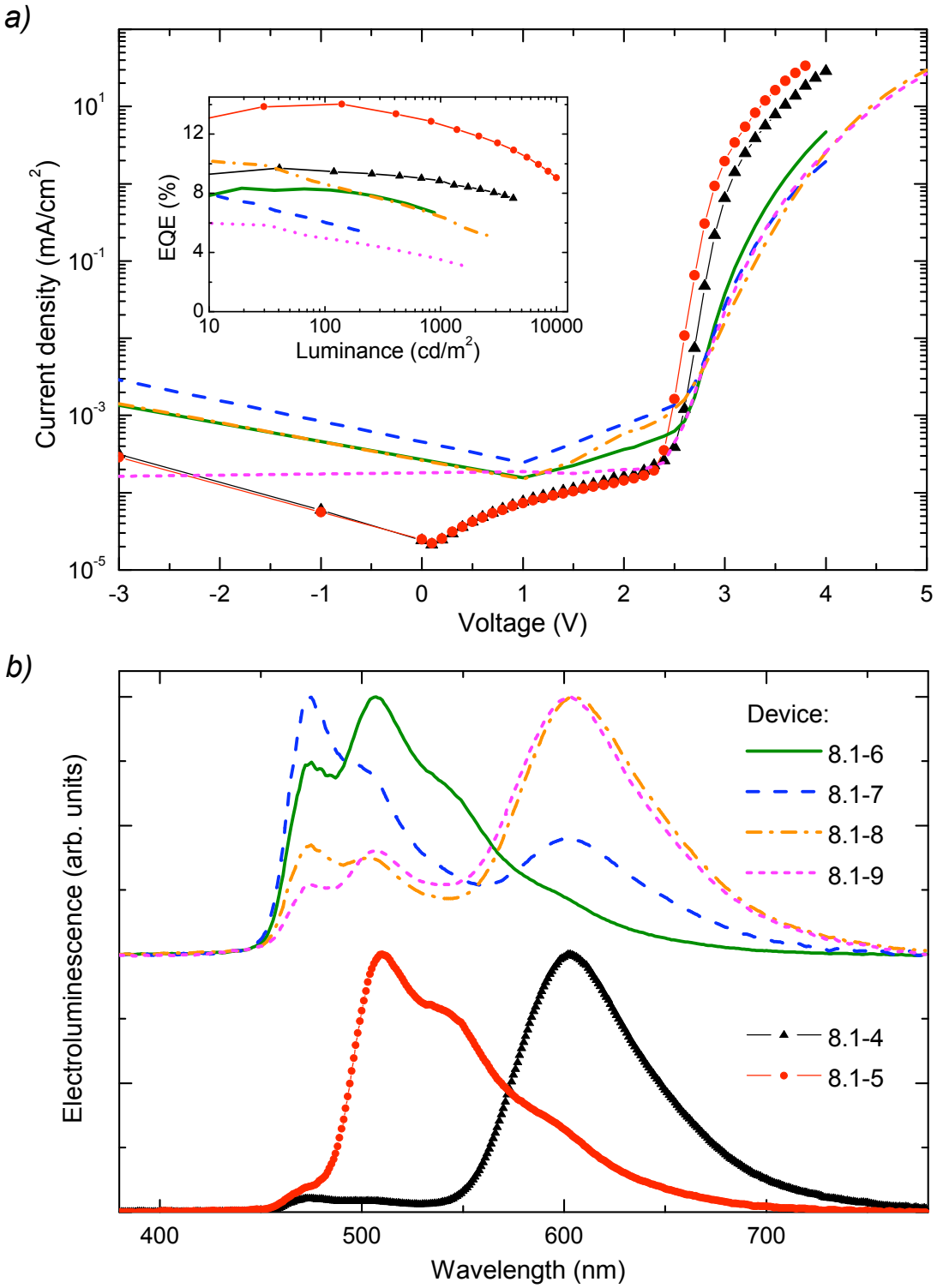

Figure 7.4: Overall performance of Devices 8.1-4 to 8.1-9. a) Current density-voltage characteristics. Inset shows the EQE of all devices as a function of luminance. b) Electroluminescence spectra of all devices. For better visibility, two groups of devices are split vertically.

On the other hand, the balance between the blue and red emission strongly changes from Device 8.1-7 to 8.1-8, which indicates that more than one sub-EML in the TPBi system contributes to the light emission. Here, the red emission is strongly increased because the corresponding red sub-EML moved much closer to the generating interface. To further confirm this result, a last device of this series (Device 8.1-9) is prepared that only comprises TPBi as matrix material (cf. Fig. 7.3). From left to right, the colour sequence of the sub-EMLs is blue–red–green–red. Compared to the previous device, the EL spectrum shows minor but important changes. Here, for the first time, the peak at 510 nm, corresponding to the $Ir(ppy)_3$ emission, is higher in intensity compared to the blue FIrpic peak at roughly 475 nm. This clearly indicates that at least 3 sub-EMLs can be addressed using a TPBi matrix.

Electrical Performance

The discussion of the electrical characteristics and efficiency of Devices 8.1-6 to 8.1-9 was left out up to this point, because the comparison of all prepared devices leads to a better picture. In Figure 7.4 a), the current density of all discussed devices is plotted versus the operating voltage. Interestingly, in can be clearly differentiated between two groups of data. While the first two devices (Devices 8.1-4 and -5) show steep j-V-characteristics, the remaining four devices all have similar flat slopes. This suggests that an additional energy barrier must be present in these devices.

The same trend is observed in the device efficiencies. The EQE of all devices is plotted in the inset of Figure 7.4 a). Again, the Devices 8.1-6 to 8.1-9 show noticeably lower EQEs – none of them surpasses 10 % EQE at reasonably high brightness. Moreover, all of them show an unexpectedly strong efficiency roll-off. It is apparent from these observations that at least one specific material combination in the complex multilayer system causes these problems. By carefully comparing the architectures from Device 8.1-4 to 8.1-9, the only consistent difference between the two groups of devices is the red TBPI:$Ir(MDQ)_2(acac)$ system. Only Devices 8.1-6 to 8.1-9, which show this poor performance in j-V and EQE data, utilize this combination. In these devices, the HBL is additionally altered from Bphen to TPBi to check if one of these materials cause the problems but, referring to Figure 7.4, the data (mainly the j-V characteristics) remained unchanged under this variation.

Furthermore, referring to the EML design of Devices 8.1-8 and -9, the outermost sub-EMLs adjacent to the respective blocking layer have increased thickness in order to rule out strong losses of excitons to the blocking layers. These might occur if the excitons generated are not sufficiently harvested in the thin sub-EMLs, thus, a fraction of the excitons might diffusively pass the sub-EMLs ultimately reaching the non-emissive blocking layers. However, the data of Figure 7.4 a) show that this does not necessarily improve the EQE of these devices. Thus, losses to the blockers can be ruled out for the low EQE of Devices 8.1-6 to 8.1-9.

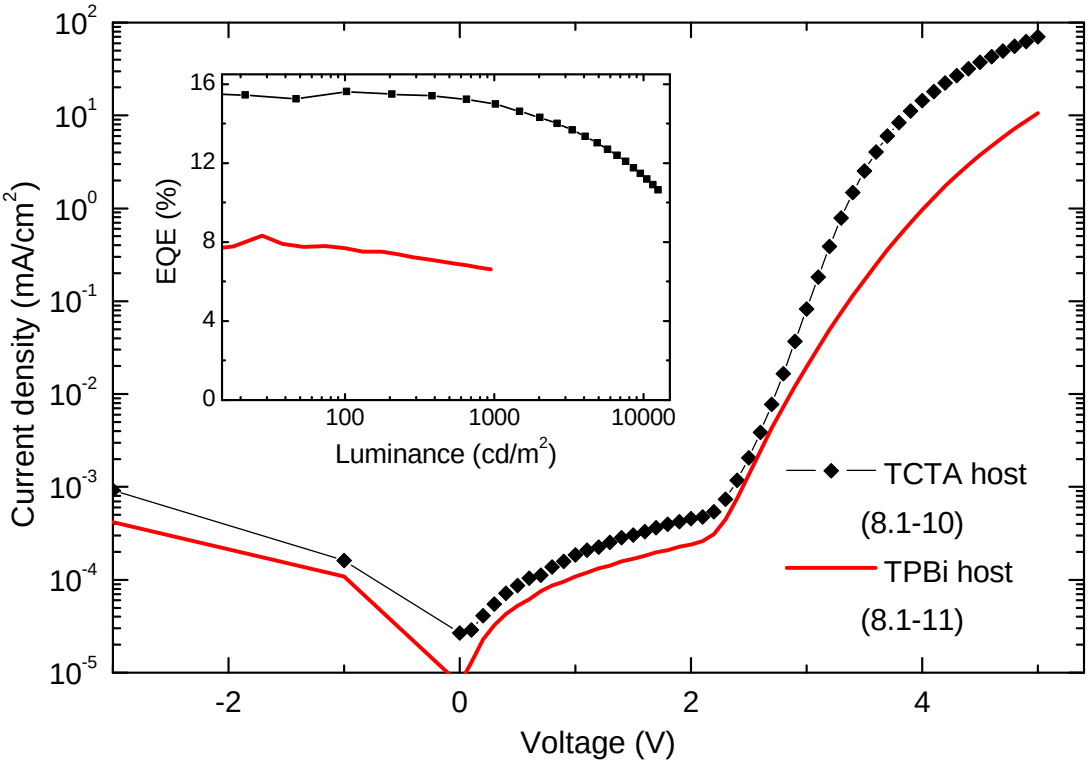

Figure 7.5: Current density-voltage characteristics of Devices 8.1-10 and -11. They comprise the red emitter $Ir(MDQ)_2(acac)$ and either TCTA or TPBi is used as matrix. Inset: EQE of both devices as a function of luminance.

Monochrome OLEDs Comprising $Ir(MDQ)_2(acac)$

The data from above suggests that the combination of TPBI and $Ir(MDQ)_2(acac)$ triggers losses in the OLED. Two red OLEDs are prepared to obtain direct evidence for this effect. Here, Bphen is used as HBL to exclude similar effects at the TCTA:$Ir(MDQ)_2(acac)$/HBL interface, when using TPBi as blocker.

Device 8.1-10: MeO-TPD:F_4-TCNQ (50 nm, 4 wt%) / NPB (10 nm) / **TCTA**: $Ir(MDQ)_2(acac)$ (20 nm, 10 wt%) / Bphen (10 nm) / Bphen:Cs (55 nm) / Al (100 nm)

Device 8.1-11: MeO-TPD:F_4-TCNQ (50 nm, 4 wt%) / NPB (10 nm) / **TPBi**: $Ir(MDQ)_2(acac)$ (20 nm, 10 wt%) / Bphen (10 nm) / Bphen:Cs (55 nm) / Al (100 nm)

The performance data of these two red OLEDs (Devices 8.1-10 and -11) are plotted in Figure 7.5 and its inset. As previously seen, the same differences in the j-V characteristics are observed: When comprising TPBi as matrix material, the slope is much flatter than the reference TCTA-based OLED. The external quantum efficiencies of these two devices are shown in the inset of Figure 7.5. Here, a dramatic change in the efficiency is observed. While the OLED with the TCTA matrix nearly reaches

16 % EQE, the values are roughly cut to half for the TPBi:Ir(MDQ)$_2$(acac) system. Apparently, this combination does not only worsen the electrical behaviour, but also introduces a severe loss channel for the excited states formed on Ir(MDQ)$_2$(acac) sites.

In a recent study, Meerheim *et al.* investigated red OLEDs based on this Ir(MDQ)$_2$(acac) emitter under a variation of the HBL material with respect to their efficiency and device stability [42]. Chemical analysis of the aged materials showed a complexation between TPBi and Ir(MDQ)$_2$(acac) that accelerated the device degradation. It is most likely that such complexes are already formed during device fabrication in the present devices, which then form trap states and/or quenching sites within the EML. This effect occurs because such large complexes will have a reduced energy gap [177]. Here, in contrast to the work of Meerheim *et al.*, the overall effect of such complexation is much more pronounced, because the emitter is diluted in the TPBi matrix. Thus, the amount of emitter material that is in direct contact to TPBi molecules is strongly increased.

Conclusion

The results of this section show that the realization of multicoloured emission from a sub-structured EML is difficult to achieve, mainly due to the very thin exciton generation zones under EL operation. Using the available matrix materials, particularly TCTA, it is already an obstacle to obtain emission from as few as two independent sub-EMLs. Furthermore, the data show that the red emitter Ir(MDQ)$_2$(acac) can not be used efficiently in combination with TPBi, which severely limits the design freedom of the sub-structured EML.

In summary, the concept of white emission from a sub-structured EML can only be used in OLEDs if a broad exciton generation can be realized, which is not the case for the present material combinations. It requires an ambipolar matrix material which can produce sufficient exciton generation, spanning at least three independent sub-EMLs (for red, green and blue). An artificial way to realize such ambipolarity is the use of mixed host materials, similar to the work of Schwartz *et al.* using a combination of TCTA:TPBi to realize an ambipolar interlayer in hybrid white OLEDs [37].

7.2 Energy Efficient White OLEDs

Despite the fact that the sub-structured emission layer concept could not be transferred to multicoloured/white electroluminescence in a reasonable way, it can still be used as a good starting point for the design of efficient white OLEDs. It is mainly the concept of the intrinsic interlayers between differently emitting sub-EMLs that will be used here to manage the exciton distribution within the EML to achieve balanced white light. The sub-structuring of the sub-EMLs, however, is not further applied, because it is regarded to be detrimental for both the colour tuning and the device processibility.

Before discussing the emission layer concept and all steps of device optimization, a few words will be given to specify the targeted emission spectrum. In the Commission Internationale d' Eclairage (CIE) colour space, two important white colour points are known: (1) the point of equal energy with CIE coordinates of (0.33, 0.33) and (2) the warm-white CIE Standard Illuminant A with (0.448, 0.408) [60]. These points are located on the *Planckian locus*, which marks *Planckian radiators* of different colour temperature within the CIE diagram. The white OLEDs of this work will be designed to emit in the range of the Standard Illuminant A, because warm-white light is preferred for general illumination. To obtain such emission from three basic blue, green and red emitters, their intensities shall have a staircase-like relation from blue to red [178]. At least this is valid for emitters whose spectra can be roughly approximated by a Gaussian shape. The colour quality of the realized white OLEDs will be addressed later in this section in the discussion of the final white device.

The Emission Layer Design

A scheme of the final EML design is depicted in Figure 7.6. At this stage, the different functionality of the various sublayers will be discussed. According to the previous section, the red emitter $Ir(MDQ)_2(acac)$ does not work well with the electron transporting matrix material TPBi. Hence, the only combination for a red system is TCTA:$Ir(MDQ)_2(acac)$. Due to a narrow exciton recombination zone in the TCTA layer, additional emitters cannot be placed in this layer. Therefore, the remaining two phosphors for blue and green have to be diluted into TPBi. Here, FIrpic is located directly at the exciton generating TCTA/TPBi interface so that it does not face any blocking materials, where exciton quenching is likely due to its high triplet energy. Consequently, the EML is finalized with a mixed layer of TPBI:$Ir(ppy)_3$.

Two intrinsic interlayers are incorporated in this EML. First, a TCTA interlayer is inserted between the red and the blue sub-EML, which is essential to control the exciton distribution at the generating interface and, consequently, the emitted colour. Because of its high triplet energy, it can suppress Dexter-type exciton diffusion from the blue layer to the red layer – a process that would be very efficient without a triplet energy barrier. Furthermore, with a thickness in the range of the Förster radius of the emitters, it can restrict Förster-type energy transfer from high energy blue to low energy red excited states. As indicated in Figure 7.6, this interlayer controls the transfer rate $k_{b\text{-}r}$. Besides, a TPBi interlayer between the blue and green layer is

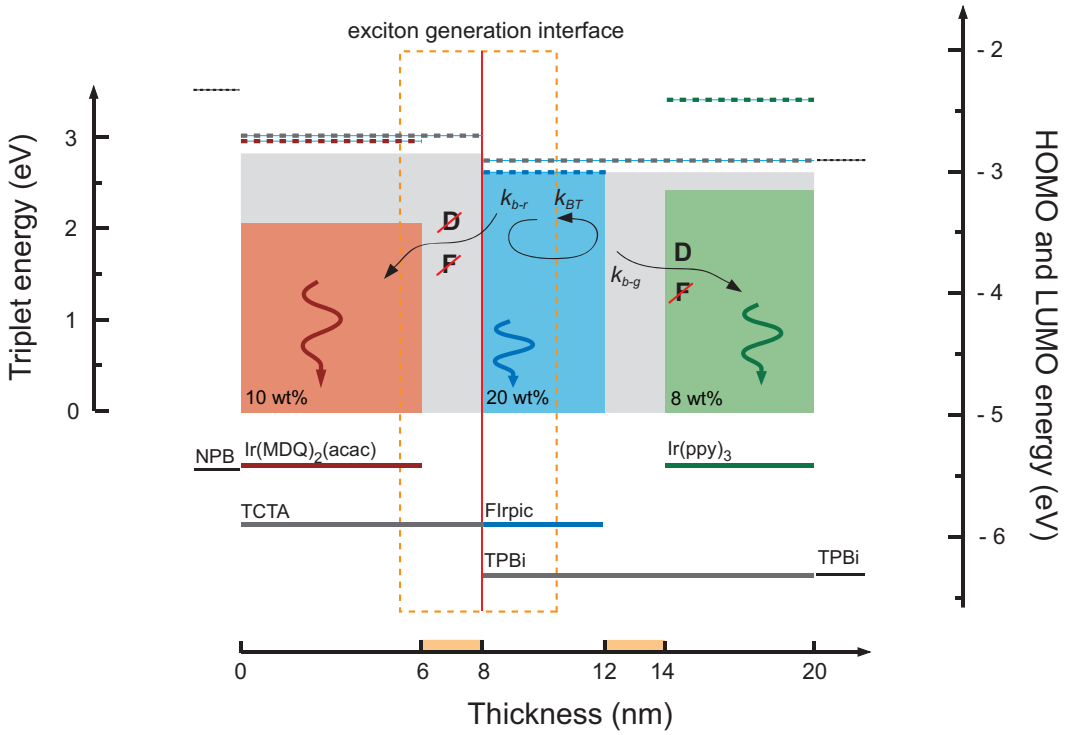

Figure 7.6: Schematic EML design with all important energy levels. Lines correspond to HOMO (solid) and LUMO (dashed) energy levels of EML and blocking materials. The coloured filled boxed represent the corresponding T_1 level. The orange marks on the x-axis indicate intrinsic interlayers. The orange dashed box indicates the region of exciton formation. D and F denote Förster- and Dexter-type energy transfers. Rate constants k_i are given for various transfers: blue–to–red ($k_{\text{b-r}}$), blue–to–green ($k_{\text{b-g}}$), and energy back-transfer (k_{BT}).

inserted. It decouples Förster-type energy transfer between the blue and green layer similar to the TCTA interlayer. However, in contrast to the latter, the TPBi layer cannot suppress diffusive triplet energy transfer to the green layer, because no triplet energy barrier is present. Hence, the $Ir(ppy)_3$ doped sub-EML diffusively harvests excitons that can not be used for recombination in the blue layer – expressed by a rate $k_{\text{b-g}}$. In summary, TCTA controls Förster- and Dexter-type transfers while the thin TPBi interlayer only affects the Förster-type energy transfer from FIrpic to $Ir(ppy)_3$.

As discussed in Section 7.1, the EML is based on the well known double emission layer concept [170]. The HOMO and LUMO levels of all EML and blocking materials are shown in Figure 7.6. The exciton generation is fixed to the TCTA/TPBi interface because of their preferentially hole- and electron-transporting character [37]. Holes are injected nearly barrier-free from the NPB EBL into the HOMO level of the red emitter $Ir(MDQ)_2(acac)$, where efficient hopping transport is possible owing to the high emitter concentration of roughly 10 wt% [42]. Electrons are resonantly injected from the HBL to the EML, because TPBi is also used as a hole blocking material.

Hence, both holes and electrons can reach the TCTA/TPBi interface almost without the need to overcome energy barriers, which is essential for low operating voltages.

Resonant Triplet Energies in the Blue Sub-EML

According to the energy scheme of Figure 7.6, the triplet energies of TPBi and FIrpic are obviously in resonance. At first glance, this seems to be detrimental for high efficiency, because highly efficient phosphorescence is typically only obtained for mixed host-guest systems with exciton confining abilities [78]. However, to achieve white emission from a fully phosphorescent EML with low operating voltages, this EML design proves to be essential.

In general, as just mentioned, high triplet energy matrix materials are needed for the blue emitter as well, which increases the transport gap of the device and, consequently, the operating voltage [179–181]. However, in the present design, TPBi is used as matrix material for FIrpic – a material that is commonly used as host for the green emitter $Ir(ppy)_3$ [38, 178]. Therefore, the operating voltage is expected to be comparable to conventional green DEML OLEDs (cf. Ch. 6). However, in such resonant systems, the confinement of triplet excitons to the phosphor is not given anymore, which reduces the quantum yield. Therefore, the blue sub-EML is followed by a combination of a thin TPBi interlayer and an $Ir(ppy)_3$ doped TPBi sub-EML. Here, it is attempted to locate the green layer as close to the blue layer as possible, so that it can efficiently harvest unused triplet excitons of the blue system. The latter can only diffuse to the green sub-EML, as they are reflected on the TCTA interlayer, having a high triplet level of $T_1 = 2.83\,\mathrm{eV}$.

The resonant blue system is expected to be accompanied with a energy back-transfer rate k_{BT}, similar to endothermic host-guest combinations. Here, excitons can be continuously transferred from a guest to a host site and back, resulting in a delayed component in the transient signal of such systems [78, 82, 182]. The following OLEDs are prepared to directly investigate this delayed component (k_{BT}) in a complete device structure. The first three devices are prepared as monochrome reference devices. In order to obtain the delayed component, which is one of several decay channels within the present EML architecture, the blue sub-EML of Device 8.2-4 is chosen to be 8 nm. For the red, green, and blue reference OLEDs, the typical standard EML structures are used [25, 42, 174]. In contrast to the three reference structures, the n-doped ETL of Device 8.2-4 is 10 nm thinner, similar to the transport layers of the white devices which will be discussed later.

OLED stack: MeO-TPD:NDP-2 (60 nm, 4 wt%) / NPB (10 nm) / **emission layer** / TPBi (10 nm) / Bphen:Cs (50 nm) / Al (100 nm)

Device 8.2-1: NPB:$Ir(MDQ)_2(acac)$ (20 nm, 10 wt%)

Device 8.2-2: TCTA:$Ir(ppy)_3$ (20 nm, 8 wt%)

Device 8.2-3: TCTA:FIrpic (20 nm, 20 wt%)

Device 8.2-4: $TCTA_6$(R) / i_2 / $TPBi_8$(B) / i_2 / $TPBi_4$(G) / ... / Bphen:Cs (40 nm) / ...

The exciton dynamics of Device 8.2-4 are investigated in a spectrum- and time-resolved fashion. Here, the set-up introduced in Chapter 4 is used. Figure 7.7 a) plots the transmission of Device 8.2-4 as obtained using different colour filters, starting from solely red emission (1) to the complete emitted spectrum (5). The phosphorescence of TCTA and TPBi (measured at 77 K) are additionally plotted, showing that the highest energy peaks of TPBi and FIrpic are roughly at the same position. TCTA has the highest triplet energy of all materials in the present EML design. Similar to Device 8.1-8 of the previous section, the present device shows a lower intensity of the 510 nm feature, compared to the peak at 475 nm (cf. (5) in Fig. 7.7 a)). This indicates that the $Ir(ppy)_3$ emission is very weak, which is a direct consequence of the 8 nm thick TPBi:FIrpic layer.

Figure 7.7 b) plots the electroluminescence transients, corresponding to the filtered spectra in a). Additionally, the transients of the reference Devices 8.2-1, -2, and -3 are plotted. First, a monoexponential decay with a time constant of 1.4 µs is observed, which agrees with the corresponding decay of the red reference device (8.2-1). With increasing transmission, a second decay component appears with a time constant of approximately 3.0 µs. The arrows in Figure 7.7 b) indicate the onset of this slow component. Its spectral dependence can be directly linked to the FIrpic emission (cf. Fig. 7.7 a)). Furthermore, no such slow component is observed for the other two monochrome reference devices (8.2-2 and -3). Here, the high triplet level of TCTA assures efficient exciton confinement to FIrpic molecules, which suppresses the delayed component in the blue reference device.

The Blue–To–Green Transfer Rate $k_{\text{b-g}}$

Apart from the dynamic investigation of the delayed component, photoluminescence quantum efficiency measurements are carried out in an integrating sphere [183–185] to investigate the blue–to–green transfer rate $k_{\text{b-g}}$. In general, the PL efficiency is determined as the ratio between the radiative decay channel (k_{r}) and the sum of radiative and non-radiative (k_{nr}) channel. However, in a host-guest system without efficient exciton confinement, the rate of recombination on host sites k_{H} (which is non-radiative) must be included. This transforms the PL efficiency to:

$$\eta_{\text{PL}} = \frac{k_{\text{r}}}{k_{\text{r}} + k_{\text{nr}} + k_{\text{H}}}. \tag{7.1}$$

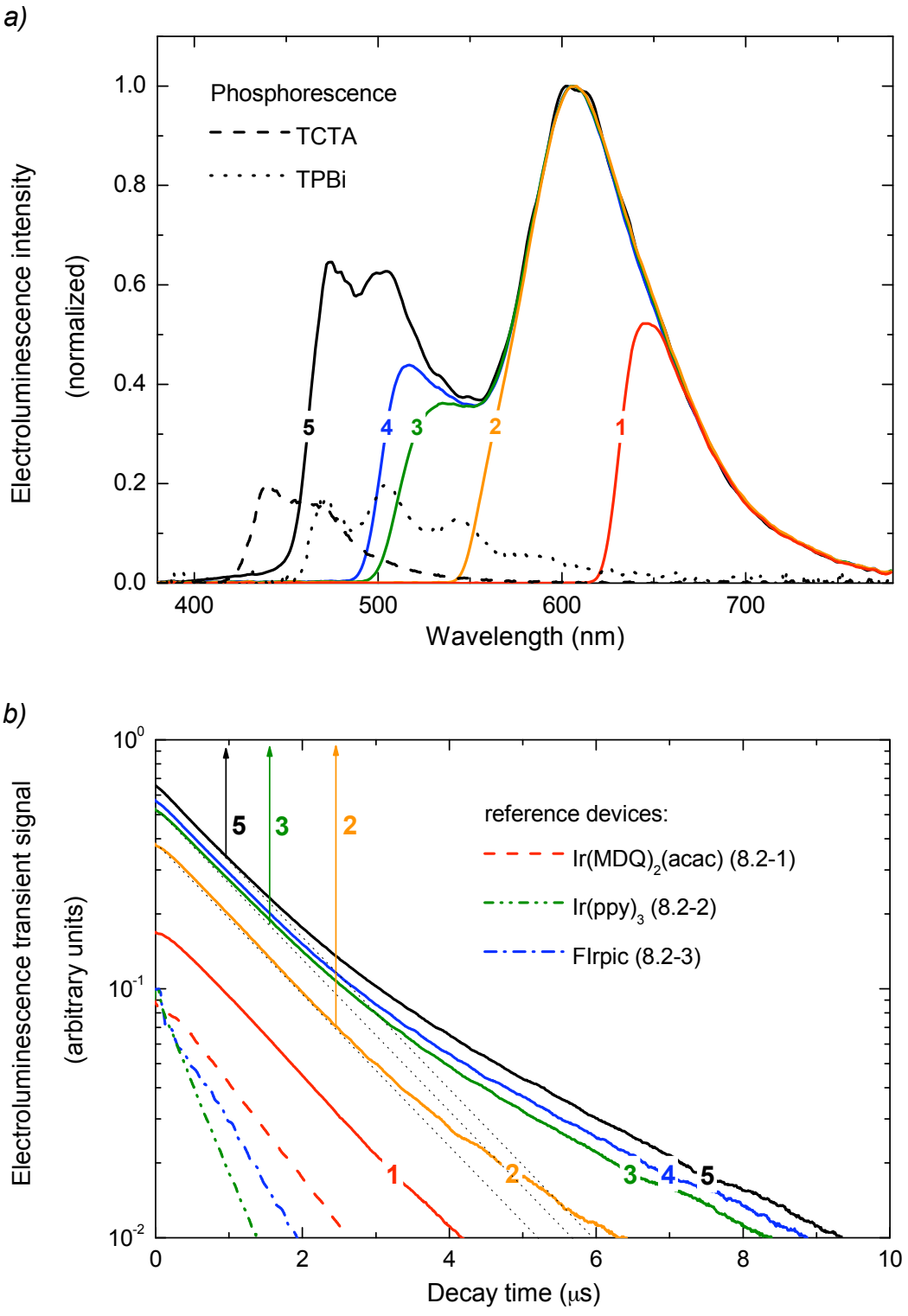

Figure 7.7: a) Electroluminescence spectra of Device 8.2-4 as obtained using different colour filters. The spectra are labelled from solely red emission (1) to the complete white emission (5). Additionally, the phosphorescence spectra of TCTA and TPBi are plotted, as determined at 77 K using a gated phosphorescence set-up. b) EL decay according to the transmitted spectrum as shown in a). The arrows indicate the onset of a slower component in the transient signal. The decay curves of the three reference devices are given additionally.

FIrpic is doped into either TCTA or TPBi with an emitter concentration of 1.7 wt% each. These mixed films show very different photoluminescence efficiency of 81 % and 14 % for TCTA and TPBi as matrix material, respectively. If the emitter concentration in the TPBi system is increased to 10 wt%, the PL efficiency increases to 32 %. This indicates that the low efficiency observed for the TPBi:FIrpic mixed films is not an intrinsic feature of the emitter, but rather depends on the probability of an excited state to find a FIrpic site for recombination. Similar results have been reported for CBP:FIrpic, showing a parabolic dependency of η_{PL} on the emitter concentration, having a maximum at approximately 20 mol% [78]. These systems can be well compared, because CBP and TPBi have nearly identical triplet energies of approximately 2.6 eV.

By knowing the time constant for the TCTA:FIrpic system, which is $\tau = 1/(k_{\mathrm{r}} + k_{\mathrm{nr}}) = 1.35\,\mu\mathrm{s}$ [174], it is possible to calculate the rate of recombination on host sites for the TPBi based system to $k_{\mathrm{H}} = 3.5 \times 10^6\,\mathrm{s}^{-1}$. This is roughly six times larger than the radiative recombination $k_{\mathrm{r}} = 6.0 \times 10^5\,\mathrm{s}^{-1}$ of the mixed film. Clearly, an EML that solely consists of TPBi doped with FIrpic cannot be used for an efficient OLED. However, in the present white EML design, the excitons that would non-radiatively recombine in the blue sub-EML are efficiently transferred to $\mathrm{Ir(ppy)_3}$, where they can recombine with nearly 100 % PL efficiency [78]. This efficient conversion proceeds, because the lifetimes of matrix triplet states are typically orders of magnitude longer than the corresponding emitter time constants [18, 76]. Furthermore, the green sub-EML is placed very close to the blue emission layer, so that it lies within the triplet diffusion length of TPBi [178, 186].

Maximizing the Blue Emission

The above discussion shows that the blue emission in the present EML design is the bottleneck owing to the low PL efficiency of the TPBi:FIrpic mixed layer. Hence, it is important to find the best compromise for sufficiently intense blue emission while at the same time realizing the highest possible overall device EQE. The EL spectrum of Device 8.2-4 already suggests that a thickness of the blue sub-EML of 8 nm is too high to realize strong green emission for a balanced white spectrum. Therefore, the TBPi:FIrpic layer thickness is reduced to 4 nm in the following two devices. Additionally, the FIrpic concentration is varied, having values of 10 and 20 wt %.

OLED stack: MeO-TPD:NDP-2 (60 nm, 4 wt%) / NPB (10 nm) / **emission layer** / TPBi (10 nm) / Bphen:Cs (40 nm) / Al (100 nm)

Device 8.2-5: $\mathrm{TCTA_6}$(R) / $\mathrm{i_2}$ / $\mathrm{TPBi_4}$(B) (**10 wt%**) / $\mathrm{i_2}$ / $\mathrm{TPBi_6}$(G)

Device 8.2-6: $\mathrm{TCTA_6}$(R) / $\mathrm{i_2}$ / $\mathrm{TPBi_4}$(B) (**20 wt%**) / $\mathrm{i_2}$ / $\mathrm{TPBi_6}$(G)

The electroluminescence spectra of Devices 8.2-5 and -6 are plotted in Figure 7.8, comparing the influence of the FIrpic concentration. These spectra are measured at the same luminance of 1,000 $\mathrm{cd/m^2}$ and are normalized to the peak wavelength

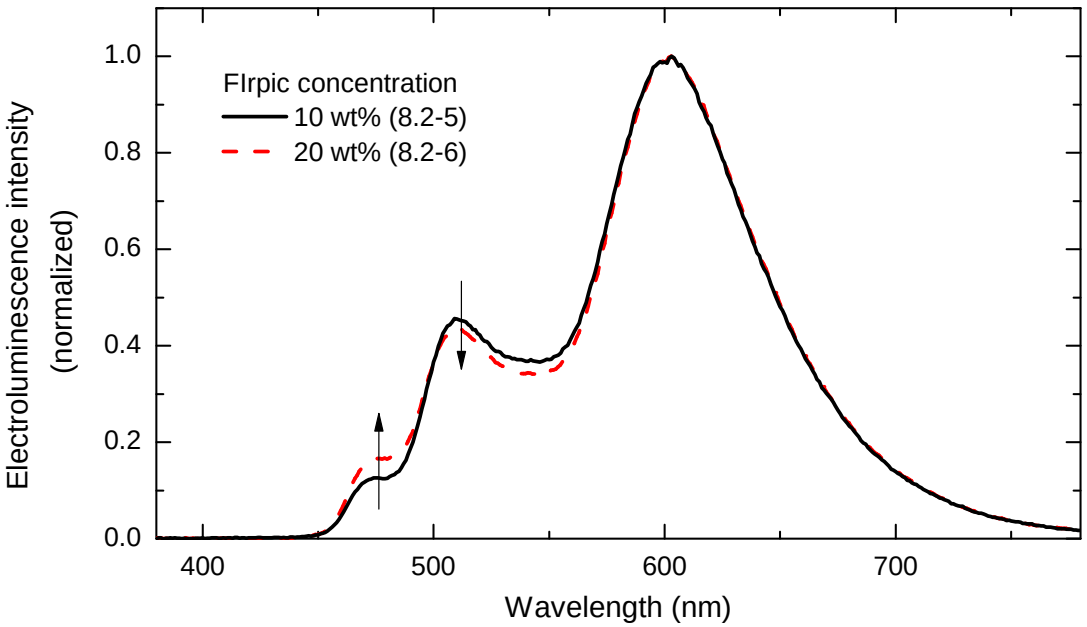

Figure 7.8: Electroluminescence spectrum of Devices 8.2-5 and -6 obtained at 1,000 cd/m^2 in forward direction (normalized to red emission peak at roughly 600 nm). The arrows indicate that the blue intensity increases with increasing FIrpic contribution while at the same time the green intensity decreases.

of the red emitter at roughly 600 nm. Both spectra show a balanced emission with increasing intensity from blue to red, indicating the sufficiency of a 4 nm thick blue layer. The arrows in Figure 7.8 show the changes occurring upon an increase of the FIrpic concentration. The blue FIrpic intensity increases parallel to a decrease in the green emission from Ir(ppy)$_3$. Similar to the PL efficiency increase of the TPBi:FIrpic mixed films from 1.7 to 10 wt%, the recombination efficiency further increases for devices with a doping ratio of 20 wt%. Again, this is a result of enhanced probability for excitons to find a site for emissive relaxation. According to the literature data for CBP:FIrpic, a maximum is found for a concentration of 20 mol% [78]. Upon further increasing emitter concentration, the PL efficiency η_{PL} drops similar to the exothermic host-guest systems as a consequence of concentration quenching [79].

Because FIrpic captures a larger fraction of excitons generated at the TCTA/TPBi interface in the 20 wt% sub-EML, less excited states are able to diffuse to the green layer, explaining the decrease in Ir(ppy)$_3$ intensity. Despite these spectral changes, the external quantum efficiencies of both devices reach identical values of 13.1 % at 1,000 cd/m^2. This suggests a compensation of the lower green emission, which would result in a reduced overall EQE, by the increasing quantum efficiency of the TPBi:FIrpic sub-EML. Hence, according to results of Devices 8.2-5 and -6, a 4 nm TPBi:FIrpic layer with a concentration of 20 wt% exhibits the optimum for the blue layer. However, during the remaining device optimization, a FIrpic concentration of 10 wt% is used (in part, because some other variations are actually processed previously to this sample series).

Variation of the Red and Green Layer Thickness

As a next step, the influence of the layer thickness of the red and green sub-EMLs is investigated. Therefore, the following two series of devices are prepared, one varying the TCTA:Ir(MDQ)$_2$(acac) the other the TPBi:Ir(ppy)$_3$ layer thickness. All these devices are prepared in the same run for best comparability, using the single chamber tool with combinatorial capabilities.

OLED stack: MeO-TPD:NDP-2 (60 nm, 4 wt%) / NPB (10 nm) / **emission layer** / TPBi (10 nm) / Bphen:Cs (40 nm) / Al (100 nm)

Series 8.2-7: **TCTA$_{6,\ 8,\ 10,\ 12}$(R)** / i$_2$ / TPBi$_4$(B) / i$_2$ / TPBi$_6$(G)

Series 8.2-8: TCTA$_6$(R) / i$_2$ / TPBi$_4$(B) / i$_2$ / **TPBi$_{4,\ 6,\ 8,\ 10}$(G)**

The aim of this thickness variation of the red and green sub-EMLs is to find the optimum for high quantum efficiency and low operating voltage in order to realize very high power efficiencies. The EQE, measured at 1,000 cd/m^2, and the corresponding operating voltage are summarized in Table 7.1 for all devices of Series 8.2-7 and -8. For the variation of the red TCTA:Ir(MDQ)$_2$(acac) layer, a slight increase in the EQE from 11.9 to 12.5 % is observed for larger thickness. At the same time, the operating voltage increases from 3.25 to 3.50 V for doubling the layer thickness from 6 to 12 nm. The latter is detrimental for high power efficiencies. At first glance, the increase in EQE suggests that excitons are still lost to the NPB electron blocker for the thinnest red layers. However, the thickness variation of the TCTA:Ir(MDQ)$_2$(acac) layer is accompanied with distinct spectral changes. In Figure 7.9 a), the EL spectra measured at 1,000 cd/m^2 under a variation of the thickness of the red layer are plotted. They are normalized to equal integrated intensities. The arrows indicate the changes with increasing layer thickness. Here, with increasing layer thickness of TCTA:Ir(MDQ)$_2$(acac), the red intensity increases, while the contribution from blue and green decreases. It is therefore not valid to compare the EQE data of Series 8.2-7, because the PL quantum efficiency of each phosphor is different. Among the used emitters, Ir(MDQ)$_2$(acac) is the most efficient material, being known for the realization of internal quantum efficiencies approaching unity [42]. Recent literature data discussing Ir(ppy)$_3$ suggest that its internal efficiency is lower than 100 %, i.e. in the range of $\sim$ 70 %, even in a well optimized device [112]. Finally, referring to the above discussion, the TPBi:FIrpic layer results in the lowest recombination efficiency. Hence, the increase in external quantum efficiency with increasing red layer thickness is not a consequence of losses to the adjacent EBL, but rather a result of a changing colour balance, favouring the highly efficient red emission. Therefore, the thinnest layer of 6 nm TCTA:Ir(MDQ)$_2$(acac) will be used as the optimum value since it results in the lowest operating voltage of 3.25 V.

The effects observed for the variation of the TPBi:Ir(ppy)$_3$ layer thickness are less pronounced. Referring to the data in Table 7.1, the EQE increases with increasing layer thickness. Here, the largest improvement is observed between 4 and 6 nm from 10.8 to 11.5 % EQE, while the improvements upon further thickness increase are

TCTA:Ir(MDQ)$_2$(acac)	6 nm	8 nm	10 nm	12 nm
EQE (%)	11.9	11.8	12.2	12.5
voltage (V)	3.25	3.33	3.42	3.50
TPBi:Ir(ppy)$_3$	4 nm	6 nm	8 nm	10 nm
EQE (%)	10.8	11.5	11.8	12.2
voltage (V)	3.27	3.31	3.33	3.37

Table 7.1: EQE at 1,000 cd/m^2 and the corresponding operating voltage for all devices of Series 8.2-7 and -8. Consecutively, the layer thickness of the red and the green sub-EML are varied.

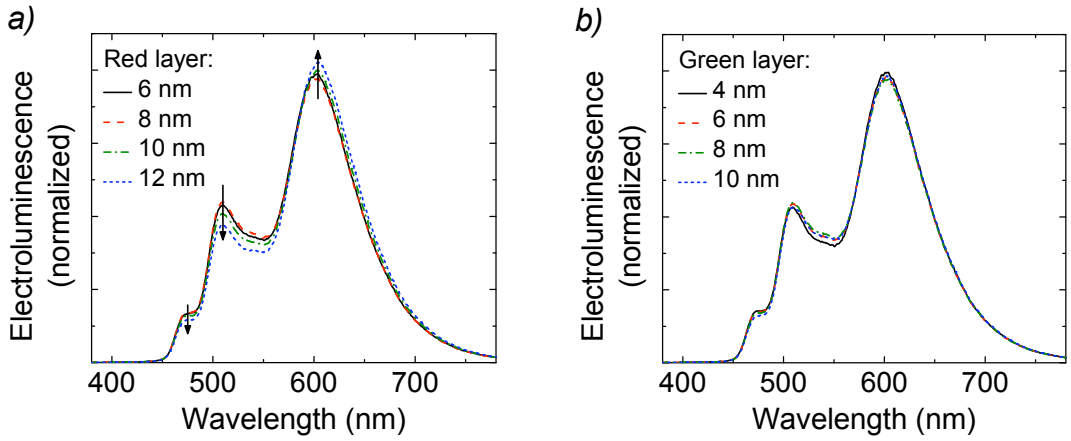

Figure 7.9: All spectra are measured at 1,000 cd/m^2 in forward direction and are normalized to equal integrated intensity. a) EL spectra of the devices of Series 8.2-7, where the thickness of the red TCTA:Ir(MDQ)$_2$(acac) layer is varied. The arrows indicate increasing red and decreasing blue/green intensity. b) EL spectra of all devices of Series 8.2-8 varying the green TPBi:Ir(ppy)$_3$ layer thickness.

smaller. Similar to the red layer, the operating voltage increases with increasing TPBi:Ir(ppy)$_3$ thickness, even though showing smaller changes. Here, in contrast to the case of TCTA:Ir(MDQ)$_2$(acac), the emitted spectra, as shown in Figure 7.9 b), remain nearly unchanged. Only a slight decrease in blue and an increase in green emission is observed upon increasing layer thickness. Despite the fact that blue and green sub-EMLs have different η_{PL}, it cannot be directly distinguished, whether the changes in EQE are a result caused by a different colour balance or due to lost excitons in the case of thin TPBI:Ir(ppy)$_3$ layers. With respect to low operating voltages, 6 nm of the green sub-EML will be used as an optimum value.

Weakly Doped Blocking Layers

The discussion of the device series from above left some uncertainty, whether the changes in the EQE can be solely attributed to the change of in the EL spectra. It is not completely proven that the thickness values for both layers are sufficiently large to harvest all excitons that are created in or reach the corresponding sub-EML. To clarify this open issue, additional devices are prepared. The reference device (Device 8.2-9) has the optimum layer thickness for both layers, i.e. 6 nm for red and green sub-EML. In the other two devices, either one of the blocking layers is weakly doped with the phosphorescent emitter that is adjacent to the corresponding layer. The concentration is kept low at 1 wt% to assure that the presence of the emitter does not influence the electrical performance, and thus the exciton distribution within the device.

OLED stack: MeO-TPD:NDP-2 (60 nm, 4 wt%) / EBL (10 nm) / **emission layer** / HBL (10 nm) / Bphen:Cs (40 nm) / Al (100 nm)

Device 8.2-9: NPB / $TCTA_6$(R) / i_2 / $TPBi_4$(B) / i_2 / $TPBi_6$(G) / TPBi

Device 8.2-10: **NPB:$Ir(MDQ)_2$(acac) (1 wt%)** / $TCTA_6$(R) / i_2 / $TPBi_4$(B) / i_2 / $TPBi_6$(G) / TPBi

Device 8.2-11: NPB / $TCTA_6$(R) / i_2 / $TPBi_4$(B) / i_2 / $TPBi_6$(G) / **TPBi: $Ir(ppy)_3$ (1 wt%)**

It is expected that both the EQE and the intensity of the corresponding emitter in the white spectrum increases, when excitons created in the EML reach the doped blocking layer, where they ultimately recombine. Figure 7.10 plots the EQE of Devices 8.2-9 to 8.2-11 in a) and the their corresponding EL spectra in b). The latter are normalized to equal integrated intensities. Interestingly, the EQE of the reference device (8.2-9) has the highest values of all three devices. Doping of the EBL with $Ir(MDQ)_2$(acac) virtually does not influence the EQE. In contrast, the external quantum efficiency distinctly decreases for the device with the $Ir(ppy)_3$ doped HBL. The EL spectra of all devices are very similar. Comparing to earlier devices, these three OLEDs show an increased green intensity, so that the desired staircase relation of the three emitters is not given. Presumably an unwanted processing error, most likely in the thickness of the TCTA interlayer, leads to this problem. Its effect will be discussed in the next subsection, however, the given difference has no effect on the validity of this discussion.

The operating voltages of these devices at 1,000 cd/m^2 are 3.22, 3.22, and 3.24 V for Devices 8.2-9 to 8.2-11, respectively. This directly proves that doping of the blocking layers does not affect the electrical performance of the OLEDs. Hence, by using the concept of weakly doped blocking layers, it is possible to show that the thicknesses chosen for the red and green sub-EML exhibit optimum values with respect to high external quantum efficiency. It can be ruled out that excitons are diffusively lost to the adjacent blocking layers, i.e. NPB and TPBi (cf. Fig. 7.6).

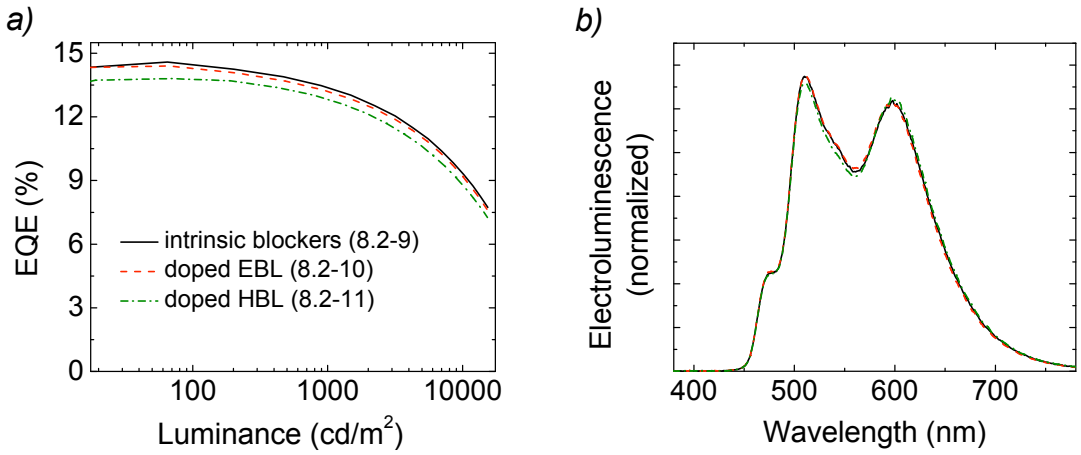

Figure 7.10: a) External quantum efficiency as a function of luminance for Devices 8.2-9 to 8.2-11. b) EL spectra, measured in forward direction at 1,000 cd/m^2, of the corresponding device in a). The spectra are normalized to equal integrated intensity.

The Influence of the TCTA Interlayer Thickness

Referring to Figure 7.6, the TCTA layer has probably the strongest influence on the internal exciton distribution and, consequently, on the emission spectrum of the white OLED. It controls both the Förster- and Dexter-type contribution $k_{\text{b-r,F}}$ and $k_{\text{b-r,D}}$ to the total energy transfer from the blue to the red sub-EML. It is obvious that both rates strongly depend on the thickness of the TCTA layer. For the diffusive Dexter-type contribution, this dependence has two reasons: (i) The interlayer is not a fully closed layer and, hence, excitons will still find Ir(MDQ)$_2$(acac) sites to hop on, that are closer in distance than the nominal spacing given by the TCTA thickness. (ii) Once the interlayer is closed, excitons are able to tunnel through the thin energy barrier, with a probability that scales with the thickness of the interlayer [187].

To investigate the influence of the TCTA interlayer thickness, the following device series is prepared, increasing the layer interlayer thickness from 2.0 to 2.6 nm in 0.2 nm steps.

OLED stack: MeO-TPD:NDP-2 (60 nm, 4 wt%) / NPB (10 nm) / **emission layer** / TPBi (10 nm) / Bphen:Cs (40 nm) / Al (100 nm)

Series 8.2-12: TCTA$_6$(R) / **TCTA (2.0, 2.2, 2.4, and 2.6 nm)** / TPBi$_4$(B) / i$_2$ / TPBi$_6$(G)

The EL spectra of all OLEDs of Series 8.2-12 are plotted in Figure 7.11, the corresponding EQE are shown in the inset. The spectra, measured at 1,000 cd/m^2, are normalized to equal integrated intensity. The arrows indicate increasing TCTA interlayer thickness. Here, changing the thickness by 0.6 nm in total, strong changes are observed. The red emission intensity is reduced, while at the same time, the blue and green intensity increase in a similar fashion. The EQE for the two thinnest

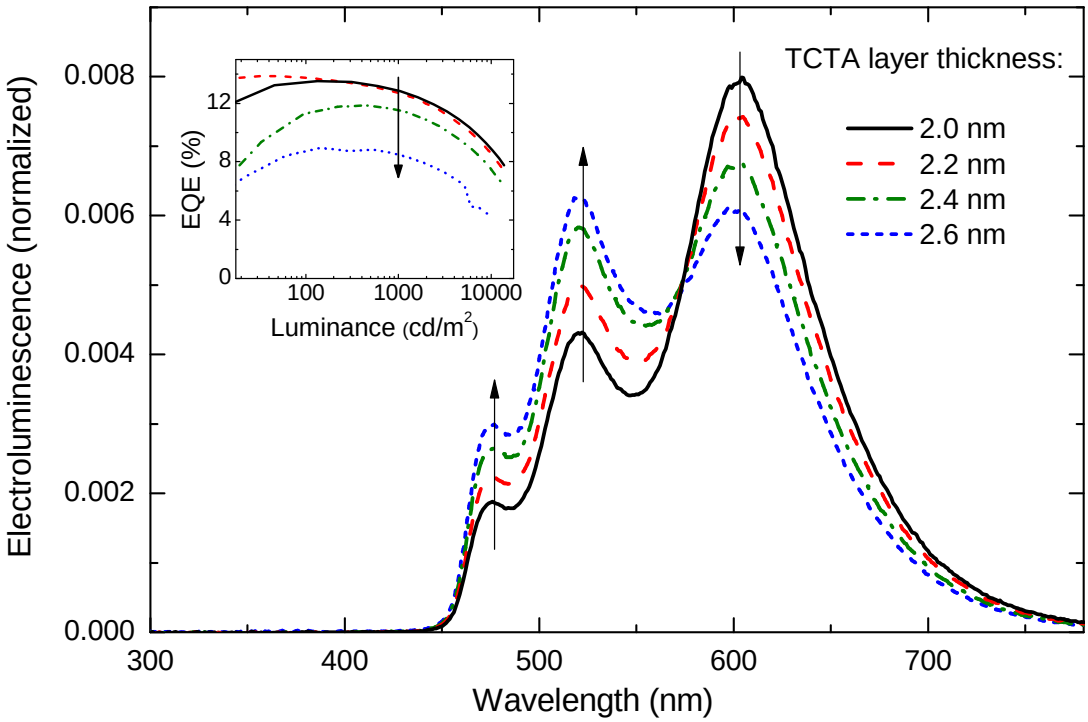

Figure 7.11: Electroluminescence spectra of devices of Series 8.2-12, where the TCTA interlayer thickness is varied. They are obtained at 1,000 cd/m^2 and are normalized to equal integrated intensity. Arrows indicate decreasing red and increasing blue and green emission with increasing TCTA interlayer thickness. Inset: External quantum efficiency of all devices of Series 8.2-12 as a function of luminance.

interlayers of 2.0 and 2.2 nm remain unchanged, however, a further increase of the TCTA layer results in decreasing EQE values (cf. inset of Fig. 7.11).

The reasons for the decreasing EQE with increasing layer thickness are twofold. Of course, in accordance with the discussion on the influence of the red and green sub-EML thickness, this efficiency change can be a result of a changed spectral balance. Here, the thicker TCTA layers amplify the lower η_{PL} of the blue and green systems, while at the same time taking intensity from the efficient red layer, by lowering of the overall blue–to–red energy transfer rate $k_{\mathrm{b-r}}$. Furthermore, owing to the fact that the exciton generation profile decays fast into the TCTA layer, less excitons reach emitter molecules and more relax non-radiatively in the intrinsic TCTA (cf. Fig. 7.6). Thus, to obtain the highest possible external quantum efficiencies of this EML concept, the thickness of the TCTA interlayer should be as thin as possible. The criterium for the optimal thickness is the rate $k_{\mathrm{b\text{-}r}}$. It must be non-zero, otherwise the EQE of the OLED severely drops. On the other hand, the rate can not be fully optimized, because this would result in too strong red emission. In Series 8.2-12, the thickness of 2.2 nm shows the best performance in respect to efficiency and colour. Even though the efficiency of the 2.0 nm device shows identical EQE, the EL spectrum already contains too much red emission.

In summary, the thickness of the intrinsic TCTA layer is the most critical parameter in the present white EML design, as it directly controls the blue–to–red energy transfer rate $k_{\text{b-r}}$. The last series of devices showed that the performance of the devices is affected by changes of the interlayer thickness even only in the sub-nanometer regime. Considering the accuracy of the evaporation tools used being in the same range, optimization and reproduction become very challenging. Therefore, if this concept will be used for future experiments, the delicate influence of the TCTA interlayer should be considered from the very beginning.

The Performance of the Optimized White OLED

In the last part of this section, the performance of the final white OLED will be discussed. Combining the key parameters determined above results in the following final device architecture. In contrast to all devices that are prepared for the above discussions, Device 8.2-13 comprises a silver cathode. It is used instead of the standard aluminum cathode, because it has a slightly higher reflectivity that results in improved EQE data [188]. Aluminum is used during the optimization to keep the material costs low. For the remaining part of this chapter, the device efficiencies are measured in an integrating sphere, in order to state the exact values by correctly taking the angular emission pattern into account. For clarity, the values are marked with an asterisk (*).

OLED stack: MeO-TPD:NDP-2 (60 nm, 4 wt%) / NPB (10 nm) / **emission layer** / TPBi (10 nm) / Bphen:Cs (40 nm) / **Ag (100 nm)**

Device 8.2-13: $TCTA_6$(R) (10 wt%) / i_2 / $TPBi_4$(B) (20 wt%) / i_2 / $TPBi_6$(G) (8 wt%)

The performance data of Device 8.2-13 are shown in Figure 7.12. In a), the current density and luminance are plotted as a function of the operating voltage. The corresponding inset shows the emitted spectra of the device, measured in forward direction at different brightness. In b), its EQE* and the power efficiency* (PE*) are plotted versus the luminance. The inset in b) shows the CIE diagram with the CIE coordinates of the corresponding spectrum in a).

The j-V-characteristics of this device indicate a turn-on voltage of approximately 2.3 V, followed by a steep rise in current density. This results in very low operating voltages. Table 7.2 summarizes the important quantities of the device for different brightness. A luminance level of 100 cd/m^2, which can be compared to a typical computer screen brightness, is already reached below 3 V. Operation at 1,000 cd/m^2 only needs slightly higher voltages of 3.22 V. Even a very high luminance of 10,000 cd/m^2 is reached below 4 V. These very low voltages can only be obtained using the p-i-n OLED concept [8], otherwise much higher voltages would be necessary [53].

At low brightness, Device 8.2-13 reaches 14 % EQE*. This value decreases to 13.1 % at 1,000 cd/m^2 (cf. Tab. 7.2), which is among the highest values reported for white OLEDs based on three phosphorescent emitters [36, 189, 190] and comparable to alternative concepts comprising blue fluorophors [11, 186]. The power efficiency of this device is very high, which is a consequence of the p-i-n concept and the previously

luminance (cd/m^2)	voltage (V)	EQE* (%)	PE* (lm/W)
100	2.93	14.0	35.4
1,000	3.22	13.1	30.3
10,000	3.96	9.8	18.2

Table 7.2: Performance data of Device 8.2-13, determined at different brightness levels. EQE and power efficiency (PE) are measured in an integrating sphere, indicated by the asterisks.

discussed, nearly barrier-free EML design [27]. A power efficiency* of 30.3 lm/W is reached at 1,000 cd/m^2 without any outcoupling enhancing techniques – a value that mostly requires additional outcoupling concepts [189].

The electroluminescence spectrum of Device 8.2-13 (see inset of Fig. 7.12 a)) shows the desired staircase relation of the different emitter intensities, increasing from blue to red. The CIE colour coordinates are (0.45, 0.47), being displaced from the Standard Illuminant A to the yellow region (cf. inset of Fig. 7.12 b)). This is mainly a consequence of the blue emitter FIrpic, showing a rather sky-blue emission, resulting in a relatively high CIE y value.

It is necessary to note that the scope of this work is to show novel concepts rather then developing 'ideal light sources' that fulfill industry specifications. In general, emission at the Standard Illuminant A could be achieved by only using FIrpic and Ir(MDQ)$_2$(acac), which is apparent from the CIE diagram in the inset of Figure 7.12. For instance, the CIE coordinates of Device 8.2-4, which was used to investigate the exciton dynamics in the present EML design, are (0.44, 0.41), almost perfectly resembling the values of the Standard Illuminant A. However, such two-colour approaches lead to a poor illumination quality, because the green emission in the center of the spectrum is missing [39]. Thus, the available three emitters are used as a model system to show that highly efficient OLEDs can be realized with a balanced spectrum having contributions of three basic emitters.

An interesting feature of the present EML design is the excellent colour stability as a function of brightness. The inset of Figure 7.12 a) plots the EL spectra of Device 8.2-13 at different luminance levels, spanning the complete range of desired applications from 100 to 5,000 cd/m^2. Upon this variation, no significant changes in the EL spectra are observed, which is a great improvement on many literature reports [11, 36, 38]. Typically, the relative intensity of the different emitters change as a function of current passing through the device, which is a result of energy barriers within the OLED layer stack. However, the present concept realizes nearly barrier-free injection and transport of holes and electrons to the exciton generating interface TCTA/TPBi (cf. Fig. 7.6). Hence, the relative charge carrier distributions of holes and electrons remain unchanged for different current densities, and consequently, brightness. This leads to the observed colour stable emission spectra.

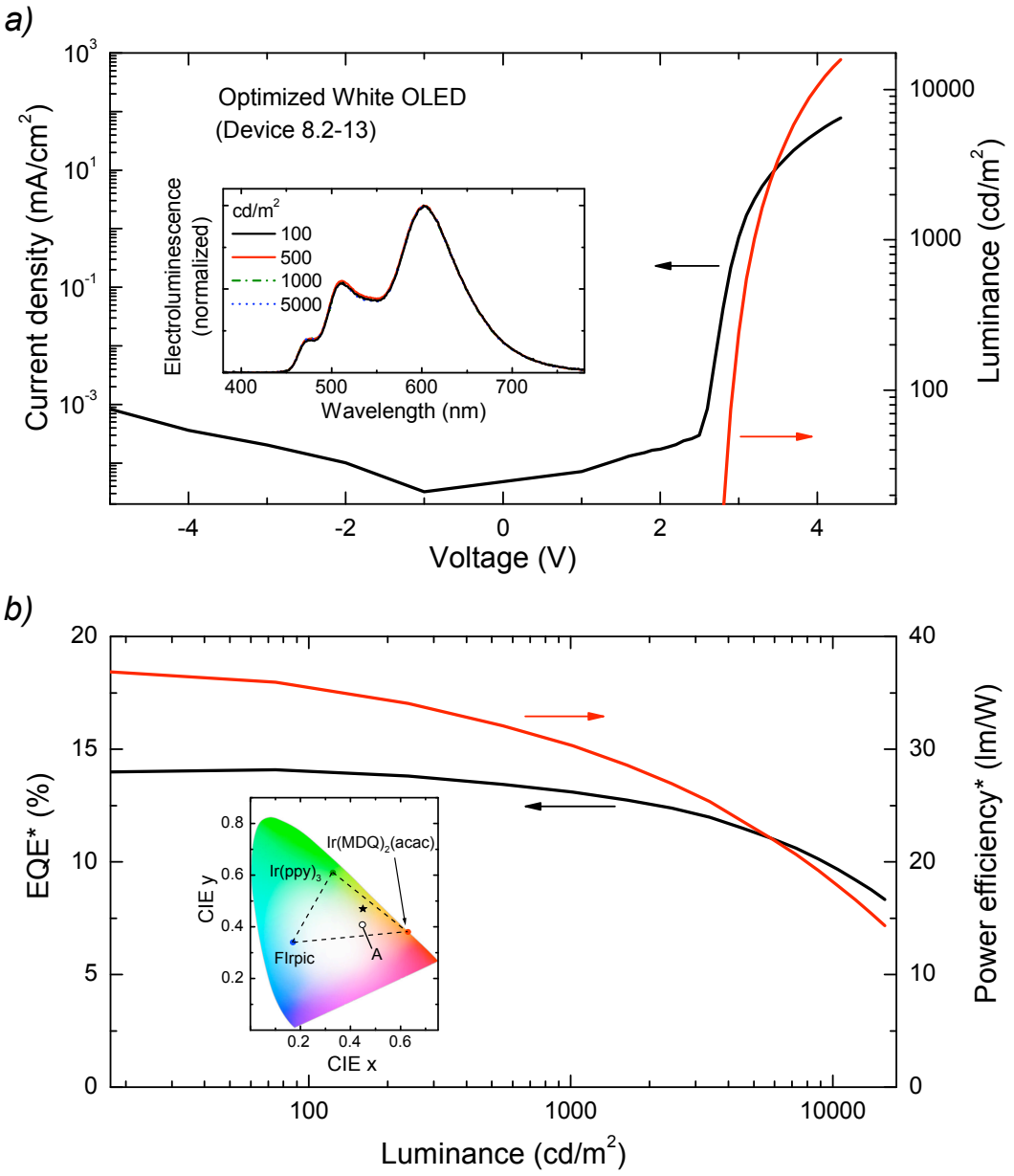

Figure 7.12: Overview of the performance of the optimized white OLED structure (Device 8.2-13). a) Current density and luminance versus voltage. Inset: Normalized EL spectra measured at different luminance levels in forward direction. b) External quantum efficiency and power efficiency versus luminance. An asterisk indicates that these measurements are performed in an integrating sphere. Inset: CIE diagram showing the CIE coordinates of Devices 8.2-13. Additionally, the corresponding coordinates of reference red, green, and blue OLEDs are given, which span the colour space that can be realized with these emitters. The circle marks the Standard Illuminant A.

7.3 High Refractive Index Substrates for Improved Light Outcoupling

In order to realize white OLEDs with even higher efficiency, this three-colour phosphorescent EML concept will be used in this and the following section, where the light outcoupling efficiency will be addressed. For these upcoming studies, the optimum parameters for the EML design found in the preceding section will be used without further changes.

When comparing the efficiency of the present white OLED (Device 8.2-13) to existing technologies [191], its power efficiency already reaches twice the value of conventional incandescent light bulbs. At the same time there is still a gap of roughly 30 lm/W to state-of-the-art compact fluorescent lamps (CFLs), typically reaching 60 lm/W. Hence, even highly efficient white OLEDs need a strong efficiency boost to compete with existing light sources. In this section, the white OLED design developed will be transferred to high refractive index substrates to increase the light outcoupling efficiency η_{out}.

Without changing the parameters of the optimized EML design, the following device is prepared comprising a high index glass substrate with a refractive index of $n = 1.78$. Previously to the preparation of white OLEDs on high index substrates, a similar study is carried out based on a monochrome red OLED system comprising $\text{Ir(MDQ)}_2\text{(acac)}$ as emitter to determine the potential of this approach. The results of this study are summarized in Appendix C. The transparent ITO anode is similar to the one of the standard devices. Based on a thin-film optics calculation[1] prior to the device preparation, the optimal thickness of the p-doped HTL is found to be 45 nm instead of the 60 nm used for the OLEDs described in Section 7.2. The other layer thicknesses are kept identical.

Device 8.3-1: **high n substrate ($n = 1.78$)** / ITO (90 nm) / **MeO-TPD: NDP-2 (45 nm, 4 wt%)** / NPB (10 nm) / *EML (cf. Device 8.2-13)* / TPBi (10 nm) / Bphen:Cs (40 nm) / Ag (100 nm)

The current density voltage characteristics and the EL spectrum are plotted in Figure 7.13 a) and b), respectively. The data are compared to the reference OLED (Device 8.2-13) of the previous section. Besides slight deviations in the high field regime, the j-V data coincide for both OLEDs. Stronger changes are observed in the electroluminescence. In comparison to the low index OLED, Device 8.3-1 shows a slight increase of FIrpic and a strong increase of Ir(ppy)_3 emission. However, the changes in the CIE coordinates are small. Here, the two OLEDs have CIE coordinates of (0.44, 0.46) and (0.45, 0.47) for low and high index substrate, respectively. Considering these data, the reason for these spectral changes still remains unclear. Of course, it is possible that the actual EML design has varied between the two samples. On the other hand, the modified optics of the high index OLED might cause these

[1] Calculations are done using Etfos thin-film optics software v1.3, Fluxim AG, Winterthur, Switzerland.

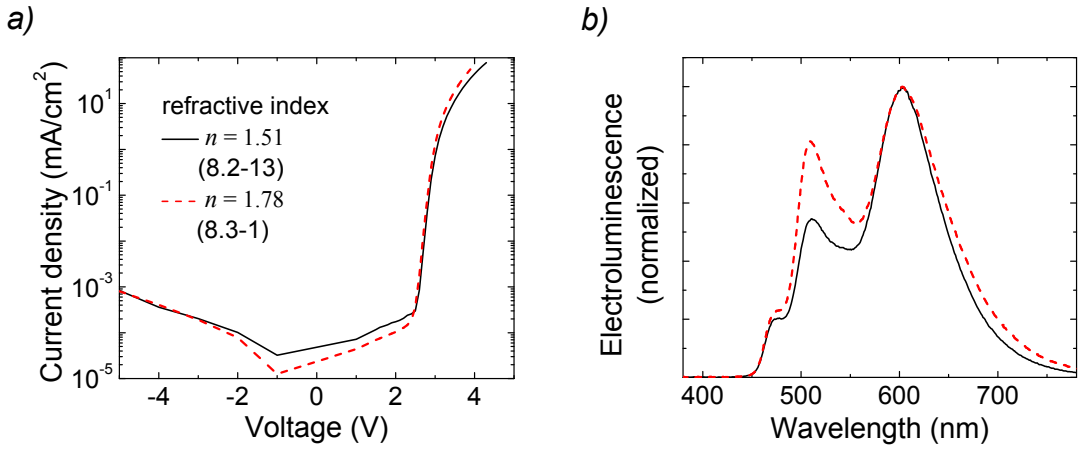

Figure 7.13: a) Current density versus voltage for Devices 8.2-13 and 8.3-1, which differ in the refractive index of the glass substrate. b) Corresponding EL spectra of the devices in a) measured at 1,000 cd/m^2.

differences. When using an index-matched high n glass substrate, the number of optical interfaces within the complete OLED is – in the most ideal picture – reduced from two to one. Here, the substrate assures index-matching from the metal/organic to the glass/air interface. As a consequence, the high index substrate weakens the interference conditions for an emitter within the OLED, possibly resulting in a change in the extracted power $A(\lambda, \theta)$ of the OLED stack [110], which depends on the wavelength of the emission.

High Index Outcoupling Structure

Prior to discussing the high index OLED efficiency, an outcoupling structure fabricated within this work will be introduced. As already discussed in Chapter 3, periodic structures are commonly used to increase the light outcoupling of substrate modes, because they are able to couple out light at higher angles of incidence to the substrate normal. For standard glass substrates with a refractive index $n = 1.51$, many vendors for microlens arrays exist, but there is no supplier for $n > 1.7$.[2] Therefore, such a structure is created by modifying the surface of a high index glass plate.

In general, a lens array with single lens dimensions between $10-500\,\mu$m would suit perfectly as an outcoupling surface. Hot-embossing techniques are ideal for realizing such lens arrays and similar periodic shapes. However, they require a master of high cost – too high to realize only one single outcoupling structure. Therefore, a cheaper solution is required. Using high-precision glass cutters, a pyramidal structure is realized. A photograph of the outcoupling structure is shown in Figure 7.14. V-shaped grooves are cut into the glass plate (Schott N-LAF 21) in horizontal and vertical direction, resulting in ordered pyramids. A single pyramid of this structure

[2]Optmate Corp. offers a microlens array with $n = 1.71$, however it immediately reacts chemically with the index-matching fluid purchased from Cargille Labs, making it useless as an outcoupling structure.

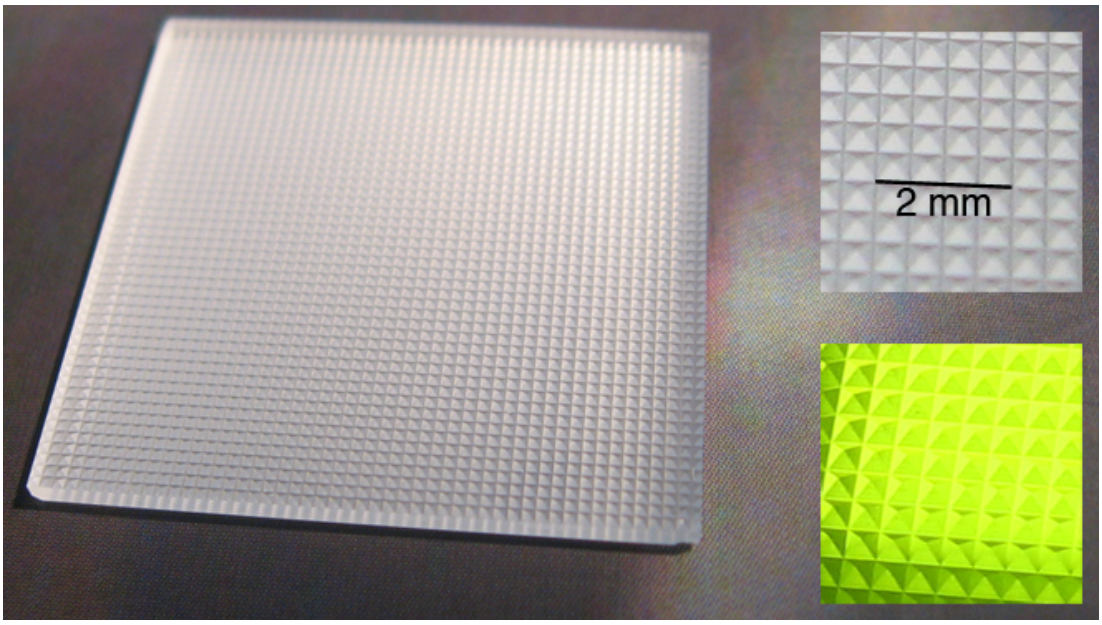

Figure 7.14: Photograph of the high refractive index outcoupling structure. The pattern consists of pyramids with a base length of 500 µm and a height of 250 µm arranged in a square lattice. Insets: Zoom-in of the photograph on the left (top) and part of the the pattern on top of a yellow test OLED in operation (bottom).

has a height of 250 µm and a base length of 500 µm. Despite the fact that the pitch of this structure is about one to two orders of magnitude larger than commercially available microlens arrays (e.g. HR592 (Optmate Corp., Japan) with 5 or 10 µm pitch [186]), it can still be used as a model system for an outcoupling structure with the potential to be scaled to larger sizes. The precision of the glass cutting process limited the pitch to this minimum value of 500 µm. This outcoupling structure is applied to the OLED surface using an appropriate index-matching fluid.

External Quantum Efficiency

The external quantum efficiency of Device 8.2-13 (low n) and Device 8.3-1 (high n) are plotted in Figure 7.15. The flat measurement corresponds to the standard measurement without any outcoupling structure. Both OLEDs reach similar values (thin lines). The reference OLED has 13.1 % EQE* at 1,000 cd/m^2, where the high index device yields a slightly higher value of 14.4 % EQE*. As a next step, an index-matched half-sphere is attached to the OLEDs, with a diameter much larger than the active area of the device, to couple out all substrate modes, showing a remarkable difference (thick lines). While the EQE* of the reference OLED is increased by a factor of 1.8, the EQE* of the high index OLED is raised to 34 % – a 2.4-fold improvement. These values correspond to 55 and 81 lm/W at 1,000 cd/m^2. The improvement factors determined agree with the results of the red monochrome model system (cf. App. C) for which 1.72 and 2.45 are obtained, respectively. This clearly indicates that much

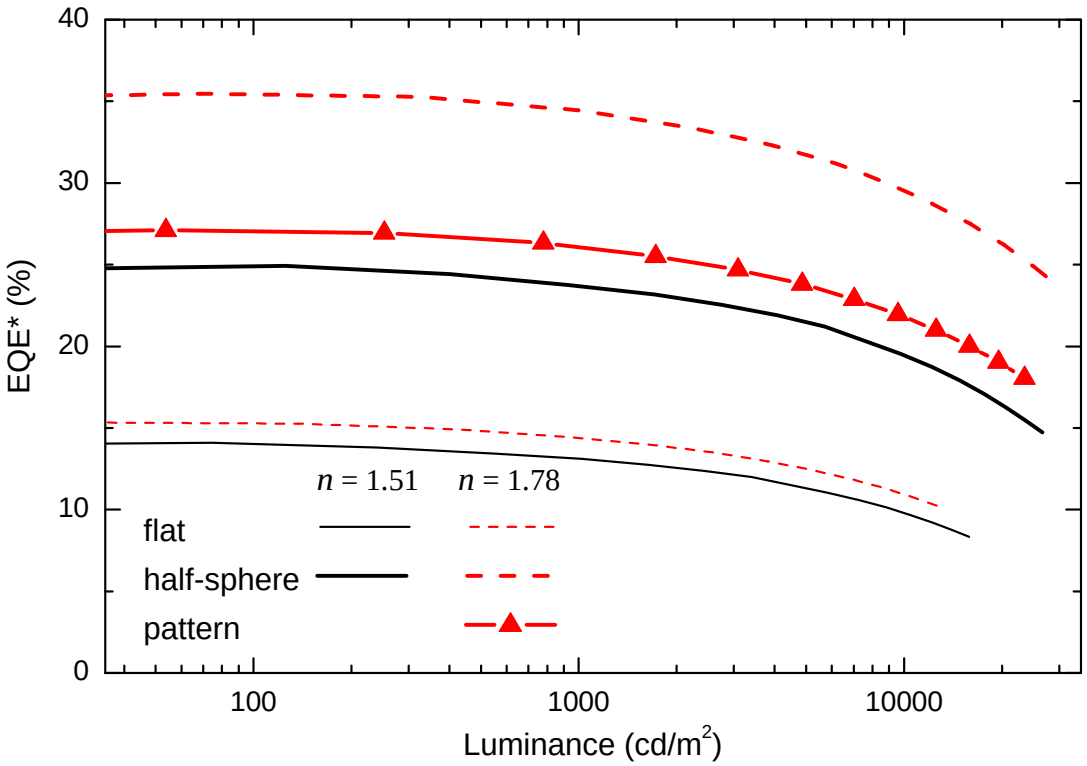

Figure 7.15: External quantum efficiency of Devices 8.2-13 (low n) and 8.3-1 (high n). All data are obtained in an integrating sphere, as indicated by the asterisk. The EQE is measured in three configurations: flat, i.e. without outcoupling enhancement, with index-matched half-sphere, and for the high n case with the patterned pyramidal structure.

more light is coupled into the high index glass substrate. Thus, in accordance with the discussion of the mode power spectrum of Section 3.6, a part of the organic modes are converted into substrate modes, which can be easily coupled out [109, 117].

Finally, the efficiency of the high index OLED (Device 8.3-1) is plotted in Figure 7.15 as obtained with the pyramidal outcoupling structure (triangles). It is slightly higher than the half-sphere data of the reference device. However, taking the slight differences in standard measurement (flat) into account, it shows an improvement by a factor of 1.8 to 26 % EQE* and 63 lm/W – similar to the improvement observed by applying the half-sphere to Device 8.2-13. Table 7.3 summarizes the EQE* and PE* values obtained at 1,000 cd/m^2 using the different outcoupling configurations. These data already exhibit the great potential of high index glass substrates, showing an outcoupling improvement by 80 % compared to standard glass substrates, which is more than the best values obtained for standard substrates modified by microlens arrays, where improvements up to a factor of 1.68 have been realized [113, 115, 186].

At the same time, the efficiency data of Device 8.3-1 shows that the outcoupling by the pyramidal structure is still limited to about $50 - 60$ % of the theoretical limit, which is given by the half-sphere measurement. Thus, new strategies to fabricate high quality, large-area outcoupling structures with high refractive indices to even further

				flat	**pattern**	half-sphere	flat	**pattern**	half-sphere
Device No.	n	ETL (nm)	voltage (V)	EQE* (%)			PE* (lm/W)		
8.2-13	1.51	40	3.22	13.1	–	24	30	–	55
8.3-1	1.78	40	3.08	14.4	26	34	33	63	81
8.3-2	1.78	205	3.11	13.3	**34**	46	37	**90**	124
8.2-3	1.78	210	3.11	12.8	34	44	36	87	111

Table 7.3: EQE* and PE* of Device 8.2-13 (reference) and Devices 8.3-1 (high n), 8.4-1, and -2 (high n, thick ETL). All values are obtained at 1,000 cd/m^2 in an integrating sphere. The highest values obtained for the patterned outcoupling structure are displayed in boldface.

improve the outcoupling efficiency are required in the future. The power efficiency of 63 lm/W at 1,000 cd/m^2 (cf. Tab. 7.3) demonstrate that highly efficient OLED structures, fabricated on top of a high index glass substrate, are on par with CFLs in terms of efficiency.

7.4 Suppressing Plasmonic Losses with Thick Electron Transport Layers

A concept to even further improve the overall efficiency of an OLEDs is the use of thick electron transport layers. Here, with increasing distance between the EML and the metal cathode, the coupling of the emitting dipoles to surface plasmons can be suppressed [120]. However, while losses to plasmons steadily decrease with increasing distance and drop to a negligible level at roughly 200 nm, organic modes increase with increasing ETL thickness [118]. Due to these opposing trends, it is hard to observe improvements in the overall light outcoupling from the device. However, the increase of organic modes with increasing EML-cathode distance is only observed for OLEDs on standard glass substrates as a consequence of the optical interface between ITO and glass [118]. This effect vanishes when high n substrates are used because the optical interface ITO/glass is eliminated [112] (cf. discussion of the mode spectrum in Sec 3.6). Since the second field antinode is in the range of 200 nm [112, 120], placing the emission layer at such distances will be sufficient to avoid plasmonic losses.

The following two white OLEDs are prepared to realize emission in the second emission maximum. The thicknesses of the n-doped ETL is experimentally determined by broadly scanning the thickness of the ETL in 5 nm steps starting from 190 to 230 nm in an earlier optimization using the combinatorial capabilities of the single-chamber evaporation tool. The optimum efficiency is found for the range of 200 to 210 nm. However, at these thick ETLs, the outcoupled spectrum is very sen-

sitive to slight thickness changes. To show this effect, two thickness values (205 and 210 nm) will be discussed in the following. Again it is emphasized that the transition to thick ETLs on high n substrates has been investigated beforehand on the red $Ir(MDQ)_2(acac)$ based model OLED. The discussion of this study is given in Appendix C.

Device 8.4-1: **high n substrate ($n = 1.78$)** / ITO (90 nm) / MeO-TPD: NDP-2 (45 nm, 4 wt%) / NPB (10 nm) / *EML (cf. Device 8.2-13)* / TPBi (10 nm) / **Bphen:Cs (205 nm)** / Ag (100 nm)

Device 8.4-2: **high n substrate ($n = 1.78$)** / ITO (90 nm) / MeO-TPD: NDP-2 (45 nm, 4 wt%) / NPB (10 nm) / *EML (cf. Device 8.2-13)* / TPBi (10 nm) / **Bphen:Cs (210 nm)** / Ag (100 nm)

In order to obtain a better comparability to the results of the low n reference OLED and its high n counterpart, the results of the present Devices 8.4-1 and -2 are compared to Devices 8.2-13 and 8.3-1 in the following discussion.

Electrical Characteristics

The current density and luminance of the two organic LEDs with thick ETLs are compared to the reference devices 8.2-13 (low n) and 8.3-1 (high n) in Figure 7.16 a). Remarkably, the OLEDs comprising thick electron transport layers show very comparable j-V characteristics and operating voltages, although their total thickness is significantly increased compared to the first order devices. Here the advantage of the doped transport layers appears: It is of great importance to realize similar operating voltages for the OLEDs with the thick ETLs, otherwise the power efficiency would suffer even if improvements in the EQE are realized. In comparison with the high n OLED with 40 nm ETL (Device 8.3-1), which is prepared on the same substrate plate, the two devices with thick ETLs show slightly higher voltages for the same current density. However, these differences are negligible with regard to the operating voltages for e.g. 1,000 cd/m^2 (cf. dashed line in Fig. 7.16 a)).

External Quantum Efficiency

Similar to the device evaluation discussed in the preceding section, the OLEDs are measured in an integrating sphere in flat, patterned, and half-sphere configuration. All data of Devices 8.4-1 and -2 are summarized in Table 7.3 of the previous section. In the flat configuration, both devices yield 13.3 and 12.8 % EQE^*, which is comparable to the data of the reference white OLED. By applying the index-matched half-sphere

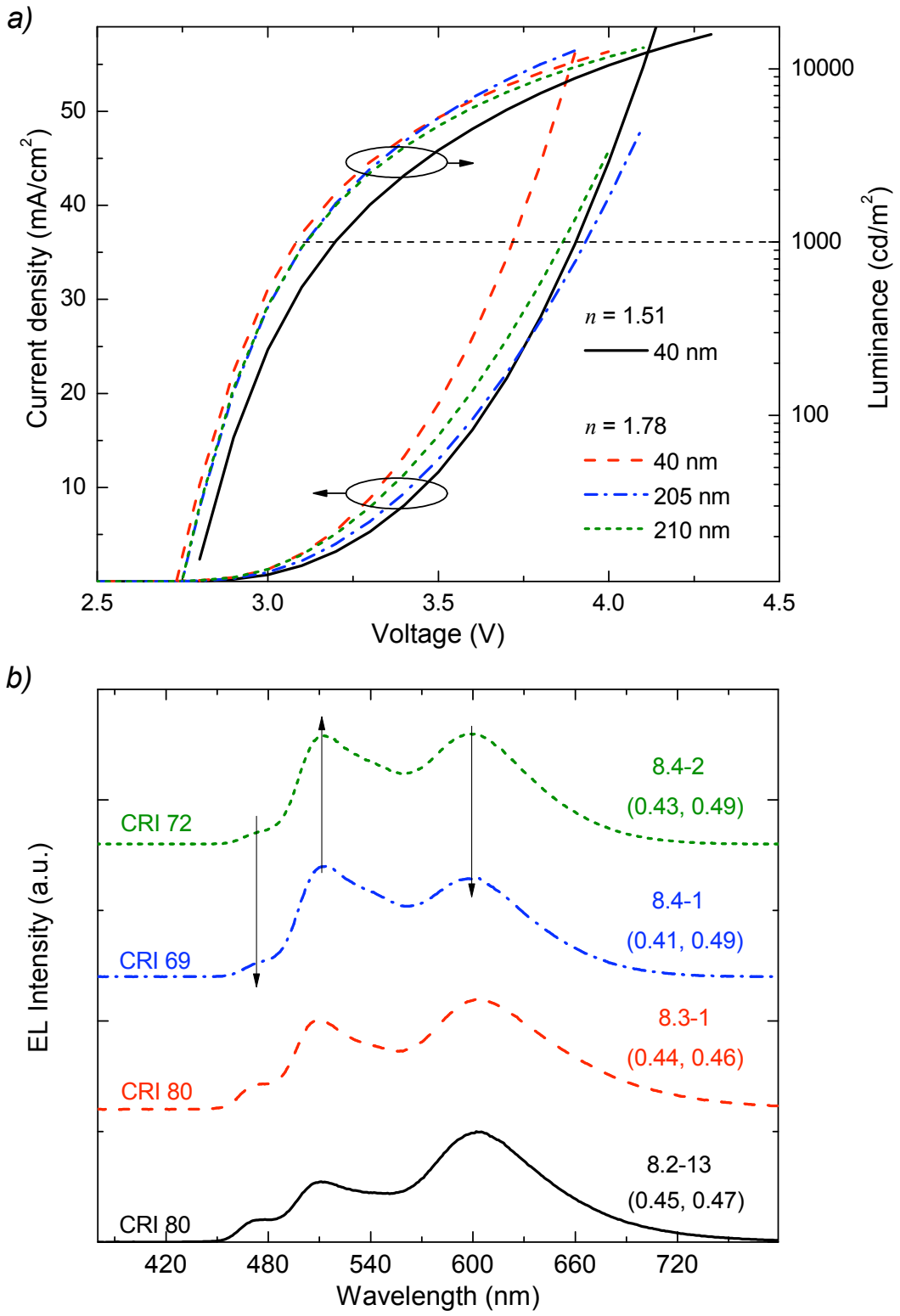

Figure 7.16: a) Current density and luminance as a function of operating voltage for Devices 8.2-13 (low n), 8.3-1 (high n), and 8.4-1 and -2 (high n, thick ETL). b) Corresponding normalized EL spectra of the devices in a). They are split vertically for better visibility. CRI and CIE coordinates are provided additionally. Arrows indicate the spectral changes observed for the OLEDs with thick ETLs.

to the OLEDs, very high values of 46 and 44 % EQE* are obtained at 1,000 cd/m^2. With an improvement factor between flat and half-sphere configuration of roughly 3.4 for both devices, the improvement is even higher than observed for the monochrome test OLEDs (cf. App. C), showing a threefold improvement.

The efficiency of the two OLEDs with thick ETLs can be raised to 34 % EQE* at 1,000 cd/m^2, when the pyramidal outcoupling structure is attached to the substrate surface. Referring to Table 7.3, this coincides with the data obtained for the first maximum device on high index substrates, when measured in the half-sphere configuration. Thus, by combining the concepts of high index substrates with thick ETLs, an improvement factor of approximately 2.6 is realized – the highest factor known to date for a flat outcoupling structure. So far, the concept of low index grids reported by Sun *et al.* marked the best value of 2.3 [115].

Effects of Thick ETLs on the Electroluminescence Spectra

The EL spectra of Devices 8.4-1 and -2 are plotted in Figure 7.16 b). In direct comparison to the spectra of the OLEDs with 40 nm ETL, strong spectral changes are observed. The arrows indicate that the blue and red emission intensities are reduced and/or the green intensity is enhanced. This has negative influence on the colour quality of the emitted spectrum. First, the colour rendering index (CRI), a measure for the colour reproduction quality of a light source, is reduced from 80 for the reference OLEDs to 69 and 72 for Devices 8.4-1 and -2, respectively. Furthermore, the CIE coordinates shift to the yellow region in the colour space, having coordinates of (0.41-0.43, 0.49). This trend is plotted in Figure 7.17 a), where all CIE coordinates of the OLEDs are shown in the CIE diagram. This effect will be discussed later in detail. As mentioned before, the OLEDs in the second emission maximum are very sensitive to a change in the ETL thickness. This becomes apparent by comparing the CIE coordinates of the two second antinode OLEDs. Here, only by changing the ETL thickness by 5 nm, the CIE x coordinate changes from 0.41 to 0.43. As already discussed in Section 7.2, the CIE y coordinates of the present white OLEDs are higher than requested to meet the Standard Illuminant A. However, the blue emitter FIrpic is not fully suitable to realize a balance three-colour white spectrum at Standard Illuminant A, hence these results serve as a first proof-of-principle.

A direct consequence of the thick ETLs is the more forward-directed emission of the OLEDs [120]. Figure 7.17 b) plots the integrated intensity of two OLEDs (Devices 8.2-13 and 8.4-2) in an angular resolved fashion. Interestingly, and in contrast to the commonly made assumption that OLEDs emit light with a Lambertian pattern, the reference OLED shows sub-Lambertian characteristics. Hence, measuring OLED efficiency data in an integrating sphere or with a high precision goniometer is definitely required for a correct efficiency determination. Compared with the reference device, the emission for the high n OLED with thick Bphen:Cs layer has an even more narrow angular intensity distribution. At first glance this seems to be detrimental, however, light outcoupling concepts that address the glass modes benefit from this direct emission. This is because surface modifications, e.g. the pyramidal structure used in this study, do not reach the values obtained with the large half-sphere, indicating that

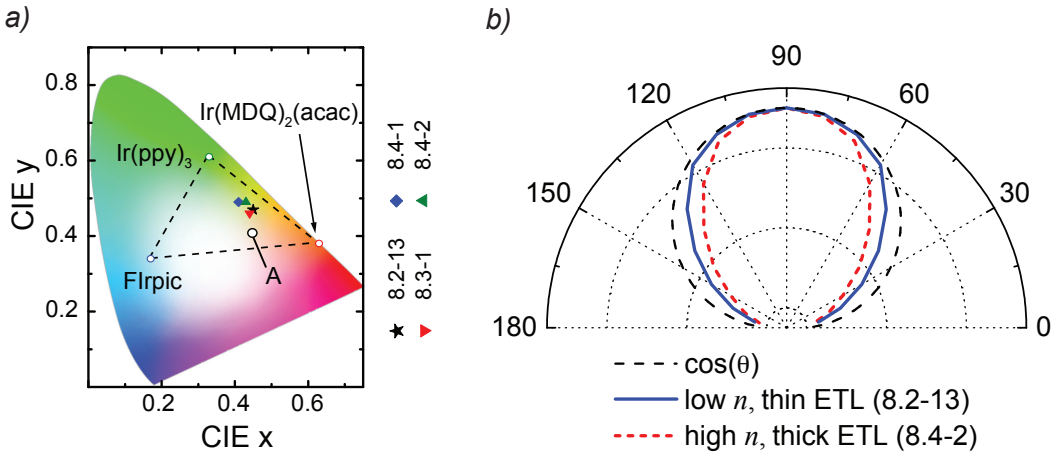

Figure 7.17: a) CIE diagram showing the CIE coordinates of all devices discussed in this section. 'A' marks the Standard Illuminant A, the dashed lines indicate the colour space that is spanned by the used emitter materials. b) Polar diagram showing the angular dependence of the integrated emitted intensity for Devices 8.2-13 and 8.4-2. The black dashed line represents a Lambertian emission pattern.

they are still only able to couple out light to a certain angle. Hence, these outcoupling structures have an effective escape cone within the glass [113]. Therefore, more light can be coupled out if the angular distribution of the light in the glass is more direct, having a larger fraction of light with small angles of incidence to the surface normal. This effect is even more important for high n substrates because their escape cone for a flat surface is in the first place much smaller (critical angle for TIR: $\theta_g = 33.7\,^\circ$). In addition to the reduced escape cone compared to the half-sphere configuration, the outcoupling efficiency of the pyramidal structure is worsened due to absorption losses of light traveling multiple cycles in the optical structure.

Wavelength-Dependent Second Emission Maximum

The reasons for the strong changes in the EL spectra of the white OLEDs with thick ETLs are the different interference conditions in the OLED cavity for different wavelength. It is necessary to optimize the cavity length of differently emitting OLEDs in the first emission maximum to obtain the highest light output [116]. Furthermore, the optimum thicknesses for the second emission maximum diverge for different colours with increasing layer thickness.

Using the thin-film optics software Etfos v1.3, model calculations are performed based on the present OLED stack. Input parameters are the refractive index and absorption coefficients of each layer, their thickness, and the PL spectra of the three emitters FIrpic, $Ir(ppy)_3$ and $Ir(MDQ)_2(acac)$. Figure 7.18 shows the calculated forward radiance of each emitter in the complete layer stack, by simply setting the emission intensity of the other two emitters to zero. Apparently, while the first emis-

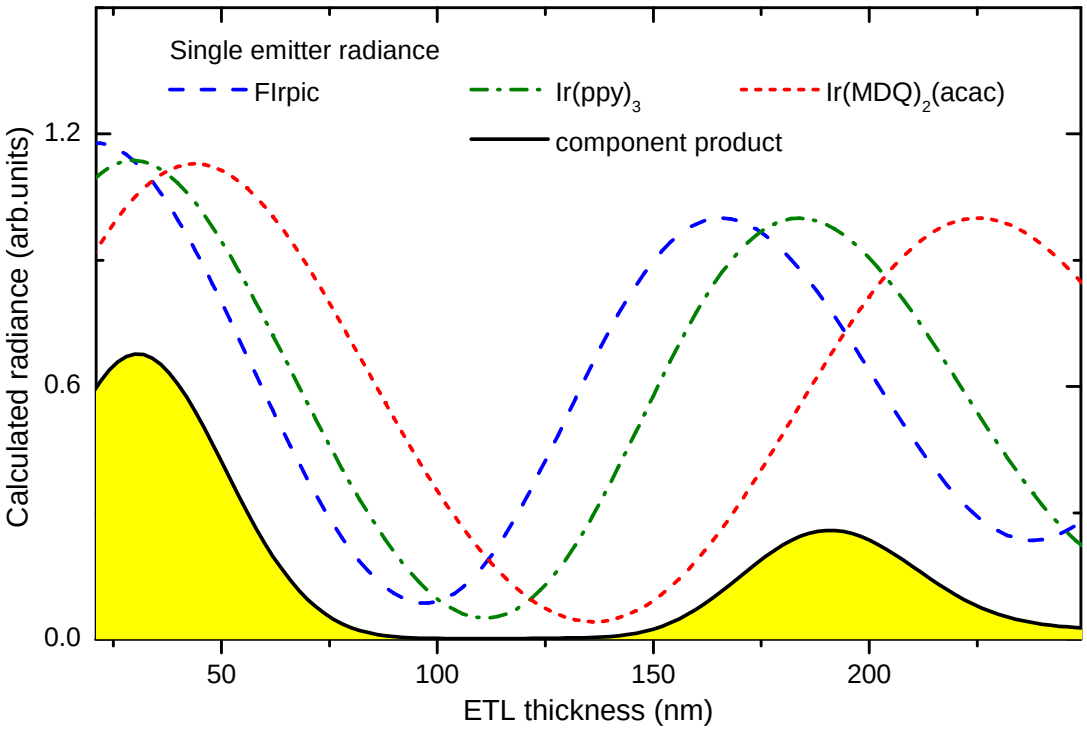

Figure 7.18: Calculated emitted radiance in forward direction as a function of ETL thickness. Based on the white OLED layer stack, the radiance is calculated for each emitter independently, by turning the emission of the other emitters off. The black solid line corresponds to the product of the single emitter radiance plots.

sion maxima of all emitters lie very closely together, the corresponding optimum values in the second maximum differ by approximately 60 nm from the FIrpic to the $Ir(MDQ)_2(acac)$ emission. In addition, the product of the radiance curves for each emitter is calculated, plotted as the black solid line. It shows the overlap being larger in the first maximum by a factor of roughly two. It is the component product that determines the optimal thickness for the spectrally integrated radiance maximum. Clearly, the peak of the product almost perfectly coincides with the radiance maximum for $Ir(ppy)_3$ – the green emitter.[3] Thus, by optimizing the ETL thickness in the second order range to maximum outcoupling values, the green emission is inevitably enhanced, while at the same time blue and green intensities are suppressed. This effect agrees with the experimentally observed changes in the EL spectra for the OLEDs with thick ETLs (Devices 8.4-1 and -2). Further, it explains the differences in the improvement factor from flat to half-sphere configuration between the white devices and the red model OLEDs (3.45 versus 3.00, respectively – cf. App. C). As mentioned above, the white OLEDs are optimized for the highest overall light output which coincides with the maximum value of the green $Ir(ppy)_3$ emission. Con-

[3]It is worth noting that the calculated maximum at 195 nm is slightly smaller than the experimentally determined values of 205 – 210 nm. However, the error in determining the thickness in the evaporation tool is about 5 %, which results in a 10 nm error at 200 nm total thickness.

sequently, blue and red emissions are slightly off their maximum and, with respect to their emission spectrum, located in a detuned cavity. Similar to the discussion of the red model OLEDs in Appendix C, an emitter in a detuned cavity will couple more light at larger angles into the substrate. This high angle contribution can be extracted to air with the half-sphere lens, leading to a larger improvement factor for the white OLEDs.

There are basically two ways to counteract this effect. To some extent, it is possible to re-optimize the EML design (cf. Fig. 7.6), based on the outcoupled spectrum for the OLEDs in the second maximum. For instance, the red emission can be increased artificially by slightly decreasing the TCTA interlayer thickness. In a similar fashion, the blue intensity could be raised by using a thicker TPBi:FIrpic layer. This will reduce the $Ir(ppy)_3$ contribution (which is desired to a certain amount), because the green layer is moved further away from the exciton generating interface. However, the latter change will probably reduce the overall internal quantum efficiency of the EML, because more inefficient blue and less efficient green is used. Apart from re-adressing the EML design, a possible solution to obtain a better colour quality could be the optimization at even higher field maxima. Based on the same calculation, the 5^{th} and 4^{th} order outcoupling maxima fall together for blue and red, respectively, at a calculated ETL thickness of 580 nm. At this position, the green intensity reaches about 60 % of its radiance maximum (5^{th} order), which is located at 630 nm. However, this would cause much higher material consumption, which, in turn, would strongly increase the cost of OLEDs.

Power Efficiency Reaching Fluorescent Tube Values

Finally, in comparison to the OLEDs emitting in the first field antinode, the power efficiencies of the white devices with thick ETLs on high n substrates will be discussed. The power efficiencies* (in flat, patterned, and half-sphere configuration) as a function of luminance are plotted for all four OLEDs discussed in Figure 7.19. The corresponding values at 1,000 cd/m^2 are summarized in Table 7.3. Taking all the substrate modes into account by attaching the half-sphere lens to the OLEDs, very high PEs* of 124 and 111 lm/W are obtained for the devices with the 205 and 210 nm thick Bphen:Cs layers, respectively. These values mark the theoretical limit for the present devices, since all substrate light is coupled out.

By applying the pyramidal structure to these OLEDs, very high values of 90 and 87 lm/W are obtained - to date, the highest values reported in open literature [27]. These efficiencies are on par with commercially available fluorescent tubes (87.5 lm/W [191]). Considering that the latter are conventionally placed in reflector housings, their power efficiency typically drops to $60-70$ lm/W. Such housings are not necessary for OLED lighting tiles, because they will emit all light through their front face. Only inorganic LEDs with about $50-60$ lm/W for commercially available [191] and up to 138 lm/W for lab devices [192] represent an alternative high efficiency technology. However, these devices have a completely different form factor, being a nearly ideal point source. Thus, they are mainly used in applications where direct high-intensity light is desired, e.g. as front lights in the automotive sector, spotlights, or flash lamps.

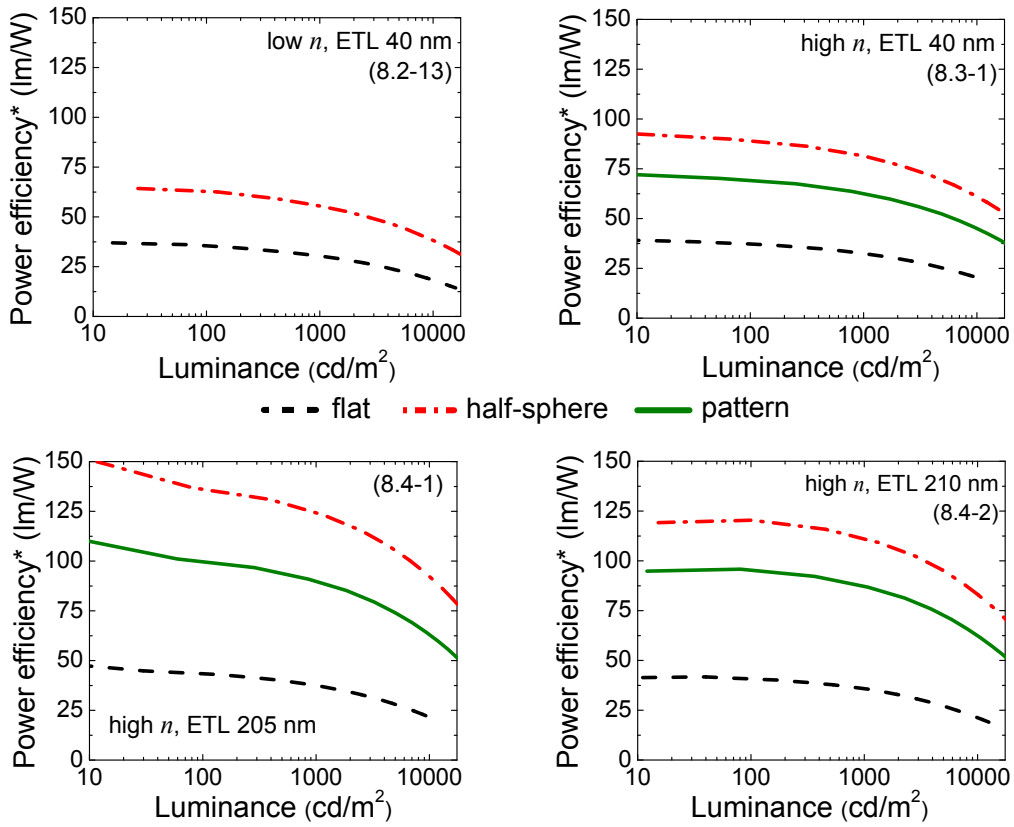

Figure 7.19: Power efficiencies* as a function of luminance of the discussed white OLEDs. Expect for the low refractive index Device 8.2-13, where no patterned structure is available, the PE* is obtained for the flat, patterned, and half-sphere configuration.

Soft, large area light, as naturally emitted by OLEDs, can only be realized with LEDs when diffusive elements are integrated, which will reduce their efficiency.

7.5 Efficiency Roll-Off Characteristics

In this last section of Chapter 7, the efficiency roll-off characteristics of the white OLEDs will be discussed. Despite the fact that the concept of the sub-structured EML design with 1D exciton confinement could not be successfully extended to white light emission, these devices still have an very low roll-off.

From the EQE, the critical current density j_c is estimated to $(100 \pm 20)\,\mathrm{mA/cm^2}$ for all four devices, which is one of the best values reported for phosphorescent white OLEDs [39, 189]. Even though $1{,}000\,\mathrm{cd/m^2}$ are established throughout the literature as an illumination relevant device brightness, even higher luminescence levels are desired for lighting applications which will reduce the size and the cost of lighting tiles. $5{,}000\,\mathrm{cd/m^2}$ represent a realistic device brightness for white OLED applications. The above determined critical current density j_c is about one order of magnitude higher than the current density needed for $5{,}000\,\mathrm{cd/m^2}$, clearly showing the very good high brightness performance of the present white OLED design.

Low Power Efficiency Roll-Off

It is a common fact that the EQE and PE roll-off characteristics are different, with the stronger decrease in efficiency observed for the PE. This is a consequence of additional resistive losses that occur under device operation. Despite the fact that the power efficiency is the most important measure for lighting applications, the increased roll-off in PE did not raise much attention in scientific literature.

In order to quantify the influence of resistive losses, the ratio $\beta_{\mathrm{resistive}}$ of the normalized PE and EQE data is calculated as a function of luminance L (or current density j):

$$\beta_{\mathrm{resistive}} = \frac{\eta_{\mathrm{PE}}(x)/\eta_{\mathrm{PE}}(100\,\mathrm{cd/m^2})}{\eta_{\mathrm{EQE}}(x)/\eta_{\mathrm{EQE}}(100\,\mathrm{cd/m^2})}, \quad \text{where } x \text{ is } L \text{ or } j. \tag{7.2}$$

The corresponding EQE and PE data sets are normalized to a value of $100\,\mathrm{cd/m^2}$, at which the highest efficiency is observed. This is a result of their relatively high leakage currents compared to conventional, electrically undoped OLEDs [193]. This $\beta_{\mathrm{resistive}}$ quantifies the contribution of injection and transport losses of carriers to the PE roll-off. If $\beta_{\mathrm{resistive}}$ would be equal to one, the shape of the normalized EQE and PE data would coincide. This calculation assumes that thermalization losses prior to exciton emission are constant at any luminance. Such losses are for instance the energy difference between a formed singlet exciton on a matrix molecule that is transferred to a lower energy triplet state of the phosphorescent emitter.

The calculated ratio $\beta_{\mathrm{resistive}}$ is plotted in Figure 7.20 versus current density j in a) and versus luminance L in b) for the low n reference OLED and the high n device with thick ETL (205 nm). Additionally, the $\beta_{\mathrm{resistive}}$ ratio is calculated for two highly efficient white OLED concepts from literature, i.e. the reports from Sun *et al.* [11] and Su *et al.* [39]. In comparison to the latter data, the resistive contribution to the PE is the lowest being reported for the present devices. At $5{,}000\,\mathrm{cd/m^2}$, they reach a value of $\beta_{\mathrm{resistive}} = 0.8$, while the corresponding ratios are 0.6 and 0.7 for the devices

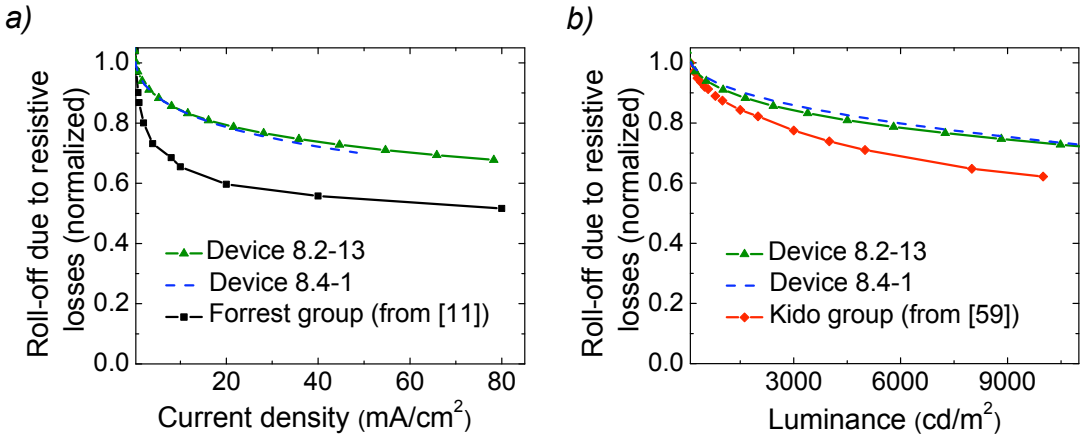

Figure 7.20: Roll-off due to resistive losses ($\beta_{\text{resistive}}$ is plotted on the y-axis), as calculated using Equation (7.2) as a function of a) current density and b) luminance of the present white OLEDs is compared with two highly efficient white OLED concepts from literature (data are taken from Refs. [11, 39]).

of Sun *et al.* [11] and Su *et al.* [39]. It is impressive that $\beta_{\text{resistive}}$ does not differ for OLEDs with thin (8.2-13) and thick (8.4-1) n-doped ETLs. This indicates that the resistive losses are not caused by the doped transport layers (at least this is direct evidence for the n-doped case). At very high fields, which could not be reached for these devices, the j-V characteristics is expected to be limited by the serial resistance of the ITO anode, having a sheet resistance of 25 Ω/square. This would ultimately result in a linear dependence between $\beta_{\text{resistive}}$ and the current density j. However, at low current densities, this ratio decreases super-linearily. Hence, most of the losses must be caused by injection barriers and the remaining electrically undoped organic layers of the OLEDs.

The comparably low roll-off in $\beta_{\text{resistive}}$ allows obtaining extremely high power efficiency values for the present white OLEDs. Using the patterned outcoupling structure, the OLEDs on top of high n substrates still reach very high PE* of 74 and 73 lm/W at very high brightness of 5,000 cd/m² for 205 and 210 nm thick Bphen:Cs layers, respectively. These values are still comparable with the efficiency of fluorescent tubes in a fixture (60 − 70 lm/W) and even better than the average power efficiency of state-of-the-art CFLs (60 lm/W) [191]. Only by considering the decrease of $\beta_{\text{resistive}}$ with increasing luminance or current density, the contribution of resistive losses to the PE roll-off bears great potential for further device improvements.

Chapter 8

Concluding Remarks

Phosphorescent organic LEDs suffer from a drop in efficiency with increasing luminance as a result of bimolecular quenching processes, where triplet-triplet annihilation (TTA) dominates. Thus, many applications can not fully make use of the high potential of electrophosphorescence. Within this work, the underlying microscopic mechanisms that lead to triplet-triplet annihilation and, based on the experimental findings, new concepts for improved high brightness performance of phosphorescent organic LEDs were investigated.

8.1 Triplet-Tiplet Annihilation

The well-known host-guest system CBP:$Ir(ppy)_3$ was studied and compared to a reference system comprising TCTA as matrix in time-resolved photoluminescence experiments. The results showed that host-guest TTA – an unwanted additional TTA channel – sets in at high excitation densities, despite the fact that it reaches a PL efficiency of almost unity at low brightness [78]. This was ascribed to the close lying triplet levels of CBP and $Ir(ppy)_3$, which are only split 150 meV in energy, enabling energy transfer from the guest sites to host species and by that host-guest TTA. With this result, the triplet level arrangement in phosphorescent mixed films should be reconsidered to prevent this unwanted bimolecular annihilation.

This study further focussed on the understanding of TTA in mixed phosphorescent solid films comprising the archetype emitter $Ir(ppy)_3$. By carefully analyzing photoluminescence transients using different triplet-triplet annihilation models, it could be shown that this emitter system cannot reach the theoretical limit, as predicted by calculations. Aggregation of $Ir(ppy)_3$ molecules, which has been suggested before in literature [83], was investigated in transmission electron microscopy, providing direct evidence. Based on these findings, a novel sub-structured emission layer design was introduced that efficiently suppresses exciton motion in one direction of space, leading to a decreased TTA contribution. This concept was successfully integrated in an OLED, for which improved high brightness performance could be realized. Finally, two very similar emitter molecules were compared with respect to their tendency to form aggregates in the mixed film, i.e. $Ir(ppy)_3$ and $Ir(ppy)_2(acac)$. These molecules

have much different permanent dipole moments of 6.26 and 1.91 debye [169], respectively, suggesting that the packing of the molecules also differ. Indeed, the OLEDs comprising $Ir(ppy)_2(acac)$ having a smaller dipole moment showed improved efficiency at high brightness, which was explained by a reduction of TTA. This picture was supported by photoluminescence experiments, in which a smaller TTA rate constant was found for $Ir(ppy)_2(acac)$.

Outlook

Both the results of the sub-structured emission layer concept and of the emitter with a lower dipole moment implicate the large potential to improve the efficiency of phosphorescent OLEDs at high luminance levels. Future investigations should focus on the molecular arrangement of the emitter in the mixed film on microscopic scales. The model calculations in this work show that most of the future OLED applications could fully benefit from the intrinsically high efficiency of phosphorescent emitters, if the theoretical limit for TTA would be reached. Therefore, as a very important first step, future investigations should focus on the understanding of the microscopic mechanisms leading to the formation of emitter aggregates. As said before, the results of this work suggest that the permanent emitter dipole moment influences the molecular packing, but still a deeper understanding of the molecular coupling is necessary. Once the origin of the aggregation is understood, efficient methods are required to prevent the aggregation of the emitter.

It is worth checking if the aggregation depends on the matrix material used and, further, if the tendency of aggregate formation is affected by the fabrication process. For instance, the influence of the substrate temperature and evaporation rate should be addressed with high priority in future research. Apart from that, more effort must be spent on the engineering of improved molecules with lower tendency to form aggregates in the mixed film. Here, the permanent dipole moment is one of various parameters, which should be investigated with respect to triplet-triplet annihilation in the future.

In Chapter 6 it was shown that TTA in photoluminescence is also reduced when the emitter concentration is decreased (from 10 to 1 mol%). However, this effect could not be successfully utilized in real devices, mainly because not all excitons created recombined on the phosphorescent emitter. It is plausible that the excited triplet lifetime of the phosphors, typically in the range of microseconds [6], lead to a saturation of the highly diluted emissive sites. Thus, in order to make use of the reduced TTA in OLEDs, the triplet lifetime of the phosphorescent emitters need to be shortened even further – a very challenging requirement, because it is widely believed that the state-of-the-art emitters are close to the optimum. However, recently Han *et al.* reported on a modified Ir-based emitter which incorporates an active hydrogen [194]. In comparison to $Ir(ppy)_3$, for which they measured an excited lifetime of 713 ns, the modified emitter $Ir(ppi)_2(acac)$ had a drastically reduced time constant of only 52 ns – more than one order of magnitude shorter. When incorporated in real devices using CBP as matrix material, they observed a improved efficiency roll-off for $Ir(ppi)_2(acac)$ at a concentration of 2 wt%. Despite the fact that the absolute

efficiency of these devices were comparably low (7.1 % EQE), their results show that phosphorescent emitter molecules with much shorter lifetimes can be synthesized, which reduces TTA by lowering the exciton density needed for emission. Even more important, such emitters offer the freedom to decrease the emitter concentration in the mixed film. Thus, it should be considered to investigate TTA and emitter aggregation in mixed solid films with shorter lifetimes and lower concentration of the phosphorescent emitter.

8.2 White Phosphorescent Organic LEDs

Based on the results of the various experiments focussing on triplet-triplet annihilation in organic phosphorescent mixed films, a novel, highly efficient concept for white OLEDs was developed. The sub-structured emission layer concept introduced to reduce TTA was the basis of the white emission layer design. Low operating voltages and high external quantum efficiencies were realized by comprising a host-guest system for the blue emitter FIrpic with resonant triplet energies. It was placed in the center of the emission layer so that unused excitons could be harvested in adjacent red and green layers. The emission of these white OLEDs was analyzed in time- and spectrally resolved fashion, where a delayed component in the transients was observed, giving direct evidence for the special design of the blue sub-emission layer.

Additional concepts were followed to further increase the device efficiency of the white OLEDs developed in this work. First, high index glass substrates were used to increase the amount of light coupling into the substrate and, second, thick electron transport layers were comprised to suppress plasmonic losses to the metal cathode. The combination of these results could substantially increase the device performance – compared to a reference OLED: the best device showed a 2.6-fold improvement in the external quantum efficiency. However, as a result of the blue emitter used, the colour of these devices does not meet industry specifications for standard illumination applications. Thus, future work should focus on improving the colour quality while at the same time retaining the high efficiency of this concept. This will be discussed in the following.

Efficiency Forecast

Based on the performance of the white organic LEDs presented in this work, an estimation of a realistic and near-future limit of white OLED power efficiency will be provided. Despite the fact that the following calculation is based on specific device data, it can still be used for general considerations. It includes two very important factors: (i) only emission at the Standard Illuminant A will be considered, and (ii) according to the cost factor of OLED lighting panels in Chapter 2, a more realistic brightness of 5,000 $\mathrm{cd/m^2}$ is used instead of the 1,000 $\mathrm{cd/m^2}$ standard value. All individual steps and assumptions are summarized in Figure 8.2.

To discuss the influence of the emitted spectrum on the power efficiency, the luminous efficacy K_r of a given spectrum, as introduced in Section 4.2, is used. It is defined

as the ratio of luminous and radiant flux with units of lumen per Watt (lm/W), thus, it weights the emitted spectrum with respect to the sensitivity $V(\lambda)$ of the human eye. As mentioned, the white OLED with highest efficiency (Device 8.4-1, 90 lm/W) emits a spectrum that is shifted to the yellow region of the CIE colour space. Its emission corresponds to an efficacy value of 366 lm/W. As a first step in this calculation, the corresponding efficacy of a simulated spectrum is determined having CIE coordinates of the Standard Illuminant A (0.44, 0.41). Therefore, the PL spectra of the three emitters FIrpic, $Ir(ppy)_3$, and $Ir(MDQ)_2(acac)$ are taken (cf. Fig. 3.12) and added to realize emission at colour point A. The resulting spectrum is plotted in Figure 8.1 as the black solid line. This spectrum has an efficacy of 316 lm/W, a value that is noticeably lower compared to the value of Device 8.4-1. The black dotted spectrum in Figure 8.1 represents the PL emission of FIrpic, clearly indicating that the contribution of $Ir(ppy)_3$ is very low. However, the green emission is very important to obtain high efficacies. In order to achieve a balanced spectrum at colour point A, the blue phosphor must emit at shorter wavelength. This influence is simulated in Figure 8.1 by shifting the FIrpic emission to shorter wavelength down to a peak wavelength of 452 nm, which represents a total shift of 23 nm. The resulting simulated spectrum at colour point A corresponds to an increased efficacy of 328 lm/W. Again, by referring to the dotted FIrpic spectrum, the $Ir(ppy)_3$ contribution is strongly enhanced, resulting in a balanced staircase spectrum. Apparently, to realize emission at the Standard Illuminant A, the OLED power efficiency will be lower than the value of Device 8.4-1. In order to realize emission with these specifications, a deeper blue emitter must be incorporated into the present white OLED concept. The emitter iridium(III) bis(4',6'-difluorophenylpyridinato)tetrakis(1-pyrazolyl)borate (FIr6) is a promising candidate for future research having a peak wavelength of approximately 460 nm which corresponds to an increase in triplet energy of roughly 100 meV compared to FIrpic [190, 195, 196]. An appropriate matrix material could be a derivative of spirofluorene based phosphine oxide (SPPO1) [197]. It is an electron transporting material with a LUMO level of 2.7 eV which would fit well into the present white emission layer design.

Starting at a power efficiency of 90 lm/W at 1,000 cd/m^2 that was obtained in Chapter 7 for Device 8.4-1, the transition to a brightness of 5,000 cd/m^2 will decrease the PE to 74 lm/W and the recalculation to colour point A further to 64 lm/W. It is worth noting that this calculation assumes equal internal efficiencies of the three phosphors, which is a good approximation for the emitters used [42, 78], and unchanged operating voltages.

For the conventional OLED configuration with thin electron transport layers and standard glass substrates, the outcoupling efficiency is between $20 - 25\,\%$ [107, 109], however the external quantum efficiency of Device 8.2-13 (reference OLED) is only 14 % EQE at 100 cd/m^2. Assuming that the efficiency can be lifted to 20 % EQE using highly efficient (proprietary) emitters, the device performance could be increased by a factor of 1.43.

Further improvement should be feasible by optimizing the high index outcoupling structure. The present devices used a pyramidal pattern (improvement factor 2.6), however the obtained values differ strongly from the half-sphere data (improvement

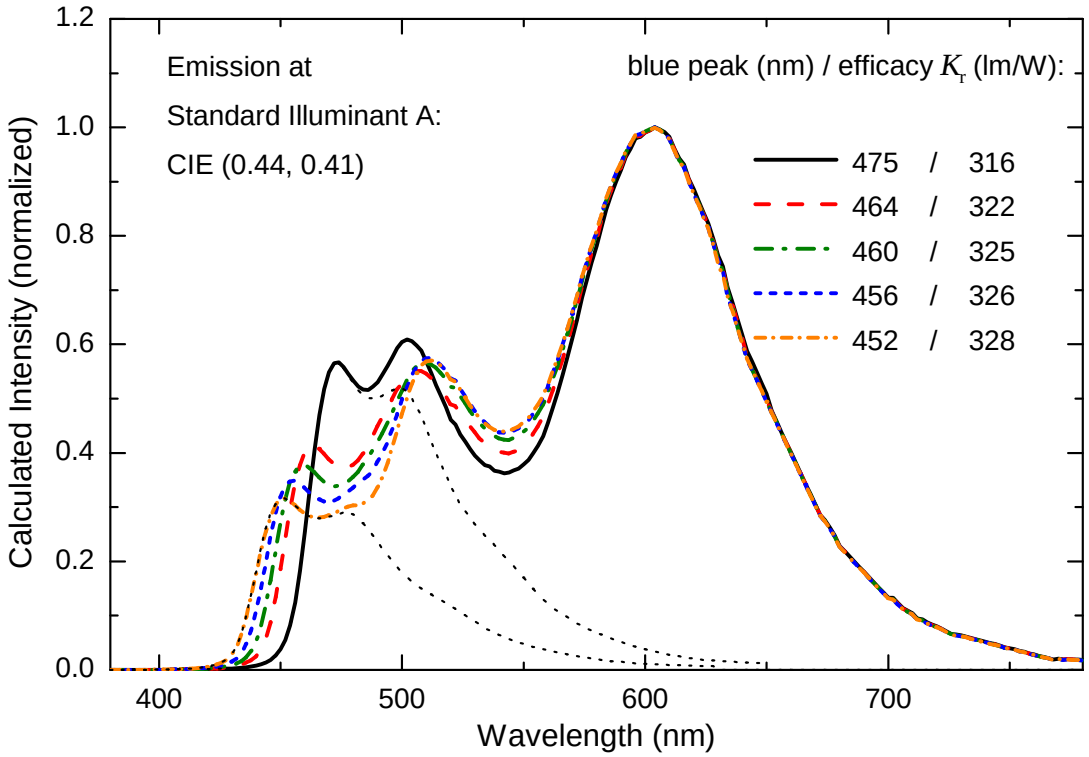

Figure 8.1: Using the PL spectra of the three emitters FIrpic, $Ir(ppy)_3$, and $Ir(MDQ)_2(acac)$, a white spectrum is calculated to meet the colour coordinates of the Standard Illuminant A. Further white spectra with CIE (0.44, 0.41) are calculated by consecutively shifting the blue emitter to shorter wavelengths. For each spectrum, the blue peak wavelength and the resulting luminous efficacy K_r are given. Dotted lines represent the corresponding emission from the blue emitter.

factor 3.45), which mark the theoretical limit of light outcoupling from glass to air. It is worth noting that the pyramidal structure has not been optically optimized, rather it is an early proof-of-principle. Thus, it is reasonable to assume that further improvement can be achieved with an optimized structured, large area outcoupling structure. In present calculation, the outcoupling factor is assumed to increase by 15 % to 3.0 (however this assumption is made without detailed physical reason). One possible structure for better outcoupling would be a microlens array [115] made of high refractive index material.

In accordance with the discussion of the high brightness performance of phosphorescent organic systems in this work, the OLED efficiency can substantially be increased by reducing the efficiency roll-off, both due to bimolecular annihilation (mainly TTA) and to resistive losses ($\beta_{\text{resistive}}$). For the white OLEDs of Chapter 7, the EQE at 5,000 cd/m^2 drops to approximately 80 % of its value obtained at low brightness, where no quenching is expected. Future research should reduce the efficiency roll-off to a point where it is negligible at 5,000 cd/m^2. For instance, green OLEDs can already maintain 97 % of their low brightness EQE using the emitter

$Ir(ppy)_2(acac)$ (cf. Ch. 6). Finally, resistive losses, which are quantified in the $\beta_{\text{resistive}}$ factor, should be reduced by further minimizing energy barriers and improving the charge carrier transport, especially in intrinsic materials. By carefully optimizing the device architecture, it should be feasible to increase $\beta_{\text{resistive}}$ from 0.8 of the present white OLEDs at 5,000 cd/m^2 to 0.9.

In total, taking all the aspects from above together, the power efficiency could be further increased to 155 lm/W at 5,000 cd/m^2 (cf. Fig. 8.2). Note that compared to the performance of Device 8.4-1 this forecasted value corresponds to a much higher device brightness and an improved colour quality that meets lighting industry specifications. Despite the fact that most of the discussed improvement factors are not too far fetched, they show that much more effort must be spend on research and development of white organic LEDs in future to fully make use of their potential.

Device 8.4-1: 90 lm/W at 1,000 cd/m^2 with CIE (0.41, 0.49)

	factor of change	*total change*
operation at 5,000 cd/m^2 (90 lm/W decrease to 74 lm/W)	0.82	0.82
emission at colour point A (efficacy decreases from 366 lm/W to 316 lm/W)	0.86	0.71
deeper blue emitter (efficacy increases from 316 lm/W to 328 lm/W)	1.04	0.74
higher EQE (13.1 % to 20 %)	1.43	1.06
improved outcoupling structure (improvement factor increases from 2.6 to 3.0)	1.15	1.22
reduced EQE roll-off (relative roll-off to 5,000 cd/m^2 increases from 0.8 to 1)	1.25	1.53
reduced resistive losses ($\beta_{\text{resistive}}$ increases from 0.8 to 0.9)	1.13	**1.72**

→ **155 lm/W at 5,000 cd/m^2**

Figure 8.2: Based on the performance of Device 8.4-1, different aspects that contribute to the OLED power efficiency are discussed in respect to their potential for future improvement. For each point, the factor of change is given in the first column and the total change, taking all previous factors into account, in the second column.

Appendix A

Field-Induced Triplet State Dissociation

Referring to the discussion of bimolecular quenching processes in Chapter 3, exciton dissociation is one possible channel that contributes to the efficiency roll-off of organic LEDs. In general, excited states, or their precursor states prior to the exciton formation, can dissociate into free charges due to an applied electric field F [21]. Here, this process is investigated at state-of-the-art multilayer phosphorescent OLEDs mainly to show that for such devices, field-induced exciton dissociation can be ruled out as significant quenching channel [20], although various research groups reported field-induced quenching for both singlet [198, 199] and triplet [21] excitons.

Prepared Devices

To investigate field-induced triplet quenching, the following OLEDs are prepared. Additionally to the phosphors introduced in Chapter 3, a deep red emitting phosphorescent emitter, tris(1-phenylisoquinoline) iridium [$Ir(piq)_3$], is used. Its emission maximum lies at approximately 630 nm [20], therefore the low triplet-gap material NPB is used as a suitable host material.

Device A-1: MeO-TPD:F_4-TCNQ (60 nm, 4 wt%) / NPB (10 nm) / NPB:$Ir(piq)_3$ (20 nm, 20 wt%) / Bphen (10 nm) / Bphen:Cs (60 nm) / Al (100 nm)

Device A-2: MeO-TPD:F_4-TCNQ (60 nm, 4 wt%) / NPB (10 nm) / TCTA: $Ir(ppy)_3$ (20 nm, 7 wt%) / Bphen (10 nm) / Bphen:Cs (60 nm) / Al (100 nm)

Field-Induced Dissociation

Khan *et al.* discussed and differentiated the electric field-induced dissociation of excitons on the one side and of their precursor states on the other [199]. If excitons are quenched, a shorter radiative lifetime τ of the emissive species is expected. In contrast to that, a decrease of the PL intensity without a change in τ indicates a dissociation of precursor states, prior to the exciton formation. Two experiments are

carried out to investigate these processes of field assisted quenching, both using the time-resolved set-up discussed in Chapter 4.

Beforehand, the effective field present in the OLEDs operated at a voltage U needs to be estimated. Due to the use of doped transport layers in this study, the effective field within the device can be calulated as follows:

$$F = \frac{U}{d_{\mathrm{in}}} - \frac{U_{\mathrm{bi}}}{d_{\mathrm{in}}}, \tag{A.1}$$

with U_{bi} being the built-in potential and d_{in} the thickness of the intrinsic (non-doped) layers. The built-in potential is roughly determined by the difference between the LUMO level of the n-doped ETL and the HOMO of the p-doped HTL. This results in $U_{\mathrm{bi}} \sim 2\,\mathrm{V}$. From the current density and luminance versus voltage data (cf. Ref. [20]), the upper limit of applied field strength to $F \sim 0.75\,\mathrm{MV/cm}$ at 5 V operating voltage can be estimated.

Experiments

Photoluminescence transients are recorded as a function of the applied electric field to check if the radiative lifetime τ changes with F. Therefore, an OLED structure is excited with a nitrogen pulse laser at 337 nm. The applied field is increased in reverse bias direction from a roughly field-free condition up to 2.5 MV/cm. Applying reverse bias to an OLED has the great advantage to investigate the influence of the electric field while the current density j is very low. The result is exemplarily shown for Device A-2, comprising TCTA:Ir(ppy)$_3$ as EML, in Figure A.1 a). No difference, neither in amplitude nor in lifetime τ, can be observed up to a field of 1.0 MV/cm. A small amplitude decrease of 5 % is observed at a field strength of approximately 2.5 MV/cm. This value exceeds the upper limit of OLED operation conditions by at least a factor of two. Device A-1 showed qualitatively the same results, i.e. no significant change in the PL amplitude.

To investigate possible dissociation of charge-transfer states that are formed prior to exciton generation, a second experiment is carried out. Here, the OLEDs are pumped with a short voltage pulse of 6.6 V and a duration of 20 µs. The EL mode assures that the exciton dynamics including their generation can be investigated under the conditions within an OLED. Directly after the positive voltage pulse, the voltage is switched to negative values resulting in an electric field during the exciton decay. The EL transients and the corresponding effective field strength F are plotted in Figure A.1, exemplarily depicted for the Device A-1 comprising NPB:Ir(piq)$_3$. Clearly, the EL decay is unaffected by the field variation. This experiment yields the same results for the Device A-2, i.e. no observable change of the EL transient as a function of F.

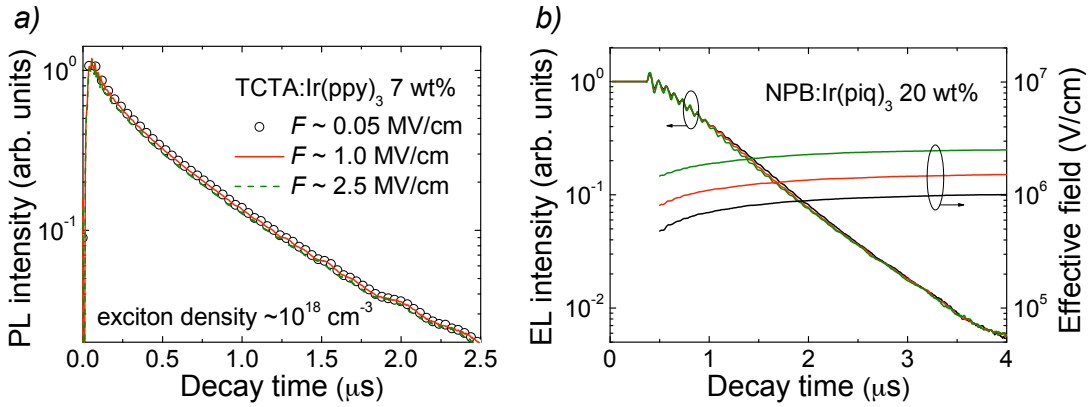

Figure A.1: a) PL transient of the TCTA:$Ir(ppy)_3$ based OLED with variation of the effective electric field strength F. The sample is excited with a 500 ps laser pulse with a wavelength of 337 nm. b) EL time decay of the NPB:$Ir(piq)_3$ based device. Here, a 20 µs positive voltage pulse is used to drive the OLED. The plotted field strength F is achieved by applying a negative voltage immediately after the EL pump pulse.

In conclusion and in contrast to previous work, e.g. by Kalinowski *et al.* [21], field-assisted exciton quenching can be ruled out as the reason for the EQE roll-off in state-of-the-art phosphorescent OLEDs. This is reasonable considering the localized nature of the excited triplet state. The required energy for the dissociation of a triplet state can be estimated by comparing the HOMO-LUMO gap and the triplet state energy. For the case of $Ir(ppy)_3$, the triplet energy amounts to 2.4 eV while the HOMO-LUMO gap is 3.0 eV [8]. This results in an exciton binding energy of approximately 0.6 eV which supports the experimental data that field-induced exciton dissociation is unlikely under OLED operation conditions.

One possible explanation of the experimentally observed field-induced quenching by Kalinowski *et al.* might be the choice of the host material for $Ir(ppy)_3$. In their work, TPD (cf. Sec. 5.1) is used as matrix material. It has a triplet energy of 2.3 eV [77] which is below the corresponding energy of $Ir(ppy)_3$. This leads to a pronounced triplet population of the host material. Possibly, the host triplet states are more likely to be quenched by an external field, partly because of the long triplet state lifetime of TPD ($\sim$ 200 µs) that is two orders of magnitude higher than the $Ir(ppy)_3$ value ($\sim$ 1.5 µs).

Appendix B

Measuring Carrier Mobility by Delayed Exciton Generation

B.1 Established Techniques

As discussed in Chapter 3, the charge carrier mobility μ greatly influences the performance of organic electronic devices. In detail, it determines the carrier drift velocity within the material under an applied electric field F. In consequence, the charge distribution within a device under operation will directly depend on the carrier mobilities of the various materials.

There are many established methods for the measurement of charge carrier mobility, most prominent being: (i) the evaluation of space charge limited currents [92], (ii) the determination of the mobility in an organic field effect transistor (OFET) [89], and (iii) the extraction in a time of flight experiment [88]. It is a widely known fact that the mobility values for a certain material system can strongly differ which is mainly the result of the measurement technique itself as well as due to different preparation techniques. In the SCLC approach (i), one needs to prepare a unipolar device in which ohmic injection to the system is essential. Preparing such a device is a considerable effort and cannot be guaranteed for every material composition. Measuring the mobility in an OFET architecture (ii), in contrast to other techniques, is not necessarily reproducing the bulk property because the transport in an OFET is within the first monolayers adjacent to the dielectric, resulting in orders of magnitude higher carrier densities (cf. Ch. 3 for charge carrier dependent mobility). Time-of-flight experiments (iii), where field-dissociated excitons lead to a current flow through the sample under a constant electric field, has its greatest drawbacks in the necessity of thick layers. It must be assured that the total sample thickness is large compared to the region of light absorption, leading to thicknesses in the micrometer range, thus being not applicable to many materials. In particular for mixed films, it is hard to achieve such a thick layer of uniform quality.

In addition to the above mentioned methods, the charge carrier mobility can be determined by a technique of transient electroluminescence [200–202]. Here, the transit time is determined from the delay of EL-onset with respect to the start of a

voltage pulse. However, this technique becomes more complicated when the number of layers within the device increases. Then, the determined mobility only reflects an effective transport through all layers.

B.2 Delayed Exciton Generation

Here, using the time-resolved set-up introduced in Chapter 4, the mobility of one carrier type is determined directly in a multilayer OLED without the need to take transport through layers adjacent to the EML into account [203]. By evaluating the EL transient of a phosphorescent OLED, in particular the time development following the pump voltage turn-off, a second, strongly field dependent EL feature, is observed. Similar EL features have been reported in literature before [204–206]. Tak *et al.* could attribute such an EL spike following the voltage pulse to an increase in recombination probability of electrons upon switching off the external fields [206]. After careful analysis, this feature can be attributed to a delayed exciton generation, monitored by the phosphorescence of the emitter, which is due to spatially separated electrons and holes under steady state conditions. By determining the transit time t_r required for exciton generation, the applied field F, and the thickness of the EML d, the mobility of the faster charge carrier can be calculated within the OLED. In contrast to alternative methods introduced above, this technique has the great advantage that it reflects the material properties in the device.

Prepared Devices

The following three devices are prepared. Similar to Appendix A, tris(1-phenyl-isoquinoline) iridium [Ir(piq)$_3$] is used as phosphorescent emitter. Again, NPB is used as host material. All devices have the same general architecture, i.e.: glass substrate / anode / HTL / EBL / EML / HBL / ETL / cathode. The HTL is a p-doped mixed system, either MeO-TPD:F_4-TCNQ (cf. Ch. 4) or NHT-5:NDP-2 [1]. An additional HBL in this study is bis(2-methyl-8-quinolinato)-4-phenylphenolate aluminum (BAlq).

Device B-1: Ag (50 nm) / NHT-5:NDP-2 (55 nm, 4 wt%) / NPB (10 nm) / NPB:Ir(piq)$_3$ (20 nm, 20 wt%) / BAlq (10 nm) / Bphen:Cs (40 nm) / Ag (15 nm)

Device B-2: MeO-TPD:F_4-TCNQ (60 nm, 4 wt%) / TCTA (10 nm) / NPB (10 nm) / NPB:Ir(piq)$_3$ (20 nm, 20 wt%) / Bphen (10 nm) / Bphen: Cs (50 nm) / Ag (50 nm)

Device B-3: NHT-5:NDP-2 (55 nm, 4 wt%) / NPB (10 nm) / NPB:Ir(piq)$_3$ (20 nm, 20 wt%) / BAlq (10 nm) / Bphen:Cs (40 nm) / Ag (15 nm)

[1] This p-doped HTL is provided by Novaled AG, Germany.

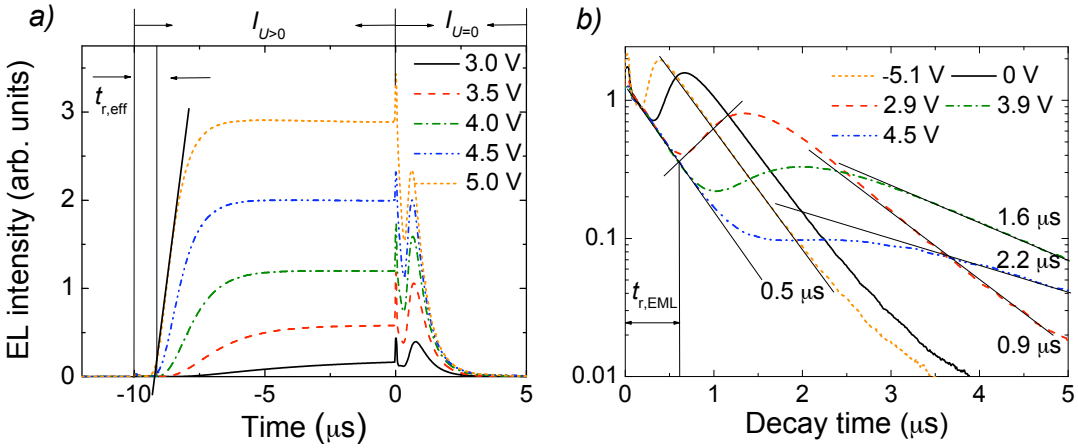

Figure B.1: Electroluminescence transient of Device B-1. a) Variation of the ON-Voltage. b) EL decays for different selected OFF-voltages. The pump voltage pulse ranges from -10 µs to 0 µs. The corresponding current density in the ON-state is 43 mA/cm^2.

In Device B-2, TCTA is additionally inserted between EBL and EML. Devices B-1 and B-3 were stored in nitrogen atmosphere for more than half a year, serving as untreated reference samples in an OLED lifetime study. After the time-resolved measurements of those devices, Device B-2 is prepared intentionally to reproduce the observed effect, as will be discussed subsequently.

Experimental Observation

In Figure B.1, selected EL transients of Device B-1 are shown. The sample is pumped with a 10 µs voltage pulse, starting at -10 µs. As expected (cf. Fig. B.1 a)), the EL intensity is increasing, with a certain delay in respect to the voltage pulse, until a steady-state value is reached. One would expect the EL transient to decay, according to the disactivation of the excited states, with the corresponding excited state radiative lifetime τ. In contrast (cf. Fig. B.1 b)), within the first two microseconds after the voltage pulse, a strong EL feature is observed as an additional increase in EL intensity.

The current-voltage-characteristics of each device are shown in Figure B.2 a). Strong differences in the j-V-data of Device B-1 and B-3 are observed, despite the fact that the OLED structure only differs in the additional bottom Ag contact on top of the ITO stripes. In contrast, these two devices showed similar j-V-characteristics directly after preparation so that the difference can be ascribed to a degradation of the anode of Device B-1, leading to a poor hole injection and, consequently, to a charge carrier imbalance. To achieve a similar carrier imbalance in a reference device, TCTA is inserted between the HTL and EBL in Device B-2, having a low HOMO of -5.9 eV and, thus, hindering the hole injection. Referring to Figure B.2 a), the j-V-data of Device B-1 and B-2 strongly differ from the corresponding data of Device B-3, the latter representing a typical current-voltage dependence. Comparing with Device

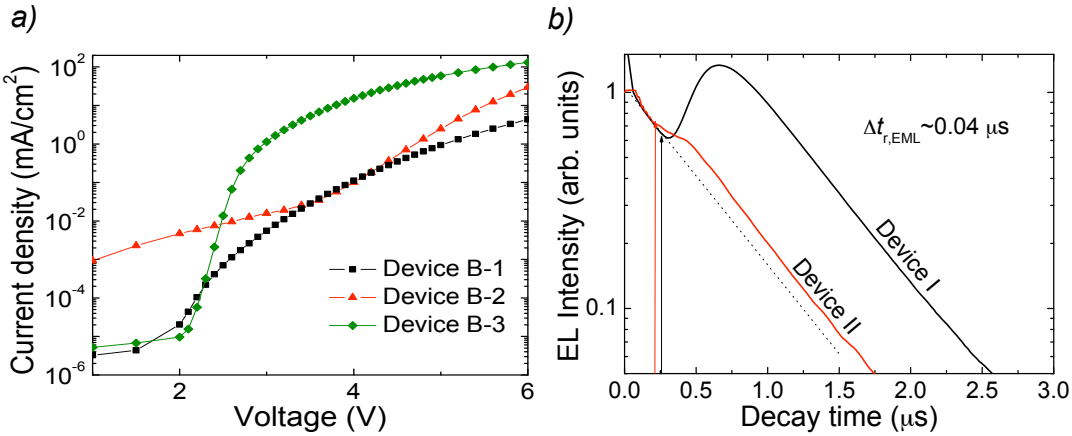

Figure B.2: a) Current density versus operating voltage of all three devices. b) EL transients of Devices B-1 and B-2 at an OFF-voltage of 0 V. The arrows indicate the onset of the delayed recombination.

B-1, Device B-2 shows higher currents below and above approximately 4 V where the curves intersect. The higher current densities for low voltages can be ascribed to higher leakage currents which are the result of suboptimal preparation conditions. The fact that the current is higher for Device B-2 above 4 V suggests that the carrier imbalance in Device B-1 is even higher.

Figure B.2 b) shows the delayed recombination feature to be reproducible with Device B-2. Despite the fact that the intensity of the delayed feature is different, the onset, defined as the deviation from monoexponential decay of the emitter (indicated as the dotted line), is observed at similar times ($\Delta t_{\mathrm{r,EML}} \sim 0.04\,\mu\mathrm{s}$). The layer sequence of Device B-2 is selected to exclude as many origins for this decay feature as possible, i.e. the OLED structure (top- vs. bottom-emitting), the HBL (Bphen vs. BAlq) and the p-doped HTL (NHT-5:NDP-2 vs. MeO-TPD:F_4-TCNQ). None of these variations lead to a missing delayed recombination feature in the EL transient (cf. Fig. B.2 b)).

Delayed Recombination

Referring to Figure B.1 b), the feature of increasing intensity is strongly depending on the electric field (in the OFF-state), showing differences in both its delay and shape. Accordingly, this increase in EL intensity posterior to the voltage pulse cannot be a solely excitonic effect, i.e. an effect due to excitons created in adjacent layers, which are transferred to the emitting sites. Rather, the experimental findings give rise to a population scheme where spatially separated excess charge carriers will diffuse towards each other. Finally, they will form excitons and recombine, leading to the observed EL intensity increase.

To investigate the spectral properties of the delayed emission, the following measurements are carried out. The EL spectra are recorded under cw- and pulsed-mode excitation with a CCD-based fibre spectrometer (cf. Chapter 4) having an integration

time $t_{\mathrm{int}} > 1\,\mathrm{ms}$, far exceeding the time of a single EL pulse. Therefore, referring to Fig. B.1 a), the exciting voltage pulse is adjusted to maintain the highest possible intensity ratio $R := I_{U=0}/I_{U>0}$. No spectral difference between a pulsed-mode spectrum with R=0.8 and a corresponding cw-spectrum could be observed. Additionally, the spectrum remained unchanged under a variation of either the ON- or OFF-voltage. Therefore, the emission of the delayed feature has the same origin as the OLED main emission, i.e. the emission from the triplet state of $Ir(piq)_3$. In difference to the report of Tak *et al.*, the intensity of the delayed generation feature is independent of the length of the excitation voltage pulse [206].

In Figure B.3 a), a scheme of the EML with its adjacent layers is depicted which will be used to explain phenomenologically the appearance of the delayed recombination. The HOMO and LUMO energy values of these materials are given in Ref. [203]. In the present OLED structure, the exciton recombination is in the proximity of the EBL [20]. This is even more pronounced for Devices B-1 and B-2 in which the hole injection is hindered (Device B-2: path 4 in Fig. B.3 a)), as discussed above. Due the carrier imbalance in the EML, excess electrons will most certainly pile up at the EBL. Here, NPB acts as efficient EBL, because the electrons are transported directly on the emitter dopant $Ir(piq)_3$ (cf. Fig. B.3 a) path 1) because of the high dopant concentration of 20 wt%. Furthermore, even though there is no direct proof, an excess hole concentration is expected to be close to the HBL. Despite the fact that holes are the minority carrier type for recombination at the EBL/EML interface, holes will to a limited amount be able to reach the HBL. A possible reason could be the direct trapping of holes at $Ir(piq)_3$ sites (with a certain possibility of hopping transport there - path 2) or the transport on the HOMO of NPB (path 3). The accumulated holes at the HBL will not completely be captured for exciton generation because there is no energy barrier for the electrons.

The spatially separated electrons and holes under steady-state conditions will, in turn, diffuse towards each other when the electrical excitation is turned off, leading to delayed generation and recombination of excitons, as observed in the EL transients. Additionally, the charges can either be accelerated or decelerated, depending on the sign and strength of the applied electric field in the OFF-state. The triplet lifetime of this system within an OLED cavity is approximately 0.5 µs [174]. This value can be extracted from the decay before and after the delayed recombination for vanishing and negative electric fields. In this case, the decay is completely limited by the triplet exciton decay rate. When positive fields are applied during the EL transient, the radiative lifetime increases. Here, the decay is no longer limited by the triplet decay rate, but rather by diffusive processes of the charge carriers prior to exciton formation.

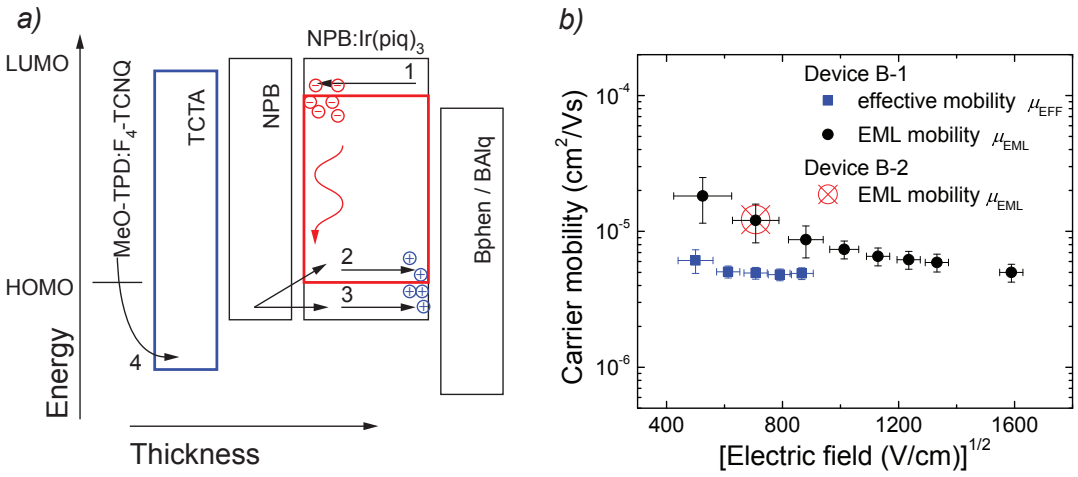

Figure B.3: a) Energy level diagram of the EML and adjacent blocking layers. It illustrates the generation of the delayed exciton generation. b) Carrier mobility versus the electric field, as determined from the delayed EL feature. An additional data point of Device B-2 shows that the reproducibility of this method.

B.3 Determination of the Carrier Mobility

The movement of charge carriers in the EML under a constant electric field, as it can be detected in a time-resolved experiment, is similar to a time-of-flight experiment [88]. Instead of monitoring the current as a function of time, the electroluminescence signal is used to define the time it takes for the carriers to move through the layer. Therefore, the following relationship holds:

$$\mu = \frac{d}{t_{\mathrm{r}} F}, \tag{B.1}$$

with the thickness d of the layer, in which the carriers are transported, the electric field F and the transit time t_{r}. Here, the influence of the accumulated charges is neglected ($F \neq F(x)$ in the EML) simply because their presence and, consequently, the resulting change in $F(x)$, cannot be quantified in experiments.
The electric field is estimated using Equation (A.1) by considering the built-in potential ($U_{\mathrm{bi}} \sim 2\,\mathrm{V}$). The transit time of the charges can be determined in two ways:

- The time from the start of the voltage pulse until the onset of light emission (cf. Fig. B.1 a)). In the case of p- and n-doped transport layers, this corresponds to the time it takes for the faster carrier type to be transported through the blocking and emission layer, denoted $t_{\mathrm{r,EFF}}$. This is similar to the transient EL technique [200–202].

- The time from the end of the voltage pulse until the onset of the delayed recombination (cf. Fig. B.1 b)). Here, the time is a measure for the transport solely through the EML, therefore called $t_{\mathrm{r,EML}}$.

Generally, it is only possible to determine an effective mobility, reflecting the sum of hole (μ_h) and electron (μ_e) mobility because both hole and electron contribute to the delayed exciton generation. Here, it is assumed that only the faster carrier type determines the mobility, which holds for a number of organic compounds:

$$t_r = \frac{d}{(\mu_\mathrm{h} + \mu_\mathrm{e})F} \approx \frac{d}{\mu_\mathrm{faster} F}. \tag{B.2}$$

The corresponding mobility data is plotted in Figure B.3 b). Taking into account that the recombination takes place at the EBL, it is assumed that the electrons are the faster charge carriers in this OLED system. Therefore, the effective mobility μ_EFF corresponds to a transport through BAlq and the NPB:Ir(piq)$_3$ EML and μ_EML to the electron mobility of the EML. Figure B.3 b) shows that the electron mobility of the NPB:Ir(piq)$_3$ EML is on the order of $10^{-5}\mathrm{cm}^2(\mathrm{Vs})^{-1}$, slightly decreasing with increasing electric field.

The negative slope of the data is not fully understood. According to Bässler's Gaussian Disorder Model (GDM), at low fields, the mobility decreases with increasing field strength whenever the off-diagonal disorder exceeds the energetic (diagonal) disorder [94]. Upon further field enlargement, the mobility-field-dependence should change its sign to positive values. Unfortunately, higher fields cannot be accessed with the present technique. Still, it is observed that the negative slope decreases to higher fields, approaching zero.

In this study, the field is simply assumed to homogeneously drop over all intrinsic layers, both for the built-in potential and the external fields, and the effect of the accumulated charges is neglected. Both might affect the dependence of mobility as a function of the electric field.

Referring to Figure B.3 b), the carrier mobility for the heterosystem BAlq / NPB:Ir(piq)$_3$, measured with the common EL transient technique [200–202], is slightly lower compared to the EML data. This suggests that the electron mobility for BAlq is lower than the EML data.

Strong simplifications are applied for the evaluation of the data in this investigation, since in reality both charge carriers will move under the applied field. Even though, compared to completely ambipolar transport, where the carriers meet in the middle of the EML, the difference to the determined data would only be a factor of two. Hence, this data represent the upper limit for the faster carrier type. Comparing to hole mobilities for NPB, i.e. $\mu_\mathrm{h} = (6-8) \times 10^{-4}\mathrm{cm}^2(\mathrm{Vs})^{-1}$ for comparable field strengths, it can be derived that the presence of the emitter dopant Ir(piq)$_3$ strongly reduces the hole mobility of the mixed film of NPB:Ir(piq)$_3$ [207]. Otherwise, this method should yield comparable mobility values.

Appendix C

Monochrome OLEDs on High n Substrates with Thick ETLs

In Sections 7.3 and 7.4 of the chapter dealing with highly efficient white OLEDs, high refractive index substrates and thick electron transport layers were introduced as effective methods to drastically increase the light outcoupling. Preceding to the preparation of those white OLEDs, the two concepts are applied to a monochrome red model OLED system in order to determine their potential. It has the further great advantage that the interference conditions within the OLED cavity only have to be fulfilled for one emitter, resulting in a more straightforward optimization of the ETL thickness.

For this study, the already introduced red emitter $Ir(MDQ)_2(acac)$ is used, diluted into a NPB matrix at a concentration of 10 wt% [42]. The thickness of the p-doped HTL and the n-doped ETL, the latter showing a thickness variation from first to second emission maximum, are determined using the thin-film optics simulation software Etfos v1.3 (Fluxim AG, Winterthur, Switzerland). In contrast to the silver cathode of the white OLEDs in Chapter 7, aluminum is used as standard cathode material. The substrate type is varied from standard glass with $n = 1.51$ to high index glass substrates with $n_{\text{high}} = 1.78$. Similar to the measurements of the white OLEDs, the devices are measured in flat and half-sphere configuration. The patterned structure was not available at that time.

OLED Stack: **substrate** / ITO (90 nm) / MeO-TPD:NDP-2 (65 nm, 4 wt%) / NPB (10 nm) / NPB:$Ir(MDQ)_2(acac)$ (20 nm, 10 wt%) / Bphen (10 nm) / **ETL** / Al (100 nm)

Device C-1: substrate: $n = 1.51$, ETL: Bphen:Cs (40 nm)

Device C-2: substrate: $n = 1.51$, ETL: Bphen:Cs (210 nm)

Device C-3: substrate: $n = 1.78$, ETL: Bphen:Cs (40 nm)

Device C-4: substrate: $n = 1.78$, ETL: Bphen:Cs (210 nm)

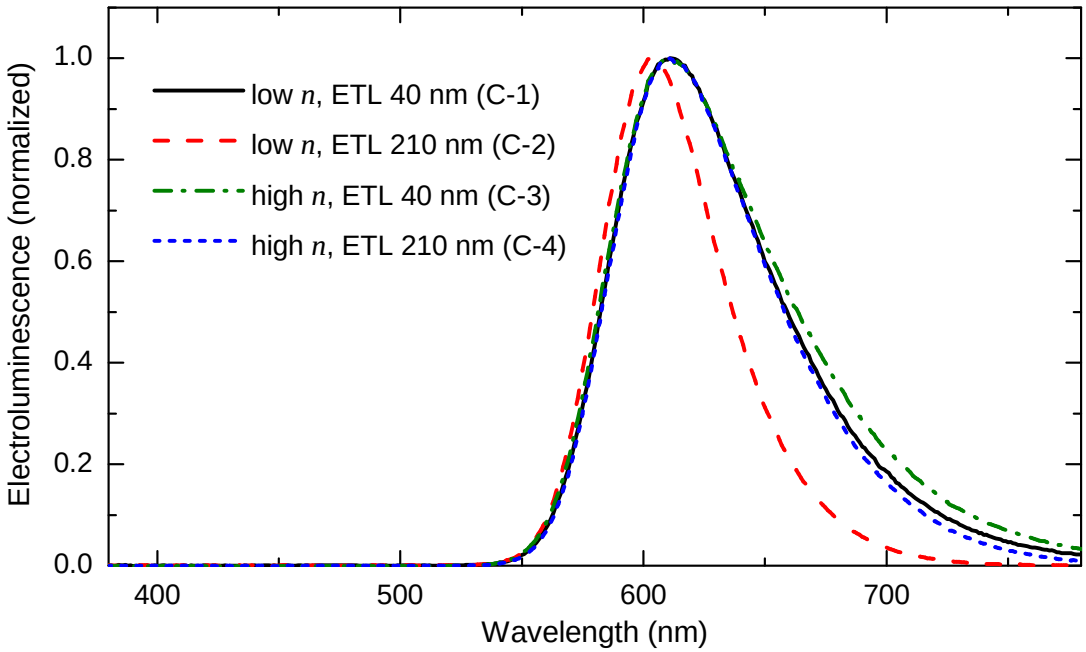

Figure C.1: Electroluminescence spectra of all devices, measured at 1,000 cd/m^2 in forward direction. Device C-2 with the low n substrate and thick ETL shows a noticeable blue-shift and spectral narrowing.

				flat	half-sphere	
Device No.	n	ETL (nm)	voltage (V)	EQE* (%)		improvement
C-1	1.51	40	2.75	14.6	25.2	1.72
C-2	1.51	210	2.79	[7.4]	[19.5]	[2.60]
C-3	1.78	40	2.73	14.5	35.6	2.45
C-4	1.78	210	2.72	14.3	42.8	3.00

Table C.1: Performance overview of red OLEDs with variations in the substrate refractive index n and the thickness of the ETL. EQE* of all devices are obtained at 1,000 cd/m^2 in an integrating sphere. In the last column, the improvement factor between flat and half-sphere data is shown. The efficiency values for Device C-2 are given in parentheses because the OLED has a detuned cavity, resulting in the low flat value and the large improvement factor.

The EL spectra of all four OLEDs are plotted in Figure C.1. The reference OLED with low index substrate and first order ETL thickness shows an emission peak at roughly 610 nm. Both devices on the high index substrate resemble this spectrum, but the OLED C-2 with the thick ETL on low n substrate shows a blue-shift to 602 nm and a spectral narrowing. This suggests that the thickness of the ETL for Device C-2 does not agree with the second maximum resonance, resulting in a detuned OLED cavity. It is most likely that this is a result of a processing error, i.e. a wrong ETL thickness is evaporated.

The performance of these OLEDs is summarized in Table C.1. First of all, it is remarkable that all devices show nearly the same operating voltage of roughly 2.75 V at 1,000 cd/m^2, despite the fact that they are accompanied with a variation of the ETL thickness from 40 to 210 nm. This is only possible using the doped transport layers, which clearly underlines their importance for the optical optimization of OLEDs. The external quantum efficiencies of these OLEDs are given at 1,000 cd/m^2 as well. Except for OLED C-2, all devices reach about 14.5 % EQE* in the flat configuration. As a result of the detuned cavity, Device C-2 only yields 7.4 % EQE*. The lower efficiency of Device C-2 also explains its slightly higher operating voltage of 2.79 V (cf. Tab. C.1).

These devices are further measured in the half-sphere configuration to couple out all glass modes, in order to determine the potential of the different concepts applied. The EQE* data are given in Table C.1 as well. While the reference OLED reaches 25.2 % EQE*, which corresponds to an improvement of 1.72, the Device C-3 on high n substrates yields 35.6 % EQE*. This corresponds to an improvement factor of 2.45, which indicates that, compared to the standard glass, about twice as much light can be coupled out from the high index glass substrate. Finally, by placing the emission layer into the second field antinode, an EQE* of 42.8 % is observed that corresponds to an improvement by a factor of 3.00 (cf. discussion of the OLED mode spectrum in Sec 3.6). Thus, the light outcoupling can be further increased by about 38 % by suppressing plasmonic losses to the metal cathode [118].

Interestingly, OLED C-2 with the detuned cavity shows a large improvement factor between flat and half-sphere measurement of 2.60. This is a direct consequence of the wrong ETL layer thickness. If the thickness of the ETL is moved away from the interference condition towards the field node, the light is mainly coupled into the glass at large angles [112]. Thus, it can hardly be coupled to air because of total internal reflection. However, by attaching the large half-sphere to the OLED, all trapped light is coupled out, resulting in this large improvement.

List of Abbreviations

1D	one-dimensional
3D	three-dimensional
AFM	atomic force microscopy
AO	atomic orbital
CFL	compact fluorescent lamp
CIE	Commission Internationale d'Eclairage
CRI	colour rendering index
CT	charge-transfer
cw	continuous wave
DEML	double emission layer
DOS	density of states
EBL	electron blocking layer
EL	electroluminescence
EML	emission layer
EQE	external quantum efficiency
EQE*	external quantum efficiency; determined using an integrating sphere
ETL	electron transport layer
FWHM	full width at half maximum
GDM	Gaussian disorder model
HAADF	high angle annular dark field
HBL	hole blocking layer
HOMO	highest occupied molecular orbital
HTL	hole transport layer
IC	internal conversion
IR	infrared
ISC	intersystem crossing
ITO	indium tin oxide
LCAO	linear combination of atomic orbitals
LCD	liquid crystal display
LED	light-emitting diode
LUMO	lowest unoccupied molecular orbital
MO	molecular orbital
OFET	organic field effect transistor
OLED	organic light-emitting diode

OVPD	organic vapor phase deposition
p-i-n	a layer sequence (typically an OLED stack) with p-doped, intrinsic, and n-doped layers
PD	photodiode
PE	power efficiency
PE*	power efficiency; determined using an integrating sphere
PID	proportional–integral–derivative
PL	photoluminescence
PLED	polymer organic light-emitting diode
QCM	quartz crystal microbalance
RT	room temperature
RZ	recombination zone
SCLC	space charge limited current
SEML	single emission layer
TEM	transmission electron microscopy
TFLC	trap filled limited current
TIR	total internal reflection
TOF	time-of-flight
TPQ	triplet-polaron quenching
TTA	triplet-triplet annihilation
UPS	ultraviolet photoelectron spectroscopy
UV	ultraviolet
VIS	visible
VR	vibrational relaxation

Bibliography

[1] W. Helfrich and W. G. Schneider, "Recombination Radiation In Anthracene Crystals," *Physical Review Letters* **14**, 229 (1965).

[2] C. W. Tang and S. A. VanSlyke, "Organic Electroluminescent Diodes," *Applied Physics Letters* **51**, 913 (1987).

[3] C. W. Tang, S. A. VanSlyke, and C. H. Chen, "Electroluminescence Of Doped Organic Thin-Films," *Journal Of Applied Physics* **65**, 3610 (1989).

[4] M. A. Baldo, D. F. O'Brien, M. E. Thompson, and S. R. Forrest, "Excitonic singlet-triplet ratio in a semiconducting organic thin film," *Physical Review B* **60**, 14422 (1999).

[5] M. Segal, M. A. Baldo, R. J. Holmes, S. R. Forrest, and Z. G. Soos, "Excitonic singlet-triplet ratios in molecular and polymeric organic materials," *Physical Review B* **68**, 075211 (2003).

[6] M. E. Thompson, "The Evolution of Organometallic Complexes in Organic Light-Emitting Devices," *MRS Bulletin* **32**, 694 (2007).

[7] M. A. Baldo, D. F. O'Brien, Y. You, A. Shoustikov, S. Sibley, M. E. Thompson, and S. R. Forrest, "Highly efficient phosphorescent emission from organic electroluminescent devices," *Nature* **395**, 151 (1998).

[8] G. F. He, M. Pfeiffer, K. Leo, M. Hofmann, J. Birnstock, R. Pudzich, and J. Salbeck, "High-efficiency and low-voltage p-i-n electrophosphorescent organic light-emitting diodes with double-emission layers," *Applied Physics Letters* **85**, 3911 (2004).

[9] R. Meerheim, K. Walzer, M. Pfeiffer, and K. Leo, "Ultrastable and efficient red organic light emitting diodes with doped transport layers," *Applied Physics Letters* **89**, 061111 (2006).

[10] J. Kido, M. Kimura, and K. Nagai, "Multilayer White Light-Emitting Organic Electroluminescent Device," *Science* **267**, 1332 (1995).

[11] Y. R. Sun, N. C. Giebink, H. Kanno, B. W. Ma, M. E. Thompson, and S. R. Forrest, "Management of singlet and triplet excitons for efficient white organic light-emitting devices," *Nature* **440**, 908 (2006).

[12] C. W. Tang, "2-Layer Organic Photovoltaic Cell," *Applied Physics Letters* **48**, 183 (1986).

[13] F. Ebisawa, T. Kurokawa, and S. Nara, "Electrical-Properties Of Polyacetylene Polysiloxane Interface," *Journal Of Applied Physics* **54**, 3255 (1983).

[14] A. Tsumura, H. Koezuka, and T. Ando, "Macromolecular Electronic Device - Field-Effect Transistor With A Polythiophene Thin-Film," *Applied Physics Letters* **49**, 1210 (1986).

[15] K. Kudo, M. Yamamashina, and T. Moriizumi, "Field-Effect Measurement Of Organic-Dye Films," *Japanese Journal Of Applied Physics Part 1-Regular Papers Short Notes & Review Papers* **23**, 130 (1984).

[16] H. Boerner, "OLEDs for Lighting," *Proceedings of SPIE* **6192**, 61920U (2006).

[17] I. Sokolik, R. Priestley, A. D. Walser, R. Dorsinville, and C. W. Tang, "Bimolecular reactions of singlet excitons in tris(8-hydroxyquinoline) aluminum," *Applied Physics Letters* **69**, 4168 (1996).

[18] N. C. Giebink and S. R. Forrest, "Quantum efficiency roll-off at high brightness in fluorescent and phosphorescent organic light emitting diodes," *Physical Review B* **77**, 235215 (2008).

[19] M. A. Baldo, C. Adachi, and S. R. Forrest, "Transient analysis of organic electrophosphorescence. II. Transient analysis of triplet-triplet annihilation," *Physical Review B* **62**, 10967 (2000).

[20] S. Reineke, K. Walzer, and K. Leo, "Triplet-exciton quenching in organic phosphorescent light-emitting diodes with Ir-based emitters," *Physical Review B* **75**, 125328 (2007).

[21] J. Kalinowski, W. Stampor, J. Mezyk, M. Cocchi, D. Virgili, V. Fattori, and P. Di Marco, "Quenching effects in organic electrophosphorescence," *Physical Review B* **66**, 235321 (2002).

[22] T. W. Canzler and J. Kido, "Exciton quenching in highly efficient europium-complex based organic light-emitting diodes," *Organic Electronics* **7**, 29 (2006).

[23] S. Reineke, G. Schwartz, K. Walzer, and K. Leo, "Direct observation of host-guest triplet-triplet annihilation in phosphorescent solid mixed films," *Physica Status Solidi RRL* **3**, 67 (2009).

[24] S. Reineke, G. Schwartz, K. Walzer, M. Falke, and K. Leo, "Highly phosphorescent organic mixed films: The effect of aggregation on triplet-triplet annihilation," *Applied Physics Letters* **94**, 163305 (2009).

[25] S. Reineke, G. Schwartz, K. Walzer, and K. Leo, "Reduced efficiency roll-off in phosphorescent organic light emitting diodes by suppression of triplet-triplet annihilation," *Applied Physics Letters* **91**, 123508 (2007).

[26] S. Reineke, T. C. Rosenow, B. Lüssem, and K. Leo, "Improved High-Brightness Efficiency of Phosphorescent Organic LEDs Comprising Emitter Molecules with Small Permanent Dipole Moments," *Advanced Materials* , DOI: 10.1002/adma.201000529 (2010).

[27] S. Reineke, F. Lindner, G. Schwartz, N. Seidler, K. Walzer, B. Lüssem, and K. Leo, "White organic light-emitting diodes with fluorescent tube efficiency," *Nature* **459**, 234 (2009).

[28] N. Zheludev, "The life and times of the LED - a 100-year history," *Nature Photonics* **1**, 189 (2007).

[29] H. Riel, S. Karg, T. Beierlein, B. Ruhstaller, and W. Riess, "Phosphorescent top-emitting organic light-emitting devices with improved light outcoupling," *Applied Physics Letters* **82**, 466 (2003).

[30] V. Bulovic, G. Gu, P. E. Burrows, S. R. Forrest, and M. E. Thompson, "Transparent light-emitting devices," *Nature* **380**, 29 (1996).

[31] Z. L. Shen, P. E. Burrows, V. Bulovic, S. R. Forrest, and M. E. Thompson, "Three-color, tunable, organic light-emitting devices," *Science* **276**, 2009 (1997).

[32] H. Kanno, N. C. Giebink, Y. R. Sun, and S. R. Forrest, "Stacked white organic light-emitting devices based on a combination of fluorescent and phosphorescent emitters," *Applied Physics Letters* **89**, 023503 (2006).

[33] H. Kanno, R. J. Holmes, Y. Sun, S. Kena-Cohen, and S. R. Forrest, "White stacked electrophosphorescent organic light-emitting devices employing MoO_3 as a charge-generation layers," *Advanced Materials* **18**, 339 (2006).

[34] F. Steuber, J. Staudigel, M. Stossel, J. Simmerer, A. Winnacker, H. Spreitzer, F. Weissortel, and J. Salbeck, "White light emission from organic LEDs utilizing spiro compounds with high-temperature stability," *Advanced Materials* **12**, 130 (2000).

[35] B. W. D'Andrade, J. Brooks, V. Adamovich, M. E. Thompson, and S. R. Forrest, "White light emission using triplet excimers in electrophosphorescent organic light-emitting devices," *Advanced Materials* **14**, 1032 (2002).

[36] B. W. D'Andrade, R. J. Holmes, and S. R. Forrest, "Efficient organic electrophosphorescent white-light-emitting device with a triple doped emissive layer," *Advanced Materials* **16**, 624 (2004).

[37] G. Schwartz, K. Fehse, M. Pfeiffer, K. Walzer, and K. Leo, "Highly efficient white organic light emitting diodes comprising an interlayer to separate fluorescent and phosphorescent regions," *Applied Physics Letters* **89**, 083509 (2006).

[38] G. Schwartz, M. Pfeiffer, S. Reineke, K. Walzer, and K. Leo, "Harvesting triplet excitons from fluorescent blue emitters in white organic light-emitting diodes," *Advanced Materials* **19**, 3672 (2007).

[39] S. J. Su, E. Gonmori, H. Sasabe, and J. Kido, "Highly Efficient Organic Blue- and White-Light-Emitting Devices Having a Carrier- and Exciton-Confining Structure for Reduced Efficiency Roll-Off," *Advanced Materials* **20**, 4189 (2008).

[40] G. Schröder and H. Treiber, *Technische Optik*, Vogel Industrie Medien GmbH & Co. KG, Würzburg (2007).

[41] E. Sutter, *Schutz vor optischer Strahlung – Laserstrahlung, inkohärente Strahlung, Sonnenstrahlung*, VDE-Verlag Berlin Offenbach (1999).

[42] R. Meerheim, S. Scholz, S. Olthof, G. Schwartz, S. Reineke, K. Walzer, and K. Leo, "Influence of charge balance and exciton distribution on efficiency and lifetime of phosphorescent organic light-emitting devices," *Journal Of Applied Physics* **104**, 014510 (2008).

[43] M. Pfeiffer and S. R. Forrest, *Nanoelectronics and Information Technology*, Wiley VCH GmbH & Co. KGaA, Weinheim (2003).

[44] H. Yersin, ed., *Highly efficient OLEDs with phosphorescent emitters*, Wiley VCH GmbH & Co. KGaA, Weinheim (2008).

[45] M. Klessinger and J. Michl, *Lichtabsorption und Photochemie organischer Moleküle*, VCH Verlagsgesellschaft mbH, Weinheim (1989).

[46] R. A. Serway and J. S. Faughn, eds., *College Physics - Third Edition*, Harcourt Brace College Publishers, Orlando (1992).

[47] P. W. Atkins and J. de Paula, *Atkins' Physical Chemistry*, Oxford University Press, Oxford (2006).

[48] M. Pope and C. E. Swenberg, *Electronic processes in organic crystals*, Oxford University Press, New York (1999).

[49] J. Bienlein and R. Wiesendanger, *Einführung in die Struktur der Materie*, B. G. Teubner GmbH, Wiesbaden (2003).

[50] M. Klessinger, *Elektronenstruktur organischer Moleküle*, Verlag Chemie GmbH, Weinheim (1982).

[51] H. G. O. Becker, *Photochemie*, Deutscher Verlag der Wissenschaften, Berlin (1991).

[52] S. Okada, K. Okinaka, H. Iwawaki, M. Furugori, M. Hashimoto, T. Mukaide, J. Kamatani, S. Igawa, A. Tsuboyama, T. Takiguchi, and K. Ueno, "Substituent effects of iridium complexes for highly efficient red OLEDs," *Dalton Transactions* , 1583 (2005).

[53] M. A. Baldo, S. Lamansky, P. E. Burrows, M. E. Thompson, and S. R. Forrest, "Very high-efficiency green organic light-emitting devices based on electrophosphorescence," *Applied Physics Letters* **75**, 4 (1999).

[54] H. Yersin, D. Donges, W. Humbs, J. Strasser, R. Sitters, and M. Glasbeek, "Organometallic Pt(II) compounds. A complementary study of a triplet emitter based on optical high-resolution and optically detected magnetic resonance spectroscopy," *Inorganic Chemistry* **41**, 4915 (2002).

[55] E. L. Williams, K. Haavisto, J. Li, and G. E. Jabbour, "Excimer-based white phosphorescent organic light emitting diodes with nearly 100% internal quantum efficiency," *Advanced Materials* **19**, 197 (2007).

[56] D. Pentlehner, I. Grau, and H. Yersin, "Triplet state properties of $[Os(phen)_2(dppene)]^{2+}$ in different host materials and host to guest energy transfer in PVK," *Chemical Physics Letters* **455**, 72 (2008).

[57] M. A. Baldo, M. E. Thompson, and S. R. Forrest, "High-efficiency fluorescent organic light-emitting devices using a phosphorescent sensitizer," *Nature* **403**, 750 (2000).

[58] C. Adachi, M. A. Baldo, M. E. Thompson, and S. R. Forrest, "Nearly 100% internal phosphorescence efficiency in an organic light-emitting device," *Journal Of Applied Physics* **90**, 5048 (2001).

[59] H. Yersin, "Triplet emitters for OLED applications. Mechanisms of exciton trapping and control of emission properties," *Transition Metal And Rare Earth Compounds III* **241**, 1 (2004).

[60] G. Schwartz, "Novel Concepts for High-Efficiency White Organic Light-Emitting Diodes," PhD thesis, Technische Universität Dresden (2008).

[61] H. Yersin and D. Donges, "Low-lying electronic states and photophysical properties of organometallic Pd(II) and Pt(II) compounds. Modern research trends presented in detailed case studies," *Transition Metal And Rare Earth Compounds: Excited States, Transitions, Interactions II* **214**, 81 (2001).

[62] E. I. Rashba and M. D. Sturge, eds., *Excitons; Selected Chapters*, North-Holland Physics Publishing, Amsterdam (1987).

[63] S. Adachi, *GaAs and Related Materials - Bulk Semiconducting and Superlattice Properties*, World Scientific Publishing Co. Pte. Ltd. (1999).

[64] S. Kasap, ed., *Springer Handbook of Electronic and Photonic Materials*, Springer Science+Business Media, Inc., New York (2006).

[65] M. Knupfer, "Exciton binding energies in organic semiconductors," *Applied Physics A-Materials Science & Processing* **77**, 623 (2003).

[66] T. Förster, "Zwischenmolekulare Energiewanderung und Fluoreszenz," *Ann. Physik* **2**, 55 (1948).

[67] S. E. Braslavsky, E. Fron, H. B. Rodriguez, E. S. Roman, G. D. Scholes, G. Schweitzer, B. Valeur, and J. Wirz, "Pitfalls and limitations in the practical use of Förster's theory of resonance energy transfer," *Photochemical & Photobiological Sciences* **7**, 1444 (2008).

[68] H. Tanaka, T. Ise, D. Shiomi, K. Sato, and T. Takui, "Ground-state triplet biradicals of nitronyl nitroxide containing a nucleobase substituent as synthons for bio-inspired organic magnets," *Journal Of Low Temperature Physics* **142**, 601 (2006).

[69] J. Reinhold, *Quantentheorie der Moleküle: Eine Einführung*, B. G. Teubner Verlag / GWV Fachverlage GmbH, Wiesbaden (2004).

[70] E. Wigner and E. E. Witmer, "Über die Struktur der zweiatomigen Molekelspektren nach der Quantenmechanik," *Zeitschrift für Physik A Hadrons and Nuclei* **51**, 859 (1928).

[71] D. L. Dexter, "A Theory of Sensitized Luminescence in Solids," *Journal of Chemical Physics* **21**, 836 (1953).

[72] C. B. Murphy, Y. Zhang, T. Troxler, V. Ferry, J. J. Martin, and W. E. Jones, "Probing Förster and Dexter energy-transfer mechanisms in fluorescent conjugated polymer chemosensors," *Journal Of Physical Chemistry B* **108**, 1537 (2004).

[73] A. Fick, "On Liquid Diffusion (Reprinted From The London, Edinburgh, And Dublin Philosophical Magazine And Journal Of Science, Vol 10, Pg 30, 1855)," *Journal Of Membrane Science* **100**, 33 (1995).

[74] Y. C. Zhou, L. L. Ma, J. Zhou, X. M. Ding, and X. Y. Hou, "Effect of a sensing layer on triplet exciton diffusion in organic films," *Physical Review B* **75**, 132202 (2007).

[75] N. C. Giebink, Y. Sun, and S. R. Forrest, "Transient analysis of triplet exciton dynamics in amorphous organic semiconductor thin films," *Organic Electronics* **7**, 375 (2006).

[76] M. A. Baldo and S. R. Forrest, "Transient analysis of organic electrophosphorescence: I. Transient analysis of triplet energy transfer," *Physical Review B* **62**, 10958 (2000).

[77] J. Kalinowski, W. Stampor, J. Szmytkowski, D. Virgili, M. Cocchi, V. Fattori, and C. Sabatini, "Coexistence of dissociation and annihilation of excitons on charge carriers in organic phosphorescent emitters," *Physical Review B* **74**, 085316 (2006).

[78] Y. Kawamura, K. Goushi, J. Brooks, J. J. Brown, H. Sasabe, and C. Adachi, "100% phosphorescence quantum efficiency of Ir(III) complexes in organic semiconductor films," *Applied Physics Letters* **86**, 071104 (2005).

[79] Y. Kawamura, J. Brooks, J. J. Brown, H. Sasabe, and C. Adachi, "Intermolecular interaction and a concentration-quenching mechanism of phosphorescent Ir(III) complexes in a solid film," *Physical Review Letters* **96**, 017404 (2006).

[80] T. Kobayashi, N. Ide, N. Matsusue, and H. Naito, "Temperature dependence of photoluminescence lifetime and quantum efficiency in neat *fac*-Ir(ppy)$_3$ thin films," *Japanese Journal Of Applied Physics Part 1-Regular Papers Brief Communications & Review Papers* **44**, 1966 (2005).

[81] K. Goushi, R. Kwong, J. J. Brown, H. Sasabe, and C. Adachi, "Triplet exciton confinement and unconfinement by adjacent hole-transport layers," *Journal Of Applied Physics* **95**, 7798 (2004).

[82] C. Adachi, R. C. Kwong, P. Djurovich, V. Adamovich, M. A. Baldo, M. E. Thompson, and S. R. Forrest, "Endothermic energy transfer: A mechanism for generating very efficient high-energy phosphorescent emission in organic materials," *Applied Physics Letters* **79**, 2082 (2001).

[83] W. Staroske, M. Pfeiffer, K. Leo, and M. Hoffmann, "Single-step triplet-triplet annihilation: An intrinsic limit for the high brightness efficiency of phosphorescent organic light emitting diodes," *Physical Review Letters* **98**, 197402 (2007).

[84] E. Engel, K. Leo, and M. Hoffmann, "Ultrafast relaxation and exciton-exciton annihilation in PTCDA at high excitation densities," *Chemical Physics* **325**, 170 (2006).

[85] S. Chandrasekhar, "Stochastic problems in physics and astronomy," *Reviews Of Modern Physics* **15**, 0001 (1943).

[86] R. C. Powell and R. G. Kepler, "Evidence For Long-Range Exciton-Impurity Interaction In Tetracene-Doped Anthracene Crystals," *Physical Review Letters* **22**, 636 (1969).

[87] A. Suna, "Kinematics Of Exciton-Exciton Annihilation In Molecular Crystals," *Physical Review B* **1**, 1716 (1970).

[88] R. G. Kepler, "Charge Carrier Production And Mobility In Anthracene Crystals," *Physical Review* **119**, 1226 (1960).

[89] G. Horowitz, "Organic field-effect transistors," *Advanced Materials* **10**, 365 (1998).

[90] B. Maennig, "Dotierung polykristalliner und amorpher Farbstoffaufdampfschichten - Struktur, Morphologie und Halbleitereigenschaften," Diploma thesis, Technische Universität Dresden (2001).

[91] M. A. Lampert, "Volume-controlled current injection in insulators," *Reports on Progress in Physics* **27**, 329 ((1964)).

[92] P. W. M. Blom, M. J. M. de Jong, and J. J. M. Vleggaar, "Electron and hole transport in poly(p-phenylene vinylene) devices," *Applied Physics Letters* **68**, 3308 (1996).

[93] S. Berleb, "Raumladungsbegrenzte Ströme und Hoppingtransport in organischen Leuchtdioden aus Tris-(8-hydroxy-quinolin)-Aluminium," PhD thesis, Universität Bayreuth (2001).

[94] H. Bässler, "Charge Transport In Disordered Organic Photoconductors - A Monte-Carlo Simulation Study," *Physica Status Solidi B-Basic Research* **175**, 15 (1993).

[95] M. Hoffmann and M. Pfeiffer, *Skript Organische Halbleiter*, lecture notes, Technische Universität Dresden (2004).

[96] P. W. M. Blom, C. Tanase, D. M. de Leeuw, and R. Coehoorn, "Thickness scaling of the space-charge-limited current in poly(p-phenylene vinylene)," *Applied Physics Letters* **86**, 092105 (2005).

[97] P. N. Murgatroyd, "Dimensional Considerations For Space-Charge Conduction In Solids," *Journal Of Physics D-Applied Physics* **3**, 1488 (1970).

[98] C. Tanase, P. W. M. Blom, and D. M. de Leeuw, "Origin of the enhanced space-charge-limited current in poly(p-phenylene vinylene)," *Physical Review B* **70**, 193202 (2004).

[99] J. Staudigel, M. Stossel, F. Steuber, and J. Simmerer, "A quantitative numerical model of multilayer vapor-deposited organic light emitting diodes," *Journal Of Applied Physics* **86**, 3895 (1999).

[100] W. F. Pasveer, J. Cottaar, C. Tanase, R. Coehoorn, P. A. Bobbert, P. W. M. Blom, D. M. de Leeuw, and M. A. J. Michels, "Unified description of charge-carrier mobilities in disordered semiconducting polymers," *Physical Review Letters* **94** (2005).

[101] R. Coehoorn, W. F. Pasveer, P. A. Bobbert, and M. A. J. Michels, "Charge-carrier concentration dependence of the hopping mobility in organic materials with Gaussian disorder," *Physical Review B* **72** (2005).

[102] H.-H. Perkampus, *Encyclopedia of Spectroscopy*, VCH Verlagsgesellschaft mbH, Weinheim (1995).

[103] R. Morris and M. Silver, "Direct Electron-Hole Recombination In Anthracene," *Journal Of Chemical Physics* **50**, 2969 (1969).

[104] U. Albrecht and H. Bässler, "Efficiency Of Charge Recombination In Organic Light-Emitting-Diodes," *Chemical Physics* **199**, 207 (1995).

[105] D. Y. Kondakov, "Characterization of triplet-triplet annihilation in organic light-emitting diodes based on anthracene derivatives," *Journal Of Applied Physics* **102**, 114504 (2007).

[106] M. Segal, M. Singh, K. Rivoire, S. Difley, T. Van Voorhis, and M. A. Baldo, "Extrafluorescent electroluminescence in organic light-emitting devices," *Nature Materials* **6**, 374 (2007).

[107] N. C. Greenham, R. H. Friend, and D. D. C. Bradley, "Angular-Dependence Of The Emission From A Conjugated Polymer Light-Emitting Diode - Implications For Efficiency Calculations," *Advanced Materials* **6**, 491 (1994).

[108] M. H. Lu and J. C. Sturm, "Optimization of external coupling and light emission in organic light-emitting devices: modeling and experiment," *Journal Of Applied Physics* **91**, 595 (2002).

[109] H. Greiner, "Light extraction from organic light emitting diode substrates: Simulation and experiment," *Japanese Journal Of Applied Physics Part 1-Regular Papers Brief Communications & Review Papers* **46**, 4125 (2007).

[110] M. Thomschke, R. Nitsche, M. Furno, and K. Leo, "Optimized efficiency and angular emission characteristics of white top-emitting organic electroluminescent diodes," *Applied Physics Letters* **94** (2009).

[111] C. H. Hsiao, Y. H. Chen, T. C. Lin, C. C. Hsiao, and J. H. Lee, "Recombination zone in mixed-host organic light-emitting devices," *Applied Physics Letters* **89** (2006).

[112] S. Mladenovski, K. Neyts, D. Pavicic, A. Werner, and C. Rothe, "Exceptionally efficient organic light emitting devices using high refractive index substrates," *Optics Express* **17**, 7562 (2009).

[113] S. Möller and S. R. Forrest, "Improved light out-coupling in organic light emitting diodes employing ordered microlens arrays," *Journal Of Applied Physics* **91**, 3324 (2002).

[114] C. F. Madigan, M. H. Lu, and J. C. Sturm, "Improvement of output coupling efficiency of organic light-emitting diodes by backside substrate modification," *Applied Physics Letters* **76**, 1650 (2000).

[115] Y. Sun and S. R. Forrest, "Enhanced light out-coupling of organic light-emitting devices using embedded low-index grids," *Nature Photonics* **2**, 483 (2008).

[116] R. Meerheim, R. Nitsche, and K. Leo, "High-efficiency monochrome organic light emitting diodes employing enhanced microcavities," *Applied Physics Letters* **93**, 043310 (2008).

[117] T. Nakamura, N. Tsutsumi, N. Juni, and H. Fujii, "Thin-film waveguiding mode light extraction in organic electroluminescent device using high refractive index substrate," *Journal Of Applied Physics* **97**, 054505 (2005).

[118] S. Nowy, B. C. Krummacher, J. Frischeisen, N. A. Reinke, and W. Brütting, "Light extraction and optical loss mechanisms in organic light-emitting diodes: Influence of the emitter quantum efficiency," *Journal Of Applied Physics* **104**, 123109 (2008).

[119] B. C. Krummacher, S. Nowy, J. Frischeisen, M. Klein, and W. Brütting, "Efficiency analysis of organic light-emitting diodes based on optical simulation," *Organic Electronics* **10**, 478 (2009).

[120] C. L. Lin, T. Y. Cho, C. H. Chang, and C. C. Wu, "Enhancing light outcoupling of organic light-emitting devices by locating emitters around the second antinode of the reflective metal electrode," *Applied Physics Letters* **88**, 081114 (2006).

[121] G. Gärtner and H. Greiner, "Light extraction from OLEDs with (high) index matched glass substrates," *Proceedings of SPIE* **6999**, 69992T (2008).

[122] K. Neyts, "Simulation of light emission from thin-film microcavities," *J. Opt. Soc. Am. A* **15**, 962 (1998).

[123] M. Pfeiffer, K. Leo, X. Zhou, J. S. Huang, M. Hofmann, A. Werner, and J. Blochwitz-Nimoth, "Doped organic semiconductors: Physics and application in light emitting diodes," *Organic Electronics* **4**, 89 (2003).

[124] J. Kido and T. Matsumoto, "Bright organic electroluminescent devices having a metal-doped electron-injecting layer," *Applied Physics Letters* **73**, 2866 (1998).

[125] J. Blochwitz, M. Pfeiffer, T. Fritz, and K. Leo, "Low voltage organic light emitting diodes featuring doped phthalocyanine as hole transport material," *Applied Physics Letters* **73**, 729 (1998).

[126] J. Blochwitz, T. Fritz, M. Pfeiffer, K. Leo, D. M. Alloway, P. A. Lee, and N. R. Amstrong, "Interface electronic structure of organic semiconductors with controlled doping levels," *Organic Electronics* **2**, 97 (2001).

[127] M. Pfeiffer, A. Beyer, T. Fritz, and K. Leo, "Controlled doping of phthalocyanine layers by cosublimation with acceptor molecules: A systematic Seebeck and conductivity study," *Applied Physics Letters* **73**, 3202 (1998).

[128] B. Maennig, M. Pfeiffer, A. Nollau, X. Zhou, K. Leo, and P. Simon, "Controlled p-type doping of polycrystalline and amorphous organic layers: Self-consistent description of conductivity and field-effect mobility by a microscopic percolation model," *Physical Review B* **64**, 195208 (2001).

[129] J. S. Huang, M. Pfeiffer, J. Blochwitz, A. Werner, J. Salbeck, S. Y. Liu, and K. Leo, "Low operating voltage and high efficiency organic multilayer electroluminescent devices with p-type doped hole injection layer," *Japanese Journal Of Applied Physics Part 1-Regular Papers Short Notes & Review Papers* **40**, 6630 (2001).

[130] A. Nollau, M. Pfeiffer, T. Fritz, and K. Leo, "Controlled n-type doping of a molecular organic semiconductor: Naphthalenetetracarboxylic dianhydride (NTCDA) doped with bis(ethylenedithio)-tetrathiafulvalene (BEDT-TTF)," *Journal Of Applied Physics* **87**, 4340 (2000).

[131] A. G. Werner, F. Li, K. Harada, M. Pfeiffer, T. Fritz, and K. Leo, "Pyronin B as a donor for n-type doping of organic thin films," *Applied Physics Letters* **82**, 4495 (2003).

[132] K. Harada, A. G. Werner, M. Pfeiffer, C. J. Bloom, C. M. Elliott, and K. Leo, "Organic homojunction diodes with a high built-in potential: Interpretation of the current-voltage characteristics by a generalized Einstein relation," *Physical Review Letters* **94**, 036601 (2005).

[133] K. Walzer, B. Maennig, M. Pfeiffer, and K. Leo, "Highly efficient organic devices based on electrically doped transport layers," *Chemical Reviews* **107**, 1233 (2007).

[134] H. Hartnagel, A. Dawar, A. Lain, and C. Jagadish, *Semiconducting Transparent Thin Films*, Institute of Physics Publishing, Bristal, UK (1995).

[135] I. G. Hill, A. Rajagopal, and A. Kahn, "Energy-level alignment at interfaces between metals and the organic semiconductor 4,4'-*N,N'*-dicarbazolyl-biphenyl," *Journal Of Applied Physics* **84**, 3236 (1998).

[136] B. W. D'Andrade, M. E. Thompson, and S. R. Forrest, "Controlling exciton diffusion in multilayer white phosphorescent organic light emitting devices," *Advanced Materials* **14**, 147 (2002).

[137] S. Lamansky, P. Djurovich, D. Murphy, F. Abdel-Razzaq, R. Kwong, I. Tsyba, M. Bortz, B. Mui, R. Bau, and M. E. Thompson, "Synthesis and characterization of phosphorescent cyclometalated iridium complexes," *Inorganic Chemistry* **40**, 1704 (2001).

[138] S. Lamansky, P. Djurovich, D. Murphy, F. Abdel-Razzaq, H. E. Lee, C. Adachi, P. E. Burrows, S. R. Forrest, and M. E. Thompson, "Highly phosphorescent bis-cyclometalated iridium complexes: Synthesis, photophysical characterization,

and use in organic light emitting diodes," *Journal Of The American Chemical Society* **123**, 4304 (2001).

[139] A. B. Tamayo, B. D. Alleyne, P. I. Djurovich, S. Lamansky, I. Tsyba, N. N. Ho, R. Bau, and M. E. Thompson, "Synthesis and characterization of facial and meridional tris-cyclometalated iridium(III) complexes," *Journal Of The American Chemical Society* **125**, 7377 (2003).

[140] A. Tsuboyama, H. Iwawaki, M. Furugori, T. Mukaide, J. Kamatani, S. Igawa, T. Moriyama, S. Miura, T. Takiguchi, S. Okada, M. Hoshino, and K. Ueno, "Homoleptic cyclometalated iridium complexes with highly efficient red phosphorescence and application to organic light-emitting diode," *Journal Of The American Chemical Society* **125**, 12971 (2003).

[141] S. Olthof, R. Meerheim, M. Schober, and K. Leo, "Energy level alignment at the interfaces in a multilayer organic light-emitting diode structure," *Physical Review B* **79** (2009).

[142] V. I. Adamovich, S. R. Cordero, P. I. Djurovich, A. Tamayo, M. E. Thompson, B. W. D'Andrade, and S. R. Forrest, "New charge-carrier blocking materials for high efficiency OLEDs," *Organic Electronics* **4**, 77 (2003).

[143] Q. Xin, W. L. Li, W. M. Su, T. L. Li, Z. S. Su, B. Chu, and B. Li, "Emission mechanism in organic light-emitting devices comprising a europium complex as emitter and an electron transporting material as host," *Journal Of Applied Physics* **101** (2007).

[144] S. R. Forrest, D. D. C. Bradley, and M. E. Thompson, "Measuring the efficiency of organic light-emitting devices," *Advanced Materials* **15**, 1043 (2003).

[145] T. Tsuboi, "Electronic states of phosphorescent molecules $Ir(ppy)_3$ and PtOEP used in organic light emitting diodes," *Journal Of Luminescence* **119**, 288 (2006).

[146] A. Rihani, L. Hassine, J. L. Fave, and H. Bouchriha, "Study of the transient EL slow rise in single layer OLEDs," *Organic Electronics* **7**, 1 (2006).

[147] L. Hassine, H. Bouchriha, J. Roussel, and J. L. Fave, "Transient response of a bilayer organic electroluminescent diode: Experimental and theoretical study of electroluminescence onset," *Applied Physics Letters* **78**, 1053 (2001).

[148] N. Seidler, "Entwicklung einer Architektur for effiziente blaue OLEDs," Diploma thesis, TU Dresden (2009).

[149] S. Watanabe, N. Ide, and J. Kido, "High-efficiency green phosphorescent organic light-emitting devices with chemically doped layers," *Japanese Journal Of Applied Physics Part 1-Regular Papers Brief Communications & Review Papers* **46**, 1186 (2007).

[150] D. Tanaka, H. Sasabe, Y. J. Li, S. J. Su, T. Takeda, and J. Kido, "Ultra high efficiency green organic light-emitting devices," *Japanese Journal Of Applied Physics Part 2-Letters & Express Letters* **46**, L10 (2007).

[151] S. Haneder, E. Da Como, J. Feldmann, J. M. Lupton, C. Lennartz, P. Erk, E. Fuchs, O. Molt, I. Münster, C. Schildknecht, and G. Wagenblast, "Controlling the radiative rate of deep-blue electrophosphorescent organometallic complexes by singlet-triplet gap engineering," *Advanced Materials* **20**, 3325 (2008).

[152] D. Tanaka, Y. Agata, T. Takeda, S. Watanabe, and J. Kido, "High luminous efficiency blue organic light-emitting devices using high triplet excited energy materials," *Japanese Journal Of Applied Physics Part 2-Letters & Express Letters* **46**, L117 (2007).

[153] J. Kalinowski, W. Stampor, M. Cocchi, D. Virgili, V. Fattori, and P. Di Marco, "Triplet energy exchange between fluorescent and phosphorescent organic molecules in a solid state matrix," *Chemical Physics* **297**, 39 (2004).

[154] K. Goushi, Y. Kawamura, H. Sasabe, and C. Adachi, "Unusual phosphorescence characteristics of $Ir(ppy)_3$ in a solid matrix at low temperatures," *Japanese Journal Of Applied Physics Part 2-Letters & Express Letters* **43**, L937 (2004).

[155] E. B. Namdas, A. Ruseckas, I. D. W. Samuel, S. C. Lo, and P. L. Burn, "Photophysics of fac-tris(2-phenylpyridine) iridium(III) cored electroluminescent dendrimers in solution and films," *Journal Of Physical Chemistry B* **108**, 1570 (2004).

[156] E. B. Namdas, A. Ruseckas, I. D. W. Samuel, S. C. Lo, and P. L. Burn, "Triplet exciton diffusion in fac-tris(2-phenylpyridine) iridium(III)-cored electroluminescent dendrimers," *Applied Physics Letters* **86**, 091104 (2005).

[157] Y. Y. Noh, C. L. Lee, J. J. Kim, and K. Yase, "Energy transfer and device performance in phosphorescent dye doped polymer light emitting diodes," *Journal Of Chemical Physics* **118**, 2853 (2003).

[158] Y. Divayana and X. W. Sun, "Observation of excitonic quenching by long-range dipole-dipole interaction in sequentially doped organic phosphorescent host-guest system," *Physical Review Letters* **99**, 143003 (2007).

[159] O. L. Krivanek, N. Dellby, and A. R. Lupini, "Towards sub-angstrom electron beams," *Ultramicroscopy* **78**, 1 (1999).

[160] S. J. Pennycook and D. E. Jesson, "High-Resolution Incoherent Imaging Of Crystals," *Physical Review Letters* **64**, 938 (1990).

[161] C. Adachi, M. A. Baldo, S. R. Forrest, and M. E. Thompson, "High-efficiency organic electrophosphorescent devices with tris(2-phenylpyridine)iridium doped into electron-transporting materials," *Applied Physics Letters* **77**, 904 (2000).

[162] G. F. He, O. Schneider, D. S. Qin, X. Zhou, M. Pfeiffer, and K. Leo, "Very high-efficiency and low voltage phosphorescent organic light-emitting diodes based on a p-i-n junction," *Journal Of Applied Physics* **95**, 5773 (2004).

[163] F. Lindner, K. Walzer, and K. Leo, "Organic heterostructure device with non-volatile memory behavior using electrically doped layers," *Applied Physics Letters* **93** (2008).

[164] S. F. Alvarado, P. F. Seidler, D. G. Lidzey, and D. D. C. Bradley, "Direct determination of the exciton binding energy of conjugated polymers using a scanning tunneling microscope," *Physical Review Letters* **81**, 1082 (1998).

[165] M. Castellani and D. Berner, "Competition between excitons and exciplexes: Experiments on multilayered organic light emitting diodes," *Journal Of Applied Physics* **102** (2007).

[166] M. Mazzeo, D. Pisignano, F. Della Sala, J. Thompson, R. I. R. Blyth, G. Gigli, R. Cingolani, G. Sotgiu, and G. Barbarella, "Organic single-layer white light-emitting diodes by exciplex emission from spin-coated blends of blue-emitting molecules," *Applied Physics Letters* **82**, 334 (2003).

[167] S. L. Lai, M. Y. Chan, Q. X. Tong, M. K. Fung, P. F. Wang, C. S. Lee, and S. T. Lee, "Approaches for achieving highly efficient exciplex-based organic light-emitting devices," *Applied Physics Letters* **93** (2008).

[168] M. Cocchi, D. Virgili, C. Sabatini, and J. Kalinowski, "Organic electroluminescence from singlet and triplet exciplexes: Exciplex electrophosphorescent diode," *Chemical Physics Letters* **421**, 351 (2006).

[169] N. G. Park, G. C. Choi, Y. H. Lee, and Y. S. Kim, "Theoretical studies on the ground and excited states of blue phosphorescent cyclometalated Ir(III) complexes having ancillary ligand," *Current Applied Physics* **6**, 620 (2006).

[170] X. Zhou, D. S. Qin, M. Pfeiffer, J. Blochwitz-Nimoth, A. Werner, J. Drechsel, B. Maennig, K. Leo, M. Bold, P. Erk, and H. Hartmann, "High-efficiency electrophosphorescent organic light-emitting diodes with double light-emitting layers," *Applied Physics Letters* **81**, 4070 (2002).

[171] G. Schwartz, T. H. Ke, C. C. Wu, K. Walzer, and K. Leo, "Balanced ambipolar charge carrier mobility in mixed layers for application in hybrid white organic light-emitting diodes," *Applied Physics Letters* **93**, 073304 (2008).

[172] N. Matsusue, S. Ikame, Y. Suzuki, and H. Naito, "Charge carrier transport in an emissive layer of green electrophosphorescent devices," *Applied Physics Letters* **85**, 4046 (2004).

[173] S. Kodate and I. Suzuka, "Assignments of lowest triplet state in Ir complexes by observation of phosphorescence excitation spectra at 6 K," *Japanese Journal*

Of Applied Physics Part 1-Regular Papers Brief Communications & Review Papers **45**, 574 (2006).

[174] Q. Huang, S. Reineke, K. Walzer, M. Pfeiffer, and K. Leo, "Quantum efficiency enhancement in top-emitting organic light-emitting diodes as a result of enhanced intrinsic quantum yield," *Applied Physics Letters* **89**, 263512 (2006).

[175] S. Mladenovski, S. Reineke, and K. Neyts, "Measurement and simulation of exciton decay times in organic light-emitting devices with different layer structures," *Optics Letters* **34**, 1375 (2009).

[176] S. A. Swanson, G. M. Wallraff, J. P. Chen, W. J. Zhang, L. D. Bozano, K. R. Carter, J. R. Salem, R. Villa, and J. C. Scott, "Stable and efficient fluorescent red and green dyes for external and internal conversion of blue OLED emission," *Chemistry Of Materials* **15**, 2305 (2003).

[177] S. Scholz, C. Corten, K. Walzer, D. Kuckling, and K. Leo, "Photochemical reactions in organic semiconductor thin films," *Organic Electronics* **8**, 709 (2007).

[178] G. Schwartz, S. Reineke, T. C. Rosenow, K. Walzer, and K. Leo, "Triplet Harvesting in Hybrid White Organic Light-Emitting Diodes," *Advanced Functional Materials* **19**, 1319 (2009).

[179] R. J. Holmes, S. R. Forrest, Y. J. Tung, R. C. Kwong, J. J. Brown, S. Garon, and M. E. Thompson, "Blue organic electrophosphorescence using exothermic host-guest energy transfer," *Applied Physics Letters* **82**, 2422 (2003).

[180] R. J. Holmes, S. R. Forrest, T. Sajoto, A. Tamayo, P. I. Djurovich, M. E. Thompson, J. Brooks, Y. J. Tung, B. W. D'Andrade, M. S. Weaver, R. C. Kwong, and J. J. Brown, "Saturated deep blue organic electrophosphorescence using a fluorine-free emitter," *Applied Physics Letters* **87**, 243507 (2005).

[181] M. H. Tsai, Y. H. Hong, C. H. Chang, H. C. Su, C. C. Wu, A. Matoliukstyte, J. Simokaitiene, S. Grigalevicius, J. V. Grazulevicius, and C. P. Hsu, "3-(9-carbazolyl)carbazoles and 3,6-di(9-carbazolyl)carbazoles as effective host materials for efficient blue organic electrophosphorescence," *Advanced Materials* **19**, 862 (2007).

[182] I. Tanaka, Y. Tabata, and S. Tokito, "Energy-transfer and light-emission mechanism of blue phosphorescent molecules in guest-host systems," *Chemical Physics Letters* **400**, 86 (2004).

[183] Y. Kawamura, H. Sasabe, and C. Adachi, "Simple accurate system for measuring absolute photoluminescence quantum efficiency in organic solid-state thin films," *Japanese Journal Of Applied Physics Part 1-Regular Papers Short Notes & Review Papers* **43**, 7729 (2004).

[184] H. Mattoussi, H. Murata, C. D. Merritt, Y. Iizumi, J. Kido, and Z. H. Kafafi, "Photoluminescence quantum yield of pure and molecularly doped organic solid films," *Journal Of Applied Physics* **86**, 2642 (1999).

[185] N. C. Greenham, I. D. W. Samuel, G. R. Hayes, R. T. Phillips, Y. A. R. R. Kessener, S. C. Moratti, A. B. Holmes, and R. H. Friend, "Measurement Of Absolute Photoluminescence Quantum Efficiencies In Conjugated Polymers," *Chemical Physics Letters* **241**, 89 (1995).

[186] G. Schwartz, S. Reineke, K. Walzer, and K. Leo, "Reduced efficiency roll-off in high-efficiency hybrid white organic light-emitting diodes," *Applied Physics Letters* **92**, 053311 (2008).

[187] V. V. Eremenko, V. A. Karachevtsev, and V. V. Slavin, "Phonon termoactivated exciton tunneling in crystals of weak charge transfer complexes N-TCPA doped with Nd8-TCPA," *Chemical Physics* **216**, 1 (1997).

[188] P. Freitag, S. Reineke, B. Lüssem, and K. Leo, "Top emitting white organic light-emitting diodes with high color quality and low voltage characteristics," submitted (2009).

[189] Y. Sun and S. R. Forrest, "High-efficiency white organic light emitting devices with three separate phosphorescent emission layers," *Applied Physics Letters* **91**, 263503 (2007).

[190] Y. R. Sun and S. R. Forrest, "Multiple exciton generation regions in phosphorescent white organic light emitting devices," *Organic Electronics* **9**, 994 (2008).

[191] R. V. Steele, "The story of a new light source," *Nature Photonics* **1**, 25 (2007).

[192] Y. Narukawa, J. Narita, T. Sakamoto, K. Deguchi, T. Yamada, and T. Mukai, "Ultra-high efficiency white light emitting diodes," *Japanese Journal Of Applied Physics Part 2-Letters & Express Letters* **45**, L1084 (2006).

[193] B. W. D'Andrade, M. A. Baldo, C. Adachi, J. Brooks, M. E. Thompson, and S. R. Forrest, "High-efficiency yellow double-doped organic light-emitting devices based on phosphor-sensitized fluorescence," *Applied Physics Letters* **79**, 1045 (2001).

[194] L. L. Han, D. F. Yang, W. L. Li, B. Chu, Y. Chen, Z. S. Su, D. Y. Zhang, F. Yan, Z. Z. Hu, and Z. Q. Zhang, "The reduced triplet-triplet annihilation of electrophosphorescent device doped by an iridium complex with active hydrogen," *Applied Physics Letters* **93**, 153303 (2008).

[195] S. H. Eom, Y. Zheng, N. Chopra, J. Lee, F. So, and J. G. Xue, "Low voltage and very high efficiency deep-blue phosphorescent organic light-emitting devices," *Applied Physics Letters* **93**, 133309 (2008).

[196] R. J. Holmes, B. W. D'Andrade, S. R. Forrest, X. Ren, J. Li, and M. E. Thompson, "Efficient, deep-blue organic electrophosphorescence by guest charge trapping," *Applied Physics Letters* **83**, 3818 (2003).

[197] S. O. Jeon, K. S. Yook, C. W. Joo, and J. Y. Lee, "High efficiency blue phosphorescent organic light emitting diodes using a simple device structure," *Applied Physics Letters* **94**, 013301 (2009).

[198] W. Stampor, J. Kalinowski, P. Di Marco, and V. Fattori, "Electric field effect on luminescence efficiency in 8-hydroxyquinoline aluminum (Alq_3) thin films," *Applied Physics Letters* **70**, 1935 (1997).

[199] M. I. Khan, G. C. Bazan, and Z. D. Popovic, "Evidence for electric field-assisted dissociation of the excited singlet state into charge carriers in MEH-PPV," *Chemical Physics Letters* **298**, 309 (1998).

[200] C. Hosokawa, H. Tokailin, H. Higashi, and T. Kusumoto, "Transient-Behavior Of Organic Thin-Film Electroluminescence," *Applied Physics Letters* **60**, 1220 (1992).

[201] C. Hosokawa, H. Tokailin, H. Higashi, and T. Kusumoto, "Transient Electroluminescence From Hole Transporting Emitting Layer In Nanosecond Region," *Applied Physics Letters* **63**, 1322 (1993).

[202] A. J. Pal, R. Österbacka, K. M. Källman, and H. Stubb, "Transient electroluminescence: Mobility and response time in quinquethiophene Langmuir-Blodgett films," *Applied Physics Letters* **71**, 228 (1997).

[203] S. Reineke, F. Lindner, Q. Huang, G. Schwartz, K. Walzer, and K. Leo, "Measuring carrier mobility in conventional multilayer organic light emitting devices by delayed exciton generation," *Physica Status Solidi B-Basic Solid State Physics* **245**, 804 (2008).

[204] D. J. Pinner, R. H. Friend, and N. Tessler, "Transient electroluminescence of polymer light emitting diodes using electrical pulses," *Journal Of Applied Physics* **86**, 5116 (1999).

[205] B. Ruhstaller, S. A. Carter, S. Barth, H. Riel, W. Riess, and J. C. Scott, "Transient and steady-state behavior of space charges in multilayer organic light-emitting diodes," *Journal Of Applied Physics* **89**, 4575 (2001).

[206] Y. H. Tak, J. Pommerehne, H. Vestweber, R. Sander, H. Bässler, and H. H. Horhold, "Pulsed electroluminescence from organic bilayer light emitting diodes," *Applied Physics Letters* **69**, 1291 (1996).

[207] W. Y. Hung, T. H. Ke, Y. T. Lin, C. C. Wu, T. H. Hung, T. C. Chao, K. T. Wong, and C. I. Wu, "Employing ambipolar oligofluorene as the charge-generation layer in time-of-flight mobility measurements of organic thin films," *Applied Physics Letters* **88**, 064102 (2006).

Acknowledgements

I would like to acknowledge the support of many people that was essential to successfully finish this work. Especially the friendly and motivating atmosphere among the members of the Institut für Angewandte Photophysik (TU Dresden) created an excellent basis for a fruitful and successful scientific work throughout the years.

I am deeply indebted to my supervisor Prof. Dr. Karl Leo for giving my the opportunity to work on this topic and for his continuous academic support and motviation. I am especially grateful for the scientific freedom I always had. Furthermore, I thank him for the preparation of the first review of this work.

I would like express gratitude to Prof. Dr. Josef Salbeck (Universität Kassel) for his effort and expertise in preparing the second review of this thesis.

I would like to acknowledge the advice and guidance of Dr. Karsten Walzer during the first years of my work. I am especially thankful for making the transmission electron microscopy study possible.

I am grateful for the support and interest of Dr. Björn Lüssem as the head of the OLED group in the last year. His thorough examination of my work truly helped to further improve it.

Personally, Frank Lindner deserves my greatest gratitude. I would like to acknowledge his constant and invaluable willingness to assist me at many everyday life issues of experimental work. Most importantly, he always gave me the chance to discuss many (not-yet-thought-to-the-end) ideas – a major contribution to the progress of my work.

I would like to thank Dr. Gregor Schwartz for various discussions we had about processes that take place in OLEDs. Many of the complex problems that arose during my work, I could not have sorted out without our brainstorming. Finally, it was a great help that he introduced my the the topic of white OLEDs.

Dr. Karsten Fehse deserves my thanks for introducing my to the technique of spin-coating and, equally important, for many chats we had about OLEDs in general.

I would like to express my thanks to Dr. Maiken Falke (TU Chemnitz) for her excellent and uncomplicated collaboration in preparing the transmission electron microscopy images.

Finally, a 'big hand' for Nico Seidler helping me getting a nice white OLED photograph done ("Das Foto ist einfach zu gut. Perfekt in Szene gesetzt!" - FAZ Redakteur) and setting up various OLED demos. It has been a great time.

Further thanks go to:
... all other members of the OLED group for their support and cooperation,
... Eva Schmidt, Annelies Wortmann, and Jutta Hunger for their endless patience getting all the paperwork done,
... Kai Schmidt for his IT, photography, and microscopy support,
... Dr. Martin Pfeiffer and Dr. Michael Hoffmann for many fruitful discussions about the aggregation of emitter molecules,
... Prof. Dr. Horst Hartmann for discussions of the quantum chemistry of organic compounds,
... Dr. Sergej Bagnich for teaching me a lot of optical spectroscopy tricks,
... Dr. Sylvia Gang for careful checking and improving the language of the manuscript,
... Christian Kolberg and Carsten Wolf for her technical assistance,
... and Tobias Günther and Jan Förster for their effort in preparing many OLED devices.

My scientific work would not have been possible without the constant support of my parents, for which I am deeply grateful. Throughout my life, they gave me a save and encouraging feeling. It is as important for me to thank my family: Julia, Lilli, and Paula. Julia tremendously supported me during these years, always having an open ear for my problems, even if they were far-off her expertise. It was and is an invaluable enrichment to have them around me, making it much easier to leave the workload behind. Finally, I would like to thank Ute and Lutz, Julias parents, for her enormous support – many things would not have been possible without their help.

Versicherung

Hiermit versichere ich, dass ich die vorliegende Arbeit ohne unzulässige Hilfe Dritter und ohne Benutzung anderer als der angegebenen Hilfsmittel angefertigt habe; die aus fremden Quellen direkt oder indirekt übernommenen Gedanken sind als solche kenntlich gemacht. Die Arbeit wurde bisher weder im Inland noch im Ausland in gleicher oder ähnlicher Form einer anderen Prüfungsbehörde vorgelegt.

Diese Arbeit wurde am Institut für Angewandte Photophysik der Technischen Universität Dresden unter der wissenschaftlichen Betreuung von Prof. Dr. Karl Leo angefertigt.

Hiermit erkenne ich die Promotionsordnung der Fakultät Mathematik und Naturwissenschaften der Technischen Universtität Dresden vom 20. März 2000 an.

Dresden, den 27. November 2009

(Sebastian Reineke)